12-2019

# Methods and Algorithms for Cardiovascular Hemodynamics with Applications to Noninvasive Monitoring of Proximal Blood Pressure and Cardiac Output Using Pulse Transit Time

Yashar Seyed Vahedein
ys5978@rit.edu

# Methods and Algorithms for Cardiovascular Hemodynamics with Applications to Noninvasive Monitoring of Proximal Blood Pressure and Cardiac Output Using Pulse Transit Time

---

Yashar Seyed Vahedein

*Dec, 2019*

KATE GLEASON COLLEGE OF ENGINEERING
ROCHESTER INSTITUTE OF TECHNOLOGY
ROCHESTER, NEW YORK

CERTIFICATE OF APPROVAL

---

Ph.D. DEGREE DISSERTATION

---

The Ph.D. Degree Dissertation of Yashar Seyed Vahedein
has been examined and approved by the
committee as satisfactory for the
dissertation required for the
Ph.D. degree in Engineering

David S. Ross, Chair

Alexander S. Liberson, Advisor

Steven W. Day

David A. Borkholder

Akhtar A. Khan

Date

# Declaration

This dissertation is a presentation of my original research work. Wherever contributions of others are involved, every effort is made to indicate this clearly, with due reference to the literature, and acknowledgment of collaborative research and discussions.

I hereby grant permission to Wallace Center Library of R.I.T. to reproduce my thesis in whole or in part. Any reproduction will not be for commercial use or profit.

*Rochester, Dec, 2019*

Yashar Seyed Vahedein

Rochester Institute of Technology

RIT | Kate Gleason College of Engineering

Kate Gleason College of Engineering

Engineering PhD Program

Ph.D. Dissertation

A Dissertation Submitted in

Partial Fulfillment of the Requirements for the

Degree of Doctorate of Philosophy in Engineering

# Methods and Algorithms for Cardiovascular Hemodynamics with Applications to Noninvasive Monitoring of Proximal Blood Pressure and Cardiac Output Using Pulse Transit Time

Yashar Seyed Vahedein

Dec, 2019

Signature of Author _____

Accepted by _____

Engineering PhD Program Director Date

**Yashar Seyed Vahedein**

*Methods and Algorithms for Cardiovascular Hemodynamics with Applications to Noninvasive Monitoring of Proximal Blood Pressure and Cardiac Output Using Pulse Transit Time*

Ph.D. Dissertation, Dec, 2019

Advisor: Alexander S. Liberson

Committee Chair: David S. Ross

Committee Members: Steven W. Day and David A. Borkholder and Akhtar A. Khan

**Rochester Institute of Technology**

Kate Gleason College of Engineering

1 Lomb Memorial Dr

14623 and Rochester

# Abstract

Advanced health monitoring and diagnostics technology are essential to reduce the unrivaled number of human fatalities due to cardiovascular diseases (CVDs). Traditionally, gold standard CVD diagnosis involves direct measurements of the aortic blood pressure (central BP) and flow by cardiac catheterization, which can lead to certain complications. Understanding the inner-workings of the cardiovascular system through patient-specific cardiovascular modeling can provide new means to CVD diagnosis and relating treatment. BP and flow waves propagate back and forth from heart to the peripheral sites, while carrying information about the properties of the arterial network. Their speed of propagation, magnitude and shape are directly related to the properties of blood and arterial vasculature. Obtaining functional and anatomical information about the arteries through clinical measurements and medical imaging, the digital twin of the arterial network of interest can be generated. The latter enables prediction of BP and flow waveforms along this network. Point of care devices (POCDs) can now conduct in-home measurements of cardiovascular signals, such as electrocardiogram (ECG), photoplethysmogram (PPG), ballistocardiogram (BCG) and even direct measurements of the pulse transit time (PTT). This vital information provides new opportunities for designing accurate patient-specific computational models eliminating, in many cases, the need for invasive measurements.

One of the main efforts in this area is the development of noninvasive cuffless BP measurement using patient's PTT. Commonly, BP prediction is carried out with regression models assuming direct or indirect relationships between BP and PTT. However, accounting for the nonlinear FSI mechanics of the arteries and the cardiac output is indispensable. In this work, a monotonicity-preserving quasi-1D FSI modeling platform is developed, capable of capturing the hyper-viscoelastic vessel wall deformation and nonlinear blood flow dynamics in arbitrary arterial networks. Special attention has been dedicated to the correct modeling of discontinuities, such as mechanical properties mismatch associated with the stent insertion, and the intertwining dynamics of multiscale 3D and 1D models when simulating the arterial network with an aneurysm. The developed platform, titled Cardiovascular Flow ANalysis (CardioFAN), is validated against well-known numerical, in vitro and in vivo arterial network measurements showing average prediction errors of 5.2%, 2.8% and 1.6% for blood flow, lumen cross-sectional area, and BP, respectively. CardioFAN evaluates the local PTT, which enables patient-specific calibration and its application to input signal reconstruction. The calibration is performed based on BP, stroke volume and PTT measured by POCDs. The calibrated model is then used in conjunction with noninvasively measured peripheral BP and PTT to inversely restore the cardiac output, proximal BP and aortic deformation in human subjects. The reconstructed results show average RMSEs of 1.4% for systolic and 4.6% for diastolic BPs, as well as 8.4% for cardiac output. This work is the first successful attempt in implementation of deterministic cardiovascular models as add-ons to wearable and smart POCD results, enabling continuous noninvasive monitoring of cardiovascular health to facilitate CVD diagnosis.

# Acknowledgement

This work was made possible with the help of many people along the way. I would like to take a moment to recognize a few of them here. First and foremost my advisor Dr. Alexander Liberson. I am extremely fortunate that I had the chance to work with you for the past four years. Your advice, brilliant ideas, and thoughtful suggestions helped bring out my best effort to shape this work. Thank you for always treating me as equal and for creating a friendly but productive environment. I cannot even begin to list all the technical and professional skills that I have learned from you, which I will surely carry into my future professional life. I will be forever grateful for your support and will always look forward to our future conversations.

I am deeply indebted to my advisory committee, without whom this work would not be possible. To Dr. Steven Day, thank you for never hesitating to share your deep technical insight and your willingness to include me in collaboration opportunities. I was fortunate to have known you during my time at RIT. Your dept of biofluids knowledge and pleasant way of communication will always be an ideal role model for my future career. To Dr. David Borkholder, I am extremely grateful to you for your valuable comments and guidance. Thank you for giving me the opportunity to conduct my experiments in your lab, and for connecting me with the right people that helped me in running those tests. I would also like to extend my deepest gratitude to Dr. Akhtar Khan. It was always a pleasure speaking with you, and hearing your comments and suggestions. I was fortunate to learn many new applied math concepts during each of your insightful lectures. To Dr. David Ross, thank you for your always thoughtful questions and for your constant willingness to share your expert opinion on the wave propagation phenomena.

I would like to thank Dr. Karl Schwarz, for allowing me to visit the echocardiology lab and for facilitating the ultrasound data acquisition session at university of Rochester, strong memorial hospital. It was always inspiring and fascinating for me to see your dedication to both medical and engineering aspect of healthcare. I would also like to thank Jennifer from the echocardiology lab who directly helped me in obtaining ultrasound images. Special thanks to Krittika Goyal from the Borkholder lab, you tirelessly helped me during the data recordings using FIT seat. I am also grateful to Nicholas Conn, thank you for sharing your expertise and providing me with access to use the FIT seat for data acquisition sessions.

To engineering department head Dr. Edward Hensel, thank you for your tireless guidance and continuous support. I am extremely grateful for your help when I wanted to start the doctoral student association, and when I found an internship opportunity that was related to my research. Thank you for being such a professional role model for all of us at the engineering department. I was fortunate to learn a lot from you on how to systematically approach

research questions and to network effectively. I also wish to thank Rebecca Ziebarth for her continuous support during my PhD studies. Dr. Jeff Cox, Dr. Risa Robinson, Dr. Twyla Cummings, Kate Caliel, Belinda Dunwoody, Rauncie Ryan and the board members of doctoral student association who showed me how to become a better leader in my professional life.

I wish to thank my friends and my second family away from home, who were always there for me during my time studying abroad, Paarth Mehta, Shadi Maleki, Milad Kordeh, Dr. Baharak Eshghipour, Dr. Hamid Tofighi, Dr. Sahar Hashemgeloogerdi, Dr. Mohammad Kazemi Dehkordi, Dr. Niaz Abdolrahim, Dr. Hesam Askari, Shima Khamooshi, Koosha Abdolrahim, Dr.Majid Rabbani and Dr.Mojgan Rabbani, I will always be indebted to all of you.

I am forever indebted to my parents, Nastaran Mesbahi and Mehdi Seyed Vahedein, who gave me the opportunity to seek my dreams and become who I am now with their continuous love and support.

Finally, to my dearest Nargess Hassani, thank you for always being there for me and for your love and support throughout this journey. Thank you for always believing in me and for transforming even the most difficult days of my PhD studies into a pleasant memory.

# Contents

# List of Figures

# 1 Introduction

## 1.1 *in silico* Modeling of Cardiovascular Hemodynamics

Cardiovascular diseases (CVDs) are the number one cause of human fatalities in the world [1]. Human cardiovascular system consists of heterogeneous interacting components, such as organ systems, laminar and turbulent blood flow, regulatory mechanisms, electrical pulses, and interactions between vessel wall tissue and the blood. Interdisciplinary nature of these mechanisms compels researchers from various disciplines to investigate the workings of this system, in order to answer the pressing questions regarding identification and treatment of CVDs. In the last two decades, disease detection devices are becoming smaller and more accessible, with the goal of reducing CVD related deaths by enabling point of care measurements of patient vitals.

Traditionally, medical doctors were diagnosing cardiovascular problems by clinical measurements, requiring multiple hospital visits and on-site tests. They were conducting diagnostic analysis according to a comparison between test results and well-known case studies of different patients or a previously recorded baseline measurements for the same patient. However, apart from being expensive and time consuming, this process had two major issues: 1- the clinical testing procedure was usually invasive, creating discomfort or pain for the patients; 2- the physical and pathological reasons behind the issue was not well-known, causing mistakes in the medical diagnosis process; [2]. Therefore, the research in this area was suffering from these limitations.

To resolve these issues, researchers developed carefully tailored clinical experiments (*in vivo*) and experimental models of the cardiovascular system (*in vitro*). This was a revolutionary step toward improving the diagnostic capabilities of medical professionals and was the onset of the fields such as biomedical engineering and biomechanics [3]. Second wave of the improvements to disease diagnostics and treatment came after the recent advances in computing technology, making computational simulations widely available. These models imitating physiological models were able to predict macroscopic phenomena such as electrical impulse propagation and contraction at the heart as well as the blood flow and pressure dynamics occurring in the heart ventricular chambers, aorta, and the rest of the cardiovascular network. Such models have been used to study a variety of clinical scenarios

and to perform risk stratification. These models are now being incorporated into clinical practice with recent regulations by food and drug administration (FDA) for approved marketed biomedical devices. In addition, they are improving our understanding of the underlying mechanisms of cardiovascular health within a clinical context [4]. Technological advances have played a key role in the popularity of computational models of human organs. They can now offer relatively accurate predictions when compared to *in vivo* and *in vitro* experiments, and are reliable for monitoring the cardiovascular health and potential abnormalities [5], [6]. Moreover, computational models are noninvasive and can be designed to perform patient-specific analysis. Therefore, when validated, they have a significant advantage over the invasive, costly and time-consuming experimental models or clinical tests. However, it should be noted that they require physical calibration to obtain meaningful inputs for each individual patient.

Some of the common questions in designing computational models of biological organs are:

- Is the computational model representing the problem, reliable and robust?
- How much time does it take to set up a computational model compared to an *in vitro* experiment?
- how can model inputs be obtained in a widely accessible procedure?
- Can it predict the parameter of interest in a desired clinical scenario such as aortic aneurysms, coronary artery disease, hypertension etc.?
- Can it be calibrated for each individual patient? or in other words, is the model **patient-specific**?

These are just a few of the main questions when designing a representative model of cardiovascular system. The model needs to be verified and validated with prior art or clinical measurements, and be tested in real patient scenarios, before its predictions can be trusted for medical decision making. Computational model should be low cost and fast enough to replace an *in vitro* model or a clinical test. A clear strategy for obtaining model inputs, such as boundary conditions and physical properties, as well as interpretation of results needs to be devised.

The physiology and anatomy of each patient is different, and thus it is important to calibrate a computational model for individual patients. Figure 1.1, demonstrates a flow chart of steps that are usually taken to develop a patient-specific model.

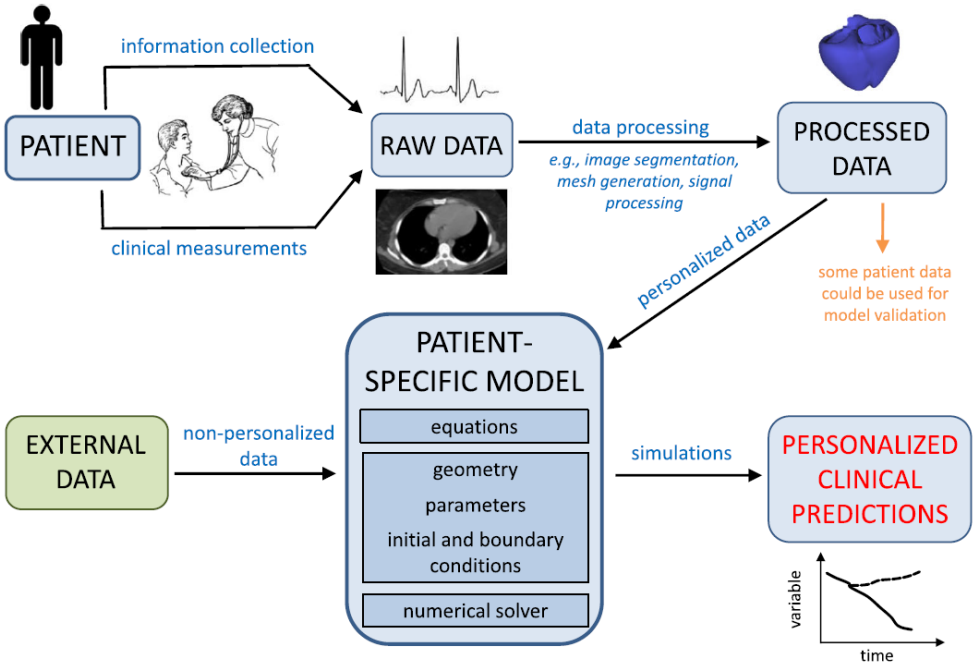


**Fig. 1.1.** – Flow chart of the steps to have personalized clinical predictions using computational models and clinical calibration, reproduced from Gray and Pathmanathan [4]

In view of creating patient-specific data sets for personalized clinical predictions, as shown in figure 1.1, the first step is to collect raw data from patients by clinical measurements and verbal communication. This raw data usually needs further processing to generate the geometrical domains and pathological boundary conditions for a patient-specific model. Other unknown parameters can be set using assumptions based on external patient data, meaning any non-personalized data obtained from sources such as patient questionnaires, or similar experiments or clinical studies in the literature. The combination of input data and mathematical equations forms the patient-specific model. This process of combining experimental data with mathematical modeling to obtain more accurate predictions is called *data assimilation* [7], and usually involves solving some type of an **inverse problem**; where one estimates input parameters using a range of known results. This allows computational cardiovascular models to be used for detecting disorders and during medical interventions, providing accurate quantification and monitoring of the distributions in vital information. For instance cardiac output, blood pressure/flow, and arterial compliance in the blood vessels of interest can be extracted with data assimilation. With that said, computational models can certainly improve our knowledge of the underlying factors responsible for the functioning of our cardiovascular system.

Cardiovascular modeling represents physiological relationships with partial differential equations (PDEs) based on conservation laws (*i.e.*, conservation of charge, species, mass, momentum, or energy). Cardiovascular disorders and medical interventions can now be investigated by numerical models that can predict distributions of cardiac

output, blood pressure/flow, and the pulse wave velocity along the aorta or any of the large arteries of interest [8]. Recently, pulse wave velocity (PWV) and its surrogate pulse transit time (PTT) have attracted significant attention from researchers, especially due to their connection with arterial compliance (*i.e.* distensibility). Many recent studies have introduced novel PWV/PTT measurement techniques and looked at its relation to arterial aging [9], hypertension [10] and even to continuous monitoring of blood pressure [11], [12]. Pulse wave propagation and arterial compliance studies are now an indispensable part of the recent cardiovascular health monitoring research. Consequently numerical models that are able to capture the distribution of vital signals and present an accurate prediction of PTT and PWV have become highly desirable [13]. By integrating them into measurement devices, these models can lead to noninvasive techniques for evaluation of cardiovascular signals, replacing the traditional invasive methods.

One of the important examples of novel noninvasive measurement opportunities is blood pressure and cardiac output measurements close to the heart, which is a common way of diagnosing cardiovascular conditions, and can be very different than the peripheral blood pressure (BP) values [14]. The gold standard method is currently BP and flow measurements using peripherally inserted central-line catheter (PICC). Patients describe catheter insertion as an uncomfortable procedure, and its risk of infection is considered high [15]. Although many valuable contributions in the areas of noninvasive, cuffless, and non-contact BP measurement techniques [12], [16], [17] has been carried out recently, they are usually focusing on predicting peripheral site BP, such as arm or wrist BPs. However, predicting central BP and cardiac output remain a nearly uncharted area. This might be a result of using regression models instead of deterministic fluid-structure interaction (FSI) simulations in the majority of these studies. A need for continuous proximal/central (close to the heart) blood pressure and flow measurement currently exists to reduce the discomfort caused by procedures such as line insertion or angiography [18] and reduce the clinician visits required for diagnosis. As a result, it will reduce cardiovascular events by introducing an accessible, fast and accurate diagnosis method.

One dimensional (1D) models of cardiovascular hemodynamics are very promising in this regard because of their ease of application in a patient-specific context and their ability to be used in conjunction with local three dimensional (3D) computational models; creating an efficient tool for quick quantification of biomarkers in human cardiovascular system [19]. They introduce acceptable accuracy in capturing the physiological mechanisms of blood hemodynamics while having marginally faster convergence rates compared to 3D models. On the other hand, wearable device technology advances now allow many of the smart devices to measure a combination of cardiovascular signals, such as electrocardiogram (ECG), Ballistocardiogram (BCG) or Photoplethysmogram (PPG) [20], [21]. Some of these devices use this data to measure pulse transit time (PTT) and heart rate in-home [22]. With *data assimilation*, these measurements can potentially be combined with 1D hemodynamic models of

cardiovascular system to create novel methods of obtaining proximal/central BP and cardiac output. Therefore, essential components of a robust 1D model for this purpose needs to be re-evaluated.

This work intends to develop an accurate 1D hemodynamics model that can potentially be integrated into a wearable/smart device to reconstruct proximal/central arterial BP and cardiac output with only a few noninvasive peripheral measurements (measured at a site away from the heart). Developed model is first validated against *in vitro* and *in vivo* studies to ensure robustness. A patient-specific calibration procedure is then introduced in conjunction with a data acquisition and testing platform to evaluate the accuracy of this technique against state of the art measurements.

## 1.2 Development and Applications of a Patient-Specific Cardiovascular Model

In last 4 decades, the number of studies on 1D and 3D cardiovascular models have increased rapidly [23], [24]. They span a range of rigid wall computational fluid dynamics (CFD) models of blood flow through arteries, to structural models of pressure distribution across tissue or vessel wall, and the models covering the fluid and structure interaction (FSI) mechanics of pulsatile blood flow. 1D models need clinical measurements to close boundary conditions (BCs) and to predict the outcome of a disorder or slight change inside the arterial network [19]. Clinical measurements, such as MRI imaging data, applanation tonometry, blood pressure from catheter insertion or CT scans, are commonly used to capture the correct BCS, however, they are not widely accessible or are very expensive. Two common road blocks for 1D cardiovascular models are uncertainties in measurements and natural noise in human body. These models usually cannot capture these effects, which in turn leads to large prediction errors when their results are compared to the patient-specific data from gold standard measurement techniques [7]. The quasi-1D FSI blood flow hemodynamics model developed here has three distinctive differences, in addition to a unique calibration procedure, making it ideal for inverse reconstruction of vital signals of the human arterial network:

1. **Monotonicity:** it preserves numerical monotonicity of blood flow and pressure pulse waves, even in case of natural property discontinuity, which can occur in case of geometrical or pathophysiological changes along the path of the blood flow in human arteries.

2. **Nonlinear Fluid and Structure Interaction:** in 1979, Fung et al. [25] showed that the blood vessel properties are not linear elastic. He introduced an anisotropic model, representing the directionality of the elastic properties (hyperelastic anisotropic model). Anisotropic models make it easier to calibrate the systolic peak and diastolic decay, allowing to match nonlinear behavior of real patient vitals. On the contrary to existing variety of elastic and viscoelastic models [26], Fung's anisotropic model is used in our work to capture the FSI effects in the reduced order settins. A combination of physiological vessel wall properties (*i.e.* hyper-viscoelasticity) and nonlinear blood flow, enables accurate representation of pulse wave propagation in compliant arteries [27].

3. **Coupling Capabilities:** Offers versatility to integrate it into other platforms such as smart devices or commercial codes with 3D simulation capabilities for multi-scale simulations.

The algorithm, uniquely developed for this work is titled CardioFAN (Cardiovascular Flow ANalysis), and is available as an open-source code for collaboration and production purposes [1]. Although methods are described here, the inverse reconstruction part of algorithm is an add-on to CardioFAN which is not available in the open-source version at the moment.

### 1.2.1 CardioFAN Applications in Modeling Stented Arteries and Aneurysms

Arterial stenting is a common procedure used to treat atherosclerosis [28], by opening the pathway to the blood flow. Stent is inserted into the clogged artery with a balloon catheter, expanding at the site of narrowing, which in turn changes the local properties of the arterial wall. Previously, the discontinuity at the arterial wall properties would either get smoothened or would not be considered [29]. Here however, monotonicity preserving total variation diminishing (TVD) scheme with an account for the bending moments allows CardioFAN to accurately capture the distensibility over a stented artery. CardioFAN is also used to capture pulse propagation in an arterial aneurysm by coupling it to commercially available 3D softwares. Aneurysms are exposed to 3D effects [30], experiencing flow recirculation and wall shear/normal stresses in the bulging location, which results to their growth and rupture [31]. To capture these properties a 3D model is required. However, finding the correct BCs for an isolated aneurysm model will require invasive clinical procedures [32]. Variational formulation is used to couple 1D and 3D equations, while a coupling MATLAB code connects the two. The 3D model no longer requires inlet and outlet BC measurements, resulting in a universally available multi-scale FSI framework for enclosed systems.

[1] CodeOcean Repository: CodeOcean
Github (Zenodo) Repository: Zenodo

### 1.2.2 Proximal/Central Blood Pressure Measurements

Peripheral pressure measurements, such as upper arm or wrist cuff BP monitors, provide useful information for calibrating a computational model of the arteries [33]. However, pulse-wave amplification at the peripheral artery renders peripheral measurements inadequate to represent the aortic or central arterial pressures [33], [34]. For medical doctors, central aortic pressure is a better predictor of cardiovascular outcome after any alterations in the normal/resting functionality of the cardiovascular system [33], [35] and when evaluating early signs of cardiovascular disease. Therefore, it is essential to develop a noninvasive method to measure the central BP and cardiac output compared to the surrogate peripheral measurements or the invasive catheter method [36].

For the first time, a simple algorithm calibration process is introduced here to calibrate 1D FSI model, CardioFAN to provide patient-specific results. It comprises calibration of the vessel wall mechanical properties and outlet boundary conditions parameters using doppler ultrasound and ECG/BCG and peripheral PPG and BP measurements. The calibrated model then takes the information from peripheral arterial sites, such as wrist BP and heart to wrist PTT to inversely restore patient-specific proximal BP and cardiac output. A single measurement session per day amounted to a minimum of 3-4 calibration and 4 to 5 validation measurement sessions per person in normal and elevated heart rate conditions. Average accuracy of the numerically reconstructed values over 4-5 days of validation are 1.63% for systolic BP, 5.55% for diastolic BP and 9.14% for cardiac output and it goes down to 0.97%, 4.7% and 6.19%, respectively, when both the ultrasound and ECG/BCG/PPG/BP calibration stages are available. This work builds the grounds for a new class of deterministic models for noninvasive prediction of BP and cardiac output which can be used as an accurate point of care tool for cardiovascular monitoring and diagnosis of abnormalities.

## 1.3 Dissertation Structure

This dissertation is divided into two main parts. The first part focuses on the development of CardioFAN, its verification, validation and some of its potential side applications. In the second part, the approach for personalization of CarioFAN and its implementation into a data assimilation platform is discussed. The proof of concept is the preliminary results for central BP and cardiac output inverse reconstruction compared with subject specific measurements. The detailed description of dissertation structure is as follows:

1. **Cardiovascular Physiology (chapter 2):** explores the necessary knowledge of the heart and arterial network physiology to provide insight on the cardiovascular hemodynamics.

2. **in silico models of cardiovascular system (chapter 3):** gives background of different types, prior advances, and applications for the models of cardiovascular system, highlighting the missing features.

3. **Pulse wave velocity and pulse transit time (PTT) (chapter 4):** discusses the current methods and challenges of applying PTT measurement for noninvasive cardiovascular diagnostics, its integration into computational algorithms and implementation in physiological sensors to enable continuous prediction of biological signals. This chapter is intended to familiarize the reader with PTT-based predictive modeling, while emphasizing on the novelty of the technology to inversely reconstruct the central vital signals.

4. **Development and validation of CardioFAN (chapters 5 and 6):** Steps to develop an in-house reduced-order numerical code to capture nonlinear pulse wave propagation in the human hyper-viscoelastic arterial system are discussed. It covers the mathematical formulation, verification and model validation with *in silico, in vitro* and *in vivo* cases. Additional applications of this code, such as multiscale modeling for aortic aneurysm and stented artery simulations are discussed in chapter 6.

5. **Noninvasive PTT-Based Central BP and Cardiac Output Measurement (chapters 7,8 and 9):** proximal BP and cardiac output reconstruction using the patient data captured at peripheral arterial sites is the focus of these chapters. In chapter 7, the formulation of the novel method is presented and it is tested against clinical measurement data for a human aorta, based on prior work available in the literature. Chapter 8, explores data acquisition protocol and how data is collected in order to calibrate CardioFAN for patient-specific tests. Lastly, chapter 9, presents the results of a validation procedure for the patient-specific CardioFAN, demonstrating accuracy of the inverse reconstruction technique for proximal BP and cardiac output prediction during daily human subject tests.

6. **Final remarks and future directions (chapter 10):** It highlights the significance and limitations of presented results and its clinical implications. Finally, future directions for noninvasive prediction of proximal/central BP and cardiac output are proposed.

## 1.4 Objectives

Three simple objectives are aimed to be met until a noninvasive approach for proximal/central BP measurement becomes a possibility. These objectives are listed in figure 1.2

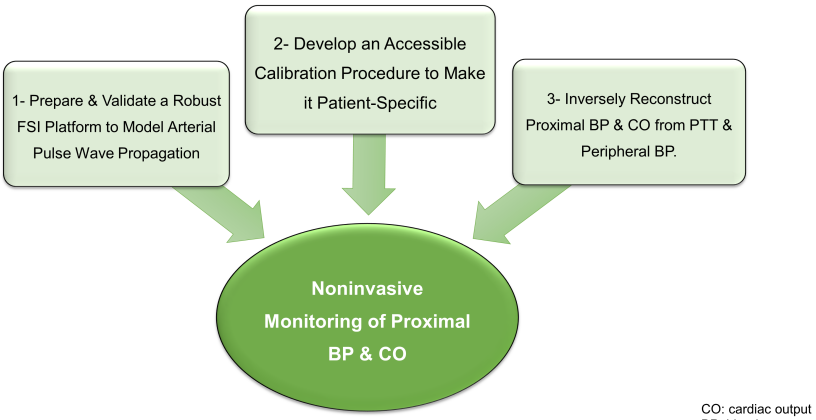


**Fig. 1.2.** – Main objectives of this dissertation

# 2 Heart and Cardiovascular System Physiology

Cardiovascular diseases (CVDs) were responsible for 17.9 million (31%) of global deaths in 2016 [1]. According to American Heart Association (AHA), in United States, an average of 1 death every 40 seconds (30.8% of total death rate) is attributed to a CVD condition [37]. In 2010, CVDs amounted to $273 billion (or 17%) of the US national health expenditure and this number is predicted to increase to $818 billion (triple) by 2030 [38]. A comprehensive understanding of the cardiovascular physiology will enable early diagnosis and treatment of CVDs. Cardiovascular disorders and medical interventions can be diagnosed by accurate quantification and monitoring of cardiovascular biomarkers [8]. Numerical simulation of blood circulation provides a non-invasive tool for modeling the blood hemodynamics and its changes due to the cardiovascular diseases.

In this section a brief overview of heart and blood flow physiology is provided, demonstrating the links to cardiovascular biomechanics.

## 2.1 Cardiovascular System Physiology and Connection to Modeling

The cardiovascular system is responsible for the convective transport of blood (and its contained gases, cells, particles, and heat) between the different organs of the body. In the microcirculation (*i.e.* capillaries), the blood flow undergoes a high resistance, and thus the transport of blood requires a relatively high perfusion. Maintaining this high perfusion pressure is not possible by heart unless the arteries are elastic (*i.e.* the windkessel effect). The heart is a four-chambered pump that propels blood into the systemic and pulmonary circulatory systems (Figure 2.1). The right atrium receives de-oxygenated blood from the systemic veins and pushes it into the right ventricle where the blood heads toward the lungs to get oxygenated. This flow returns to the left atrium, which

completes the pulmonary circulation. From left atrium, the oxygenated blood flows into the left ventricle, where it gets pumped into the aorta and the rest of the systemic arteries.

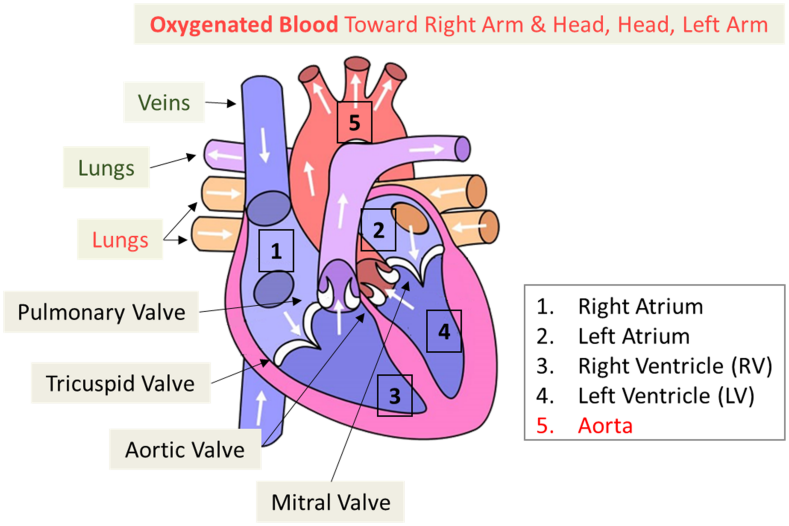


**Fig. 2.1.** – Schematics of the four-chambered heart and its connections to the systemic and pulmonary arteries and veins.

The blood pressure (BP) and flow changes when the blood is pumped from the heart into the elastic arterial system (Figure 2.2). The cardiac cycle, consists of a systolic and diastolic phase, the latter being approximately twice longer than the former. In systole, heart muscle contraction leads to a pressure increase at the left ventricle, which is separated from aortic root with aortic valve. When pressure at the ventricle passes that of the aortic root, aortic valve opens and the blood rushes into the ascending aorta. Pressure at the left ventricle continues dropping at this point until it goes below aortic pressure. This causes a short flow reversal causing the aortic valve to close resulting to a local extremum in pressure called the dicrotic notch. This is seen in figure 2.2a, Time=0.45 s.

In diastole, aortic valve closes as a result of relaxing heart muscle, and blood flows into the ventricular cavity from atrium. Intraventricular pressure falls but there is very little increase in ventricular volume (isovolumetric relaxation). Once ventricular pressure falls below atrial pressure, the mitral and tricuspid valves open and ventricular filling begins. The complete cardiac cycle takes approximately $0.7 - 1.1s$ in a normal person, ejecting approximately $70ml$ of blood from each ventricle per stroke or as it is called with a cardiac output of 5 L/min. For a more detailed overview of the various heart muscle functions during the cardiac cycle, please refer to Malanga *et al.* [39], or [40], [41].

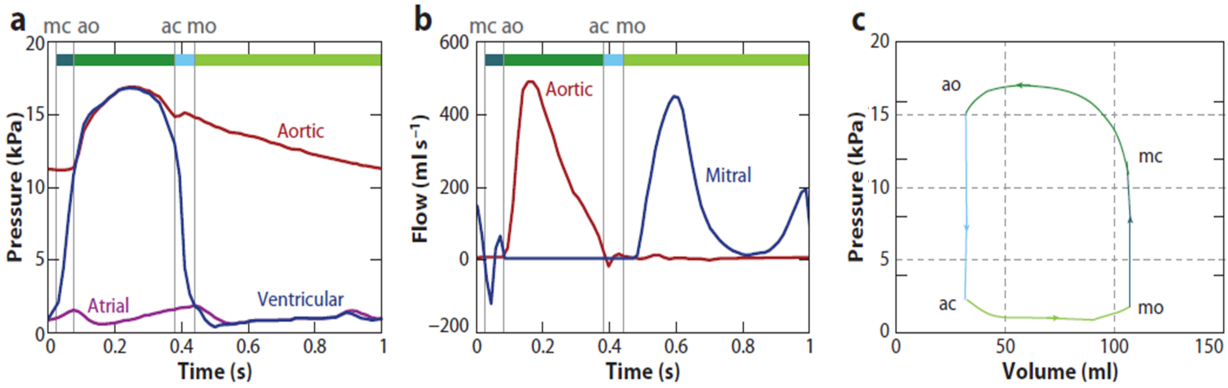


**Fig. 2.2.** – Aortic, ventricular, and atrial pressure (a); aortic and mitral flow (b); and left ventricular pressure-volume curves (c). In panel c, the periods between closure of the mitral valve (mc), opening of the aortic valve (ao), closure of the aortic valve (ac), and opening of the mitral valve (mo) are indicated (figure reproduced from [19].

In this work the cardiac output is being modeled with a pulsatile flow. The coronary arteries, which reside on the myocardium and being fed by branching out of the sinuses at the aortic root [42] are also neglected here. This simplification is justified with the small proportion of the lower blood flow to the coronary ostium compared to the much larger aorta and its different functionality.

### 2.1.1 Systemic Arteries

Arterial system is responsible for the transport of blood and nutrients to the tissues. Arterial BP is kept at a relatively high value to compensate for the resistance in peripheral sites of the arterial network, where it bifurcates into many small vessels (arterioles and capillaries) and connects to the venous system to transfer the blood back to the heart. As shown in 2.2a, large pressure pulsations from left ventricle of the heart are dampened by the elasticity of the vessels (the windkessel effect). This elastic function also aids the perfusion of blood in diastole and produces the wave-propagation phenomenon [19]. In the arterial system, unlike the heart, where only inertial forces and pressure forces are dominant (Reynolds $Re > 2500$ and Strouhal number $St = 0.1$), viscous forces may become significant as a result of a decrease in characteristic velocity and length scales, with an average Reynolds number of approximately $Re < 500$ and strouhal number $St = 0.05$ in large arteries.

Pressure waveform in the aorta changes as we get further from the heart (Figure 2.3, left panel). A phase shift in the pressure waveform is an indicator of wave propagation along the aorta. By moving toward the phery, the shape of pressure wave shows an increase in amplitude, a steepening of the front, and a moderate fall of the mean pressure (see figure 2.3, right panel). This wave phenomenon is a direct consequence of the distensibility of the arterial wall. As can be seen in the right panel in figure 2.3, the pressure wave dampens as it moves toward

smaller arteries, arterioles and capillaries, until it becomes a uniform pressure at the capillaries. This is due to the rigidity of the smaller blood vessels, nullifying the distensibility effects of the blood vessels.

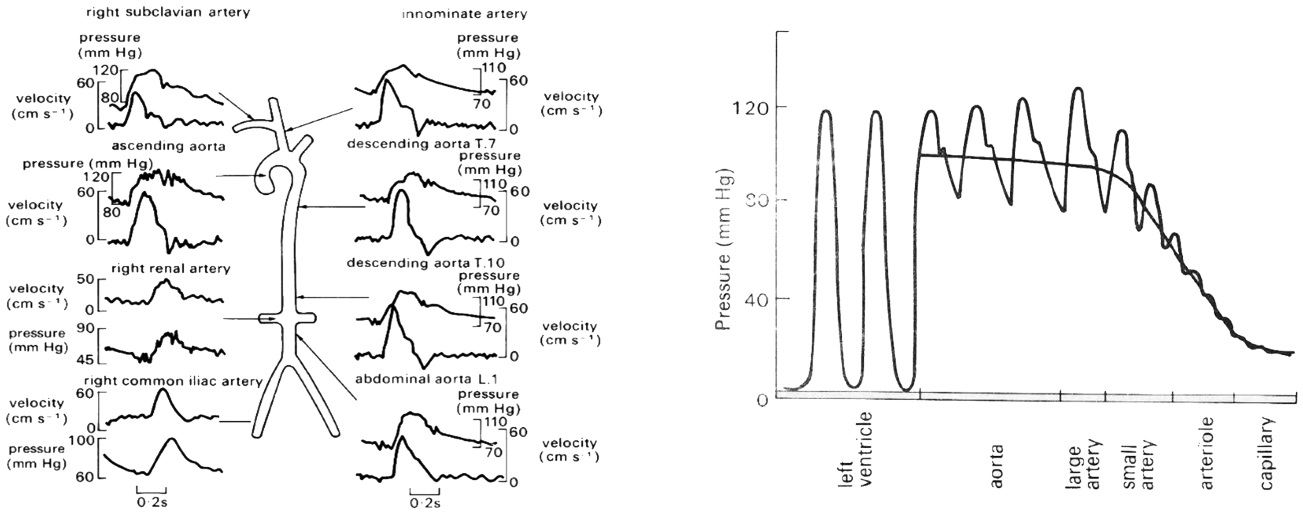


**Fig. 2.3.** – Pressure and velocity waveforms at numerous points along the arteries (reproduced from Mills *et al.,* [43], picture on the left, and Caro *et al.,* [44], pictures on the right).

The instantaneous cross-sectional area of the arteries depends on the transmural pressure difference across the wall. Nonlinear anisotropic and viscoelastic properties of the arterial wall were first shown by [25]. The transmural pressure and cross-sectional area $A$ of the lumen have a nonlinear and frequency dependent relationship. This relationship is described by compliance $C$ of the vessel, which depends on $P_{transmural}$ or $P_{tr}$ and is defined as

$$C\,(\,p_{tr}\,) = \frac{\partial A}{\partial p_{tr}} \tag{2.1}$$

Here $A$ is the inner cross sectional area of the blood vessel (or lumen area). Compliance strongly depends on pressure. At high transmural pressures, such as the case of smaller blood vessels, the artery becomes stiffer, due to the progressive recruitment of stiff collagen fibers (see section 2.1.2).

## 2.1.2 Blood Vessel Structure

Blood vessels consist of intima (the most inner layer), internal elastic lamina ($2^{nd}$ layer), media (middle layer), external elastic lamina ($4^{th}$ layer) and adventitia (the outer layer) [41]. Media has the most varying properties,

consisting of fibrous proteins and smooth muscle cells. The elasticity of the arteries depend on two fibrous proteins: *Elastin* and *Collagen* [45]. *Elastin* determines the distensibility while *collagen* makes the arteries stiffer. Proportion of these proteins in the media layer determines the arterial compliance. In an un-stretched artery, collagen fibers are aligned in bent condition and as the pressure increases they reach to their normal resting length. Meanwhile, the smooth muscle cells contract, making the artery stiffer. This results to one of the most important properties of arterial walls: **nonlinear distensibility**.

### 2.1.3 Blood Flow Properties

1. **Rheology**: *in vitro* measurements have shown that the apparent viscosity of the blood is a function of both red blood cell count (or hematocrit) and vessel diameter [46]; this is known as the Fahraeus–Lindqvist effect. Some of the studies involved with the smaller arteries are using a non-Newtonian blood rheology model, introduced by Pries *et al.* [47] (Equations 2.2, 2.3), fit an empirical model for blood viscosity as a function of hematocrit and blood vessel radius.

$$\zeta_{rel,0.45} = 220e^{-1.3D} + 3.2 - 2.44e^{-0.06D^{0.645}} \tag{2.2}$$

$$\zeta_{rel} = 1 + (1 - \zeta_{rel,0.45})\frac{\left[(1 - Hct_D)^C - 1\right]}{\left[(1 - 0.45)^C - 1\right]} \tag{2.3}$$

   $\zeta_{rel}$ is apparent blood viscosity, $H_{ct}$ - blood hematocrit, C – data curvature and D is the diameter. This type of non-Newtonian model is particularly important when small arteries ($diameter < 100\ \mu m$) are being simulated [48]. According to Sankar *et al.* (Sankar and Hemalatha 2007), non-Newtonian fluid model is only required for small arteries with diameters $D < 100\ \mu m$., were the shear rate reduces to less than $1\ s^{-1}$. Therefore, for larger arteries we can use the **Newtonian fluid** assumption. Other studies also show that the overall rheology model in large human arteries does not significantly affect the pulse wave velocity (PWV) [45], [49] assumption (see section 2.1.4).

2. **viscous-incompressible-laminar**: 90% of the blood consists of water [45], [49], and since the suspended materials are several order of magnitudes smaller than arterial diameter, the blood can be considered homogeneous and incompressible with a density of $1060Kg/m^{\wedge 3}$ and viscosity of $4.0\ mPa\ s$ [50]; it is also laminar in normal heart rates, as Reynold's number is way less than 2000 [51], except at the aortic arch.

### 2.1.4 Pulse Wave Propagation in Arteries

Pressure and flow waveforms are generated at the time of blood ejection at the aortic root and due to interaction with the compliant arteries. These waves start propagating from the aortic root toward the peripheral sites in the arterial tree (away from the heart). At any pathological or geometrical obstacle, such as bifurcations or when experiencing high resistance close to the capillaries, the pulse waveform generates a backward component going back toward the heart. These forward and backward moving waves are orders of magnitude faster than the velocity of blood, meaning they go back and forth between the heart and the arterioles several times during a single heartbeat. Superposition of the waveform components is responsible for changing the intraluminal pressures and blood velocities along the blood flow pathway. The speed of pulse wave propagation relative to the speed of blood is called the pulse wave velocity (PWV). This value increases as the elasticity module is increased in the arteries. The vessel wall elasticity is also responsible for smoothing the pressure and flow waveforms from the discontinuous left ventricle pressure and cardiac output, and assists the perfusion to capillaries during the diastole. However, if arteries were rigid, the arterial pressure would have change simultaneously throughout the network along with the left ventricle pressure variations, eventually leading to zero flow at the diastole. This was the premise of the **Windkessel effect**, first introduced in 1733 by Hales. Frank [52], was the first to put this concept into mathematical form. As it is inferred from the Windkessel assumption, the mathematical model does not account for the pulse wave propagation, and thereby it is not ideal for modeling the large arteries. However, in the smaller arteries, arterioles and capillaries, high wall stiffness results to nearly constant flows and synchronous changes to pressures everywhere, facilitating the diffusive delivery of nutrients. This can be described by Windkessel models.

## 2.2 Common Scenarios of Cardiovascular Diseases

### 2.2.1 Heart Failure

Heart failure refers to a cardiac dysfunction, where as a result, the heart may not pump enough blood. Some of the most probable heart failure scenarios are listed in the following:

1. *Systolic dysfunction*, in which the contraction of the heart due to the electrical signals of the heart (*i.e.* myocardial contraction) is diminished, thus blood accumulates in the lungs or veins.

2. *Coronary artery disease*, is a common cause of systolic dysfunction due to coronary artery occlusions and plaques, leading to a reduction of the flow of oxygenated blood to the heart muscle [18], [53].

3. *Heart-valve disorders*, heart-valve disorders such as stenosis or leakage can also cause systolic dysfunction, leading to the enlargement of the heart and its inadequate pumping power.

4. *Diastolic dysfunction*, heart muscle becomes stiffer making blood filling less effective.

5. *Hypertension*, high BP [54], is the most common cause of diastolic dysfunction and is studied by many researchers [55]–[57]. This causes the heart to eject blood into a high pressured arterial system, causing the heart tissue to get thicker (*i.e.* hypertrophy) and harder.

These conditions might lead to certain surgical decisions to resolve the issue, such as using left ventricle assist devices (LVADs) or open heart surgery. These can have further effects on the body's circulatory system. As another example of the broad applications of numerical hemodynamics models in disease diagnostics and surgical planning, the interested reader is referred to [58], where we numerically show the effect of LVAD on cerebrospinal fluid circulation.

### 2.2.2 Cardiovascular Diseases

1. *arteriosclerosis*, is one of the leading causes of death and an inevitable part of aging by the hardening of the arterial walls. Atherosclerosis, is a type of *arteriosclerosis*, leading to the developing plaque like fatty deposits inside the arteries. This is usually caused by high BP, diabetes, and high level of cholesterol in the blood. Hemodynamical factors such as disturbed blood flow, low wall shear rate, and wall shear stress [59] are the signs of atherosclerosis development. Growth of plaque can cause the narrowing of blood vessels and disturbance in the blood flow path. The narrowing is also called stenosis. Some of the other issues resulting from a plaque in the blood vessel are embolism, blood clot, and even aneurysms.

2. *Aneurysm*, Atherosclerosis causes the weakening of the blood vessel walls, and forces them to remodel and bulge to compensate for the transmural arterial pressure. This aneurysm can grow over time and eventually rupture, resulting to severe internal bleeding [19] and death. These aneurysms can occur at any part of the body, such as the blood vessels inside the brain [60].

### 2.2.3 Importance of the Arterial Blood Pressure and Flow Pulses

From the above sections, it can be concluded that BP and flow are important biomarkers in identifying cardiovascular disorders and monitoring the overall cardiovascular health. Complete blood flow network is a heterogeneous large-scale system, and an insight over the local cardiovascular characteristics are needed to study these diseases. Having a general insight on the pressure and flow distributions is indispensable, especially in case of creating a treatment plan and in special cases of arterial diseases altering the compliance and wave reflections, such as hypertension [54].

# 3

# Direct and Inverse *in silico* Models of Cardiovascular System

Cardiovascular system is complex and heterogeneous. Three dimensional simulation of the nonlinear blood flow behavior and its interaction with the hyper-viscoelastic arteries is extremely time and resource consuming process. Previous efforts in this direction by others [61], [62], depict the advantages and obstacles of these models, such as their applicability in studying cardiovascular diseases, drug delivery, perfusion in the brain and other pathologies. Successful *in silico* products are good examples of how the simulation based diagnosis can lead to advanced and usually less invasive diagnostic and therapeutic tools while keeping the costs lower than traditional techniques [63], [64]. HeartFlow®FFR-CT tool is one of these examples used for predicting the severity of coronary artery disease without the need for catheter insertion [65]. The living heart project [66], is another example for the application of *in silico* models in FDA tests to quantify the effect of drugs on hemodynamics of the heart.

In the applications that pulse wave propagation is the main contributor to the diagnostics, it has been proven that a 3D model only shows a slight difference in terms of accuracy compared to the reduced-order 1D counterparts [67], [68]. Even in more complex geometries, where 3D effects are crucial, such as recirculations and wall shear stresses in an aneurysm, multiscale 3D-1D-0D (as reviewed in [19], [24], [69], [70]) models are a promising and more efficient replacement for 3D simulations. They are shown to be capable of generating physiologically accurate results, comparable to *in vivo* measurements from human patients. However their sensitivity to coupling conditions at the interface can make it difficult to obtain similar results to fully 3D simulations [71].

## 3.1 Models of Cardiovascular System

In this chapter a brief overview of the reduced order models is given. Application, advantages and challenges of these models are discussed. In order to build an accurate reduced order pulse wave propagation model, recom-

mendations are provided on selecting the boundary conditions (BCs), and numerical discretization techniques to solve PDEs. Finally, some of the novel applications of such model are suggested.

### 3.1.1 A Brief History of 1D Models

In 1970, Anliker *et al.* [72], was the first to generate a 1D model based on the averaged over cross-section form of mass and momentum conservation equations for arterial system. This model was a pioneering work, which accounted for nonlinear system of equations. However, many of the blood vessel properties and the effect of simplifications to the flow field or fluid-structure interaction (FSI) were not known at that time, and thus were not included in the model. In addition, limited computing power hindered their application for parametric and sensitivity studies.

A simplified arterial network containing the 55 largest arteries in the human body was proposed and modeled using electrical circuits by Westerhof *et al.,* [73]. This work contained physiological data for diameter, wall thickness, length and elastic modulus for each of the 55 arteries; however could not account for the pulse wave propagation due to the 0D nature of the model. 0D or lumped parameter models are heavily used as a first principle estimate of the relationship between blood pressure (BP) and flow in various parts of the cardiovascular system. Since they average the parameters over space, wave propagation along arterial path as a function of time cannot be captured with 0D models. However, they perform well when used as a heart model [74], or terminal boundary conditions for a higher-order model of a desired arterial network, replacing the capillaries and venous return. The wave propagation has a lower impact on the blood pressure and flow variations in veins compared to arteries and thereby a 0D assumption is usually considered valid for venous system.

In recent years, there has been a revival of the reduced order 1D models. This might have been due to their ability to supply BCs for more complex 3D fluid-structure interaction (FSI) models or their simple but accurate representation of pulse propagation in the arteries [71]. The pioneering works on the 1D cardiovascular hemodynamics simulations include: the first attempts of creating a 1D model, Hughes and Lubliner 1973 [75]; accounting for the larger 37 or 55 main arteries and effect of artery geometry imperfections, such as stenosis and aneurysms, conducted by Stergiopulos *et al.*, Sherwin *et al.*, Matthys *et al.* and Alastruey *et al.*, [76]–[79]. Olufsen *et al.* [80], introduced a novel structured tree outlet BC, and Quarteroni *et al.* [81] and Formaggia *et al.* [29] generated a detailed one dimensional model of the arteries solved based on Taylor-Galerkin or Discontinuous Galerkin (DG) Finite Element (FEM) methods. The reduced order simulation of the systemic arteries reached to the peak number of vessels considered in a detailed model of 2000 main arteries developed by Blanco et al. [82], where they

accumulate a generic database related to the mechanical properties and dimensions of each vessel across the arterial network.

1D hemodynamics simulations create an efficient tool for quick quantification of biological markers and pulse wave propagation in human arteries [19], making them suitable for cardiovascular disease diagnostics and medical treatment in clinical settings. Their application is justified due to the long arterial waves propagated inside the wave-carrying vessel walls with relatively smaller lumen diameters (long-wave approximation). As mentioned earlier, 1D models introduce acceptable accuracy in capturing the physiological mechanisms of blood hemodynamics while having a marginally faster convergence rate compared to 3D models. This is also ideal for coupling them with local 3D models in a multiscale framework.

The geometry for a numerical model is commonly extracted by 3D reconstruction of an image taken using MRI, CT scan or ultrasound modalities. All of these imaging modalities have certain limitations in terms of the dimensions of the captured arteries and arterioles. Therefore, they cannot display arteries and arterioles smaller than their cut_off threshold, truncating them in the process of imaging. At these truncated regions, by applying appropriate BCs, resistance and compliance of the the truncated regions can be accounted for [83]. *In vivo* or *in vitro* patient-specific measurements are needed to calibrate the BCs for a generic 1D model with truncated arteries [84]. On the other hand, more clinical/experimental data might be needed to obtain constitutive models and patient-specific coefficients to generate a physiologically accurate model for the arterial wall distensibility [25].

The challenges of developing accurate 1D models of the blood flow in systemic arteries and the suggested solutions will be discussed in the following sections.

### 3.1.2 Selecting Correct Outlet Boundary Conditions

In computational models of arterial network, a physiologically sound BC is needed to replace the truncated regions. Here a few options and their applications are discussed. A similar categorization to the one discussed by Grinberg *et al.* [62], is presented here:

1. Constant pressure BC. This type of BCs are ideal for steady flow simulations where only a single outlet exists , or when pressure measurements at multiple outlets are available. The pulsatile nature of the blood flow simulations and the limited knowledge at the outlets usually prevents us from using this type of BC.

2. Resistance BC (R-BC). It considers a linear dependence between flow rate and pressure at each outlet and has been widely used in the reduced order models [74], [77]. R-BC is analogous to circuits where the ratio of voltage (*i.e.* pressure) over amperage (*i.e.* flow) gives Resistance.

3. Windkessel model BCs. Three-element windkessel (*i.e.* RCR) model is the most common type, where a resistor is in parallel to a serried resistor and capacitor [73], [81], [85]. One of these resistors represent upstream and the other, truncated domain resistances. The capacitor represents the arterial compliance [86]:

$$Compliance = \frac{dV}{dP}, \tag{3.1}$$

where $dV$ denotes volume and $dP$ the pressure variations. There are several other variations of the Windkessel BC. There are variations with an added inductance, L, which represents the fluid inertia [87] and another with only one set of resistor and capacitor [88]. Although they are very popular for how they minimize wave reflections from truncated downstream vessels, these models can be very sensitive to the selected $R$ and $C$ parameters [89] and they do not capture phase differences between downstream flow and pressure waves [19]. These $R$ and $C$ parameters cannot be measured and they need to be calibrated experimentally or by iterative numerical calibration [90]

4. Impedance BCs. The limitations of previous models led the researchers to introduce the structured-tree or impedance BCs (Olufsen *et al.* [80], [91]). Impedence BCs involve an analytical approach for modeling the outflow BCs. A key aspect here is the inclusion of peripheral network by creating a network generation procedure with a cut-off diameter threshold. This guarantees consideration for the resistance of downstream vessels. The network generation where there is no information of the downstream branches are usually assumed to follow Murray's law [92] or more recent empirical works such as the work by Zamir, looking at fractal properties of the arteries [93]. Following Olufsen *et al.* others have compared this model with previous BC types [94], [95] and utilized it for reduced order blood flow simulations [96], [97]. There have also been new suggestions such as fractal-tree BCs, which are in other words 1D representation of the structured tree models, and thereby able to capture pulse propagation at the outlets [98].

Reproduced from Guan *et al.* [95], Figure 3.1 provides a visual schematics of the components of a 1D structured tree outlet BC and 0D RCR models.

These boundary models need to be selected based on their computational cost, the properties of patient-specific arterial system and the desired hemodynamic phenomenon. According to Guan *et al.* [95], and Valdez-Jasso *et al.* [99], numerical experiments show that wave reflection from the outflow boundary models can significantly

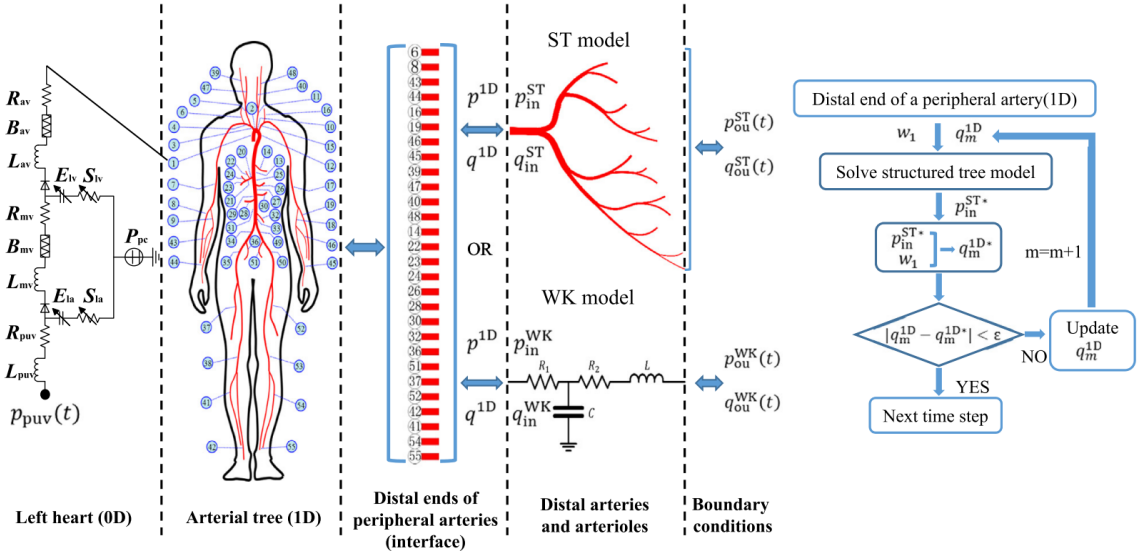


**Fig. 3.1.** – Fig 5. Schematics of 0D RCR and 1D Structured-Tree outflow BCs connected to the outlets of 1D large arterial tree model. An elastic heart model is also presented as the inlet BC. Figure reproduced from Guan *et al.* [95]

affect the characteristics of pressure/flow wave predictions at the upstream arteries, especially in case of arterial stiffening.

### 3.1.3 Fluid and Structure Interaction Mechanics

The pressure and flow pulses in the arteries are the outcomes of fluid (*i.e.* blood) and structure (*i.e.* compliant vessel walls) interactions. The governing equations are therefore required to take into account both fluid and structure mechanics. Equations for the blood flow, are derived from the Navier-Stokes equations. These non-linear equations describe viscous and incompressible pulsatile blood flow. They get recasted as a set of hyperbolic 1D PDEs of mass and momentum conservation. These equations are then complimented with a constitutive equation, connecting the structural stresses, to artery displacement. For a mathematical description please read chapter 5.

The following assumptions are usually made in a 1D FSI simulations:

1. Axial symmetry (Axisymmetric fluid velocity profile);

2. Dominance of the axial velocity component;

3. Account for the radial displacement only;

4. Constant internal pressure at each cross section;

5. Constant pressure in all branches at the bifurcation site;

6. No flow leakage at the bifurcations;

7. Constant dynamic viscosity, $\mu$,*i.e.* Newtonian fluid. $\mu$ is not a function of lumen radius and blood hematocrit[1], as is for non-Newtonian fluids [47]).

Sherwin *et al.* [77] and Formaggia *et al*. [100], derived nonlinear fluid-structure interaction governing equations in human arterial network. Sherwin *et al.*, gave a simplistic representation of the characteristic speed. Characteristic speed, *"c",* is one of the most important physical properties of hyperbolic hemodynamics governing equations [19]. in biomechanics, first introduced at the same time by two individual scientists, Moens and Korteweg, the characteristic speed (*i.e.* pulse wave velocity) is an indicator of the propagation of disturbance (in this case pulse wave) in the hyperbolic system of equations (as shown in 3.2).

$$C_{MK} = \sqrt{\frac{Eh}{2\rho r}}. \tag{3.2}$$

Where $C_{mk}$ represents the speed of propagation for pressure wave in the artery, also known as pulse wave velocity (PWV). This parameter can change as a function of the elastic modulus of the arterial wall (Young modulus $E$), its thickness ($h$), radial displacement ($r$) and blood fluid density ($\rho$). Therefore, any change in this parameter can be an indication of cardiovascular aging, disease or change in the normal function of the hemodynamic system. Therefore, speed of sound in the arteries or its surrogate pulse transit time (PTT) and its relation to CVDs are being widely investigated by researchers (please read chapter 4).

[1] Number of red blood cells.

## Choice of Constitutive Equation and its Effect on PWV

As mentioned earlier, a closure model is needed to close the system of hyperbolic governing equations. Most of the popular 1D models in the literature use a linear elastic wall model with an account for viscoelastic behavior to reduce the complexity of the structural model [29], [79], [101]. The linear elastic model combined with a simple Kelvin-Voight type viscoelastic model is related to the change in BP as a function of time. This assumes the *in vitro* arterial walls are thin (with thickness $h$), isotropic, homogeneous and incompressible, with axisymmetric deformation. Therefore, the deformation at each circular cross-section can be related to the internal pressure $P$ and the change of the vessel wall radius with Laplace's law [80]. This results to the following relationship for the constitutive law with viscoelastic assumption:

$$P = \frac{4\sqrt{\pi}Eh}{3A_0}\left(\sqrt{A} - \sqrt{A_0}\right) + \frac{2\sqrt{\pi}\Gamma h}{3A_0\sqrt{A}}\,\frac{\partial A}{\partial t}\;; \tag{3.3}$$

Where $E$ is the elastic Young's modulus, $\Gamma$ - the viscosity of the arterial wall material, and $A,\ A_0$ are the lumen cross sectional area at the current time and pre-stress conditions, respectively.

Using polarized light microscopy of the stained arterial tissue, Cranham and co-workers [102] showed the effect of elastin, collagen and smooth muscle orientation inside the arterial wall on the distensibility of vessel wall. It should be noted that viscous part of the viscoelasticity is only responsible for dispersive changes in the predicted PWV. However, as proved via an *in vivo* experiment on canine aorta by Zhou and Fung [103], neglecting nonlinear elasticity can lead to underestimating the effect of wave reflections on measuring numerical PWV. Valdez and Olufsen [99] have tested the effect of non-linear elasticity and viscoelastic behavior in human and sheep arteries and reported that the changes in the viscoelastic behavior of the arteries is not significant. They empirically show that non-linear elastic models significantly improve the predictions for pressure-area relationship. Nonlinear wall model can also significantly improve the waveform prediction capabilities in a robust reduced order model of the arterial network, as shown by Reymond *et al.* [104], where the validation is done using *in vivo* measurements from a real patient. Liberson *et al.* [105]) proved that the matching measured and numerically estimated values of the pulse wave velocity are only attained when the hyper-elastic arterial wall behavior is accounted for.

In addition it was mentioned by Humphry [106] that the physical nonlinearity is crucial for accurate prediction of the blood hemodynamics in case of studying a geometrical change, such as an aneurysm, on an arterial wall. Therefore it is suggested here to use the nonlinear anisotropic arterial wall model that was first proposed by Fung *et al.* [25] to close the governing equations.

## 3.2 Inner Workings of Hemodynamics Models

In this section a brief description of the common forms of reduced order set of governing equations, discretization techniques and pulse wave characteristics will be given to prepare the reader for detailed derivation and extension of these in chapter 5.

### 3.2.1 Governing Equations

Extensive work has been done previously with regard to developing reduced-order models, applied to specific components of hemodynamic pulsating flow, such as systemic [19], pulmonary [97], venous [107] and CSF [108] circulations. Parker [109], presents a historical review of arterial fluid mechanics models. Detailed derivation of simplified reduced FSI models for linear elastic arterial system with account for viscoelasticity and inertia of the wall can be found in Peiro and Veneziani [110] and others [29], [77]. 1D models are derived based on the Navier-Stokes equations:

$$\frac{\partial u}{\partial t} + (u.\nabla)\, u + \frac{1}{\rho}\nabla P - div\left[\nu\left(\nabla u + (\nabla u)^T\right)\right] = 0, \qquad div\ u = 0 \tag{3.4}$$

posed on a cylindrical domain, which changes in time because of the flow-induced wall movement. Here $\boldsymbol{u} = (u_x,\ u_y,\ u_z)$ is the fluid velocity, $P$ the pressure, $\nu$ the kinematic viscosity and $\rho$ the blood density; $(x,\ y,\ z)$ is a system of Cartesian coordinates.

The linear acoustic form of these equations are simplified to 3.5

$$\begin{aligned} &\frac{\partial p}{\partial t} + \rho C_{mk}^2 \frac{\partial u}{\partial x} = 0 \\ &\frac{\partial u}{\partial t} + \frac{1}{\rho}\frac{\partial p}{\partial x} = 0 \end{aligned} \tag{3.5}$$

Where $C_{mk}$ is the speed of sound propagation in the artery and $t$ is time. For the nonlinear set of equations, we have:

$$\begin{aligned} &\frac{\partial A}{\partial t} + \frac{\partial\,(uA)}{\partial x} = 0; \\ &\frac{\partial u}{\partial t} + \frac{\partial}{\partial x}\left(\frac{u^2}{2} + \frac{P}{\rho}\right) = 0. \end{aligned} \tag{3.6}$$

Set of equations are represented in terms of lumen cross-sectional area $A$, pressure $P$, and velocity $u$. The constitutive equation 3.3, as described in section 3.1.3, will close the system of equations.

### 3.2.2 Variational Formulation

The variational approach, yielding governing equations of physical phenomena, serves as an indispensable tool, when the interaction of the system components are non-trivial, for instance, when their interaction contain, strong nonlinearities, kinematic constraints, or high derivatives. The monumental book of Berdichevsky [111] presents a variety of variational principles applied separately to fluids and solids. Kock and Olson - 1991 [112] developed a variational formulation for FSI system, restricting analysis by a linear elastic thin-walled cylinder and an inviscid, irrotational and isentropic fluid flow. Lagrangian multipliers are used to enforce continuity equation constraint on BCs. Hamiltonian variational principle is used in this work for analyzing FSI, without any limitations on dissipative fluid dynamics or physical properties of the arterial wall adjacent to flow path. Lagrangian multiplier are avoided, and the continuity equation is explicitly included, which simplifies the entire procedure. The formulation is presented in chapter 5.

### 3.2.3 Numerical Discretization - DG vs TVD

Discontinuous Galerkin (DG) method is one of the popular FEM based numerical methods first introduced by Reed and Hill in 1973 [113]. DG-FEM method, approximates the evaluated function by orthogonal Legendre polynomials to get the closest approximation of the solution near the boundaries of each element. DG method reduces the number of elements required to solve the governing equations by flux upwinding and function approximations. When FEM is applied to the blood hemodynamics variational form of governing equations, Upwind flux is evaluated using pressure, area and characteristics conservation at the boundaries of each element (solution of Riemann problem), which results to continuous flux. DG method enables the decoupling of the solution on each element and reduces the number of required elements. However, there are some disadvantages when using this scheme, including explicit time derivative discretization and complex instability and dispersion analysis after choosing the polynomial approximation. When discretizing the time derivative usually an Adams-Bashforth second-order scheme is used in literature. However, viscoelastic creep and relaxation behavior in meso-scale arteries has a dispersive nature, therefore, the choice of a centered, second-order accurate Adams-Bashforth scheme can result in unstable solutions.

On the other hand, a total variation diminishing (TVD) scheme is used to preserve the monotone response in case of discontinuity in the arterial properties. As introduced by Harten [114], TVD schemes are able to provide sharper shock/discontinuity predictions, without suffering from spurious oscillations. Total variation (TV) and the condition for a TVD scheme are shown in Equation 3.7:

$$TV = \sum_{j} |u_{j+1} - u_j|, \qquad TV\left(u^{n+1}\right) \leq TV\left(u^n\right) \tag{3.7}$$

in which $u$ is an arbitrary dependent variable and it is summed over all values of $j$ (element number). TV is described as the sum of all differences between the value of the desired parameter in neighboring elements. If TV in next time step is less than TV in the current time step, the scheme is TVD. Godunov Theory states that: "Linear numerical schemes for solving partial differential equations (PDE's), having the property of not generating new extrema (monotone scheme), can be at most first-order accurate [115].

TVD schemes can replace the DG method, by using a second-order accurate scheme in time and space such as Lax-Wendroff with TVD modification (high-resolution method). This type of formulation is utilized here to alleviate spurious wave problems in hemodynamic simulations. During the discretization of a PDE, TVD condition 3.7 is satisfied by introducing the correct approximation (*i.e.* limiter) for the transporting dependent variable, at the boundaries of the elements. This limiter, transforms the discretized equation to comply with TVD condition [116].

Numerical effectiveness in a simulation of a pulsating flow is characterized by its ability to track a propagating wave for a few time periods, without suffering from numerical dissipation (errors in amplitude) or numerical dispersion (artificial oscillations). The most popular numerical methods in this area are the Lax-Wendroff finite volume method, its Taylor-Galerkin FEM counterpart, and DG spectral finite element method (As mentioned in [117]). In this work, the improvement in accuracy with the second order Total Variational Diminishing (TVD) approximation [116] is demonstrated (see A), compared to the more common Lax-Wendroff method. This higher accuracy can be essential when simulating a model with discontinuity in the load or material properties.

### 3.2.4 Characteristics

Forward and backward moving characteristics of the hyperbolic set of equations for blood flow can be derived by method of characteristics. As described first by Lighthill in 1978 [118], both waves $P\left(x \pm ct\right)$ are solutions for the set of governing equations (equation 3.5 or 3.6). The derivation of characteristics from the 1D system of equations

is provided in section 5.2.2.4. For nonlinear waves, two solutions also exist for the Riemann invariants that are constant along the nonlinear characteristic lines which are curved trajectories in the space-time plane (as shown in Figure 3.2.

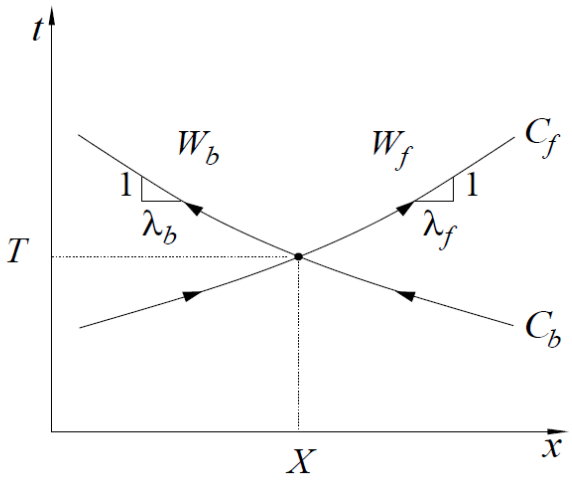


**Fig. 3.2.** – Every point in (X,T) in space (x,t) is intersected by a unique pair of characteristic curves, as described by $C_f$ and $C_b$. Pressure and velocity data is carried forward and backward directions along the curves by $W_f$ and $W_b$ (Figure reproduced from Alastruey [50].

At any location in the arterial tree, pressure and flow waves are the sum of waves traveling from the heart toward the periphery (forward running waves) and waves traveling from peripheral arteries back toward the heart (backward running or reflected waves). The latter is caused by the reflections of the forward running waves at arterial sites such as bifurcations, stenoses, aneurysms, and the truncated peripheral beds. The reduced-order models can capture both components. However, nonlinear set of equations should be solved to obtain correct trajectory of these wave components.

## 3.3 Applications of 1D Models

Previous sections were dedicated to how computational models of cardiovascular system are capturing the mechanics, their formulation, and the popular models in the literature. In this section, the focus of the reader is brought to the additional contributions that these models can bring to biomedical engineering and healthcare fields.

### 3.3.1 Inverse Problems in Cardiovascular Simulations (non-invasive diagnostics)

The aforementioned methods are designed to describe the FSI nature of the blood flow while making many assumptions. The parameters contributing to the boundary/initial conditions are also subject to high sensitivity from one patient to the other. This renders the definitive solutions of the PDEs inconsistent with the same data measured from a patient.

This gap is recently being addressed with a new combination of the modeling and measurements, as called *data assimilation* methods. With the computing power advances *data assimilation* has re-emerged in fields such as biomedical engineering. As described by Veneziani and Vergara [7] and Moireau *et al.* [119]; they describe numerical models as providers of the *background knowledge* which is not patient-specific. The patient-specific data is then collected by targeted measurements amounting to *individual knowledge*. The integration of these methods enables accurate predictions of the cardiovascular biomarkers. For instance, Cluitmans *et al.* [120] shows that the cardiac electrical activity at the heart muscle can be reconstructed using body-surface electrocardiogram (ECG) recordings and patient-specific torso-heart geometry. Some limitations usually exist. For example, sensitivity of the results to boundary and initial parameters is sometimes unclear and can be improved upon availability of patient-specific measurements; on the other hand, the quality of measurements can be enhanced when comparing with mathematical models. Descriptive examples of these limitations are presented in [121]–[124].

There have been a new wave of studies that are currently dealing with inverse problems and patient-specific reconstruction of correct BCs for computational models, such as Funamoto and Hayase [33], who tried to improve the computational pressure predictions with ultrasound measurements. In another work by Sazonov *et al.* [125], the location of an aneurysm is predicted based on inverse problem and calibration measurements. Lastly, a geometrically multiscale algorithm of the cardiovascular system is validated and improved by clinical measurements by Pant *et al.* [124]. Interested reader can also refer to other examples: inverse problem for PWV measurement [126], cardiac electrical activity from ECG and torso-heart geometry[120] or read [7]. As described in a brief review by Veneziani, inverse Cardiovascular Mathematics is re-emerging due to its intrinsic challenges and for the impact that it is anticipated to bring to clinical practice.

Here a new approach for inverse method of characterizing the BCs and nonlinear constitutive equations in the patient-specific arterial network is presented. Aortic and Brachial pressure and stroke volume will be reconstructed and validated to prove the reliability of the method and its application to patient-specific noninvasive diagnostics (see chapters 7, 8, 9, for a detailed explanation and discussion).

### 3.3.2 Geometrically Multiscale Modeling

Key contributions to 3D blood flow modeling in deformable vessels include the works of Perktold *et al.* [127], Taylor *et al.* [128], Quarteroni *et al.* [81], and Figueroa *et al.* [129] and others (see [67]). A systematic comparison between the 3D and 1D models by Xiao *et al.* [67], highlights the advantages of 3D over 1D modeling:

a) Their ability to account for secondary flow features, vessel curvature, b) nonlinear elastic vessel wall models and the external tissue support (which introduces viscous damping) in the 3-D model.

According to Hou *et al.* [26], *partitioned* and *monolithic* approaches are commonly used to model FSI. In the *partitioned* approach, the fluid and structural parts are formulated and solved separately. The changes at the interface are explicitly tracked (*e.g.* the work by Farhat *et al.* [130]), and modifications are made to each individual domain. This approach has the advantage of using well-established codes for fluid and structural problems. On the other hand, a *monolithic* approach follows the same methodology as it was described in the 1D models section, thus, it combines the fluid and structural dynamics in a unified system of equations. This formulation accounts for the interface dynamics implicitly, therefore, needs a high level of expertise and resources to develop. In addition, it needs to be modified based on the geometrical and physical properties of the problem.

However the surprising performance of 1D models cannot be neglected. Some of the 1D model highlights include: a) Estimation of the clinically accurate outflow BCs, b) sensitivity study of the arterial system under various hemodynamic conditions, and c) accurate representation of the flow and normal stresses, similar to 3D [67].

For a complete representation of the reverse flows or shear thinning effects in aneurysms/bifurcations and even the aortic arch, a coupled 3D-1D model can be used to combine the benefits of both 1D and 3D. Studies on geometrically multiscale approach (GMA) implementation were pioneered by Formaggia *et al.* [131] and continued by other research groups [132]–[135], investigating the methods for stabilizing the coupling between 3D and 1D models.

in Geometrically multiscale (GM) model proposed by Formaggia *et al.* [136], a 3D FSI model and a reduced 1D model are connected at an interface. Additional considerations are needed to address the discontinuity between field variables for full 3D and averaged quantities of the reduced model at the interface. For instance, the 1D averaged over cross section flow profile and the 3D element-wise flow profile needs to be matched at the interface between 1D and 3D. As shown in figure 3.3, A 1D model supplies the area ($A$), flow velocity ($U$), pressure ($P$) on

the left side of the coupled model (at the vicinity of the interface). These quantities also need to be defined on the right side.

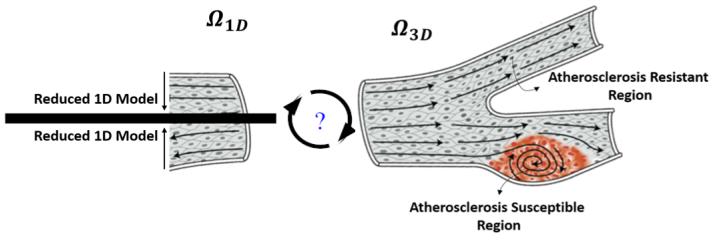


**Fig. 3.3.** – Schematics of a 3D carotid bifurcation with 1D portion attached at the inlet

In order to couple 1D and 3D models, these quantities need to be continuous along the interface. For example, the interface BC shown in equation 3.8, describes the wave continuity as well as lumen cross sectional area 3.9 and pressure 3.10 coupling equations.

$$\overline{u}\left(a^{+}\right)+2\sqrt{\frac{2}{\rho}}\left(\sqrt{\overline{P}\left(a^{+}\right)-P_{ext}+P^{*}}-\sqrt{P^{*}}\right)=W_{1}(a^{-}) \tag{3.8}$$

$$A\left(a^{+}\right)=A\left(a^{-}\right) \tag{3.9}$$

$$\overline{\sigma}\left(a^{+}\right)=\overline{P}\left(a^{-}\right). \tag{3.10}$$

Where $P^{*}$ is the pressure at the interface, and $P(a^{-}), P(a^{+})$ are the averaged over cross section pressures at the left (1D) and right (3D) side of the interface, respectively. Methods of treating this BC (called defective BC [71]), when a rigid or simplified 3D model is being used, are described in Taelman *et al.* [70], These methods are as follows: a) Lagrange multiplier approach [132], b) the do nothing approach [137], c) the extended boundaries approach, d) minimization, and e) variational formulation approach [138].

The continuity of the cross section is a concern when coupling heterogeneous models. However, as it was shown by Urquinza et al. [133], for a rigid 3D model of the arteries coupled to a 1D model, concerns for the discontinuities in cross-sectional area coupling is minimal. Therefore, by relaxing the continuity of the cross-sectional area at the

coupling interface the instabilities caused by area difference can be resolved without the need for the commonly used [136] coupling iterations.

In another research article by Galindo *et al.* [139], a coupled simulation between 1D (OpenWAM code) and 3D (ANSYS FLUENT®) CFD codes, was executed using the Method of Characteristics (MOC) to transfer the information between the two domains. This is an example of proper BC setup at the shared interface. In chapter 6, a method inspired by Galindo *et al.* will be introduced. The coupling of an in-house nonlinear quasi-1D code and the commercially available 3D FSI module of ANSYS package is executed for the first time here. The global hemodynamics are solved with our in-house 1D code which also accounts for the nonlinear vessel wall properties, and the local 3D behavior is solved by ANSYS FSI module, a powerful commercial software for 3D FSI. The coupling is intended to give accurate and fast simulation of the cardiovascular abnormalities, such as aneurysm, stenosis, or vessels with complex geometry, such as bifurcations and aortic arch.

### 3.3.3 Cardiovascular Aneurysm and Stent Modeling

After discussing the suggested features of a robust 1D numerical model, in addition to the geometrically multiscale capabilities, the aim of the following sections are to explore how such model can be used in two common cardiovascular scenarios, arterial aneurysms and stented arteries.

#### 3.3.3.1 Cardiovascular Aneurysm Modeling

The geometry, reverse flows and blood properties have compelled the modeling of cardiovascular abnormalities to be commonly conducted with 3D models. Brain aneurysm was analyzed by a 3D-1D coupled in-house model by Bazileves *et al.*, [140], and Ho *et al.*, [141]. Finol and Amon [142] developed a double aneurysm model of a cylindrical shape abdominal aneurysm in a 3D fluid model. Furthermore, the effect of geometrically multiscale models and FSI on the aneurysm modeling is analyzed by Chandra *et al.*, [143].

Although others have also developed multiscale models, the coupling between a compliant 1D FSI model and an already proven code such as ANSYS FSI module has not been used in any of these works. The advantage here would be that the reliability of the 3D and the processing speed of the 1D models are guaranteed. The code will be widely accessible for everyone to use for multiscale problems, even outside the field of cardiovascular simulations.

#### 3.3.3.2 Stent Models

Coronary artery diseases are among the major causes of death in the industrialized world. Angioplasty and stenting procedures are preferred treatments due to their good clinical results and lower invasiveness compared to the coronary artery by-pass. Stents can cause rupture of the internal elastic lamina, during and after deployment [144] and due to persistent non-physiological stresses or wall shear stresses [145], [146] inside the arterial wall.

In most cases, imaging techniques are used to quantify the changes in the blood flow, pressure and vessel wall properties before stenting, to decide if the procedure is truly needed or after stenting the artery, to measure the effectiveness [147]. Computational models on the other hand, are becoming ever more useful for predicting the nearly impossible to measure blood flow and pressure, to the extent that Food and Drug Administration (FDA) has started regulating these techniques and their usage [6]. As described by Morlacchi and Migliavacca [148], the 3D stented artery models in the literature, such as [149], show the importance of considering a detailed vessel wall model.

Stents have different mechanical properties compared to blood vessels and when inflated, they change the elasticity at the deployed location among other effects on the shear stresses [148]. If linear elastic wall models are used, this sudden change in wall properties causes numerical models to report discontinuity in flow or BP waveforms. However, clinical studies declare the wall property changes are not causing discontinuous response in pressure, flow or wall displacement distributions [150].

Current numerical works are simplifying the mechanism of discontinuous properties over a stent to overcome these spurious oscillations. For example Formaggia *et al.* [29], describes the application of smoothing mechanisms such as viscoelastic wall behavior on 1D stented artery models. In cardiovascular mathematics [117], they describe artificial smoothing and omission of the stented area as methods of circumventing the discontinuous wave issue. The model presented in chapter 6, for the prosthesis and stents, accounts for bending moments over the arteries which is on par with the more complex solid element models [151]. When used in a TVD numerical discretization scheme, this approach offers the most accurate 1D representation of stents/prosthesis.

# 4 Pulse Transit Time (PTT): Challenges of Application to the Cardiovascular Diagnostics

Pressure and flow waveforms are generated at the time of the blood ejection from the aortic valve and due to its interaction with the compliant arteries. The pulse propagates starting from the aortic root until it reaches the smaller and more rigid peripheral arteries. As mentioned earlier, these waveforms are the offsprings of hyperviscoelastic arteries and carry information on the intraluminal pressures and blood velocity along their way. The time that a pulse takes to propagate from one point in the arterial tree to another is called pulse transit time (PTT), and the speed of propagation is pulse wave velocity (PWV). If the PTT and the distance traveled along the arteries are known, an average PWV can be calculated as:

$$PWV = \frac{Distance}{PTT} \tag{4.1}$$

In this chapter PTT characteristics, methods of measurement and its application as a biomarker for cardiovascular disease diagnostics and proximal/central blood pressure measurement, will be discussed.

## 4.1 Using PTT for Cardiovascular Disease Diagnostics

If not detected and treated early, hypertension(*i.e.* high blood pressure) can lead to conditions such as heart attack, stroke, myocardial infarction, cerebrovascular or myocardial events [54], [152]. Hypertension is a silent killer that is affecting more than 40% (1.5billion) of adults worldwide, and this number is expected to increase due to an increase in elderly population and obesity. Only around 46% hypertensive patients are aware of their conditions and measure BP regularly, and only 32.5% have it under control [153]. Therefore, early detection is the key to reduce cardiovascular risk in people with hypertension.

Routine BP measurements with auscultatory mercury and oscillometric sphygmomanometer, done in a physician's lab are not adequate to reveal masked hypertension in patient [154]. Also due to the white-coat effect, the BP at doctor's office might not always be reliable. As a result, the ambulatory and self-measured BP monitoring at home can have a superior success rate in predicting mortality due to hypertension [155].

Bp monitoring at home provides patients with the ability to monitor their blood pressure changes due to lifestyle, drugs, hypertension or functional changes of the circulation system. Blood pressure variability due to any alterations in arteries or arterioles can only be measured if a continuous blood pressure measurement method is used. This enables more than just a daily snapshot of the dynamic BP throughout the day, which is usually provided by ambulatory BP measurement devices.

Targeting a lower BP value than the hypertension threshold result in lower rates of cardiovascular events and mortality among patients [156] and early prevention, detection, management, and treatment of hypertension. Measuring BP waveforms using data assimilation methods (see section 4.3) is a promising alternative to intra-arterial BP monitoring by inserting a cannula needle (*i.e.* gold standard approach), applanation tonometry and arterial volume clamp methods (*i.e.* dynamic response by pressurizing arteries). It generates no adverse effects, such as bleeding or infection, and involves minimal occlusion of arteries. PWV/PTT based BP measurement techniques utilize the connection between BP variation and the speed of pulse wave propagation.

PTT is usually obtained with a combination of techniques such as ECG, BCG, and PPG. PTT changes are usually linked to the blood pressure with a calibration procedure. Due to convenience, noninvasiveness and unobtrusiveness of the PWV/PTT based continuous BP measurement, it has recently captured a lot of attention [157]–[159]. As previously mentioned, PWV/PTT are associated with the speed of sound propagation in the visco-hyperelastic arteries. Therefore any change in arterial compliance or topology can translate to a changed PTT value. With an accurate calibration of PTT to BP relationship, patient BP may be continuously obtained [16]. The name of this field has been coined as cuffless BP measurement. Development and validation of the aforementioned methods typically require a large set of human subjects data with sufficient variety. This can be a tedious and sometimes very expensive task. Thereby, recent works suggest using direct arterial network simulation algorithms in order to generate artificial PTT, BP and SV data [160]. However, this may come with the price of neglecting real patient body's uncertainties, influencing PTT and BP relationship. This has made machine learning based techniques, which use neural network training based on a range of physiological patient data, very appealing [161]. These methods require large sets of data, however, may show better promise on taking into account the human body uncertainties.

In this work a new approach has been introduced here, closely relating to the cuffless BP measurement techniques. The physics-based reduced-order models are combined with peripheral BP and PTT measurements in order to reconstruct proximal/central BP and cardiac output. To do so, inverse problem techniques are utilized for calibration and to provide patient-specific data for continuous BP monitoring.

## 4.2 PTT Measurement

Weltman et al. 1964 [162], was the first to measure PTT over a known length using EKG and a known downstream signal. Later on, transit time was measured chronologically using the following techniques:

1. Interval between R wave of ECG and the proximal pulse [163].

2. The initiation of the pre-ejection period (PEP) and the peak of the pulse wave, Obrist *et al.* [164]. PEP relates to the time that it takes between Q wave of ECG (heart ventricle depolarization) and the aortic valve opening. Usually the R wave is easier to mark the instance of valve opening.

3. Marie *et al.* [165] introduced PTT as the time between ECG R-wave and peripheral pulse. It was suggested that the PTT differences based on location can then be calculated by peripheral PTT differences. Therefore, PTT contains both intra cardiac, pre-ejection period (PEP), and arterial components (vascular transit time), shown in 4.2:

$$PTT = PEP + VTT \tag{4.2}$$

Electrocardiography (ECG) is a measure of the electrical activity of the heart at each cardiac cycle [166]. Ballisto-cardiography (BCG) is a measure of the recoil forces of the body in response to the blood ejection from the heart and blood movement through the vasculature in each cardiac cycle [167], [168]. Photoplethysmogram (PPG) is an optical measure of local blood volume [169]. A PPG is often obtained by using a pulse oximeter which illuminates the skin and measures changes in light absorption.

ECG initiated PTT, includes PEP [164]. In [170], [171], PTT was measured as the interval between pulses arrival times (PAT) at two arterial sites, PAT being the time diference between the ECG R-wave and the peripheral pulse. According to a literature survey by [153], in recent decade, most publications are using PTT terminology as the time interval between ECG R-wave and peripheral pulse. This is a much longer established terminology and

eliminates the need of using PAT for this definition. Here we will also stick to this terminology. PTT acquisition methods are demonstrated in figure 4.1 which is reproduced from the comprehensive figure generated by [153].

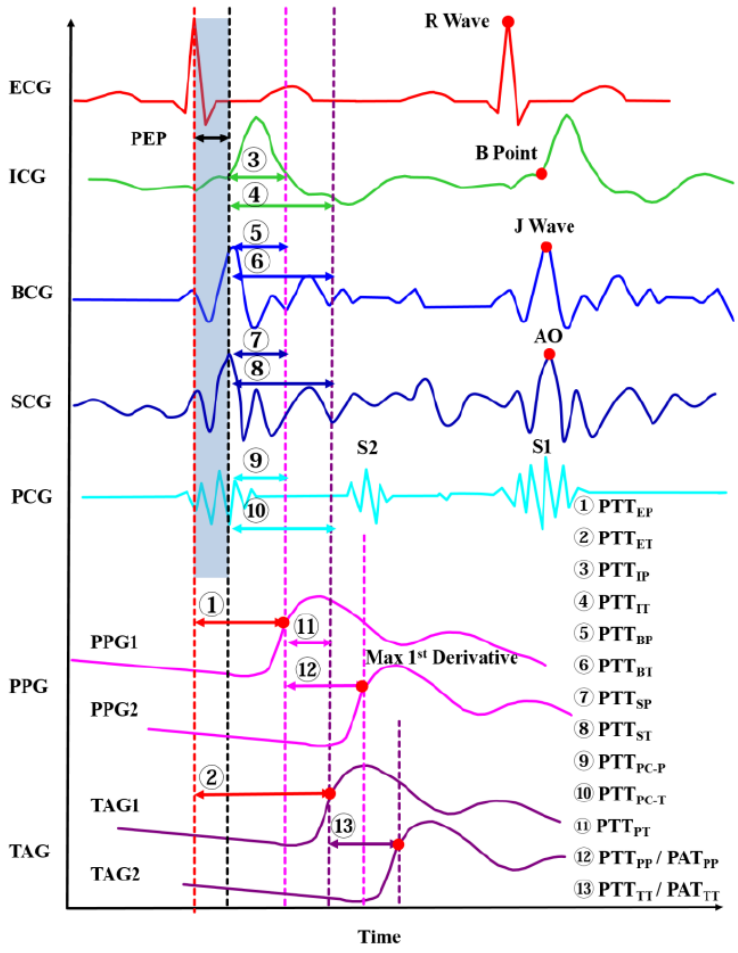


**Fig. 4.1.** – PTT acquisition techniques. Reproduced from [153].

The figure shows various techniques and uses the first one or two letters of the starting and arrival signals. Techniques comprise of the following pairs: ECG to TAG - which is an acronym for PPG/tonoarteriogram (TAG); impedance cardiogram (ICG)/ballistocardiogram (BCG)/phonocardiogram (PCG) to PPG/TAG; PPG to TAG, or by two PPGs/TAGs at diferent arterial sites, etc.

When using the peripheral pulses from PPG to account for arrival time, it is usually accepted that the foot of the pulse or intersection of the maximum tangent line to the upslope of the wave and the diastolic plateau of the

previous wave shall be used. The reason being, systolic peak is prone to the wave reflection effects and can lead to underestimation of PTT [172].

In this work, we use different instances of PTT calculation. These include: using foots of flow signals from MRI imaging at two arterial sites (extracted from Alastruey *et al.* [173] data from human aorta), ECG and PPG signals (done at the Strong Memorial hospital, university of Rochester), combination of BCG and PPG signals extracted from FIT seat [174] (a smart toilet seat, capable of recording ECG/BCG/PPG).

## 4.3 Blood Pressure Derived from PTT Based Calibration

A significant amount of work has been dedicated to relating the PTT to blood pressure using the famous Moens-Korteveq equation 3.2 as presented here in terms of global PWV number in 4.3:

$$PWV = \sqrt{\frac{Eh}{2\rho r}}. \tag{4.3}$$

This equation relates the speed of pulse wave propagation to blood density, elasticity, lumen thickness and radius of the artery. BP and PTT can then be connected to provide continuous BP measurement from PTT variations. This is done either by using a linear constitutive equation (such as the tube law), or with an empirical exponential relationship between young modulus $E$ and BP. However, nonlinear wall models cannot be used in conjunction with equation 4.3. Moens-Korteveq equation is derived based on a linear model of the fluid and structure interaction, and thus accounting for physical nonlinearity in equation 4.3 results in a different expression for PWV, which incorrectly connects mechanical property to external load, neglecting the fundamental stress-strain relationship. The robustness of a method is only approved if it can be applied to a person's normal variations to BP in different situations. BP changes can be attributed to a plethora of reasons. As hinted in Ding *et al.* review of the relevant articles [153], variations can be induced by stress, external pressure, external stimulus (such as watching a scary movie), drug administration, *etc*.

As mentioned in chapter 2, the distribution of the collagen fiber, elastin and smooth muscle cells contribute to the elastic and viscoelastic behavior of the arteries [175]. To the knowledge of the author, the main idea in the works that are relating BP to PTT is by having an accurate constitutive model and a reformulation of the Moens-Korteveq

equation to include BP instead of elasticity module. Thereby, it generates a direct relationship between the BP and PTT. The usual shapes of this relationship, as used in literature [176]–[183] are as follows:

$$BP = K_1 \ln(PTT) + K_2. \tag{4.4}$$

or another popular form being [184]:

$$BP = \frac{K_1}{PTT} + K_2. \tag{4.5}$$

demonstrating a better correlation for BP-PTT, and lastly the empirical nonlinear model [182]:

$$BP = \left(\frac{K_1}{(PTT - K_2)}\right)^2 + K_3. \tag{4.6}$$

Where $K_1$, $K_2$ and $K_3$ are patient-specific adjustable parameters. Some of the recent works in this area can be found in [16]. Mukkamala *et al.* [185] has also carried out a comprehensive review of the current regression based models [177] relating BP to PTT with one of the aforementioned equations. They came to the conclusion that the interventions are not significantly changing BP and a 3 unknown nonlinear model such as equation 4.6 might need more BP-PTT data points compared to equation 4.5. Thereby, they suggested using 4.5 with some considerations for non-physiological BPs. They suggest inducing BP variability with exercise and using least square regression to find unknown parameters. Another important factor is re-calibration which is claimed to have a high impact on improving the accuracy of the predictions.

In table 4.1, a summary of the evolution of BP-PTT regression based models over the years have been provided. It can be observed that the accuracy for systolic BP prediction based on PTT is 7% to 13% and diastolic BP is approximately 6% in popular techniques [176], [182], [186]–[188]. The method discussed in this dissertation is a physics-based BP-PTT prediction, described in more detail on chapters 5 and 7- 9, which demonstrates lower average RMSEs as shown in the table.

**Tab. 4.1.** – Summarized list of select regression models to describe BP - PTT relationship and its evolution through years. Method and accuracy described with various techniques; Mean Absolute Error (MAE), Root mean squared error (RMSE) and Mean Bias Error (MBE). The PTT evaluation method presented here takes both BP and Velocity $V$ in consideration when describing the relationship.

| First Authored on BP-PTT relationship | Method | Sample Size | Accuracy (Method) | | |
|---|---|---|---|---|---|
| | | | Method | Systolic | Diastolic |
| Young (1995,US) | $BP = K_1/PTT + K_2$ | 35 | MBE | -0.37 (-29.0 to 28.2) | -0.01 (-14.9 to 14.8) |
| Fung (2004,Canada) | $BP = K_1/(PTT)^2 + K_2$ | 22 | | −0.08 ± 11.32 | |
| Poon(2005,China) | $DBP = MBP_0 + \frac{2}{\gamma} ln\left(\frac{PTT_0}{PTT}\right) - \frac{1}{3} PP_0 \left(\frac{PTT_0}{PTT}\right)^2$ <br> $SBP = DBP + PP_0 \left(\frac{PTT_0}{PTT}\right)^2$ | 85 | | −0.6 ± 9.8 | −0.9 ± 5.6 |
| Muhlsteff (2006,Germalny) | $BP = K_1 \ln(PTT) + K_2$ <br> $BP = K_1/(PTT)^2 + K_2$ <br> $BP = K_1 * PTT + K_2$ | 18 | RMSE | 7.5 <br> 6.9 <br> 7.3 | |
| Wibmer (2014,Germany) | $BP = K_1 * PTT + K_2$ <br> $BP = (K_1/PTT - K_2)^2 + K_3$ | 20 | Mean Difference | (−10.9 to 10.9 mm Hg) <br> (−13.2 to 13.1 mm Hg). | |
| Kachuee(2015,2017,Iran) | Support Vector Machine Regression | 942 | MAE | 12.38 | 6.34 |
| Current work: Seyed Vahedein and Liberson 2019 | $PTT_{num} = \sum_{k=1}^{N_v} \int_0^{L_x} dx/(\mathrm{V} + \sqrt{A(BP)_A/\rho})$ | | RMSEs | 1.63 | 5.55 |

Another wave of recent publications are interested to predict central blood pressure from either peripheral BP [189] or a mix of peripheral BP and other biomarkers such as cross-sectional changes recorded with MRI [190].

According to [184], where they collect *in vivo* data from real patients, the effect of the following factors are usually neglected in the cuffless BP-PTT relationships. These factors are:

1. Cardiac output, CO (encompassing stroke volume, SV, and heart rate, HR)

2. The rate of ventricle contractility related to systolic intervals pre-ejection period (PEP) & left ventricle ejection time(LVET)

3. Total peripheral resistance (TPR)

4. The return of venous blood, filling of the right ventricle and controlling the cardiac preload

In 2014, Lombardi *et al.*, showed that 1D computational models are feasible to predict PWV and BP and their relationship in a deterministic manner [191]. Later in 2016, Liberson *et al.* [105], mathematically proved that the

relationship between PTT and BP can only be captured if nonlinear wall behavior and nonlinear flow equations are captured in a numerical model of the blood flow. They have experimentally demonstrated the improvement in accuracy of BP estimations when accounting for the nonlinearities of the vessel wall and blood flow [192].

In this work, a new technique is introduced that uses our reduced-order modeling platform for pulse wave propagation prediction, titled CardioFAN, and combines it with PTT and peripheral BP measurements to reconstruct an accurate central and arm BP. CardioFAN was intentionally designed with the following features in mind to accommodate predicting BP changes as a function of PTT, HR, SV, TPR. It has:

1. Nonlinear governing equations for fluid flow.

2. Quasi-1D hyperelastic arterial wall model and

3. Arbitrary arterial networks can be generated.

A recent PTT calculation feature has also been added to account for the local PWV value at each segment, providing a nonlinear PWV across the path of PTT measurement. This gives a better picture of the connection between PTT and BP. The experiment design and analysis has been presented in chapter 7.

The final goal of these implementations are a more accessible continuous blood pressure reading, leading to integration with wearable devices [193], [194].

### 4.3.1 PTT Measurement Limitations, Challenges and Concerns

Although promising, the BP measurement using PTT data can have limitations. Here some of the current challenges in this area are briefly mentioned. In later chapters, the solutions for these limitations will be addressed. Here are a few of them:

1. Interpretation of the PTT recordings can be sensitive to the measurement method 4.2. For instance PAT, when using ECG and PPG signals, not only includes PTT but also the pre-ejection period (PEP). Another alternative is PPG-PPG method. While eliminating the PEP concern, the timing of the PPG waveform may not coincide with BP and blood flow waveforms due to viscoelastic delays, wave reflection, or other factors. Data collection might also need additional considerations, for instance Huttunen *et al.* [160] states

that PPG-PPG method may require the knowledge about dicrotic notch and PPG peak in order to give an accurate estimate. BCG-PPG method signals are combined with breathing or human motion noises, which make it difficult to capture the maximum peak of BCG, resulting in an error in the calculation of PTT using BCG and ECG signals.

2. Cuff BP measurement tools, such as wrist cuff, are sensitive to the elevation, motion and baroreceptor reflex (baroreflex). These conditions, are needed to be taken into account when designing experiments, collecting data and predicting parameters using constitutive and fluid flow equations.

3. Subjects with pre-existing medical conditions cannot be easily distinguished from healthy patients and usually the determination is done based on the questionnaires filled by the patients regarding their cardiovascular health. A more direct collaboration between medical doctors and engineers and having access to real patient data can be a solution to this problem.

4. Constant calibration is usually required for improving the prediction capability of BP-PTT methods [185]. However, this can become a hurdle in having a practical and accessible product that can replace the currently tedious or invasive alternatives. There seems to be a need for a robust method that can take into account some of the variations related to stress, emotional fluctuations, external stimulus and potentially other factors.

5. Lastly, the scarcity of available PTT data for patient-specific topology of interest is preventing these methods to prove their applicability to real cardiovascular scenarios. The existence of shared databases such as Framinghamm study as recently used for machine learning based PTT to BP interpretations [161] can alleviate this issue.

With the provided background the next two chapters, 5,6, are dedicated to numerical model formulation, code development and validation taking into account what was discussed up to this point. In chapters 5, 7 a new method of calculating numerical PTT is proposed, which leads to a pilot test of PTT numerical measurement and its effect in restoring cardiac output (stroke volume times the heart rate) and proximal BP. A novel measurement method is then designed to calibrate the numerical code for patient-specific measurements in chapter 8. This is accompanied by a technique for optimizing parameters of interest and finally validating the method with unused set of experimental data. Finally, chapter 9 uses the patient-specific model to predict cardiac output and proximal/central BP values and discusses the evaluation strategy, limitations and challenges.

# 5 Noninvasive Assessment of Pulsatile Blood Flow in Hyperelastic Vascular Networks

## 5.1 Introduction

Clinical experiments (*i.e. in vivo*) and experimental (*i.e. in vitro*) models of the cardiovascular systems initiated significant improvement in diagnostic capabilities, stimulating development of the fields such as biomedical engineering and biomechanics [3]. Followed by computational simulations, the first numerical model of an artery in the cardiovascular system which accounted for the distensibility of the arteries was developed by [195]. More sophisticated models followed [50], [77], [100], [196], [197] which enhanced our understanding of the mechanism of blood flow and pulse propagation in cardiovascular system. With technological advancements, current computational models are becoming significantly more promising for the future of surgical planning, and for studying/monitoring cardiovascular health [4], [198]. Appearance of FDA-cleared devices such as (Heartflow® FFRCT and the Medtronic CardioInsight® Cardiac Mapping System) and the addition of new FDA regulations [4], are more supporting evidence that the computational methods are now producing clinically viable results.

Computational models can noninvasively capture the mechanistic behavior in a studied region of the cardiovascular system. When calibrated, these models can provide patient-specific data using pulsatile blood flow properties. Validated computational models have a significant advantage over invasive, costly and time-consuming experimental models and clinical tests. However, they require clinical measurements for calibration and evaluation of the patient-specific data [199]. Alternatively the data collected from computational models can be combined with experimental/clinical measurements to improve diagnostics capabilities of the current devics (*Data Assimilation* [7]).

Cardiovascular disorders and medical interventions can be diagnosed by quantification and monitoring distributions of the cardiac output, blood pressure, blood flow, pulse wave velocity (PWV) and arterial compliance along the aorta or any of the large arteries of interest [8]. In addition, the arterial wall stiffness, which governs the distensibility

of arterial walls, along with the wave reflections at the peripheral vascular bed, have been clinically identified as the primary biomarkers of the pulse wave propagation and cardiovascular health [200]. In recent years extensive work has been done on measuring wave reflections and PWV [161], or its surrogate pulse transit time (PTT) [11], [201]. The relation between PWV(or PTT) and cardiovascular diseases, such as a reduction in PTT as an indicator of hypertention [202], [203], among others [204], [205], have been previously studied. This has made the accurate prediction of pulse wave propagation an indispensable part of the recent cardiovascular simulations [206].

New advances in the computer power have provided researchers with the ability to model large scale one dimensional (1D) and 3D models [23], [207]. In contrast to local 3D geometrically accurate models, reduced-order models are not yet widely available as the diagnostic means for physicians. These models are usually validated against in vitro data [72], [73], since a physiologically accurate data calibration and validation is required to overcome the natural noise in the cardiovascular system [7]. Global 1D models introduce acceptable accuracy in capturing the physiological mechanisms of blood hemodynamics while having a marginally faster convergence rate compared to 3D models. Their application is justified by the long-wave approximation, making them ideal to be coupled with a local 3D model of a confined area of interest [19] or lumped parameter (0D) models replacing the outlet to the rest of a cardiovascular network.
The majority of theoretical models developed to describe the fluid-structure interaction (FSI) in the vascular circulatory system use linear elastic or viscoelastic constitutive equations for the wall coupled with the one-dimensional averaged momentum equation for the fluid. However, the stress-strain relationship for biological tissue is essentially nonlinear [25]. Fung et al. introduced an anisotropic model, which accounts for the directionality of the elastic properties. The model constants can be calibrated by measuring the pressure and diameter of the main arteries with clinical or experimental measurements. [208] mentioned that the physical nonlinearity is crucial for an accurate prediction of pulsatile blood flow properties in case of studying an aortic aneurism. It was proven by [209], that the match of measured and estimated values of PWV can be only obtained when the hyperelasticity of arterial wall is introduced.

To the knowledge of authors, the current numerical algorithms applied to the 1D (reduced order) models do not necessarily preserve the monotonic property. Monotonicity preserving (i.e. high-resolution) schemes can retain the shape of waveform without creating artificial oscillations [114]. This approach may not cause a significant difference when a smooth solution exists, such as for pressure or flow waveforms in healthy patients or when studying hypertension [56]. However, in case of a discontinuity in the properties, *e.g.* stented or prosthetic artery [28], the only class of solvers that can provide a solution without simplistic smoothing of the waveforms [100], are the monotonicity preserving solvers. Monotonicity preserving or total variation diminishing (TVD) schemes, can also be used for continuous monitoring/prediction of cardiovascular health due to the discontinuous nature

of cardiovascular events. These numerical schemes are free of dispersion caused by approximating the odd derivatives in the Taylor expansion of the governing partial differential equations (PDEs), making them ideal for resolving discontinuous properties.

The general approach of Hamilton's variational principle is utilized here to construct a unique form of the FSI equations governing the blood flow in the arterial system. The quasi-1D reduced FSI model is simple to execute and alter, can be coupled to geometrically multiscale simulations [210], [211] and provides quick solutions for the hyperbolic PDEs governing the nonlinear pulsatile flow in an arbitrary arterial network. The utilized approach demonstrates an improvement in accuracy due to the account of hyperelastic wall properties, along with the employment of a high-resolution monotone numerical scheme. The created software, named CardioFAN (Cardiovascular Flow Analysis), is validated against available data from numerical, in vitro and in vivo experiments for networks of arteries with 55, 37 and 26 main arterial segments [50], [78], [101], [212], [213], respectively. The effect of physical nonlinearity on the correct calculation of the PTT, pressure, flow and luminal vessel area is displayed. The physics based nonlinear constitutive framework can be adequately tested, calibrated and applied for patient-specific clinical diagnosis and prediction. We present the algorithm for calculating numerical PTT for hyperelastic arteries, sensitive to variation of the blood pressure and the stroke volume. This PTT calculation technique can also complement the studies investigating the feasibility of tracking variations of cardiovascular markers by measurements of the PTT or PWV [185], [214]. The new method is used here to improve the calculation of the speed of wave propagation based on the prior in vivo data provided by [213]. Compared to prior numerical simulations of this data, CardioFAN improved the flow, luminal area and pressure waveform predictions by 1.5%, with averaged relative errors smaller than 5.5% between simulated and *in vivo* waveforms. As shown in section 3.3, with the current method, assigning a uniform or non-uniform speed of propagation values as the input properties of each segment, leads to improved waveform predictions. CardioFAN is now available for free and can be accessed from the provided links. Reliability test of this code conducted here is an important step toward preparing it for noninvasive and patient-specific diagnostics and data assimilation [7] purposes.

## 5.2 Methods

### 5.2.1 Blood Properties

Although blood rheology is proved to be non-Newtonian [47], previous studies have shown that the blood viscosity model does not significantly affect the PWV when simulating large human arteries [45], [49]. According to [48],

non-Newtonian fluid model is only required for small arteries with diameters $D < 100\ \mu m$, were the shear rate reduces to less than $1\ s^{-1}$. Therefore, for the larger arteries we can use the Newtonian flow assumption. On the other hand, 90% of the blood consists of water [45], and since the suspended materials are several order of magnitudes smaller than arterial diameter, the blood can be considered homogeneous and incompressible with a density of $\rho_f = 1050\ kg/m^3$ and viscosity of $\mu = 4.0\ mPa.s$ [45] (used in 55 segment case, section 3.1). We used $\rho_f = 1050\ kg/m^3$ , $\mu = 2.0\ mPa.s$ and $\rho_f = 1060\ kg/m^3$, $\mu = 3.5\ mPa.s$ for the *in vitro* [78] and *in vivo* [213] validation cases, respectively.

## 5.2.2 Governing Equations

Reduced mathematical model for cardiovascular networks results in a hyperbolic set of partial differential equations, describing interaction of an incompressible blood fluid motion with a viscous hyperelastic vessel wall. The averaging across the section of a flow path is based on the Hamilton's variational principle governing the process of a fluid-structure interaction [215]

$$\begin{aligned} \delta I \ &= \ \delta I_{fluid} \ + \delta I_{solid} = \\ &= \int_{t_1}^{t_2} \left[ \oint_{\forall_{\text{fluid(t)},}} \rho_f \delta L_f d\forall + \oint_{\forall_{\text{solid(t)},}} \delta L_s d\forall \right] dt = 0 \end{aligned} \tag{5.1}$$

Here $\delta I_{fluid}$ ,$\delta I_{solid}$ are the variations of action components across fluid and solid volumes $\forall_{fluid(t)}$ , $\forall_{solid(t)}$; $t$ – time, $\rho_f$ density of the fluid, $L_f$, $L_s$ - the Lagrangian density functions for fluid and solids, respectively.

### 5.2.2.1 Fluid Domain

As it is mentioned by [216], variation of the Lagrange function density in Eulerian coordinates can be written as follows:

$$\delta L_f = \delta \left( \frac{\boldsymbol{V}^2}{2} - U(\rho_f, S, \nabla \boldsymbol{u}) \right) + T\delta S \tag{5.2}$$

where $\boldsymbol{V}$ – is a velocity vector, $U$ – is an internal energy as a function of density, $S$ – entropy, $\nabla \boldsymbol{u}$ (gradient of a displacement vector $\boldsymbol{u}$)- a distortion tensor, and T – is temperature. The variation of the functional must vanish for any admissible variations $\delta \boldsymbol{u}$ The derivation of fluid flow equations based on the Hamilton's variational principle is

previously shown in detail [215]. Here the effect of gravity force is added to the reduced momentum equation which affects the circulation when patient is in standing upright position

$$\begin{aligned}
&\frac{\partial \overline{V}}{\partial t}+\frac{\partial}{\partial x}\left(a_1\frac{P}{\rho_f}+a_2\overline{V}^2\right)= \\
&\qquad=\frac{1}{a_0\rho}\left[\int rf(\mathrm{r})\,\sigma(\mathrm{x},\mathrm{r},\mathrm{t})dr-R\,\tau(\mathrm{x},\mathrm{R},\mathrm{t})\right]+g_\tau \\
&a_0=\int rf(\mathrm{r})dr; \\
&a_1=\int r\varphi(\mathrm{r})f(\mathrm{r})dr; \\
&a_2=\frac{1}{a_0}\int r\varphi(\mathrm{r})^2f(\mathrm{r})dr
\end{aligned} \tag{5.3}$$

where $g_\tau$ is a gravitational acceleration in the direction of the streamline, $f(\mathrm{r})$, $\varphi(\mathrm{r})$- the specified function distributions of axial velocity and displacement accordingly, $r$ – radial coordinate, R- internal wall radius $P$ – blood pressure, $\overline{V}$ – averaged across the flow path section fluid velocity, $\boldsymbol{\sigma}$, $\boldsymbol{\tau}$ are the axial deviatoric and shear stress tensor components accordingly.

[217], showed that velocity profile is mostly flat in large arteries, unlike peripheral arteries where profile is close to the parabolic shape [80]. In case of Newtonian fluid ( $\sigma=2\rho_f\nu\frac{\partial V}{\partial x},\ \tau=\rho_f\nu\frac{\partial V}{\partial r},\ \nu$ – kinematic viscosity), by utilizing the generalized Hagen-Poiseuille velocity profile $\varphi\,(r)=\frac{\gamma+2}{\gamma}\left[1-\left(\frac{r}{R}\right)^\gamma\right]$ and a constant profile for the displacement distribution $f\ (r)=1$, Equation (5.3) takes the form presented in [218]

$$\begin{aligned}
&\frac{\partial \overline{V}}{\partial t}+\frac{\partial}{\partial x}\left(\alpha\frac{\overline{V}^2}{2}+\frac{P}{\rho_f}\right)= \\
&\qquad=\nu\left(\frac{\partial^2\overline{V}}{\partial x^2}-2\,(\gamma+2)\,\frac{\overline{V}}{R^2}\right)+g_\tau
\end{aligned} \tag{5.4}$$

Momentum equation (5.4), is complemented by an averaged over the cross-section continuity equation [219]

$$\frac{\partial A}{\partial t}+\frac{\partial}{\partial x}\left(\overline{V}A\right)=0;\qquad A=A_0(1+\eta)^2 \tag{5.5}$$

where $\eta$ is the circumferential strain (normal wall displacement normalized to radius R), $A$, $A_0$ cross sectional areas in the loaded and the stress-free conditions. Constitutive "tube model", closing these two equations for unknown variables $A,\ P$ and $\overline{V}$, follows from the analysis of a solid domain.

#### 5.2.2.2 Solid Domain: The Hyperelastic Fung's Model and the Generalized Tube Law

Consider a circular thin-wall cylinder in the polar system of coordinates. Let $R$ be the radius of the wall under the load, $R_0$ – radius in a load free state, $h$ - the wall thickness, $\rho_w$-density of the wall. Introducing wall kinetic energy $K$, elastic energy $U_{el}$, dissipative energy $U_d$ and work of external load $W_p$, the Lagrangian density function relating to the solid domain can be presented as

$$L_s = \delta K - (\delta U_{el} + \delta U_d - \delta W_p) \tag{5.6}$$

The normal velocity of the moving wall $R_0 \frac{d\eta}{dt}$ defines kinetic energy per unit length

$$K = \frac{1}{2}\rho_w h {R_0}^2 \left(\frac{\partial \eta}{\partial t}\right)^{\mathbf{2}} \tag{5.7}$$

Internal elastic energy is composed of a hyperelastic strain energy [25] and energy, accumulated by a longitudinal pre-stress force N per unit area

$$U_{el} = \frac{hc}{2}\left(e^Q - 1\right) + N\left(\sqrt{1 + {R_0}^2\left(\frac{\partial \eta}{\partial x}\right)^2} - 1\right) \tag{5.8}$$

Here $Q = a_{11}\epsilon_\theta^2 + 2a_{12}\epsilon_\theta\epsilon_x + a_{22}\epsilon_x^2$, and $c,\ a_{11},\ a_{12},\ a_{22}$ are material constants from Fung's anisotropic model [25], where $\epsilon_\theta$ and $\epsilon_x$ are the circumferential and axial strain components. Strain energy of the wall modelling as a system of independent hyper-elastic rings is simplified in a 1D case by setting $a_{12} = a_{22} = 0,\ \epsilon_\theta = \eta$, where $\eta$ is the circumferential strain. As a result, for small strains ${R_0}^2\left(\frac{\partial \eta}{\partial x}\right)^2 \ll 1$, arrive at the expression for the strain energy of a reduced model

$$U_{el} = \frac{hc}{2}\left(e^{a_{11}\eta^2} - 1\right) + N\frac{{R_0}^2}{2}\left(\frac{\partial \eta}{\partial x}\right)^2 \tag{5.9}$$

Elementary work produced by the viscous component of circumferential stress relating to the Voight-type viscoelastic material and an external pressure reads

$$\delta U_d - \delta W_p = \left( \frac{h}{R_0} \Gamma \frac{\partial \eta}{\partial t} - P \right) R_0 \delta \eta \tag{5.10}$$

where $\Gamma$ is the viscosity constant. Calculating variational derivative of the Lagrange function $L_s$ (Equation (5.6)) ( $L_s = L_s(\eta, \eta_t, \eta_x), \eta_t = \frac{\partial \eta}{\partial t}, \eta_x = \frac{\partial \eta}{\partial x}$)

$$\frac{\delta L_s}{\delta \eta} = \frac{\partial L_s}{\partial \eta} - \frac{\partial}{\partial t} \frac{\partial L_s}{\partial \eta_t} - \frac{\partial}{\partial x} \frac{\partial L_s}{\partial \eta_x} = 0 \tag{5.11}$$

obtain the equation of motion of an axisymmetric cylinder

$$\begin{aligned} P = \frac{h}{R_0} \left( c a_{11} \eta e^{a_{11} \eta^2} + \Gamma \frac{\partial \eta}{\partial t} \right) \\ + \rho_w h R_0 \frac{\partial^2 \eta}{\partial t^2} - N {R_0}^2 \frac{\partial^2 \eta}{\partial x^2} \end{aligned} \tag{5.12}$$

The physics based “tube law” follows now from Equation (5.12), where we ignore expansion terms of the fifth degree in $\eta$ and higher

$$\begin{aligned} P = \frac{h}{R_0} \left( c a_{11} \eta e^{a_{11} \eta^2} + \Gamma \frac{\partial \eta}{\partial t} \right) = \\ = \frac{h}{R_0} c a_{11} \eta \left( 1 + a_{11} \eta^2 \right) + \frac{h \Gamma}{R_0} \frac{\partial \eta}{\partial t} + O(\eta^5) \end{aligned} \tag{5.13}$$

Note that partial derivative of the circumferential stress, $\sigma_\theta = \frac{P R_0}{h}$, by circumferential strain, $\eta$, at a zero load represents tangential modulus, $\overline{E}$, at a stress-free state ($\nu_P$ is the Poisson’s ratio)

$$P \frac{\partial \left( \frac{P R_0}{h} \right)}{\partial \eta} |_{\eta \to 0} = c a_{11} = \overline{E}, \qquad \overline{E} = \frac{E}{1 - {\nu_P}^2} \tag{5.14}$$

According to Equations (5.13) and (5.14), the constitutive model is presented as a superposition of a viscoelastic and a hyperelastic terms characterized by the Fung's hyperelastic coefficient $a_{11}$ and a tangential modulus $\overline{E}$

$$\begin{aligned} P &= \frac{h}{R_0}\overline{E}\eta e^{a_{11}\eta^2} = 2\rho_f c_{mk}^2 \eta e^{a_{11}\eta^2} + 2\rho c_{mk}^2 \frac{h\Gamma}{R_0}\frac{\partial \eta}{\partial t} \\ &\text{or in a truncated form} \\ P &\cong 2\rho c_{mk}^2 \eta\left(1 + a_{11}\eta^2\right) + 2\rho_f c_{mk}^2 \beta \frac{\partial \eta}{\partial t} \quad + O(\eta^5) \end{aligned} \tag{5.15}$$

Here $c_{MK} = \sqrt{\frac{\overline{E}h}{2\rho R_0}}$ – the Moens-Korteweg speed of pulse wave propagation, $\beta = \frac{\Gamma}{\overline{E}}$. By setting $a_{11} = 0$, replacing $\eta = \sqrt{\frac{A}{A_0}} - 1$, we retain the classic form of the *tube law* for linear viscoelastic material [212]. Specifying in addition $\beta = 0$ results in a linear elastic tube law

$$P \cong 2\rho_f c_{mk}^2 \eta \tag{5.16}$$

#### 5.2.2.3 Reorganizing the Hyperelastic Vessel Formulation

In the following we simplify the notation by denoting the cross-sectional area averaged axial velocity by $V$ instead of $\overline{V}$. Assuming the generalized Hagen-Poiseuille radial velocity profile with $\gamma = 9$, justified by [220], and neglecting contribution of the axial stress component compare to the shear stress, the Equations (5.4) and (5.5) read

$$\begin{aligned} &\frac{\partial \boldsymbol{Q}}{\partial t} + \frac{\partial F(\boldsymbol{Q})}{\partial x} = \boldsymbol{f}; \\ &\boldsymbol{Q} = \begin{bmatrix} A \\ V \end{bmatrix}; \quad \boldsymbol{F} = \begin{bmatrix} AV \\ \frac{V^2}{2} + \frac{P}{\rho_f} \end{bmatrix}; \quad \boldsymbol{f} = \begin{bmatrix} 0 \\ -\frac{22kV}{A} + g_\tau \end{bmatrix}; \end{aligned} \tag{5.17}$$

Here, $P_A = \frac{\partial P}{\partial A}$ , and $A = A_0(\eta + 1)^2$. $f$ relates to the viscous source term [50], where $k = -22\pi\nu$ (since $\gamma = 9$), and kinematic viscosity $\nu = \frac{\mu}{\rho}$.

#### 5.2.2.4 The Characteristic Analysis

When enforcing numerical algorithm to the hyperbolic system, it is useful to invoke the characteristic variables, while applying the characteristic properties to the time marching algorithm and implementation of boundary

conditions. Considering arbitrary pressure – area relationship, $P = P(A)$, rewrite the homogeneous system of Equation (5.17) in the following non-conservative quasi-linear form

$$\begin{aligned} &\frac{\partial A}{\partial t} + V\frac{\partial A}{\partial x} + A\frac{\partial V}{\partial x} = 0 \\ &\frac{\partial V}{\partial t} + V\frac{\partial V}{\partial x} + \frac{P_A}{\rho_f}\frac{\partial A}{\partial x} = 0 \end{aligned} \tag{5.18}$$

where $P_A = \frac{\partial P}{\partial A}$. Multiplying each equation in system of Equations (5.18) by unknown coefficients $l_1$and $l_2$, respectively, create a linear combination

$$\begin{aligned} \left[l_1\frac{\partial A}{\partial t} + \left(l_1 V + l_2\frac{P_A}{\rho_f}\right)\frac{\partial A}{\partial x}\right] + \\ \left[l_2\frac{\partial V}{\partial t} + (l_2 V + l_1 A)\frac{\partial V}{\partial x}\right] = 0 \end{aligned} \tag{5.19}$$

Now associate each bracket of Equation (5.19) with a substantial derivative of a relating variable

$$\begin{aligned} l_1\frac{dA}{dt} &= l_1\frac{\partial A}{\partial t} + \left(l_1 V + l_2\frac{P_A}{\rho_f}\right)\frac{\partial A}{\partial x}; \\ l_2\frac{dV}{dt} &= l_{\,2}\frac{\partial V}{\partial t} + (l_2 V + l_1 A)\frac{\partial V}{\partial x} \end{aligned} \tag{5.20}$$

The latter is equivalent to the eigenvalue problem, where the eigenvalue $\lambda = \frac{dx}{dt}$ determines direction of the wave propagation in a time -space domain $(t, x)$

$$\begin{aligned} l_1 V + l_2\frac{P_A}{\rho} &= \lambda l_1 \\ l_1 A + l_2 V &= \lambda l_2 \end{aligned} \tag{5.21}$$

By equating to zero the relating determinant

$$\begin{Vmatrix} V-\lambda & \frac{P_A}{\rho_f} \\ A & V-\lambda \end{Vmatrix} = 0 \tag{5.22}$$

obtain two characteristic directions

$$\lambda_{1,2} = \left(\frac{dx}{dt}\right)_{1,2} = V \pm \sqrt{\frac{AP_A}{\rho_f}} \tag{5.23}$$

Once eigenvalues found, the normalized eigenvector components follow from Equation (5.21)

$$l_1 = \pm\sqrt{\frac{P_A}{A\rho_f}}, \qquad l_2 = 1 \tag{5.24}$$

Compatibility conditions for nonlinear hyperbolic equations can be determined by integrating the differential form following from Equations (5.19), (5.20), (5.24)

$$l_1 dA + l_2 dV = \pm\sqrt{\frac{P_A}{\rho_f A}} dA + dV = 0 \tag{5.25}$$

So that the characteristic (Riemann) variables $W_{1,2}$ read

$$W_{1,2} = V \pm \int \sqrt{\frac{P_A}{\rho_f A}} dA \tag{5.26}$$

With an employment of the hyperelastic constitutive model (*i.e.* no viscoelasticity), Equation (5.15), consider pressure as a function of area, and its derivative in an expanded form of the exponential

$$\begin{aligned} P &= 2\rho c_{mk}^2 \left[\left(\sqrt{\frac{A}{A_0}} - 1\right) + a_{11}\left(\sqrt{\frac{A}{A_0}} - 1\right)^3\right] \\ P_A &= \frac{\partial P}{\partial A} = \frac{\rho c_{mk}^2}{\sqrt{A}A_0}\left[1 + 3a_{11}\left(\sqrt{\frac{A}{A_0}} - 1\right)^2\right] \end{aligned} \tag{5.27}$$

By substituting Equation (5.27) into Equations (5.23) and (5.26), we obtain velocities of two simple waves propagating in opposite directions, and characteristic variables

$$\begin{aligned} \lambda_{1,2} &= V \pm c_{mk} \sqrt[4]{\frac{A}{A_0}} k_\lambda, \\ k_\lambda &= \sqrt{1 + 3a_{11}\left(\sqrt{\frac{A}{A_0}} - 1\right)^2} \end{aligned} \tag{5.28}$$

$$\begin{aligned} W_{1,2} &= V \pm 4c_{mk} \sqrt[4]{\frac{A}{A_0}}\, k_w, \\ k_w &\cong 1 + a_{11}\left(1.5 + 0.3\frac{A}{A_0} - \sqrt{\frac{A}{A_0}}\right) \end{aligned} \tag{5.29}$$

Equations (5.28) and (5.29), pinpoint results of a mathematical analysis of the wave propagation in compliant hyperelastic arteries, filled with a moving incompressible fluid. Here, $W_1$ and $W_2$ propagate information on velocity and pressure from proximal to distal and distal to proximal locations, respectively. By setting hyperelastic material coefficient to zero, $(a_{11} = 0 \text{ or } k_\lambda = k_w = 1)$, the known expressions relating to the linear elastic arterial wall are obtained [218]. Note that Equations (5.27) – (5.29) can also be presented in the exponential form of the hyperelastic constitutive model. Further verification of the code by introducing simple waveforms at the inlet and middle of a cylindrical or bifurcated geometry as well as testing the total variation diminishing properties are presented in appendix A.

### 5.2.3 Numerical Discretization: Finite Volume Method

CardioFAN utilizes two numerical schemes to solve set of equations (5.17), for different purposes of arterial simulations. First method is a classical explicit Lax-Wendroff scheme, that is stable when reproducing a smooth transient solution and is a counterpart of the Taylor-Galerkin method. However, when resolving discontinuity in geometry, physical properties, or the time-dependent load function Lax-Wendroff results in false spurious oscillations, giving physically unrealistic or unstable results (as shown in section 3.1). In these cases a monotonicity preserving Total Variation Diminishing (TVD) modification of Lax-Wendroff scheme [114], [221] isutilized to reduce the numerical dispersion. The latter is exceptionally important when modeling waves propagating through compliant sites that underwent endovascular aneurysm repair by arterial stent placement [222]. To expedite convergence to the pulsatile conditions the liner acoustic solution [223] was used to initialize the time marching process based

on the TVD-Lax-Wendroff scheme. Discritization of the nonlinear set of equation (5.17) is discussed with more details in the following section. The comparison between the results obtained by TVD and classic Lax-Wendroff methods, in discontinuous waves are detailed in our previous work [215]. In section 3.1, the advantages of using TVD method against other non-TVD methods are explored for a manufactured case of a stented artery.

#### 5.2.3.1 Lax-Wendroff Method

Nonlinear conservation equations listed in Equation (5.17) can be rearranged as follows

$$\frac{\partial \boldsymbol{Q}}{\partial t} = \boldsymbol{f} - \frac{\partial \boldsymbol{F}(\boldsymbol{Q})}{\partial x}; \tag{5.30}$$

Jacobian matrices of vector functions $\boldsymbol{F}_{\boldsymbol{Q}} = \frac{\partial \boldsymbol{F}}{\partial \boldsymbol{Q}}$, $\boldsymbol{f}_{\boldsymbol{Q}} = \frac{\partial \boldsymbol{f}}{\partial \boldsymbol{Q}}$ of Equation (5.17), are

$$\boldsymbol{F}_{\boldsymbol{Q}} = \boldsymbol{H} = \begin{bmatrix} V & A \\ \frac{P_A}{\rho} & V \end{bmatrix}, \qquad \boldsymbol{f}_{\boldsymbol{Q}} = \frac{k}{A} \begin{bmatrix} 0 & 0 \\ -\frac{V}{A} & 1 \end{bmatrix} \tag{5.31}$$

A detailed discretization based on Lax-Wendroff scheme is previously shown in [224]. Following notation typical for finite volume methods (as shown by [116]), here the space domain is discretized with uniformly distributed cells, whose center points are indicated by a low integer index $j$, and the edge points are noted by fractional indices $j \pm \frac{1}{2}$. Associating flux functions with the cell edges we get the Lax-Wendroff based discretized solution

$$\begin{aligned} \boldsymbol{Q}_j^{n+1} &= \boldsymbol{Q}_j^n - \frac{\Delta t}{\Delta x}(\boldsymbol{F}_{j+\frac{1}{2}}^n - \boldsymbol{F}_{j-\frac{1}{2}}^n) + \boldsymbol{Q}_{\boldsymbol{f}j}^n \\ \boldsymbol{F}_{j+\frac{1}{2}}^n &= \frac{\boldsymbol{F}_j^n + \boldsymbol{F}_{j+1}^n}{2} - \frac{\Delta t}{2\Delta x} \boldsymbol{H}_{\frac{j+1}{2}}^n \left(\boldsymbol{F}_{j+1}^n - \boldsymbol{F}_j^n\right) \\ \boldsymbol{Q}_{\boldsymbol{f}j}^n &= \Delta t f^n \\ &\quad + \frac{\Delta t^2}{2}\left[\boldsymbol{f}_{\boldsymbol{Q}}\left(\boldsymbol{f} - \frac{\partial \boldsymbol{F}(\boldsymbol{Q})}{\partial x}\right) - \frac{\partial}{\partial x}\left(\boldsymbol{F}_{\boldsymbol{Q}} \boldsymbol{f}\right)\right]^n \end{aligned} \tag{5.32}$$

Where $n$ refers to the current time step, and $\Delta t$ is the time-step. The convergence criteria for the Lax-Wendroff scheme is defined by Courant–Friedrichs–Lewy (CFL) condition

$$CFL \;=\; \frac{\tau(V + c_{MK})_{max}}{\Delta x} \;\leq\; 1 \tag{5.33}$$

#### 5.2.3.2 High-Resolution Lax-Wendroff Scheme (TVD Method)

As shown in [116], the dispersive nature of all non-monotone methods, including Lax-Wendroff, causes artificial oscillations in the vicinity of discontinuities. The idea behind high resolution schemes is in introduction of the flux limiters, that correct the flux terms depending on the local solution behavior, retaining monotonicity in case of a discontinuity.

Following Leveque, we present fluxes in a form revealing explicitly diffusive flux components $\tilde{F}_{j+\frac{1}{2}}$ (upper index dropped for simplicity)

$$\begin{aligned}
\boldsymbol{F}_{j+\frac{1}{2}} &= \frac{1}{2}\left[\boldsymbol{F}_j + \boldsymbol{F}_{j+1} - \left|\boldsymbol{H}_{j+\frac{1}{2}}\right| \boldsymbol{\Delta Q}_{j+\frac{1}{2}}\right] + \widetilde{\boldsymbol{F}}_{j+\frac{1}{2}} \\
\widetilde{\boldsymbol{F}}_{j+\frac{1}{2}} &= \frac{1}{2}\boldsymbol{R}_{j+\frac{1}{2}} \left|\boldsymbol{\Lambda}_{j+\frac{1}{2}}\right| \left(\boldsymbol{I} - \frac{\Delta t}{\Delta x}\left|\boldsymbol{\Lambda}_{j+\frac{1}{2}}\right|\right) \boldsymbol{\Delta W}_{j+\frac{1}{2}}
\end{aligned} \tag{5.34}$$

$$\begin{aligned}
&\boldsymbol{H}_{j+\frac{1}{2}} = \; \boldsymbol{R}_{j+\frac{1}{2}} \; \boldsymbol{\Lambda}_{j+\frac{1}{2}} \; \boldsymbol{R}^{-1}_{j+\frac{1}{2}}; \\
&\boldsymbol{\Delta Q}_{j+\frac{1}{2}} = \boldsymbol{Q}_{j+1} - \boldsymbol{Q}_j; \\
&\boldsymbol{\Delta W}_{j+\frac{1}{2}} = \boldsymbol{R}^{-1}_{j+\frac{1}{2}} \boldsymbol{\Delta Q}_{j+\frac{1}{2}};
\end{aligned} \tag{5.35}$$

where $I$ - identity matrix, $\boldsymbol{R}_{j+\frac{1}{2}}$, $\boldsymbol{\Lambda}_{j+\frac{1}{2}}$ – are the modal and eigenvalue matrices of Jacobian matrix $H_{j+\frac{1}{2}}$. The correction flux, satisfying to the monotonicity conditions is based on a substitution of the eigenvector increment $\boldsymbol{\Delta W}_{j+\frac{1}{2}}$ by its limited version $\boldsymbol{\Delta \tilde{W}}_{j+\frac{1}{2}}$ [116]

$$\begin{aligned}
&\boldsymbol{\Delta \widetilde{W}}_{j+\frac{1}{2}} = \psi\left(r_{j+\frac{1}{2}}\right) \boldsymbol{\Delta W}_{j+\frac{1}{2}}, \qquad r_{j+\frac{1}{2}} = \frac{\boldsymbol{W}_{j+1} - \boldsymbol{W}_j}{\boldsymbol{W}_j - \boldsymbol{W}_{j-1}}, \\
&\psi \;=\; max\left[0, min\left(2r, 1\right),\; min(\mathrm{r}, 2)\right] \qquad < ex. \quad Superbee >
\end{aligned} \tag{5.36}$$

## 5.2.4 Boundary Conditions

### 5.2.4.1 Inlet

Inlet flow rate is prescribed by enforcing known blood flow waveform, $Q(t)$, as a function of time at the inlet. At the root of aorta, this known variable is imposed at the edge of the first element. To calculate the inlet velocity and a cross section area the flow rate equation is complemented by the backward running characteristic, as shown by Equation (5.37). This assignment is previously shown to provide physiological waveform shapes (see [225]).

$$\begin{aligned} &V_{in}A_{in} = Q_0(t) \\ &V_{in} \; -4\left[c_{MK}\left(\frac{A}{A_0}\right)^{\frac{1}{4}}\right]_{in} = (W_2)_1 \end{aligned} \tag{5.37}$$

where $W_2$ is the backward propagating invariant, Equation (5.29), calculated at the first cell $n = 1$. In case of the hyperelastic form of the FSI formulation, Equations (5.28) and (5.29) are utilized, where Equation (5.37) takes the following form

$$\begin{aligned} &V_{in}A_{in} = Q_0(t) \\ &W_2 = V - 4c_{mk}\sqrt[4]{\frac{A}{A_0}}\,k_w, \\ &k_w \cong 1 + a_{11}\left(1.5 + 0.3\frac{A}{A_0} - \sqrt{\frac{A}{A_0}}\right) \end{aligned} \tag{5.38}$$

### 5.2.4.2 Outlet Boundary Condition (RCR Lumped Parameter Model)

Three-element Windkessel model, characterized by resistance (R1), capacitance (CT) and second resistance (R2) (*i.e.* RCR), is used to define the terminal BC at the truncated outlets. Details of different types of lumped parameter (*i.e.* 0-Dimensional) terminal models can be found in [87], [226]. Equation (5.39) presents the differential form of the boundary condition, comprising time dependent pressure ($P_e$) and flow ($VA$) at the exit of the truncated

vessel. The terminal condition is complemented by the forward propagating invariant $W_1$ arriving at the truncated section from the center of last cell, $n = N$, of the vessel

$$(\dot{VA})_T = \left[\frac{\dot{P}_e}{R_c} + \frac{P_e - P_{out}}{R_c R_p C_T} - \left(1 + \frac{R_c}{R_p}\right)\frac{VA}{R_c C_T}\right]_T \tag{5.39}$$

Arterial conduit resistance ($R_C$) and peripheral resistance ($R_P$) of the arteries need to be specified. One method is based on measurements of the mean arterial pressure ($P_m$), outlet pressure relating to microcirculation site, ($P_{out}$), and the mean flow at the root of the arteries ($\overline{Q}_{in}$). Total arterial compliance ($C_T$), can then be found by measuring the time of diastolic decay ($\tau$) of the pressure [67]

$$\begin{aligned} R_T &= \frac{P_m - P_{out}}{\overline{Q_{in}}}, \quad P_m = P_0 + \frac{1}{3}(P_s - P_d) \\ R_C &= \frac{\rho C_{Mk,\ seg}}{A_d}, \quad R_T = R_C + R_P, \quad C_T = \frac{\tau}{R_T} \end{aligned} \tag{5.40}$$

The conduit and peripheral compliances are calculated by a summation of the compliances of all 1D segments [67]

$$\begin{aligned} C_T &= C_p + C_C, \quad C_c = \sum_{i=1}^{N} C_{seg}^j, \quad C_{seg}^i = \frac{A_d L}{\rho_f (C_d)^2}, \\ \tilde{C}^j &= C_P \frac{R_P}{R_C + R_P} = C_P \frac{\overline{Q}_{out}^j}{\overline{Q}_{in}} \\ A_d &= \frac{1}{L}\int_0^L A_d(x)\,dx, \qquad C_d = \frac{1}{L}\int_0^L C_d(x)\,dxe \end{aligned} \tag{5.41}$$

Here, $A_d$, $C_d$, are the diastolic area and speed of wave propagation, $\overline{Q}_{out}^j$- the $j^{th}$ segment outlet flow rate, and $\tilde{C}^j$ is the terminal compliance at the $j^{th}$ segment

If measurement is not plausible, $R_T$ and $C_T$ can be approximated with the iterative method introduced by [67]. Terminal compliance is then corrected as follows

$$C^j = \tilde{C}^j \frac{R_P + R_C}{R_P} \tag{5.42}$$

Since Equation (5.39) is a time dependent differential equation, its discretized version is used at each time-step. Being complemented by the forward propagating characteristic variables at the last cell, Equation (5.39) can be solved for velocity and pressure, and thus cross-sectional area, at each time-step. For simplicity, linear forward propagating characteristic [116] can also be considered at the last cell.

#### 5.2.4.3 Bifurcated Joints

Splitting flow junctions are typical alignments in the arterial system. Let $V_1,\ P_1\ A_1$ indicate velocity, pressure and cross section area of a parent vessel at the junction interface, and $V_2,\ P_2\ A_2, V_3,\ P_3\ A_3$ – the corresponding properties of daughter vessels at the interface. The following assumptions are made to simplify the junction matching procedure: 1) energy losses at the junctions are ignored [78], 2) pressure changes across the junction is neglected, $P_1 = P_2 = P_3 = P$. Since the pressure values algebraically relate to the cross-sectional areas, (Equation (5.15)), there are only four independent quantities $V_1, V_2, V_3, P$ which need to be specified. To close the problem the conservation of mass and extrapolation of forward and backward propagating invariants present,

$$\begin{aligned} &V_1 A_1 = V_2 A_2 + V_3 A_3 \\ &V_1 + 4\left[c_{MK_1}\left(\frac{A}{A_0}\right)^{\frac{1}{4}}\right]_1 = W_1, \\ &V_{2,3} - 4\left[c_{MK_{2,3}}\left(\frac{A}{A_0}\right)^{\frac{1}{4}}\right]_2 = (W_2)_{2,3} \end{aligned} \tag{5.43}$$

where $W_1$is the forward running invariant calculated at the center of the last cell of a parent vessel (vessel 1); $(W_2)_{2,3}$ are the backward running invariant calculated at the first cell of the daughter vessels (vessels 2 and 3)

#### 5.2.4.4 Connectivity Matrix and Specification of the Segment Properties

The connectivity condition of the small segments is vital for generating a patient-specific network of vessels to solve the set of governing equations. The following properties are assigned for each vessel inside matrices, to account for the variations over the elements of each segment. The properties of interest for each segment are its length, speed of pulse wave propagation in that vessel and angle from the reference point. In addition, cross sectional area (as a function of the axial distance) of the segments from their initial point, connectivity matrix describing the connection of nodes to vessels and to each other (shown in 5.1) and terminal resistance and compliances are defined as inputs to the model.

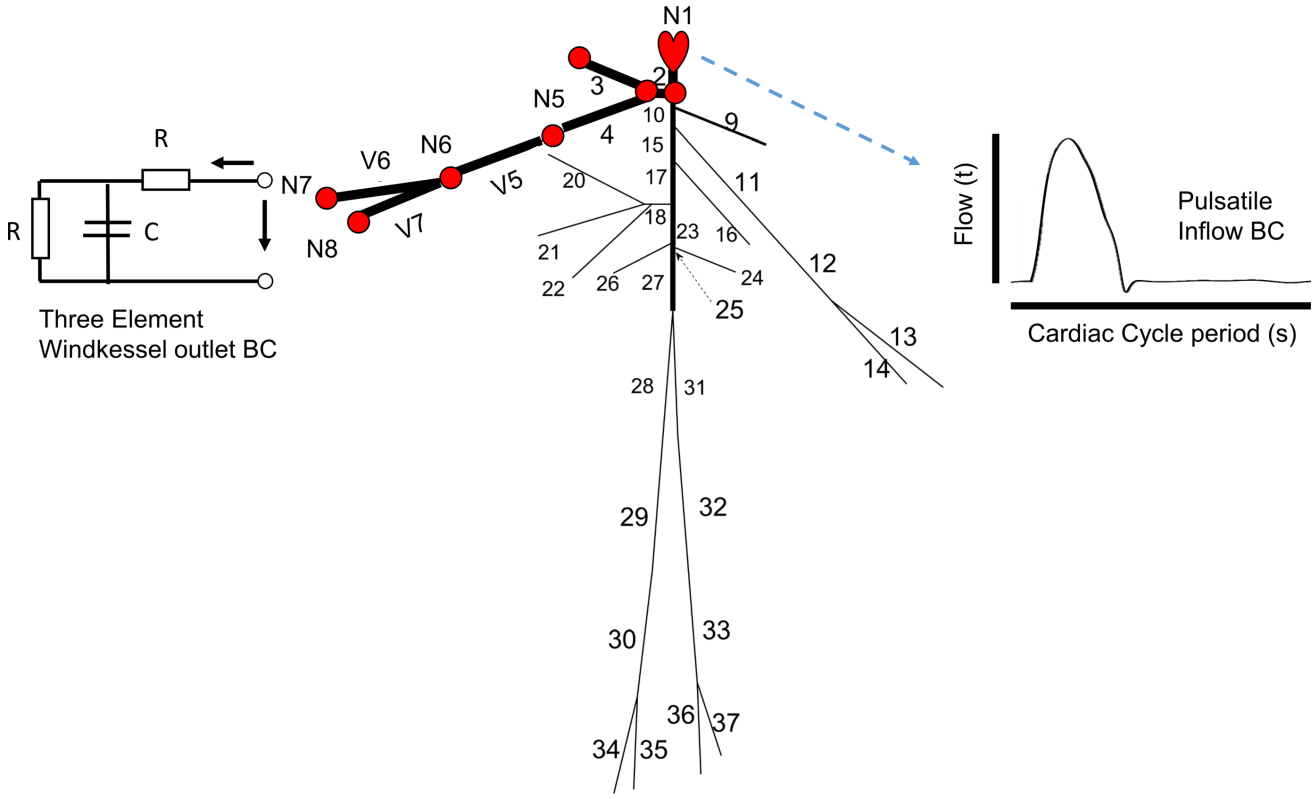


**Fig. 5.1.** – Example of the 37 main arteries geometry generated by connecting nodes and vessels in one matrix. Each node will fill out the information required for 1 row of the following matrix: [Node# Upstream-Vessel# First-Downstream-Vessel# Second-Downstream-Vessel#] Inflow flow boundary condition (BC) is imposed at the first node, and three element windkessel model at truncated locations.

## 5.3 Results and Discussion

Peripheral pressure measurements, with techniques such as upper arm or wrist cuff BP monitors can provide estimates of the central systolic and diastolic pressure, while applanation tonometry can obtain the pressure pulse waveform. This information is usually used for calibrating [33] a computational model or for data assimilation purposes [227]. Although usually used by clinicians, pulse-wave amplification at the peripheral artery renders peripheral measurements inadequate to represent the aortic or central arterial pressures [34], [228]. In addition, antihypertensive medications have different effects on central pressure despite similar reductions in brachial blood pressure [35]. Central aortic pressure is a better predictor of cardiovascular outcome after any alterations in the normal/resting functionality of the cardiovascular system [228], [229]. Thereby, this is essential to develop a reliable noninvasive method to measure the central blood pressure contrary to the currently available invasive catheter method [36]. The first step is to develop a computational hemodynamics-based approach for *data assimilation*, requiring a reliable computational framework. To evaluate the accuracy of the computational model, the patient-specific calibration and computational results validation against a manufactured case of stented artery and three well-known cases of arterial networks in the literature are presented here:

1. **Manufactured case of stented artery**: We demonstrate the blood flow and pressure waveforms in reduced-order arterial system models with stents, as an example of arteries with discontinuous vessel wall properties. We validate and compare the results of the TVD Lax-Wendroff based solver against a manufactured exact solution, and other non TVD numerical schemes such as Lax-Wendroff and MacCromack (section 3.1).

2. **Numerical**: the blood flow and pressure in 55 main arteries of a human body is simulated (section 3.2). The results are compared against the numerical work, provided by a discontinuous Galerkin model presented by [101] and [77].

3. ***In vitro***: blood flow and pressure in 37 main arteries of the human body is simulated, calibrated and compared against an *in vitro* model of the 37 arteries, developed by Matthys et al. [78] (section 3.3).

4. ***In vivo***: a patient-specific model is generated, using MRI based measurements of the arterial diameters and flow along the aorta and pressure measurements at supra aortic vessels, as presented in [213]. The blood flow model results are compared against the measurements and show improvements compared to prior numerical predictions (section 3.4).

As demonstrated here, reduced-order blood flow simulation platform, CardioFAN, provides accurate prediction of blood flow and pressure. This includes the range, systolic and diastolic values and the shape of the waveforms in all three cases and the luminal area values for *in vivo* case, where clinical measurements are available to compare.

**Computational Framework Specifications**: Mesh- dependence studied to achieve reliable results for each of the large arterial networks. The Lax-Wendroff version of the code performs calculations for all vessels during 5 cardiac cycles in less than 5 minutes and with a normal 4 CPU cores, 16 GB RAM personal computer (PC). Numerical PTT calculations and viscoelastic calculations can be set to on or off, which affect the computation time. CardioFAN is accessible through the provided links[1].

### 5.3.1 Validation Against Numerical Data of 55 Main Human Arteries

The model for 55 main arteries is presented by [77], [230] and [101] based on physiological input data extracted from a young healthy patient. They also show a numerical model of the network which was validated with available MRI data for flow and pressure data at the peripheral locations [230]. Here this model is recreated in CardioFAN by defining the connectivity matrix and input parameters based on the network presented in [101]. Vessel properties, such as vessel lengths, radii and speed of propagation at each segment etc., are provided as inputs to the software (check the link to CardioFAN for testing the code for 55 vessels). At the ascending aorta the flow as a function of time is imposed for 1 cardiac cycle and at the terminal boundaries, resistances and compliances for the RCR model are specified. Figure 5.2 demonstrates results provided by CardioFAN overlaid on top of the numerical results previously presented by [101].

[1] CodeOcean Repository: CodeOcean
Github (Zenodo) Repository: Zenodo

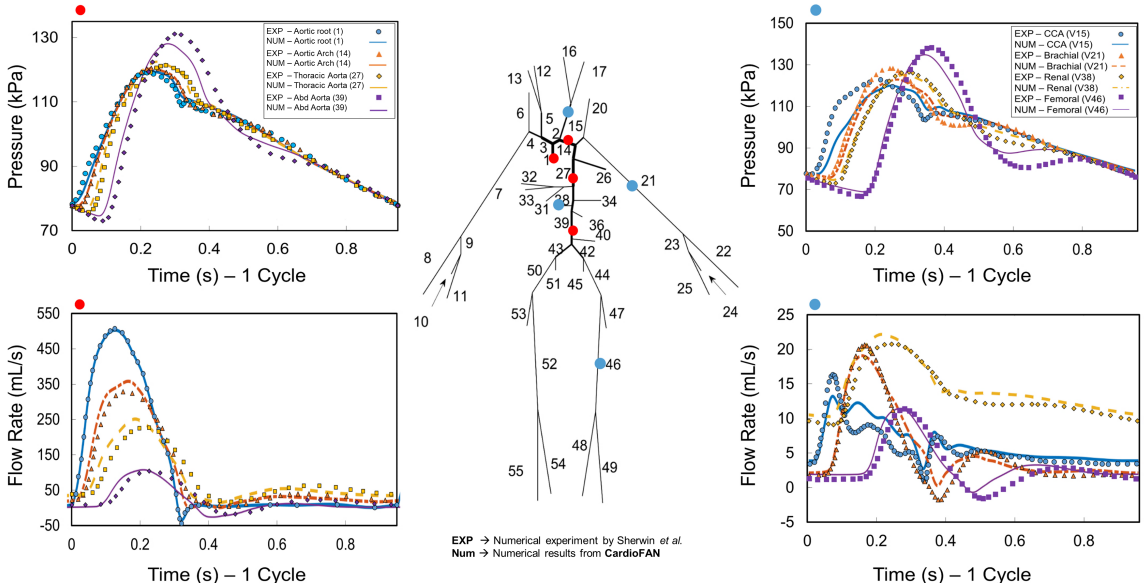


**Fig. 5.2.** – Schematics and validation of the 55 segments model of human arteries. The model is recreated based on the arterial network presented in [101]. Evaluated points along the aorta are indicated with red circles and presented at the left side (P at top and Q at bottom). Carotid aorta, left brachial artery, renal and femoral arteries, vessels 15,21,38,46, highlighted by blue dots and presented at the right side. Dotted markers represent the original data, and solid lines are the results obtained using CardioFAN (view the colored plots in online version).

As shown in figure 5.2, a good agreement between the results from CardioFAN and the numerical results from [101] was obtained. These results clearly capture features such as systolic peak an diastolic decay and the dicrotic notch, better than our previously presented Lax-Wendroff based linear elastic numerical simulation [231]. In contrast to the recreated work, instead of viscoelastic properties, we were able to retrieve the systolic peak for the data in peak of the pressure waveform (*e.g.* femoral artery, purple plot in top right), by correct selection of Fung parameter "$a$" (selected to be in 1.3-1.8 range, extracted from [232]). Although CardioFAN is capable of solving viscoelastic arterial wall properties, it has minor effect on the flow and pressure in large arteries [233], or in higher frequency waves [234]. Therefore, neglecting the viscoelastic properties, we were able to reduce the computational time significantly while getting accurate predictions compared to a model with viscoelastic properties.

### 5.3.2 Validation Against in vitro Data of 37 Main Human Arteries

We compare a numerically recreated model of 37 main arteries, with an experimental silicone based compliant model of the arteries [78]. Water-glycol mixture with a density of $\rho = 1050$ kg m $^{-3}$, and viscosity of $\mu = 2.5$ mPa s, was used to imitate blood (for more details on experimental setup, refer to [78]). Simple terminal resistance

tubes provisioned for this model allows the experimental model of Matthys et al., to reproduce the main features of pressure and flow, as observed *in vivo* (such as the dicrotic notch, diastolic decay and peaking and steepening of pulse pressure away from the heart). Here the properties of these vessels, such as, vessel length, radii, and wall thickness (see [78] or [212]), are used to recreate this network of arteries. At the inlet we have prescribed a given flow waveform, resulting to 70 beats per minute with stroke volume of 70 ml at the root. Similar to experimental setup, simple resistance terminal boundary conditions are imposed to numerical model. The simple resistance tubes at the experimental setup produces non-physiological oscillations at the peripheral locations (as mentioned by Matthys et al.), however, our code is able to capture the frequency of these oscillations. Energy losses at the network bifurcations have secondary effect on flow and pressure waveform predictions (as shown by Matthys et al.) and therefore not considered here. Resulting waveforms are presented in figure 5.3, at different locations along the arterial tree.

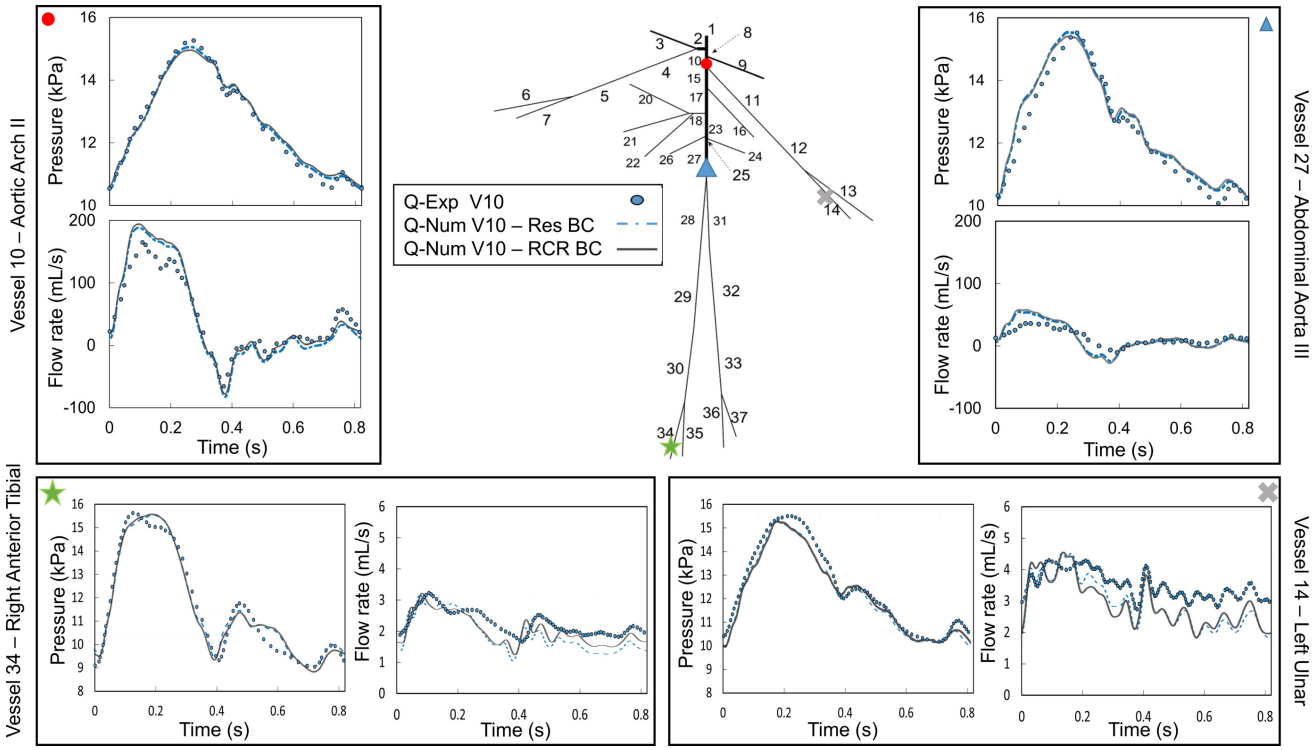


**Fig. 5.3.** – Schematics and validation of the 37 segments model of human arteries. Model recreated based on the in vitro network presented in [78]. Evaluated points along are marked by red circles. P and Q plots are shown for vessels 10-14-27-34, representing aortic arch II, left ulnar artery, abdominal aorta III and right anterior tibial arteries. Blue markers represent the original *in vitro* data, whereas, solid lines and dotted lines represent the results obtained using CardioFAN with RCR and R terminal boundary models, respectively (view the colored plots in online version).

**Tab. 5.1.** – Average relative errors of the numerical pressures and flows in all the evaluated locations of the network. Average relative errors in flows are calculated with respect to experimental data and local maximum as proposed in [67]. Bold numbers refer to the Resistance (R) terminal boundary model and normal text relate to RCR terminal boundary model, with a constant compliance C=$10^{-11}\ m^3\ Pa^{-1}$.

| Location | $\overline{\varepsilon}\, pressure\ (\%)$ | | $\overline{\varepsilon}\ flow\ (\%)$ | |
|---|---|---|---|---|
| Aortic Arch II | **0.89** | 1.15 | **9.40** | 8.83 |
| Abdominal Aorta III | **1.49** | 1.75 | **20.46** | 24.20 |
| Left Ulnar | **2.24** | 2.47 | **12.02** | 12.73 |
| Right Anterior Tibial | **1.53** | 1.82 | **10.10** | 7.41 |

Good agreement is obtained between numerical predictions and the experimental data for blood pressure and flow rate in various parts of the 37 arteries model. We see that the numerical model can completely capture the pressure waveform features, such as systolic peak, dicrotic notch and the diastolic decay of the waveforms. On the other hand, flow oscillations are fully captured, with magnitude being over-predicted at the most peripheral locations. The flow waveform errors are in complete agreement with numerical model developed by [78], [212] for the same *in vitro* data, and as mentioned before, relates to the discrepancies in flow waveform measurements. The averaged relative root mean squared errors over all segments in each network generation sequence, calculated at the experimental measurement locations was previously reported as not exceeding 4% for pressure and 19% for flow predictions. The individual errors for each segment was reported in [212], showing a range of 4.7 to 35.3% error in flow rate predictions. For CardioFAN, averaged relative RMSE in the evaluated locations are provided in Table 1. The errors are smaller than the previously reported values, even in the location of abdominal aorta and without using a viscoelastic model, except for Left Ulnar artery location.

Compared to pressures, the larger errors demonstrated in flow rate predictions correlate with the large uncertainties in experimental measurement of flow waveform [78]. The standard deviation of these measurements, captured with an ultrasonic volume flow meter, have not been displayed here (they can be viewed in [78]). In addition, viscoelastic solver may help in improving the results of oscillating flow locations, especially since the experimental setup was designed with viscoelastic material [212].

Furthermore, a comparison between viscoelastic and elastic results are demonstrated in appendix B, where only a slight wave smoothening effect can be observed due to viscoelasticity.

### 5.3.3 Validation Against in vivo Data of 26 Main Human Arteries

The 26 segments model, comprising aorta and supra aortic segments, has been created based on the *in vivo* data presented by [213]. To minimize uncertainty in their *in vivo* acquisition of non-invasive hemodynamic data, a rich array of 3D and 2D SSFP MRI clinical data was used to create the subject-specific geometry. Heart rates have been measured by MRI and applanation tonometry and the flow rate measured using PC MRI. This resulted in a more consistent determination of cross-sectional area distributions and flow rates across the aorta, which serves as the input for numerical modeling and computational results validation.

#### 5.3.3.1 Preparing the Input Parameters and Boundary Conditions

In order to extract model input parameters, the method presented by [67] is used for calculating individual resistances and compliances at the truncated arteries (as explained in section 2.4.2). In [213], the speed of wave propagation at each segment was prescribed based on a foot-to-foot method [235] as a constant value. Here, we suggest an improved method for calculating the speed of propagation in section 3.3.2, which results in a better prediction of the flow rate, cross sectional area and pressure waveforms along the flow path. Recreated model using CardioFAN is able to test the accuracy of the code against the actual patient-specific data. The properties of each segment were assigned based on the data presented in [213]. Following Alastruey et al., we have adopted two of the most successful simulation cases:

1. *BEST AREA*: Outlet pressure is selected to be equal to capillary pressure commonly used at the outlet of 1D models [236], $P_{out} = 4400$ kPa. The total resistance and compliance parameters are altered iteratively (according to the technique introduced by [67]), to match the diastolic pressure and the range of pressure at the carotid artery location, where the *in vivo* data was available.

   To comply with the recreated work this method is named *BEST AREA*, since it provides the most accurate cross – sectional area and flow predictions.

2. *BEST PRESSURE*: Outlet pressure is selected to be equal to the average value of the fitted pressure to the diastolic decay of the supra aortic pressures as a function of time, captured using applanation tonometry. This pressure is $P_{out} = 9200$ kPa, and the total resistance and compliance parameters are not required to be altered (or need a few iterations) since the outlet pressure is a patient-specific value.

This prescription of the boundary conditions is named as *BEST PRESSURE*, since it provides the most accurate prediction of the pressure waveform at the left carotid artery.

$P_{out}$ (outlet pressure at exit branches), $\overline{Q}_{out}$ (mean outlet flow rate at exit branches) and $\overline{Q}_{in}$, (the mean flow rate at the aortic root), are all measured by [213]. This enables the calculation of peripheral resistance and compliances for each outlet segment (see section 2.4.2). The algorithm for calculating the RCR parameters is embedded in CardioFAN.

#### 5.3.3.2 Improved Method for Calculating the Speed of Propagation

Foot to foot method was previously used by [213] to assign the Moens-Korteweq speed of propagation ($C_{mk}$) as the speed of sound in a fluid – structure interaction system. The evaluated flow waveforms for foot to foot method were related to the path connecting the ascending aorta to the abdominal aorta (Asc 1 to Desc 4 in figure 5).

Numerically calculated PWV have been previously used to validate experimentally measured PWV based on flow or pressure waveforms [237], [238]. It was illustrated in [215] and [192], that the modified value of the PWV calculated as the speed of a forward propagating Riemann invariant, can significantly improve prediction of the blood pressure as a function of the PWV.

Associating the measured speed of propagation values reported by [213] (named there as $c_d$) with the calculated PWV, equation (5.28) was used to recalculate the Moens-Korteweq speed of sound at each segment

$$PWV = c_d = \ V + c_{mk}\sqrt[4]{\frac{A}{A_0}}k_\lambda \tag{5.44}$$

Since the slope of a forward running characteristic line is determined by PWV

$$\frac{dt}{dx} = PWV^{-1}(x,t) \tag{5.45}$$

equation (5.45) serves to calculate the PTT required for the pulse wave to propagate between two specified sections along the flow pathway. Using the second order of accuracy Heun's method [239], Equation (5.45) is integrated by specifying the starting location for PTT evaluation.

Starting from $C_{MK} = c_d$, assigned in [213] for each segment, $C_{MK}$ was incrementally reduced until the numerically calculated PTT matched the clinical value of $63\ ms$, obtained from foot to foot method [235]. Foot to foot method includes deduction of the starting location for PTT evaluation. The numerically calculated PTT is shown in figure 5.4 as a function of the PTT calculation start time along the second cardiac cycle. The intersection of the maximum derivative of the flow waveform systolic rise and the extended horizontal line from diastolic flow, is employed to pinpoint the PTT calculation starting point matching experimentally obtained foot to foot PTT. For more detailed analysis see chapter 7.

Figure 5.4 shows that the computational PTT, based on the modified (reduced) $C_{MK}$, and relating to the same starting point as the experimental foot to foot method, matches the experimental value of $PTT \approx 63\ ms$.

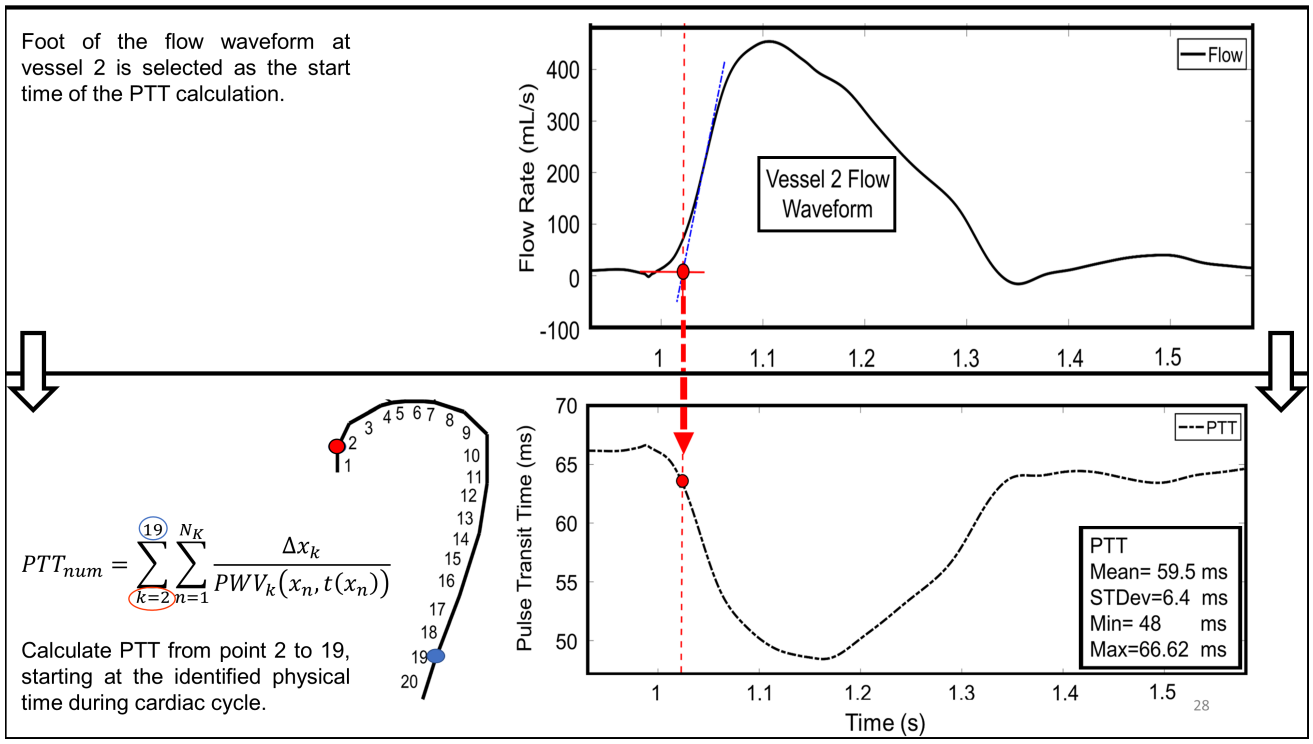


**Fig. 5.4.** – The flow waveform corresponding to the 2nd cardiac cycle is presented (top figure). PTT as a function of the onset of PTT calculation during the 2nd cardiac cycle is shown in the x axis (top figure). The crossing of the maximum derivative of the flow waveform systolic rise and the extended horizontal line from diastolic flow, is the start time (*i.e.* foot) of PTT calculation based on foot to foot method [235]. PTT calculation pathway is from ascending aorta (Asc Aorta, vessel 2 in figure 5.6) to the abdominal aorta (Desc Aorta, vessel 19).

Application of the described technique resulted in a 4.5% decrease in the speed of propagation, which corresponds to the 9.2% decrease in tangential modulus ($\overline{E}$), assigned at each segment. Therefore, instead of $C_{MK} = 4.56$ m/s, we use $C_{MK} = 4.36$ m/s in CardioFAN. Figures 5 and 6 show the resulted flow, cross-sectional area (luminal area) and pressures which imply improvement in predicting their waveform with corrected $C_{MK}$.

Another interesting result of this correction is for non-uniform values of $c_d$ or PWV, previously presented by Alastruey et al. [213]. Although the individual values of the PWV for each segment were not measured, QA loop method [240] was used to provide $C_d$ for all segments. We reduced the non-uniform $C_{MK}$ (again starting from $C_{MK} = c_d$ values) with a single multiplier until the numerically calculated PTT matched the PTT from foot to foot method ($PTT = 63$ ms). As a result, the corresponding $C_{mk}$ in all segments are found to be lower by 20% than the previously reported non-uniform $C_d$ values. It also resulted in improved flow, luminal area and pressure predictions compared to the results presented in [213].

#### 5.3.3.3 *in vivo* Validation Results with BEST PRESSURE and BEST AREA cases

**Uniform $C_{MK}$**: Figure 5.5 shows the results of both *BEST PRESSURE* and *BEST AREA* models for uniform speed of propagation (*i.e.* arterial stiffness). The results relate to the corrected constant $C_{MK}$ applied to all segments, with resistances and compliances calculated and matched at the terminal locations. The compliance and resistances are corrected with the iterative method described in [67], to correctly capture waveform range and diastolic pressure, respectively. The corrected values are $R = 1 \times R_T$ and $C_j = C_j/1.5$ for *BEST PRESSURE* and $R = 3.3 \times R_T$ and $C_j = C_j/1.6$ for *BEST AREA* case. We have applied the Fung constant $a = 8$, and $a = 2$, respectively to account for hyperelastic properties. These values are assigned as a constant number to all vessels. They were found iteratively by calibrating CardioFAN to the *in vivo* pressure data of the left carotid artery (*i.e.* segment #24). It should be noted that by having more PTT data available, the individual values of Fung hyperelastic constant can further improve the results.

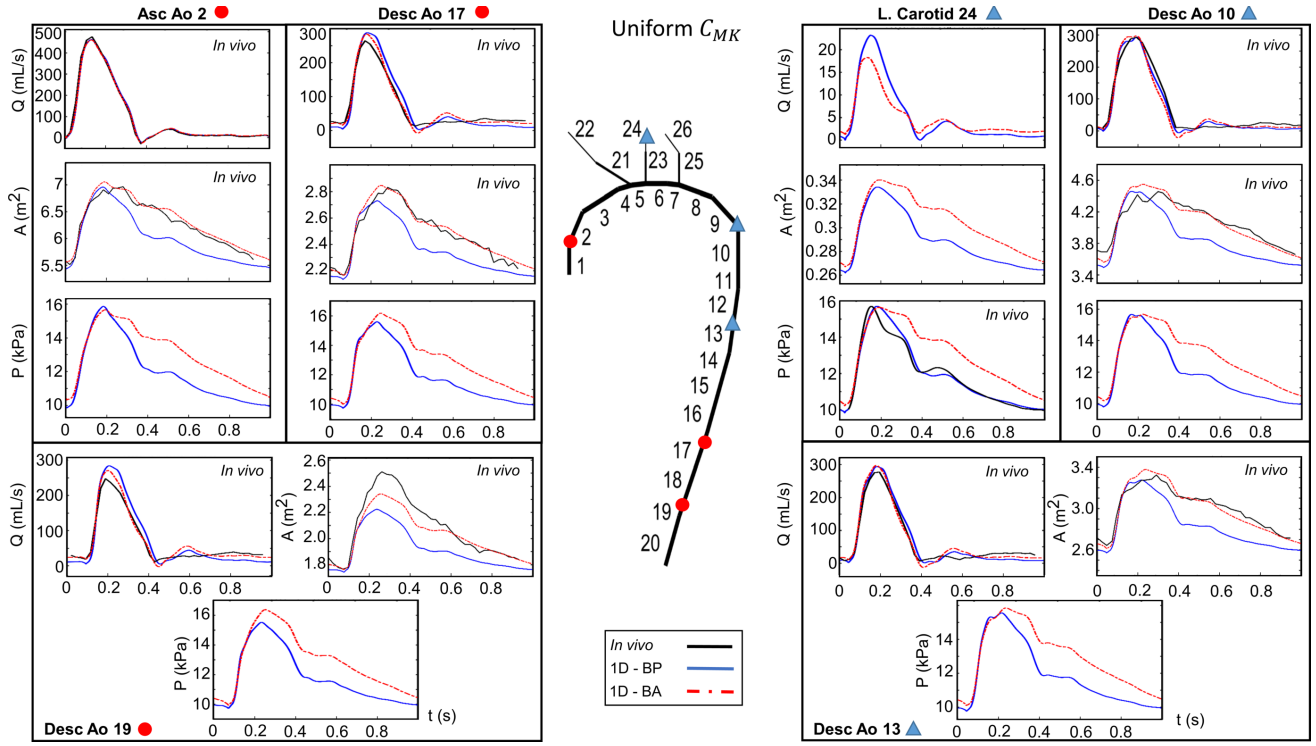


**Fig. 5.5.** – Schematics and validation of the 26 segments model of arteries along the aorta and supra aortic vessels with uniform speed of propagation. The model recreated in CardioFAN based on the same network presented in [213]. Evaluated points on the left and right, are specified on the schematics with red circles (segments 2-17-19) and blue triangles (segments 10-13-24), respectively. Pressure ($P$), flow ($Q$) and luminal area ($A$) plots show results of *BEST AREA* method (red dotted lines), *BEST PRESSURE* method (blue solid lines) and clinical *in vivo* measurements where available (black solid lines). Results are evaluated at the inlet of these segments, except for the common carotid artery, evaluated at the outlet of the segment (view the colored plots in online version).

The *BEST PRESSURE*, which prescribes a patient-specific terminal pressure measured at the common carotid artery, provides a good match with the clinically measured pressure at the same location and flow rates across all vessels, however it under-predicts the luminal area as shown in figure 5. On the other hand, the *BEST AREA* case, prescribing the capillary pressure at the terminal boundaries, correctly predicts the luminal AREA in all locations but it over predicts the diastolic decay of the pressure at the common carotid artery. These results are in agreement with the 1D and 3D numerical predictions previously obtained by [213]. Average relative errors of these predictions are shown in table 5.2. The average relative errors for flow, luminal area and pressures, predicted with the corrected uniform $C_{MK}$, are smaller than 5.2%, 2.8% and 9% for *BEST AREA* and 7.6%, 7.1% and 1.6% for *BEST PRESSURE* cases (compared to 7%, 4% and 11% for BA and 9% 8% 4% for BP reported in [213]), respectively. We see an average of 1.5% improvement using the Hyperelastic model with constant $C_{MK}$.

**Tab. 5.2.** – Average relative errors of the numerical pressures, flows and luminal areas evaluated against clinical measurements along aorta and left common carotid artery. The RMSEs are measured with the method described in [67]. Bold text refers to *BEST AREA* and normal text refer to *BEST PRESSURE* models.

| Location | $\overline{\varepsilon}\ pressure\ (\%)$ | | $\overline{\varepsilon}\ flow\ (\%)$ | | $\overline{\varepsilon}\ area\ (\%)$ | |
|---|---|---|---|---|---|---|
| Asc Aorta (V2) | - | - | **1.13** | 1.44 | **1.00** | 3.46 |
| Desc Aorta (V10) | - | - | **5.13** | 4.31 | **1.61** | 5.75 |
| Desc Aorta (V13) | - | - | **3.72** | 3.94 | **1.38** | 5.57 |
| Desc Aorta (V17) | - | - | **3.49** | 6.69 | **1.10** | 4.83 |
| Desc Aorta (V19) | - | - | **4.11** | 7.55 | **2.73** | 7.03 |
| Left CCA (V24) | **8.79** | 1.56 | - | - | - | - |

**Non-Uniform $C_{MK}$**: flow, luminal area and pressure results for corrected non-uniform $C_{mk}$ applied to each segment are shown in figure 5.6. Interested reader can refer to CardioFAN and run the non-uniform $C_{MK}$ by changing the designated parameter at the input and assigning the corrected $C_{MK}$. The compliance and resistances are corrected with the iterative method described by Xiao *et al.,* to correctly capture waveform range and diastolic pressure, respectively. The *BEST PRESSURE* case required no correction for $R$ and $C_j$, however, for the *BEST AREA* case $R = 3.2 \times R_T$ and $C_j = C_j/2$ are used. We have applied the Fung constant $a = 4$, and $a = 8$, respectively to account for hyperelastic properties, found iteratively by calibrating CardioFAN to the *in vivo* pressure data of the left carotid artery (*i.e.* segment 24).

Compared to [213], the results are demonstrating better prediction of flow rate ($Q$), luminal area ($A$) and pressure ($P$) using the TVD algorithm with hyperelastic vessel walls in both cases with uniform and non-uniform $C_{MK}$ values. The non-uniform case $C_{MK}$ shows a very good accuracy at predicting the luminal area peaks near systole. Accuracy can be further improved if the exact value of non-uniform $C_{MK}$ (or its consequent elastic modulus) is known at each segment. With the current available measurements, the numerically calculated $Q$, $A$ and $P$ waveforms with uniform $C_{MK}$ are more promising and therefore suggested for future studies.

## 5.4 Implications on the Non-invasive Diagnostics

The arterial pulse has historically been an essential source of information in the clinical assessment of health. Validation of the CardioFAN against prior numerical, *in vitro* and especially *in vivo* measurements combined with the improved method for PTT and PWV calculation, demonstrate reliability of the algorithm, and its potential application to early patient-specific prediction/diagnostics of cardiovascular biomarkers. This algorithm can be

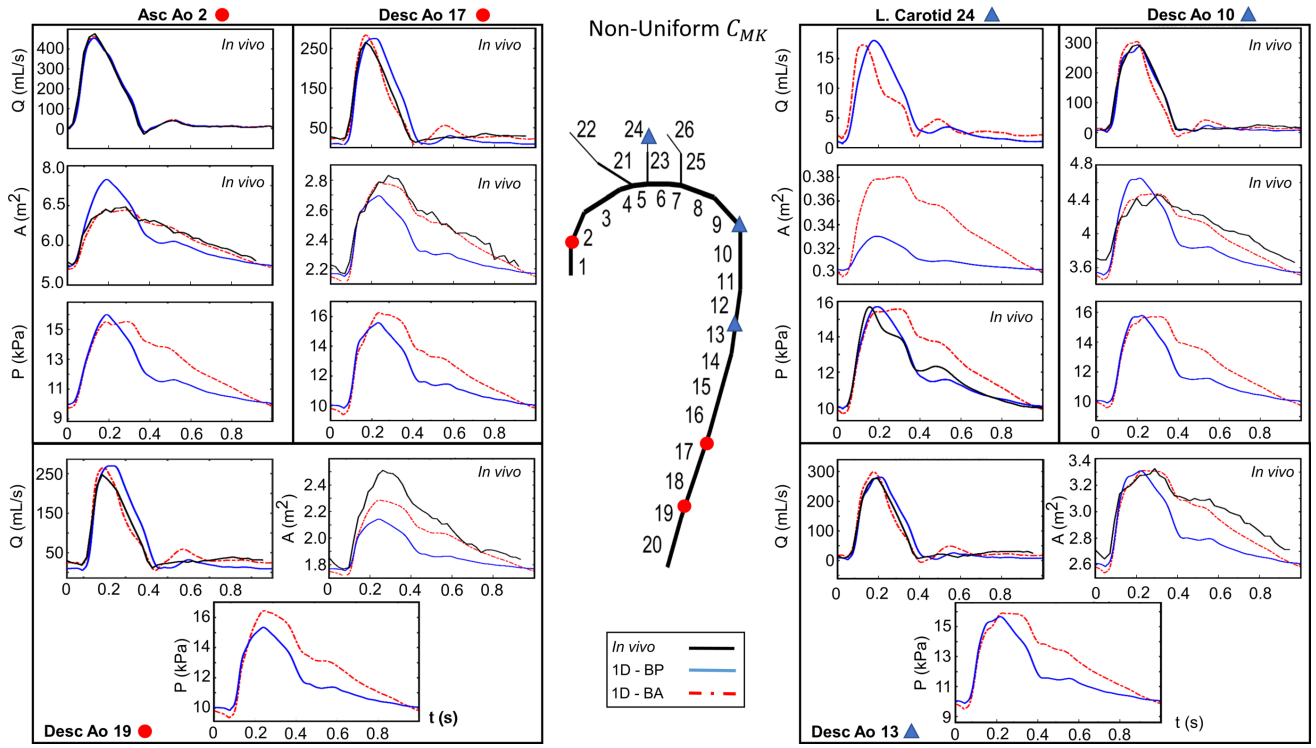


**Fig. 5.6.** – Schematics and validation of the 26 segments model of arteries along the aorta and supra aortic vessels with non-uniform speed of propagation. The model recreated in CardioFAN based on the same network presented in [213]. Evaluated points on the left and right, are specified on the schematics with red circles (segments 2-17-19) and blue triangles (segments 10-13-24), respectively. Pressure ($P$), flow ($Q$) and luminal area ($A$) plots show results of BEST AREA method (red dotted lines), BEST PRESSURE method (blue solid lines) and clinical in vivo measurements where available (black solid lines). Results are evaluated at the inlet of these segments, except for the common carotid artery, evaluated at the outlet of the segment (view the colored plots in online version).

used for non-invasive monitoring of the pressure, flow and luminal area waveforms, with minimal calibration of terminal resistance / compliances and Fung's constant $a$.

Due to the low dispersive property, it will also be possible to use the TVD version of the code for calculating the pulse wave propagation in the stented or prosthetic arteries, where discontinuous properties exist.

Further clinical studies with temporal pressure measurements available at all terminal boundaries are required to confidently suggest the reduced order numerical techniques for clinical applications. Combined with noninvasive clinical measurements (*data assimilation* [7]) CardioFAN may provide patient-specific prediction of the central blood pressure, flow, stroke volume and arterial compliances.

## 5.5 Conclusion

We present a new monotonic TVD Lax-Wendroff based platform for calculating patient-specific blood pressure, flow rate, luminal cross-sectional area and pulse transit time (PTT) inside an arbitrary cardiovascular network. This platform is free to use under the terms of the included open source license for CardioFAN. The variational formulation presented here and in our previous work makes this code ready to be coupled to 3D FSI modules to study 3D effects of diseases such as arterial aneurysms. Inlet and terminal boundary conditions are calculated based on minimal clinical or experimental calibration measurements, making it easy to run the model for patient-specific cases.

Three new validation tests are conducted here against numerical, as well as *in vitro* and *in vivo* data from three different geometries in the literature. These geometries and the vessel properties are prescribed in a demonstration version of CardioFAN, showing results of similar or improved errors compared to previous numerical simulators. We introduce a new numerical method for calculating the numerical PTT and use it in conjunction with experimental PTT to correct the speed of pulse propagation in arteries. This resulted in an average of 1.5% improvement in prediction of the clinically measured flow, luminal area and pressures. The corresponding average error of prediction are now smaller than 5.2%, 2.8% and 9% in *BEST AREA* and 7.6%, 7.1% and 1.6% for *BEST PRESSURE* simulation cases (refer to section 5.3.3), respectively.

The reliability tests conducted here and the new method for calculating the corrected global PWV, are building the groundworks for implementing CardioFAN as a means for non-invasive diagnostics of biomarkers. Further investigations can be focused on the reconstruction of patient-specific central pressure and flow (or stroke volume), using minimal peripheral measurements and calibration.

# 6 Application of CardioFAN in Geometrically Multiscale and Stented Artery Simulations

## 6.1 Modeling Stented Arteries using CardioFAN

Introduction of any geometrical or pathological changes in arteries, such as aneurysms, bifurcations, prosthetic arterial tissue or stents, results in a sudden jump in the vessel wall properties; when using a numerical model, this causes discontinuity in the solution. A stent is usually made of a high radial stiffness cylindrical wire mesh to prevent a pull back of the low compliance vascular tissue. After vascular stent implantation, the mesh cells soon appear to be filled with the excessive tissue growth causing the stent to fuse with the vessel wall (Nazarian *et al.*, [241]). As a result, the combination of a stent and vessel wall becomes a more rigid structure, regarded as a monolithic segment with an effective mechanical property.

Here the focus is put on the stented arteries, however the presented technique can also be applied to other discontinuities, such as prosthetic additions and vascular grafts. Usually numerical models in the literature treat this discontinuity by one of the following three methods:

1. Neglect the change over the stent, and only introduce a hypothetical coefficient to account for the effect of the stented location on the overall pulse wave propagation [29].

2. Artificial smoothing of the properties over the stent to resolve the discontinuity [117].

3. Identify and nullify spurious wave reflections at the stented arteries [242].

Back *et al.* [243] experimentally showed that the stented artery does not incur a discontinuity in radial displacement. Therefore, the above-mentioned assumptions are overly simplifying a problem that has roots in other simplifications

made inside the numerical schemes. Here two methods are introduced to resolve this issue. Section 6.1.1, focuses on the TVD scheme applied to the stented artery and shows how it prevents spurious osculations in the resulted waveforms compared to other numerical schemes. In section 6.1.3, bending moments are introduced in the momentum equation formulation to consider the effect of large deformations and physically damp the discontinuous oscillations.

### 6.1.1 Stented Artery Exhibiting Discontinuous Arterial Wall Properties

After a few months of the stent implantation, the stent struts fuse with the tissue growth creating a composite structure with relatively rigid monolithic properties within an elastic arterial tube. Time marching methods are applied to model pulsatile blood flow in a stented elastic artery. The Moens-Korteweg speed of propagation exhibits jumps due to the difference in compliance between more “rigid” stent and a “soft” arterial wall. In case of certain pathologies, e.g. stenosis or an aneurysm, speed of propagation can also abruptly change due to the variations in lumen cross sectional area. Compliance discontinuity is currently being handled with the following methods in the literature: 1) Data regularization, where the properties across the junction interface are artificially smoothened to eliminate discontinuity [244]; 2) Domain decomposition, where the coupling between two segments is accomplished providing flow and momentum continuity across the artery-stent interface [100]. The algorithm presented here, however, uses a regular time marching method applied to the system of PDEs with variable coefficients and without any preliminary regularization or domain splitting.

As an example, a tube model consisting of 3 segments is designed, as shown in figure 6.1. The middle segment represents an arterial stent, while the other two segments are arterial tissue. Each segment relates to the local spatial coordinate $x_i\,, \quad 0 \leq x_i \leq L_i, \;\; i = 1,\, 2,\, 3$ as shown in 6.1. The Moens-Korteweg velocity of propagation at each segment is denoted by $c_{MK,i}$.

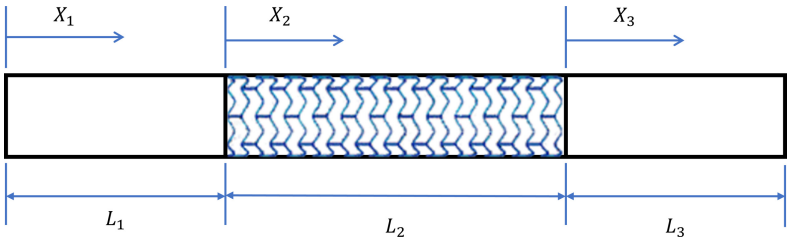


**Fig. 6.1.** – Schematics and dimensions of a hypothetical stented artery.

Here $L_1 = L_3 = 0.2\ m$, $L_2 = 0.05\ m$; $c_{MK,1} = c_{MK,3} = 4\frac{m}{s}$, $c_{MK,2} = 10m/s$; $\rho = 1000\frac{kg}{m^3}$; $A_0 = 0.0314\ m^2$. The total number of uniformly distributed computational cells are set to $N = 90$. Inlet BC for the flow rate and exit BC for the pressure are given in section 6.1.1.1 by equations 6.7 and 6.8, where $Q_0 = 50\frac{mL}{s}$, $\overline{p} = 13.3\,kPa$, $p_a = 2.66\,kPa$ are the flow rate, mean aortic blood pressure and magnitude of the pulse pressure, respectively.

#### 6.1.1.1 Exact Manufactured Solution for Linear Wave in Stented Artery

A closed form solution for the harmonic linear wave analysis is derived for the stented artery depicted in figure 6.1. Alternatively, the system (5.17) can be recast in terms of conserved variables: the total pressure $P_0 = p + \frac{1}{2}\rho V^2$and the flow rate $q = AV$

$$\frac{\partial}{\partial t}\left\{ \begin{array}{c} A \\ q/A \end{array} \right\} + \frac{\partial}{\partial x}\left\{ \begin{array}{c} q \\ P_0/\rho \end{array} \right\} = 0 \tag{6.1}$$

A linear elastic tube law complements the system (6.1) in the form of following pressure – area relationship

$$P = \ 2\rho_f c_{mk}^2 \left( \sqrt{\frac{A}{A_0}} - 1 \right) \tag{6.2}$$

The linearization around zero point for transmural pressure and the flow rate reads

$$\frac{\partial}{\partial t}\left\{ \begin{array}{c} A \\ q \end{array} \right\} + \frac{\partial}{\partial x}\left\{ \begin{array}{c} q \\ \frac{A_0}{\rho_f} p \end{array} \right\} = 0 \tag{6.3}$$

$$p = \ \rho_f c_{mk}^2 \left( \frac{A}{A_0} - 1 \right) \tag{6.4}$$

To eliminate cross-sectional area A we substitute equation (6.4) into equation (6.3), recasting final system of equations in terms of conserved variables ($p,\ q$)

$$\frac{\partial}{\partial t}\left\{\begin{array}{c} p \\ q \end{array}\right\} + \frac{\partial}{\partial x}\left\{\begin{array}{c} \frac{\rho_f c_{mk}^2}{A_0} q \\ \frac{A_0}{\rho_f} p \end{array}\right\} = 0 \tag{6.5}$$

An explicit closed-form solution has been manufactured in the form of a single harmonic wave satisfying equations (6.5) for each segment

$$\begin{aligned} q_i\left(x_i, t\right) &= \left(1+\sin(\omega t)\right) \\ &\quad \left[C_{1i}\cos\left(\frac{\omega x_i}{c_{MK,i}}\right) + C_{2i}\sin\left(\frac{\omega x_i}{c_{MK,i}}\right)\right] \\ p_i\left(x_i, t\right) &= \overline{p} + \frac{\rho_f c_{MK,i}}{A_0}\cos(\omega t) \\ &\quad \left[-C_{1i}\sin\left(\frac{\omega x_i}{c_{MK,i}}\right) + C_{2i}\cos\left(\frac{\omega x_i}{c_{MK,i}}\right)\right] \end{aligned} \tag{6.6}$$

Here $q_i\left(x_i\right), p_i\left(x_i\right)$ are the flow rate and pressure distributions for each segment as functions of a local axial coordinate $x_i$ (figure 6.1); $\omega$ is the frequency of the harmonic wave; $c_{MK,i}$ is the Moens-Korteweg speed of propagation for each segment, $i = 1,\ 2,\ 3$ (corresponding to artery, stent and artery configuration in figure 6.1). Six unknown constants $C_{1i}$, $C_{2i}$ satisfy to the inlet BCs for the flow rate

$$q_1\left(x_1 = 0,\ t\right) = \left(1+\sin(\omega t)\ \right) Q_0 \tag{6.7}$$

exit BC for the pressure

$$p_3\left(x_3 = L_3, t\right) = \overline{p} + \cos\left(\omega t\right)\ p_a \tag{6.8}$$

and four matching conditions at each interface

$$
\begin{aligned}
q_1\left(x_1 = L_1, t\right) &= q_2\left(x_2 = 0, t\right) \\
p_1\left(x_1 = L_1, t\right) &= p_2\left(x_2 = 0, t\right) \\
q_2\left(x_2 = L_2, t\right) &= q_3\left(x_3 = 0, t\right) \\
p_2\left(x_2 = L_2, t\right) &= p_3\left(x_3 = 0, t\right).
\end{aligned}
\tag{6.9}
$$

### 6.1.2 Comparing Stented Artery Signals: TVD Vs Other Techniques

Figure 6.2 presents solution of the linearized problem for the pulsatile flow inside stented artery, obtained by three different numerical methods. Second order approximation schemes such as Lax-Wendroff and MacCormack, giving an accurate result for the smooth solutions [116], fail near discontinuities where spontaneous oscillations are generated. The TVD scheme apparently has an advantage keeping the solution varying monotonically as seen in figure 6.2c. The Courant-Friedrichs-Lewy (CFL) number calculated based on the speed of wave propagation inside stent is $CFL = 1$.

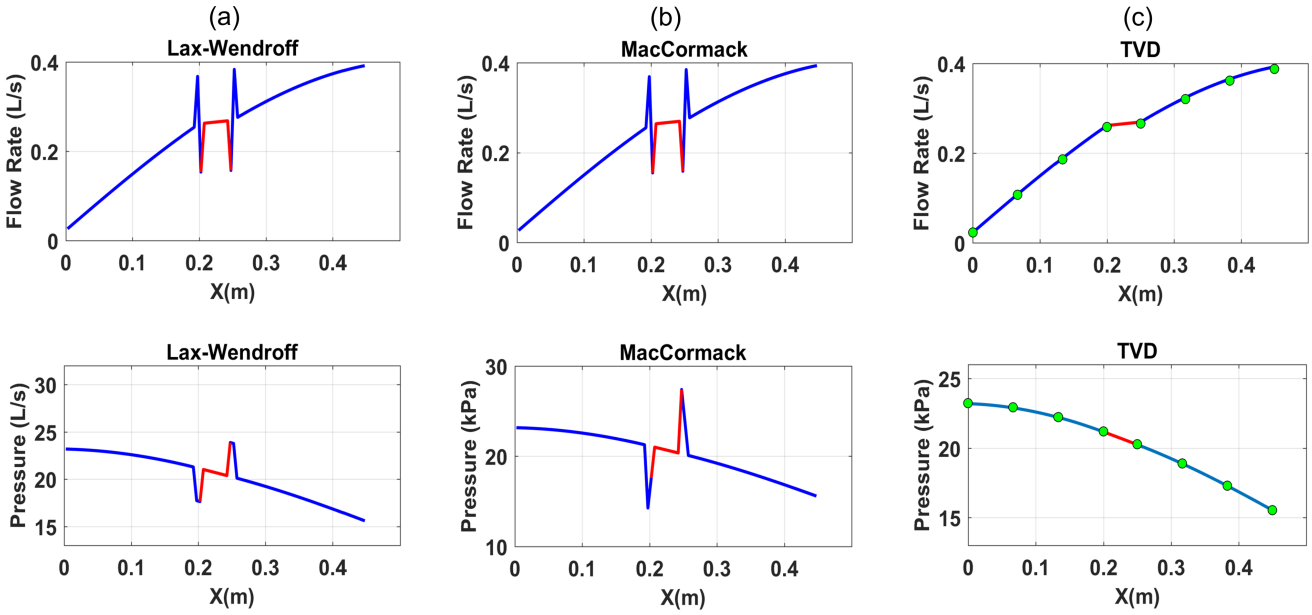


**Fig. 6.2.** – A snapshot of the results comparison for different numerical schemes for an stented artery. (a) Lax-Wendroff, (b) MacCormack, (c) TVD method (circles) vs closed form solution (solid line). Results are shown at physical time $t = 1\ s$.

In the second test, we imposed the same arterial wall properties as in linear case, for a model of stented artery with the nonlinear governing equations to describe its FSI behavior. A half-sine flow wave with a maximum magnitude of $250\frac{mL}{s}$ was imposed at the inlet, accompanied by a non-reflective outlet BC. Flow and pressure results were recorded along the tube axis in different instances of time. Figure 6.3 illustrates a comparison between the results of a second-order Lax-Wendroff and a nonlinear TVD Lax-Wendroff (equations (5.34)-(5.36) in appendix A). The artificial oscillations in the Lax-Wendroff compared to nonlinear TVD method shows the sensitivity of the non-TVD methods to discontinuity in properties. Therefore TVD schemes for are show superior performance in arterial models with discontinuous wall properties.

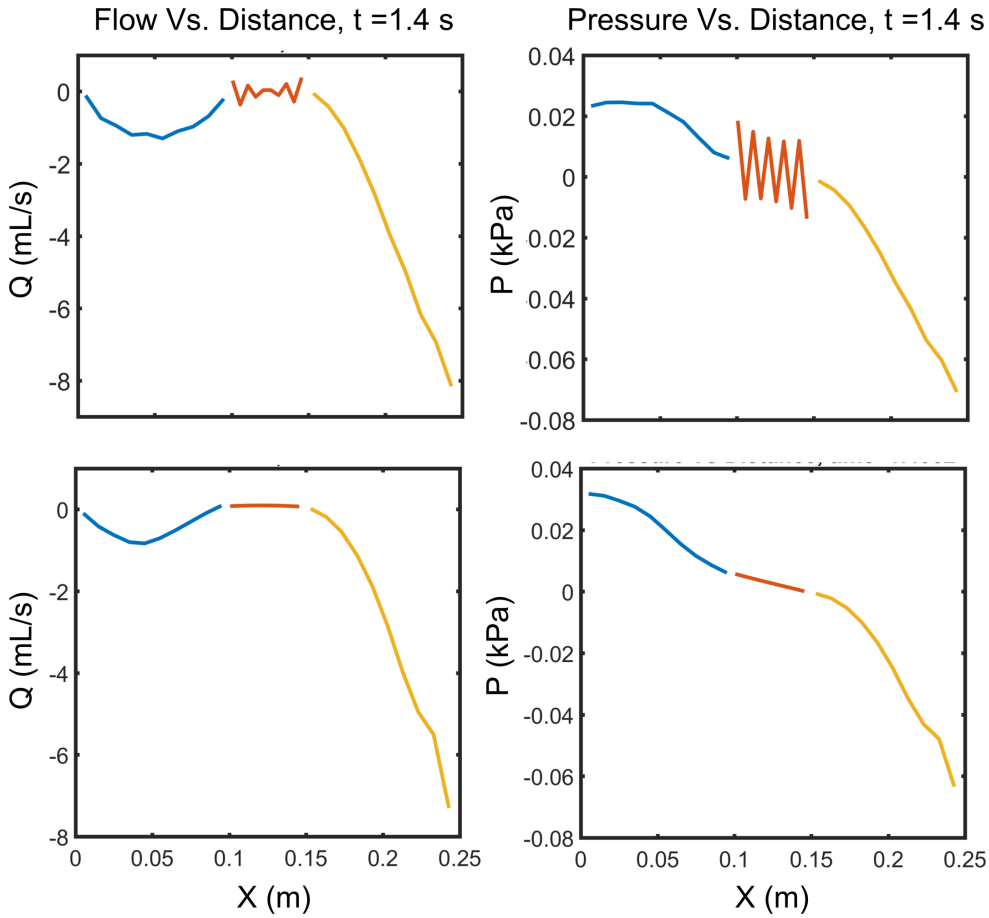


**Fig. 6.3.** – Testing numerical resolution in case of the nonlinear model of a stented artery. Lax-Wendroff (top), TVD Lax-Wendroff with van leer flux limiters(bottom). Pressure and flow results are shown at physical time t=1.4 s. Blue and yellow lines indicate normal artery wall and the middle orange line indicates the stented portion of the artery.

Although here, TVD is compared to common numerical schemes in the literature, it should be noted that a more comprehensive study might be needed to compare the TVD LW method against all of the existing numerical models used in blood flow simulations.

### 6.1.3 Bending Moments in Stented Artery Models

Bending waves, also called flexural waves, are waves propagate through the thin-walled structures deforming them transversely due to the bending stiffness. A measurable property of the bending wave is the additional local normal displacement, maintaining the continuity of kinematic and stress factors at the boundaries (or at the discontinuity interface).

Accounting for bending moments at the stented arteries can smooth out the transverse deformations to create a continuous wave expression over the discontinuities. The proposed approach uses flexural stiffness of the artery and the stent, maintaining continuity of the radial displacement, displacement slope, bending moments and the shear force at the interface between artery and the prosthesis/stent. The net effect of the compliance mismatch, such as the stress concentration and additional wave reflection sites, in the proximity of the stent-artery interface is quantified. Due to the long-wave approximation, time dependency of the bending moment equations can be neglected and we consider the axial dependency of the bending moment terms inside the constitutive equation.

$$p = \frac{Eh}{r}\eta + M^{''}, \qquad M = D.r\,\eta^{''}, \qquad D = \frac{Eh^3}{12\left(1-\nu^2\right)} \quad , \qquad A = A_0\left(1+\eta^2\right) \tag{6.10}$$

Here, $M$ is bending moment, $\nu$ - the Poisson's ratio, $\eta$ – the circumferential strain and $E$ is the young elasticity module. Therefore, neglecting the source terms, the governing equations will be solved for the following vectors,

$$Q = \begin{bmatrix} A \\ V \end{bmatrix}, \qquad Flux\ F = \begin{bmatrix} AV \\ \frac{V^2}{2} + \frac{P_e}{\rho} \end{bmatrix}_{F\ w/out\ bend} + \begin{bmatrix} 0 \\ \left[\frac{Dr}{\rho}\eta^{''}\right]^{''} \end{bmatrix}_{F\ bending\ moments} \tag{6.11}$$

The second term in the flux is originating from the bending moments. A fractional step method (as first introduced by Chorin *et al.* [245]) is proposed to decouple the bending moments part of the convective flux term. This decoupling method is described in the next subsection.

#### 6.1.3.1 Fractional Step Method and Proof of Applicability

Starting from the general form of the equations including a differential operator in space $(L)$,

$$\dot{Q} + LQ = 0; \qquad Q\,(t=0) = Q_0 \tag{6.12}$$

Where $Q$ is the vector containing variables velocity $V$ and area $A$ (or deformation $\eta$). A standard first order time marching scheme can be written as $(t_n = n\tau)$

$$\begin{aligned} Q\,(x, t_n{+}\tau) =& Q\,(x, t_n) - \tau L Q\,(x, t_n) + O\left(\tau^2\right) \\ =& \left(I - \tau L\right) Q\,(x, t_n) + O(\tau^2) \end{aligned} \tag{6.13}$$

Where, $\tau$ is the time-step value, $n$ is the number of the current time-step, $I$ is the identity matrix and $t$ is the time. To initiate the fractional step method we present the unknown field $Q(x,t)$ as a superposition of a guessed value $\overline{Q}(x,t)$ and a correction value $\Delta Q$,

$$Q = \overline{Q} + \Delta Q. \tag{6.14}$$

Assume operator $L$ can be decoupled,

$$L = L_1 + L_2. \tag{6.15}$$

$L_1$ and $L_2$ are operators. In this case equation 6.10 will be presented by

$$\dot{Q} + L_1 Q + L_2 Q = 0. \tag{6.16}$$

Equation 6.14 can be decoupled according to the following two steps

Step1:

$$\begin{aligned} &\dot{\overline{Q}} + L_1 \overline{Q} = 0; \qquad t_n \le t \le t_{n+1} \\ &\overline{Q}(x, t_n) = Q(x, t_n) \end{aligned} \tag{6.17}$$

Step 2:

$$\begin{aligned} &\Delta\dot{Q} + L_2\Delta Q = 0; \qquad t_n \le t \le t_{n+1} \\ &\Delta Q(x,t_n) = \overline{Q}(x,t_n) \end{aligned} \tag{6.18}$$

The $1^{st}$ order numerical scheme applied to each fractional step yields

$$\begin{aligned} &\overline{Q}\left(x,\ t_{n+1}\right) = \left(I - \tau L_1\right)\overline{Q}\left(x,\ t_n\right) = \left(I - \tau L_1\right)Q\left(x,\ t_n\right) + O\left(t^2\right); \\ &\Delta Q\left(x,\ t_{n+1}\right) = \left(I - \tau L_2\right)\overline{Q}\left(x,\ t_n\right) = \left(I - \tau L_2\right)Q\left(x,\ t_n\right) + O\left(t^2\right). \end{aligned} \tag{6.19}$$

Using relation 6.14 the computation of vector $Q$ at the time $t_{n+1}$ may be carried out as

$$\begin{aligned} &Q\left(x,\ t_{n+1}\right) = \overline{Q}\left(x,\ t_{n+1}\right) + \Delta Q\left(x, t_{n+1}\right) = \\ &\left[\mathrm{I} - \tau(L_1 + L_2)\right]Q\left(x,\ t_n\right) + O(t^2) \end{aligned} \tag{6.20}$$

Proves that the set of two simplified fractional problems can be solved at each of the time steps $t_n \le t \le t_{n+1}$ instead of the general form 6.12.

Solution 6.20 approximates equation 6.16 with the 1st order accuracy at each time-step which gives the ground to replace the problem 6.12 by the sequential solutions of the two simplified problems 6.17 and 6.18. Regarding application to the FSI problem, operator $L_1$ indicates a classical FSI model based on the membrane vessel deformation, whereas $L_2$ describes bending effect.

#### 6.1.3.2 Bending Moments in FSI Formulation

The system of governing equations with account for bending moments has the form:

$$\begin{aligned} &\dot{Q} + F' = 0; \\ &Q = \begin{bmatrix} A \\ V \end{bmatrix}, \qquad Flux\ F = \begin{bmatrix} AV \\ \frac{V^2}{2} + \frac{P_e}{\rho} \end{bmatrix}_{F\ w/out\ bend} + \begin{bmatrix} 0 \\ \left[\frac{Dr}{\rho}\eta''\right]'' \end{bmatrix}_{F\ bending\ moments}. \\ &A = A_0\left(1 + \eta^2\right); \qquad D = \frac{Eh^3}{12\left(1 - \nu^2\right)}. \end{aligned} \tag{6.21}$$

Where, $\nu$ is the Poisson's ratio, $\eta$ – the circumferential strain and $E$ is the young elasticity module. Applying this fractional stepping method to the system of governing equations allows us to solve this problem without the need for complex calculation of a lengthy Jacobian.

To apply the fractional step algorithm, each field component is presented as the superposition of a guessed and a correction component,

$$\begin{aligned} \eta &= \overline{\eta} + \Delta\eta \\ V &= \overline{V} + \Delta V \end{aligned} \tag{6.22}$$

We obtain the predictor function $\overline{\eta}\,(x,t)$, $\overline{V}\,(x,t)$, and $\overline{A}\,(x,t)$, as a solution for the fluid-membrane arterial wall interaction problem with a classical nonlinear/linear elastic constitutive equation

$$\begin{aligned} &\dot{Q} + F' = 0 \\ &\overline{Q} = \begin{bmatrix} \overline{A} \\ \overline{V} \end{bmatrix}, \qquad Flux\ \overline{F} = \begin{bmatrix} \overline{AV} \\ \frac{\overline{V}^2}{2} + 2\rho c_{mk}^2 \overline{\eta} \end{bmatrix} \end{aligned} \tag{6.23}$$

Substitution of 6.22 into 6.10 with the following subtraction from 6.23 yields the correction component

$$\Delta\dot{V} + \left[\frac{\Delta V^2}{2} + \overline{V}\Delta V + \frac{Eh}{r}\Delta\eta + rD(\Delta\eta + \overline{\eta})^{iv}\right]' = 0 \tag{6.24}$$

At this point we need to make two assumptions:

1. Bending moments of a membrane displacement are negligible, $\overline{\eta}^{iv} = 0$.

2. Velocity component is mainly coupled to the membrane component of displacement, $\overline{\eta}$ and thus, the boundary layer in the local proximity of a stent – artery interface has a negligible impact on the velocity, $\Delta V = 0$.

Returning to the equation 6.24 and eliminating the small terms, we reduce the problem of the coupled axisymmetric deformation

$$\Delta\eta^{iv} + 4\beta^4\Delta\eta = 0; \qquad \beta^4 = \frac{3\left(1-\nu^2\right)}{r^2h^2} \tag{6.25}$$

of a cylindrical artery and stent to the following boundary value problems (Figure 6.4)

$$\begin{aligned} \Delta\eta_a^{iv} + 4\beta_a^4\Delta\eta_a = 0; \\ \Delta\eta_s^{iv} + 4\beta_s^4\Delta\eta_s = 0. \end{aligned} \tag{6.26}$$

Subscript $s$ refers to the stented location and subscript $a$ refers to the artery. The coordinate system has been placed at the interface, as shown in Figure 6.4.

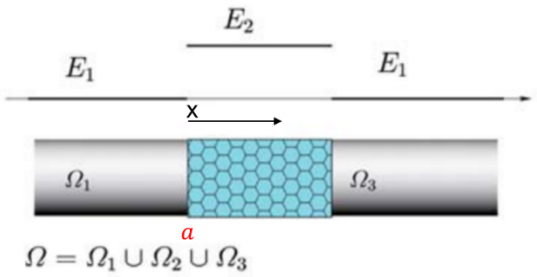


**Fig. 6.4.** – Discontinuity of Young's modulus in the case of a stented artery. $a$ indicates the interface of artery and stented location (reproduced from [117]).

Since local bending dies out rapidly as the distance, $x$, from the interface increases, we represent this effect in the solution by defining the exponential to go toward $-\infty$. Solutions for $\eta_a$ and $\eta_s$ reads

$$\begin{aligned} \Delta\eta_s &= e^{-\beta_s x}\left(c1\cos\beta_s x \; + c2\sin\beta_s x\;\right); \qquad \eta_s|x \to \infty = 0; \\ \Delta\eta_a &= e^{\beta_a x}\left(c3\cos\beta_a x \; + c4\sin\beta_a x\;\right); \qquad \eta_a|x \to -\infty = 0; \end{aligned} \tag{6.27}$$

Four constants can be determined from the conditions, continuity of displacement and slope, bending moment and shear forces, respectively.

$$\begin{aligned}
&(\overline{\eta}_s + \Delta\eta_s)_{x=0} = (\overline{\eta}_a + \Delta\eta_a)_{x=0} \\
&(\overline{\eta}'_s + \Delta\eta'_s)_{x=0} = (\overline{\eta}'_a + \Delta\eta'_a)_{x=0} \\
&D_a \Delta\eta''_a = D_s \Delta\eta''_s \\
&D_a \Delta\eta'''_a = D_s \Delta\eta'''_s
\end{aligned} \tag{6.28}$$

Differentiating the expressions, we find

$$\begin{aligned}
&\Delta\eta'_s = \beta_s e^{-\beta_s x}[-c1(\cos\beta_s x \ + \sin\beta_s x \ ) + c2(\cos\beta_s x - \sin\beta_s x)]; \\
&\Delta\eta''_s = 2\beta_s^2 e^{-\beta_s x}[c1(\sin\beta_s x) - c2(\cos\beta_s x)]; \\
&\Delta\eta'''_s = 2\beta_s^3 e^{-\beta_s x}[c1(\cos\beta_a x \ - \sin\beta_a x \ ) + c2(\cos\beta_a x \ + \sin\beta_a x \ )]; \\
&\Delta\eta'_a = \beta_a e^{-\beta_a x}[c3(\cos\beta_a x \ - \sin\beta_a x \ ) + c4(\cos\beta_a x \ + \sin\beta_a x \ )]; \\
&\Delta\eta''_s = 2\beta_s^2 e^{-\beta_s x}[-c3(\sin\beta_s x) + c4(\cos\beta_a x)]; \\
&\Delta\eta'''_s = 2\beta_s^3 e^{-\beta_s x}[-c3(\cos\beta_a x \ + \sin\beta_a x) + c4(\cos\beta_a x - \sin\beta_a x \ )].
\end{aligned} \tag{6.29}$$

The interface condition at figure 6.4a yields,

$$\begin{aligned}
&\overline{\eta}_{a0} - \overline{\eta}_{s0} = c1 - c3; \\
&\overline{\eta}'_{a0} - \overline{\eta}'_{s0} = \beta_s \left(-c1 + c2\right) - \beta_a \left(c3 + c4\right); \\
&- \beta_s^2 c_2 D_s = \beta_a^2 c_4 D_a; \\
&\beta_s^3 D_s \left(c1 + c2\right) = \beta_a D_a \left(-c3 + c4\right).
\end{aligned} \tag{6.30}$$

Solving these equations analytically will result to the correct prediction of the moments due to the membrane displacement mismatch between stented and non-stented arterial sites.

Figure 6.5, shows the distributions of shear forces and bending moments in the proximity of the left artery – stent interface. We assume the Young modulus of the stent is about 16 times larger than arterial segment. The Moens-Korteweg speed of propagation is consequently 4 times faster for the stent rather than for the artery. Both distributions reveal typical spikes of moments and shear forces in the proximity of the interface as predicted by

the classical theory of a boundary layer of thin-walled elastic shells. Unlike the classical model of a vascular FSI, based on a membrane thin-walled cylindrical shell, none of distributions: normal displacement, slope, and circumferential strain are discontinuous based on the described model.

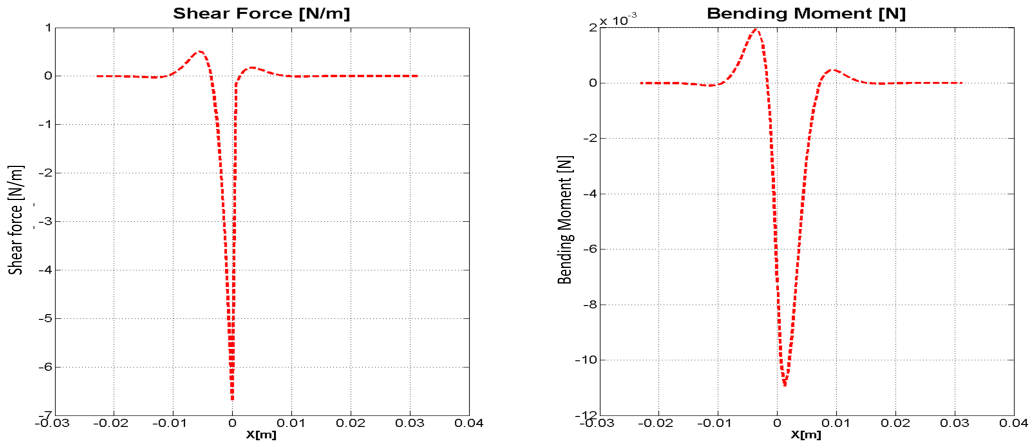


**Fig. 6.5.** – Shear forces and bending moment at the proximity of the stent interface (x=0). Left and right side of the spike are related to the effect of the bending along bare artery and stented artery, respectively.

As we see from Figure 6.5, the bending moment and shear force effects are re localized in the vicinity to the interface. However, long-term effects of these stresses can be studied further. The pulsatile von Mises stress components can be used to estimate low cycle bio-fatigue life of the artery in the proximity to the stent-artery interface.

The next step here is to validate this algorithm with the available works in the literature to see the credibility of the proposed work.

## 6.2 Geometrically Multiscale Simulations Applied to Abdominal Aneurysm

### 6.2.1 3D-1D Framework

Blood flow features such as recirculations and asymmetric changes in geometrical abnormalities can be only captured with 3D models. Multiscale models can account for 3D effects locally while keeping the rest of the model in lower dimensions [131].

Heterogeneous nature of the cardiovascular system necessitates integration of models operating with varying levels of complexity. The high aspect-ratio segments of the cardiovascular system can be accurately represented using a quasi - one dimensional (1D), non-steady, averaged over the cross section FSI model. However, when the enhanced local spatial resolution is required, for instance in case of pulmonary circulation and coronary arteries [246], [247], the intertwining of quasi-1D models with more complex 3D ones is imperative. Examples relate to the better simulation, and therefore understanding and diagnosis of the deep venous thrombosis, abdominal aneurysm, femoral stenosis, bifurcation areas, etc. [71]. The proper detection of a reverse flow (secondary flow) in a local 3D segment, analyzing the shear stresses and quantification of pulsatile mechanical stresses helps us to predict an arterial disease for large blood vessels and the fatigue life of the tissue, rendering multiscale models as accessible and accurate tools to predict arterial/pulmonary abnormalities. Other groups have developed their own 3D algorithms and have coupled them to 1D/0D codes (see [248]). The disadvantage is the overly simplified 3D models uniquely tailored for a specific case of study.

Here, a variational formulation [249] is utilized to couple 3D and 1D models. The significance of the present work is in creating a universal coupling approach that can incorporate the already developed 3D algorithms, such as ANSYS and connect it to an in-house 1D code (*e.g.* CardioFAN).

### 6.2.2 Coupling Methodology

3D-1D coupling framework is as follows: continuity – $A$, $V$ are cross sectional area and velocity

$$V_1 A_1 = V_2 A_2 \tag{6.31}$$

and momentum conservation:

$$\frac{p_1}{\rho} + \frac{1}{2} V_1^2 = \frac{p_2}{\rho} + \frac{1}{2} V_2^2 \tag{6.32}$$

forward propagating linearized characteristic wave $I_+$

$$V_1 + \frac{p_1}{\rho c} = I_+ \tag{6.33}$$

backward propagating linearized characteristic wave $I_-$

$$7)\ V_2 - \frac{p_2}{\rho c} = I_- \tag{6.34}$$

Here, the coupling is achieved by implementing a simple yet robust coupling interface formulation, which communicates between MATLAB (containing 1D code & Coupling Interface) and ANSYS FSI module (3D) for the two-way exchange of data at the 3D-1D interface. The process is shown in figure 6.6.

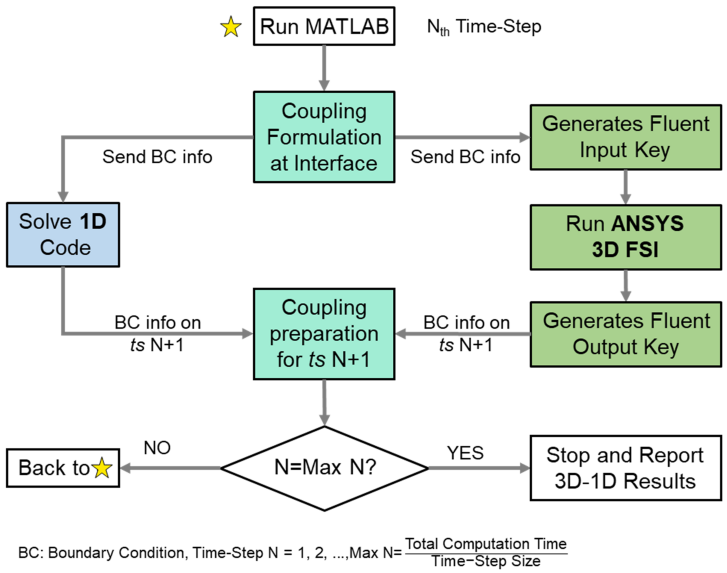


Figure 5: 3D-1D Coupling flow chart

**Fig. 6.6.** – Flow chart of the coupled model steps.

The coupling algorithm used for the cross-talk between ANSYS-FSI and MATLAB are briefly highlighted in [250].

### 6.2.3 Testing Coupling Methodology

In order to test how well the 3D-1D coupling performs compared to a fully 1D or fully 3D model, a simple test was designed as follows:

#### 6.2.3.1 Simple Elastic Cylinder Test:

Figure 6.7, depicts a comparison of results between 3D-1D model, an equivalent 3D only model and a 1D only model of a simple elastic cylinder. The presented results are pressure and flow data sets obtained from 3D model, 1D model, and 3D-1D model at the coupling interface. In all cases for a given flow condition at 3D inlet, results at the interface ideally matches. *Inlet BC:* flow rate imposed as half a sin, with the maximum amplitude of $500\frac{mL}{s}$ as a function of time, which flats after $0.3\ s$ and repeats with a period of $1\ s$. *Outlet BC:* zero resistance, meaning the pressure waves are freely exiting the domain.

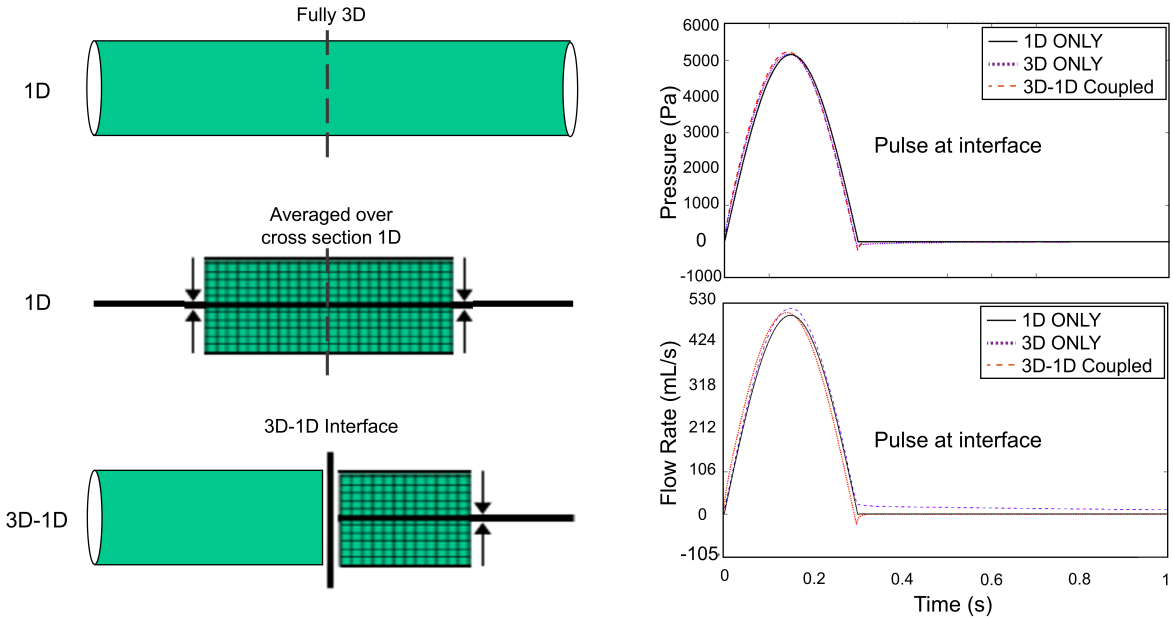


**Fig. 6.7.** – Flow chart of the coupled model steps.

Second testing case is related to a realistic aneurysm geometry extracted from a patient-specific aneurysm obtained by Mix *et al.* [251].

#### 6.2.3.2 3D-1D Aneurysm:

A two-segment cylinder is designed with a quasi-1D model, CardioFAN [252], at the outlet segment and a 3D model containing an aneurysm at the inlet of the 3D-1D interface (see figure 6.8).

Coupling between these two models at the interface of 3D model outlet and 1D segment inlet is carried out using a coupling algorithm discussed previously and also shown as a variational coupling condition, equation 6.35. The simulations were carried out using a fixed time step of $0.00005\ s$ for the 3D model and the 1D model, instead of an adaptive time-stepping to prevent potential errors. This number is selected based on a 1D only model which provided the smallest time-step size to ensure stability. A non-reflective BC was assigned at the outlet of the downstream 1D model to prevent wave reflections. Idealized symmetrical aneurysm model is extracted from Mix *et al.* using SolidWorks® spline geometry and revolving the geometry around its centerline.

$$a_1 \frac{\overline{p}}{\rho} + a_2 \overline{V}^2 = \int r\ f(r) \left( \frac{p}{\rho} + V^2 \right) dr \tag{6.35}$$

Here $a_{1,}\ a_2$ are coefficients, and $P$ and $V$ are pressure and velocity, respectively. $r$ - radius and $f(r)$ - the shape profile of velocity. Interface properties are calculated based on the characteristic waves from both 3D and 1D models. This produces the pressure and velocity at the interface for next time-step. Riemann problem is solved at the interface, resulting in

$$\begin{aligned} P_{interface} &= 0.5\,(P_{1D} + P_{3D}) - 0.5\rho C_{mk}(V_{3D} - V_{1D}); \\ A_{interface} &= 0.5\,(V_{1D} + V_{3D}) - \frac{0.5\,(P_{3D} - P_{1D})}{\rho C_{mk}}. \end{aligned} \tag{6.36}$$

Schematics of the coupled FSI BCs are shown in figure 6.8.

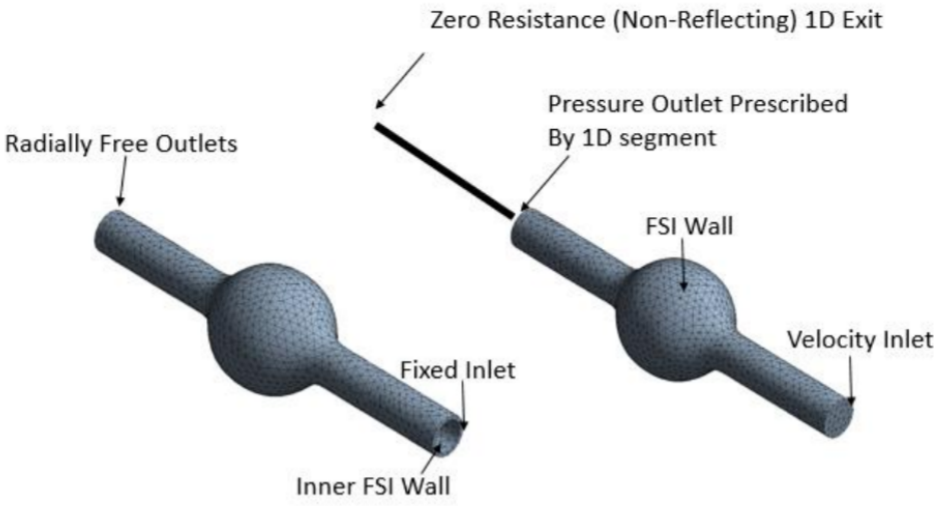


**Fig. 6.8.** – Schematics of the solid and the fluid domains in the aneurysm model, emphasizing the boundary considerations.

To simplify the problem, a velocity profile is imposed on the 3D model inlet as a $sin$ wave with a maximum amplitude of $1\frac{m}{s}$, plateauing at $0.3\ s$ and with a period of $0.8\ s$. As the FSI iterations march forward, ANSYS updates the pressure and velocity across the blood domain. At the end of each time-step, ANSYS Fluent solver extracts pressure and velocity values at the center of all the cells attached to the outlet face. Using a user defined function (UDF) the array of information is stored into an output text file and the 3D simulation is paused for $5\ s$ to receive new pressure boundary value from the 1D model at the 3D-1D interface. The new data comes from the solution of 1D simulation at the same time-step. The interface algorithm, is responsible to receive the pressure, flow and cross sectional area information from both sides and calculate their value at the boundary for the next time step.

seen in Figure 6.9, starting from a 3D segment, a successful coupling formulation resulted in physiological pressure and velocity waveforms at the interface coupling and the 3D aneurysm model.

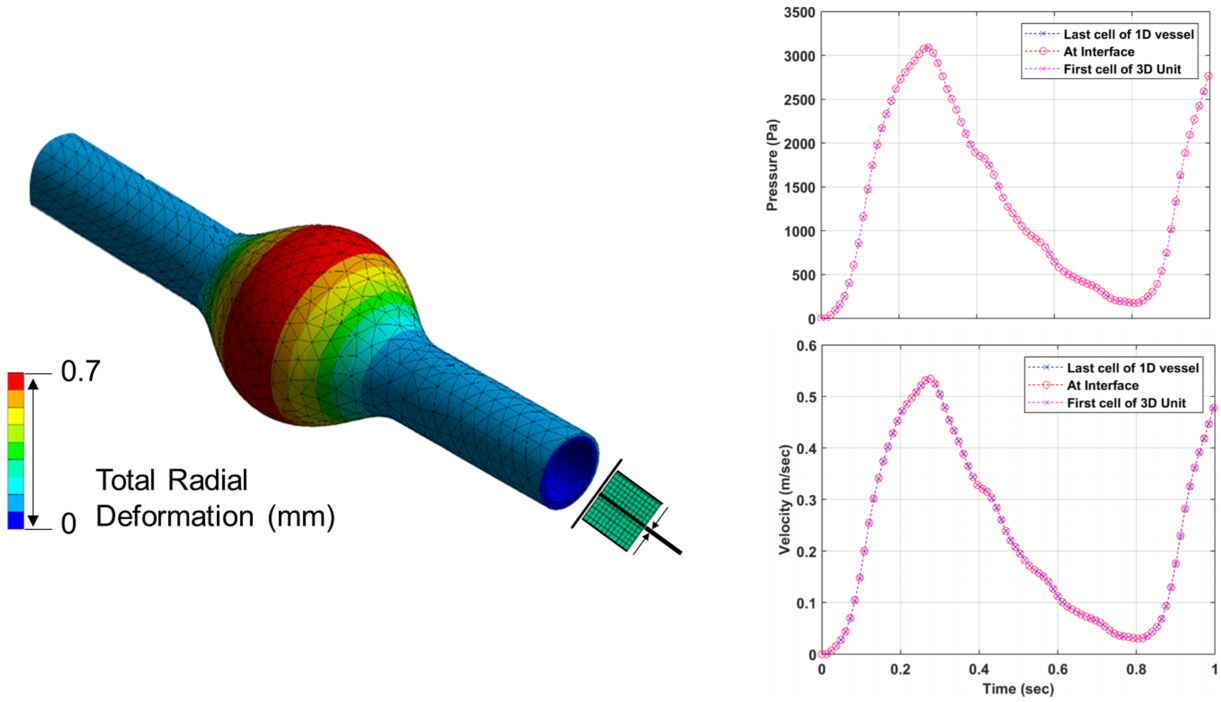


**Fig. 6.9.** – 3D Geometry of the Aneurysm Coupled to 1D outlet. Showing deformation on the surface (left), pressure and flow (right) at both sides of the interface.

Velocity contours of the aneurysm model are shown as a function of time in figure 6.10a. It can be seen that the recirculation zones are captured with the 3D-1D simulation. These are especially important in case of looking at the wall shear stresses (WSS) and aneurysm rupture [31]. On the other hand, to ensure the accuracy of 3D-1D model coupling, the results were verified with a fully 3D aneurysm model with the same length of an outlet as with the 3D-1D counterpart. Velocity profile is plotted in figure 6.10 at a cross-section over the midpoint of the aneurysm. This establishes a simple validation of the 3D-1D coupling method.

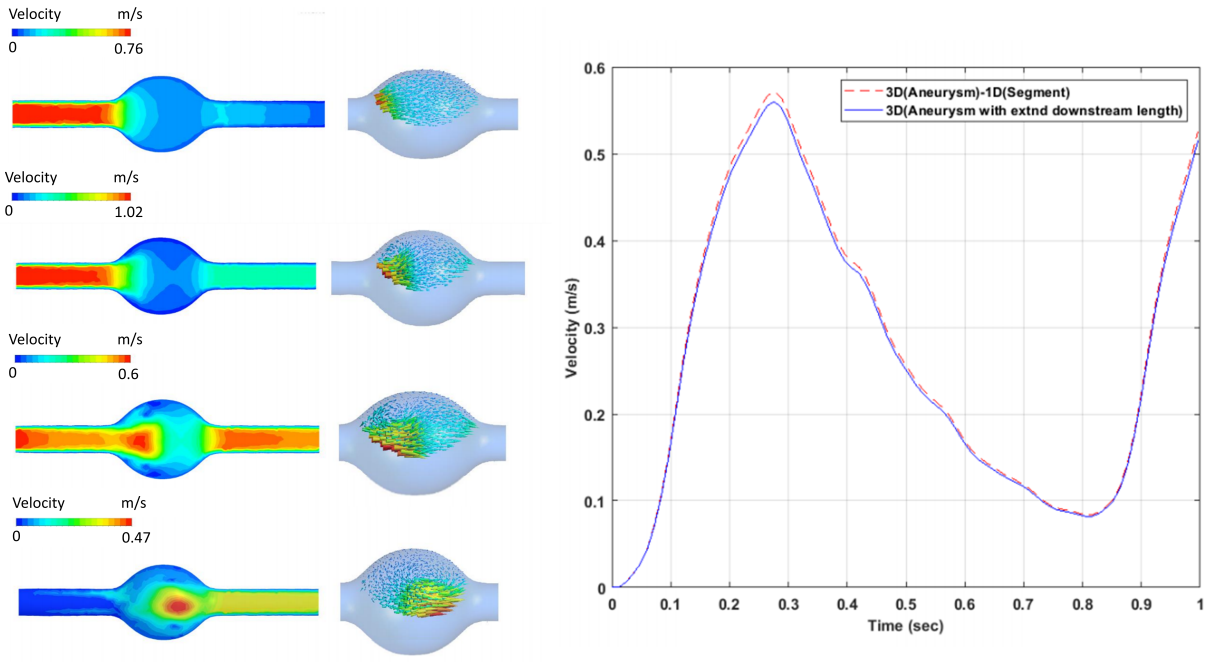


**Fig. 6.10.** – Velocity contour plots at different instances of time in 3D-1D model (left). 3D and 3D-1D Velocity over time plots at a cross-section over the aneurysm bulge.

These results show very good agreement between the coupled 3D-1D and fully 3D models, further suggesting the successful coupling with ANSYS FSI.

#### 6.2.3.3 1D-3D-1D

The most significant advantages of using geometrically multiscale models are the ease of applicability and computing speed. The pursuit for this type of models started with the goal of having a versatile modeling framework, where a 3D representation of a specific organ inside a global reduced order arterial network is possible. For instance, abdominal aortic aneurysm can be modeled in 3D and then replace segment 17 in the 1D model of the main 55 arteries (see 6.11).

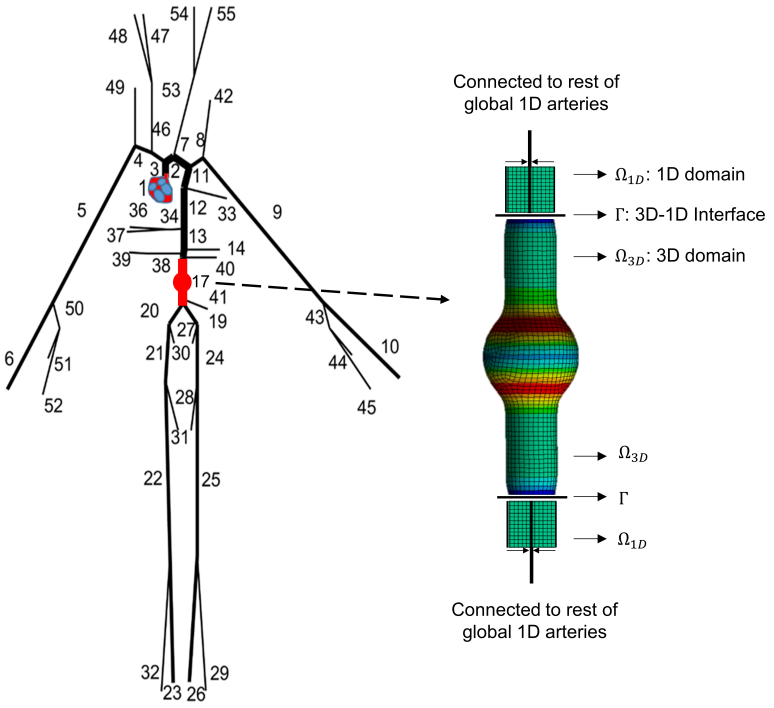


**Fig. 6.11.** – Global network of 55 vessels coupled with a 3D model of an abdominal aneurysm.

To this end the final test is designed with the following settings (see figure 6.12).

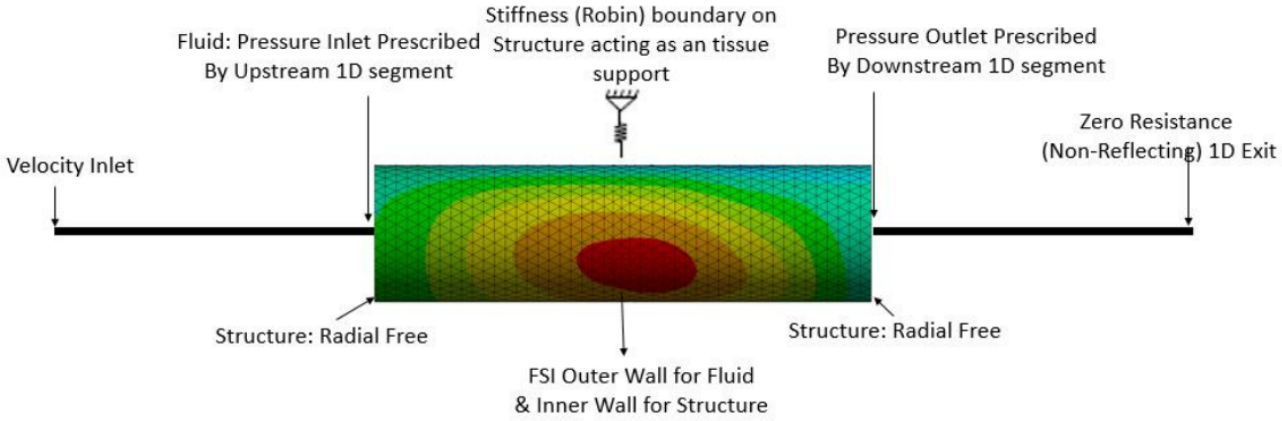


**Fig. 6.12.** – Designing a 1D-3D-1D model of a simple cylinder, with account for tissue elasticity.

As seen in figure 6.12, a tissue support is imposed to mimic the realistic BC for the 3D segment and to constraint its large deformation. The model stiffness is set to 0.01 $N/(mm^3)$ [253]. As prior sections, this model was set with similar input BCs, meaning a half $sin$ velocity wave as a function of time at inlet and non reflective BC at the

outlet. Figure 6.13, shows the velocity profiles between 1D-3D-1D model and a fully 1D and a fully 3D model. Velocity and pressure waveforms at 1D-3D and 3D-1D interfaces are presented in figure 6.14.

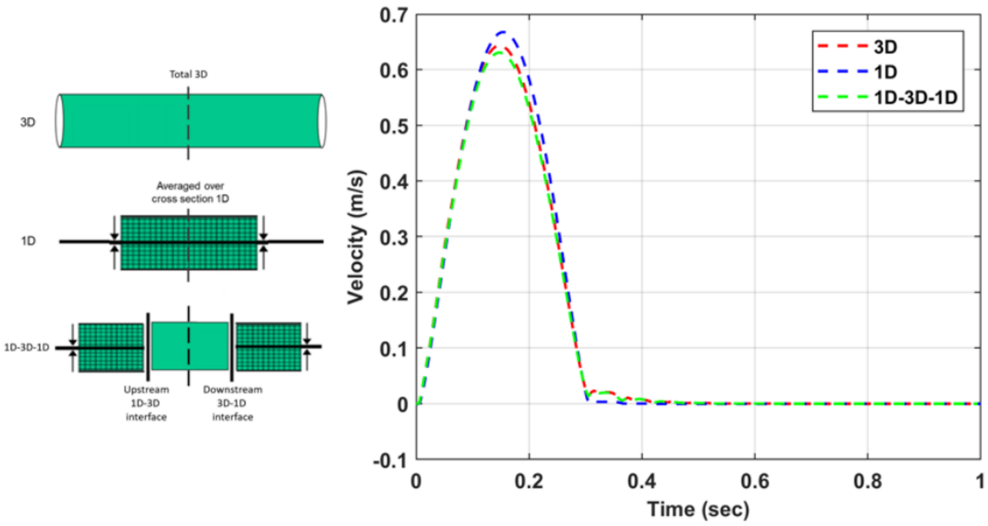


**Fig. 6.13.** – Velocity at the middle of the geometry.A comparison between fully 3D, fully 1D and 1D-3D-1D model of an elastic cylinder.

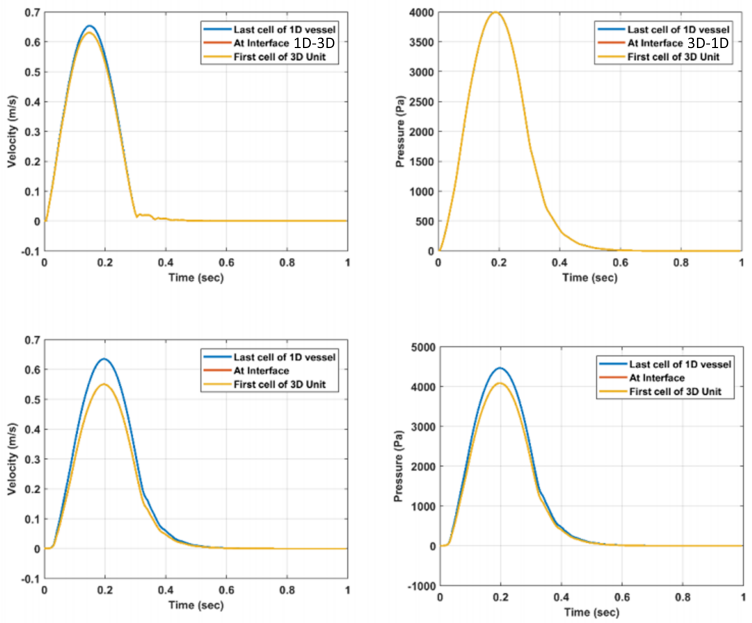


**Fig. 6.14.** – Velocity and Pressure waveforms plotted at the first and second geometrically multiscale interfaces.

It can be seen that the pressure signals are very consistent and flow at the interface show a 26% drop between 1D and 3D sides. This might be a result of area deformation which is practically kept free in the imposed interface condition. It is suggested that with additional iterations between 3D-1D at each time step, relaxation of cross sectional area or velocity this issue could be alleviated (as shown by others[67], [124], [254], [255]). Fine tuning of the tissue model can also lead to retrieving more consistent velocity signals.

It should be noted that this was the first work investigating a connection of an in-house FSI algorithm with ANSYS 3D FSI code. The intention here is to introduce this coupling as a add-on that can be used by researchers with 3D modeling softwares such as ANSYS in combination to our in-house 1D code CardioFAN. 3D segmentation of MRI pictures have been widely used recently in generating patient-specific geometries of the aneurysm and other cardiovascular diseases [65]. After 3D segmentation, extracted MRI models can be paired with the current coupling methodology to quickly solve a computational model of a patient-specific aneurysm without knowing the exact BCs. Another example is the living heart project [66] that can be easily connected with our open source code CardioFAN by using this coupling method. Lastly, 1D-3D-1D code coupling can be further exercised with 3D models of stented arteries and arterial bifurcation sites.

# 7

# Noninvasive PTT-Based Central BP and Cardiac Output Measurement Using Reduced-Order Models - Part1: Formulation and Preliminary Testing

## 7.1 Introduction

In this chapter, a method for calculating numerical pulse transit time (PTT) from the reduced-order model of the human arterial network is presented and applied to existing data sets in the literature to inversely reconstruct proximal blood pressure (BP) and Flow waveforms. PTT can be accurately predicted in a reduced-order numerical model of the cardiovascular system by accounting for the hyperelasticity and nonlinear pulsatile blood flow through large arteries [105], [252]. It is closely related to the blood pressure (BP) and stroke volume and thus correctly formulating the numerical PTT to match a clinical value, enables extracting patient-specific information for clinical diagnostics and predicting central waveforms, see chapter 4. The validated in-house open source code, CardioFAN (See chapter 5, and [252], [256]), is utilized for this study. The advantage of this platform is its monotonicity preserving capability when dealing with nonlinear flow and pressure wave propagation in arterial system. This combined with a reduced-order nonlinear elastic vessel wall formulation allows for accurate prediction of PTT, and thereby the proximal/central waveforms.

First of all the methodology is explained and simple examples are presented to show the effect of nonlinear wall model, monotoniicity preserving scheme and correct numerical PTT formulation on obtaining a better match with clinically measured PTT and BP data. Snapshots of the algorithm or its logical framework are also included. The next test involves using direct simulation and measurement data from an MRI based study [173] to demonstrate the possibility for inversely deriving BP and stroke volume.

## 7.2 Obtaining Numerical PTT

PTT is the time required for the pressure waveform to travel between proximal and distal sites of the arterial tree. The pulse pressure waveform results from the ejection of blood from the left ventricle and moves with a velocity greater than the blood itself. PTT serves as an indirect marker of the aortic compliance, stiffness, blood pressure and the stroke volume. To quantify PTT we consider the following quasi-1D mathematical formulation representing conservation of mass and the momentum balance written in a conservative form as presented in section 5.2.2.3

$$\frac{\partial Q}{\partial t} + \frac{\partial F\left(Q\right)}{\partial x} = f; \tag{7.1}$$

$$Q = \begin{bmatrix} A \\ V \end{bmatrix}; \qquad F = \begin{bmatrix} AV \\ \frac{V^2}{2} + \frac{P}{\rho} \end{bmatrix}; \qquad H = \frac{\partial F}{\partial Q} = \begin{bmatrix} V & A \\ \frac{P_A}{\rho} & V \end{bmatrix} \qquad f = \begin{bmatrix} 0 \\ \frac{kV}{A_0} \end{bmatrix}. \tag{7.2}$$

Pulse wave velocity PWV is associated with the forward propagating wave, $PWV = \lambda_f = V + \sqrt{\frac{AP_A}{\rho}}$. The characteristic variables can be found using the method of Riemann invariants. As previously described in section 5.2.2.2, To quantify PWV we are using the physiological hyperelastic constitutive model for the arterial tissue by YC Fung. The following constitutive equation is derived in chapter 5:

$$P = 2\rho c_{mk}^2 \eta \; e^{a\eta^2}; \qquad c_{mk}^2 = \frac{Eh}{2\rho r} \tag{7.3}$$

By substituting derived formula for $p = p(\eta)$ into the solution for $PWV$, we obtain the generalized pulse wave velocity expression for the FSI model for a hyperelastic arterial tissue

$$PWV = V + c_{mk}.\alpha\left(\eta\right); \qquad \alpha\left(\eta\right) = e^{\frac{a\eta^2}{2}}\sqrt{\left(1+\eta\right)\left(1+2a\eta^2\right)}; \qquad c_{mk}^2 = \frac{Eh}{2\rho r} \tag{7.4}$$

PTT can be calculated for each segment and the entire arterial tree, using the slope of a characteristic line, corresponding to the forward propagating wave at each segment

$$\frac{dx}{dt} = PWV(x,t) \tag{7.5}$$

The expression for PTT is calculated by the following numerical integration

$$PTT = \sum_{k=1}^{N_v} \int_0^{L_x} \frac{dx}{PWV\left(x, t\left(x\right)\right)} \cong \sum_{k=1}^{N_v} \sum_{n=1}^{N_k} \frac{\Delta x_k}{PWV_k\left(x_n, t\left(x_n\right)\right)} \tag{7.6}$$

Where, $t(x)$ is the time required for the forward propagating wave, starting at the 1st arterial site to reach the downstream arterial site with the coordinate $x$; $N_v$ – total number of vessels on the path from the proximal to the distal sites of the arterial tree; $N_k$ – number of elements at the $k^{th}$ vessel; $PWV_k$ – pulse wave velocity for the $k^{th}$ vessel.

Assuming the properties of the arteries along the PTT calculation path are known, this formulation report PTT as a function of the time in one cardiac cycle when PTT calculation was initiated. This will be further explained in section 7.2.1.

### 7.2.1 Reference Points to Calculate PTT

In order to track the pulse wave and calculate PTT, the starting point in time and space for the integral 7.6, needs to be defined. Experimental PTT is usually measured using the ECG/BCG and peripheral PPG signal (see section 4.2), depending on the available data. Gaddum *et al.* [235] studied the PTT measurement methods when flow waveform data from MRI is available at a proximal and a distal arterial site. They concluded that the foot to foot (F2F) method, measuring the delay between wave feet at early systole, provides the best accuracy and repeatability. As they describe, "The foot is defined as the intersection of a horizontal projection through a seven-point mean at the local minimum, and a projection through the local averaged maximum gradient during systole". Figure 7.1 is describing F2F definition.

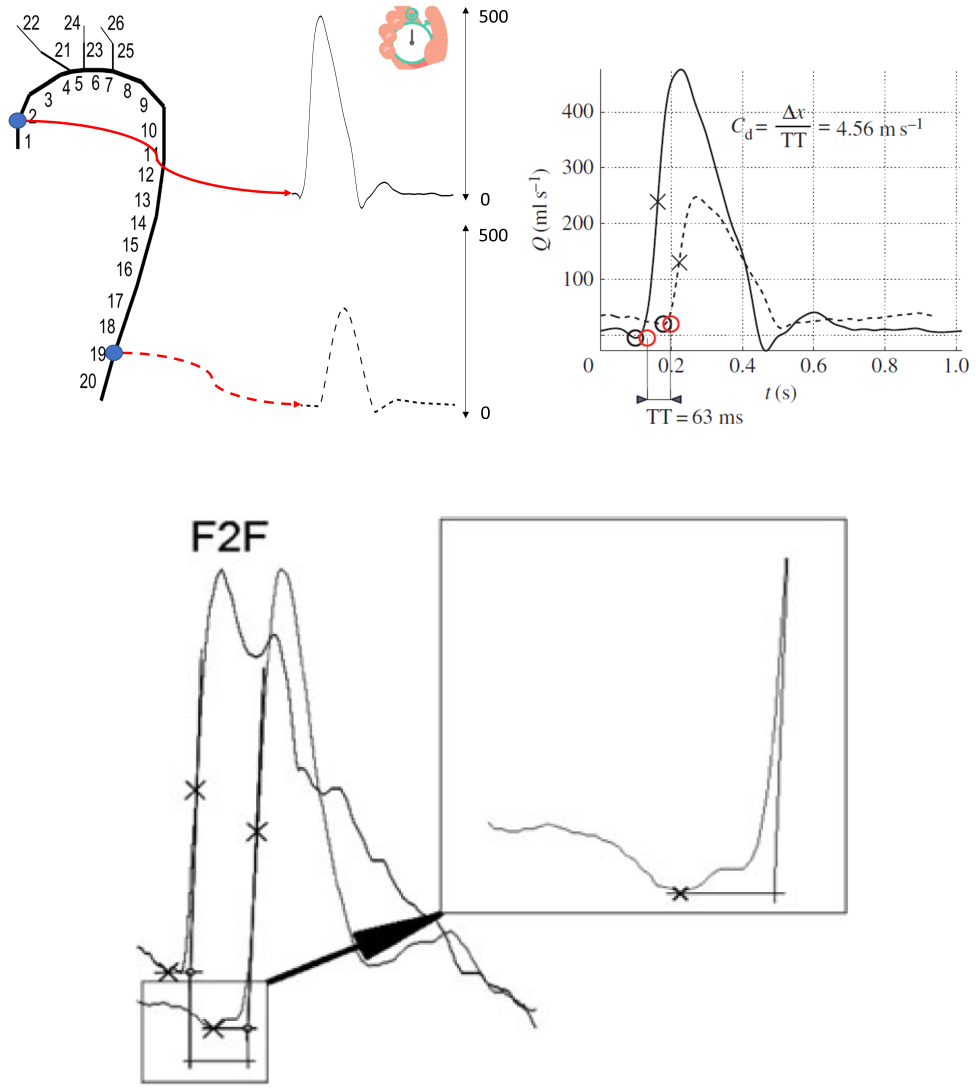


**Fig. 7.1.** – Foot to foot method for evaluating PTT using flow waveforms at two arterial sites. Bottom figure reproduced from [235].

This technique was adapted for numerical PTT calculation, as shown in equation 7.6. The foot of the flow waveform at the proximal site of PTT calculation was pinpointed using the intersection of the horizontal projection of the local minimum of the flow waveform and averaged maximum gradient during systolic up-slope (marking the onset of PTT calculation). PTT was then calculated with the pulse tracking algorithm presented, up to the distal site of PTT measurement, marking the PTT value. Figure 5.4 from chapter 5 is plotted here for a second time to demonstrate how PTT start time and PTT value as a function of start time are related in one cardiac cycle.

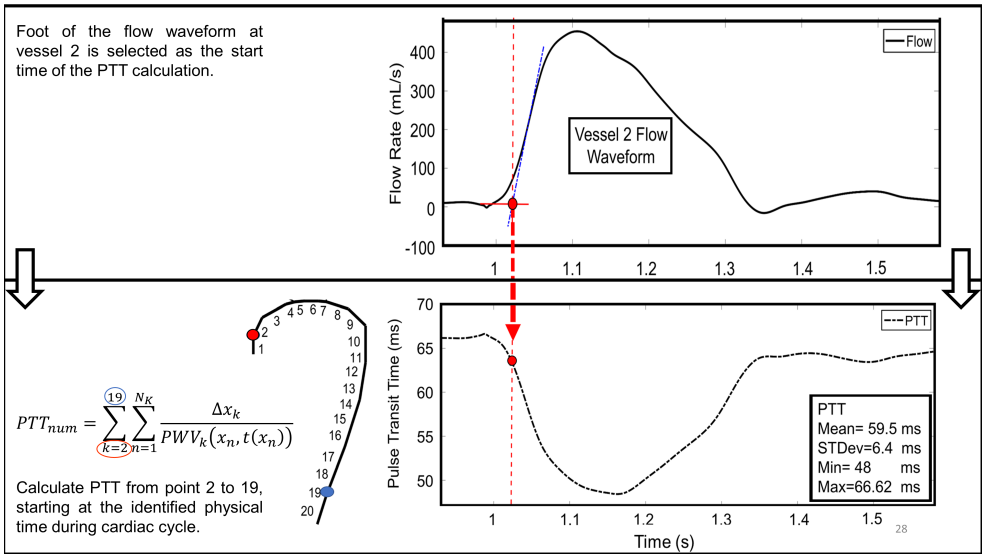


**Fig. 7.2.** – PTT as a function of the calculation start time. The time during the 2nd cardiac cycle is shown in the x axis (top figure). The flow waveform corresponding to the same time scale is presented (bottom figure). The crossing of the maximum derivative of the flow waveform systolic rise and the extended horizontal line from diastolic flow, is the start time of PTT calculation from foot to foot method, as shown by Alastruey et al. PTT calculation pathway is from ascending aorta (Asc Aorta, vessel 2) to the abdominal aorta (Desc Aorta, vessel 19).

The advantage of this technique is that instead of calculating an averaged PWV and PTT value, the variations in the time of pulse propagation at each element of each segment is being considered during PTT calculation. Therefore, flow and vessel wall nonlinearities can affect the PTT compared to linear elastic vessel wall models. An example is shown in the next section.

## 7.3 Numerical PTT Evaluation

Following the formulation of numerical PTT, this section is dedicated to the preliminary tests designed to evaluate the potential of this method.

### 7.3.1 PTT in a Cylinder with Linear and Nonlinear Elasticity

In the first example a hollow cylinder representing an arterial segment is generated with a hypothetical length of $10m$, averaged speed of wave propagation $C_{mk} = 6.17m/s$, $\rho = 1050kg/m^3$, radius $r_0 = 0.01m$, $\mu = 4e^{-3}Pa.s$, and with $N = 40$ elements. Generic flow waveform [104], is introduced at the inlet, with maximum amplitudes

ranging from $0$ to $350mL/s$ and the $PTT_{calc}$ was extracted for each flow rate. Figure 7.3 illustrates the change in PTT as a function of the stroke volume (SV) and the respective elasticity model used (linear or nonlinear models).

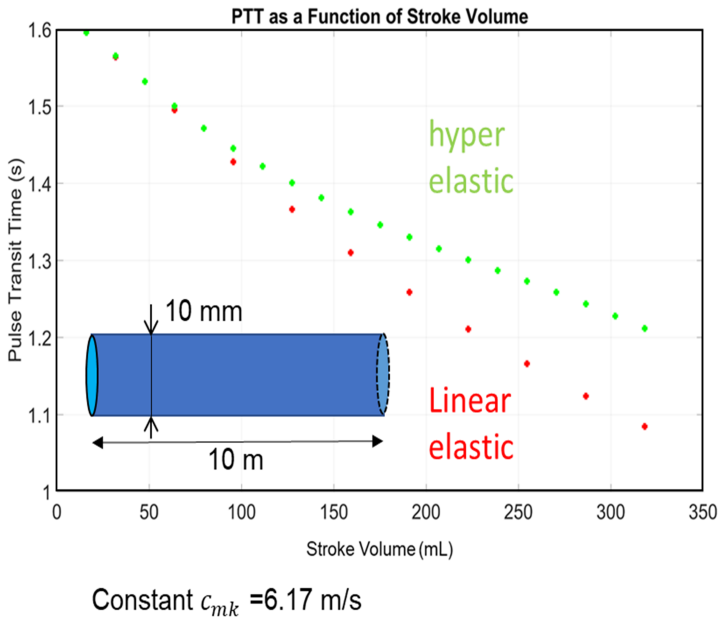


**Fig. 7.3.** – PTT as a function of stroke volume. **Red** dots represent the PTT-SV in a linear elastic model, while **Green** dots represent the curved PTT-SV for hyperelastic wall model.

SV is shown to nonlinearly affecting PTT value, when hyperelastic vessel wall model is used. This result is in agreement with previous studies [105].

### 7.3.2 Inverse Reconstruction of Known Central Pressure and Stroke Volume

In chapter 5, the capability of the presented in-house code, CardioFAN [257], is shown when dealing with blood pressure and flow measurement compared to clinically measured values. Validation was previously aimed at establishing the prediction accuracy of the code when input data is available from the clinical measurements. For instance, when validating against *in vivo* data from the human aorta, section 5.3.3.3, the numerical model was

designed using information of blood vessel properties, inlet flow rate and a calibrated outlet pressure. On the contrary, the aim here is to use only the vessel wall properties and outlet BC, in combination with the measured PTT value from [173], and reconstruct the SV at the inlet. After inversely restoring the inlet BC, blood pressure, arterial distensibility and flow waveforms at different sites can also be validated.

The numerical experiment is designed as follows:

1. Arterial segment lengths and elastic modulus is defined using MRI data. Resistance and compliances at the outlets are defined using pressure measurement at the Carotid artery, as specified by Alastruey *et al.*.

2. A generic form of inlet flow waveform [104] is used with a varying amplitude, to avoid the bias of using the same flow signal provided by [173].

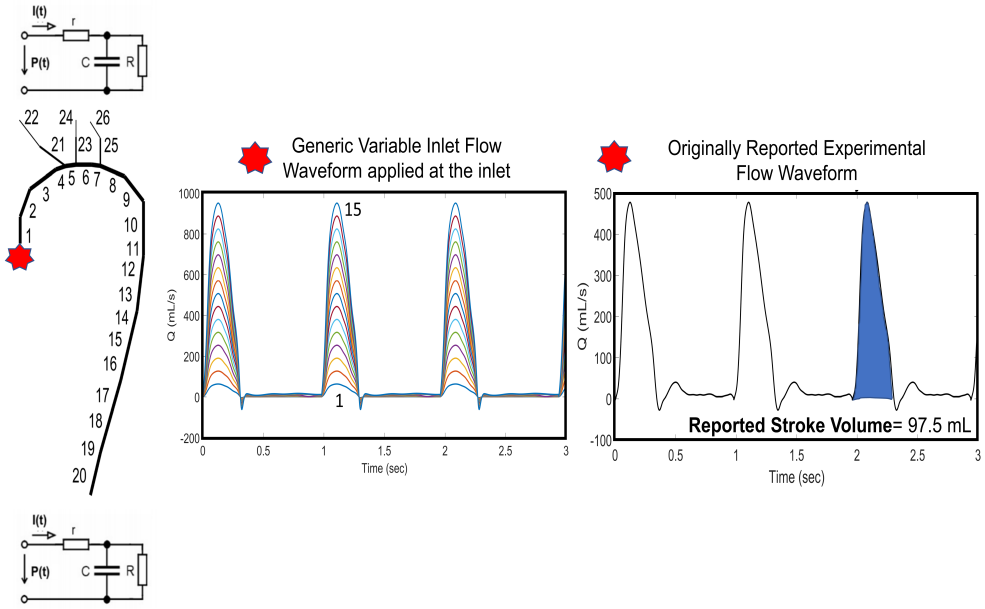


**Fig. 7.4.** – Generic inlet flow waveforms with varying amplitudes. Stroke volume as the area under the flow signal.

3. Numerical simulations with varying inlet flow values were run to numerically match the reported experimental PTT. At the matching PTT point stroke volume, Carotid BP and flow at the common carotid artery and the ascending aorta, were calculated.

The patient-specific geometry of the aorta is recreated in CardioFAN, and the PTT is measured between segments 2 and 19, see figure 7.6. Solving a generalized solution for an inverse problem blind to the input BCs and by matching the numerical PTT with the clinically measured value, BP waveform and SV are reported, figure 7.5. The results are in good agreement with the values reported in direct measurements [173] and demonstrate that an inverse solution can be used for extracting the central BP and flow. It should be noted that the SV was not reported by Alastruey *et al.* and was manually digitized and integrated from the flow waveform at the aortic root, the calculated value is shown on the figure 7.5.

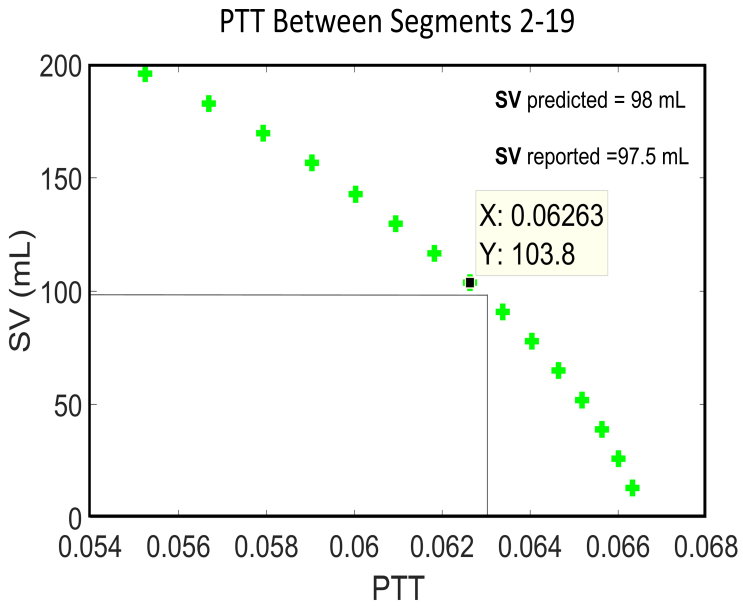


**Fig. 7.5.** – PTT as a function of stroke volume =, where PTT is matched with clinically measured value of 63 ms. Numerical stroke volume is reported and compared against the clinicaly measured value.

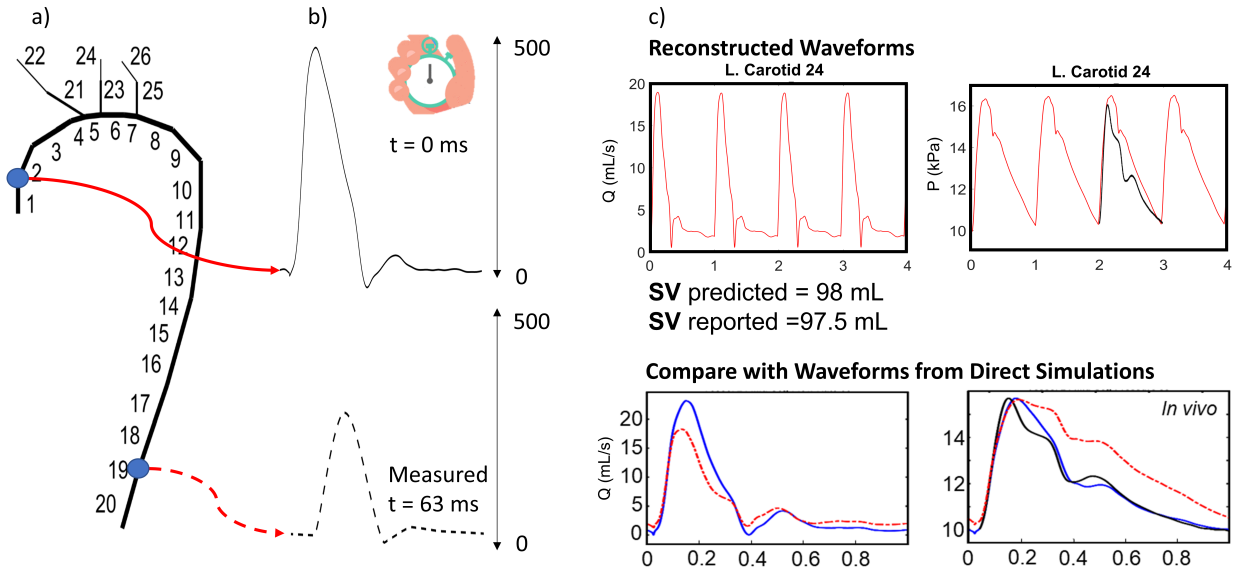


**Fig. 7.6.** – PTT measured between vessels 2 and 19 (a). Example of tracked waveforms (b). Pressure and flow waveforms, **Red** lines represent the generic outlet BC, while **Blue** line represent the direct simulation with known outlet pressure. Reconstructed waveforms (top right) and direct simulation waveforms (bottom right) are plotted (C).

Reported stroke volume, $97.5mL$, and the calculated, $98mL$, are in good agreement. In addition, BP waveform at the common carotid artery is matching the BP from applanation tonometry [173], and resembles the values obtained with direct simulations (see section 5.3.3.3). Flow waveform also has a similar shape and amplitude as the direct simulation results. These preliminary results suggest the potential application of the introduced method for reconstruction of central BP and SV. This will be further investigated in the next chapters.

# 8 Noninvasive PTT-Based Central BP and Cardiac Output Measurement - Part 2: Human Subject Calibration

## 8.1 Introduction

Novel pulse wave velocity (PWV) and pulse transit time (PTT) calculation algorithm added to the CardioFAN is evaluated in chapters 5 and 7. It was shown that in a well-controlled scenario, such as when the vessel length and compliance are known and we have information on outlet BP for a human aorta, the PTT-based blood pressure (BP) and stroke volume can be reconstructed within a good agreement with the gold standard measurements. One of the limiting factors, however, is that this method needs to be accessible, meaning it should work even with more broadly available calibration and validation techniques rather than magnetic resonance imaging (MRI) and applanation tonometry. If the aim is for this technique to be used for patient-specific applications in the future, it is imperative to test it against raw data measured from real patients, where measurement uncertainties should also be addressed. In this chapter the calibration procedure for such algorithm are discussed.

## 8.2 Clinical Model Validation and Prediction of BP and Stroke Volume

In order to test the developed PTT-based BP and SV monitoring technique in a clinical setting, a test procedure is proposed. As shown in figure 8.1, the pathways that will be considered both in computational model and clinical tests is as follows:

1. Subject_Y: A subsystem of systemic arterial tree starts at the ascending aorta, comprising brachiocephalic, subclavian, axillary, brachial, and the outlet segments being radial, ulnar, aortic arch and common carotid arteries. Together they create the pathway from heart to right arm's wrist. Similar to the outlet BCs shown in section 7.3.2, Windkessel BCs are imposed as the outlet boundary conditions at the truncated aorta, carotid, ulnar and radial arteries. For ulnar and radial arteries an alternative technique is to use blood pressure waveform when wrist BP measurements are available (see figure 8.1). Calibration of the BCs and the arterial segment properties are discussed in this chapter under *model personalization* section 8.3.

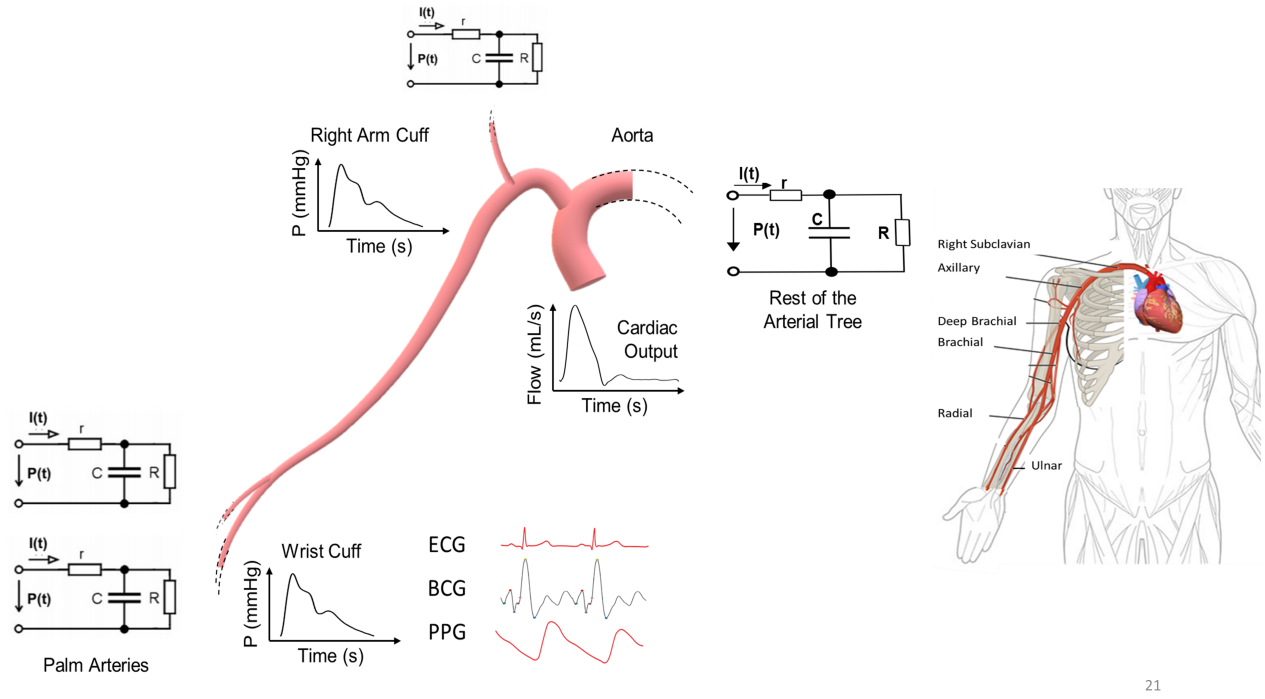


**Fig. 8.1.** – Schematics of the right arm's main arteries used for indirect measurements of cardiovascular parameters

2. Subject_K: A subsystem of systemic arterial tree starts at the ascending aorta, comprising aortic arch, artery, left subclavian, axillary, brachial arteries, and the outlets are radial, ulnar, left common carotid, thoracic aorta and brachiocephalic arteries. These arteries relate to the path from the heart to left hand's wrist 8.2.

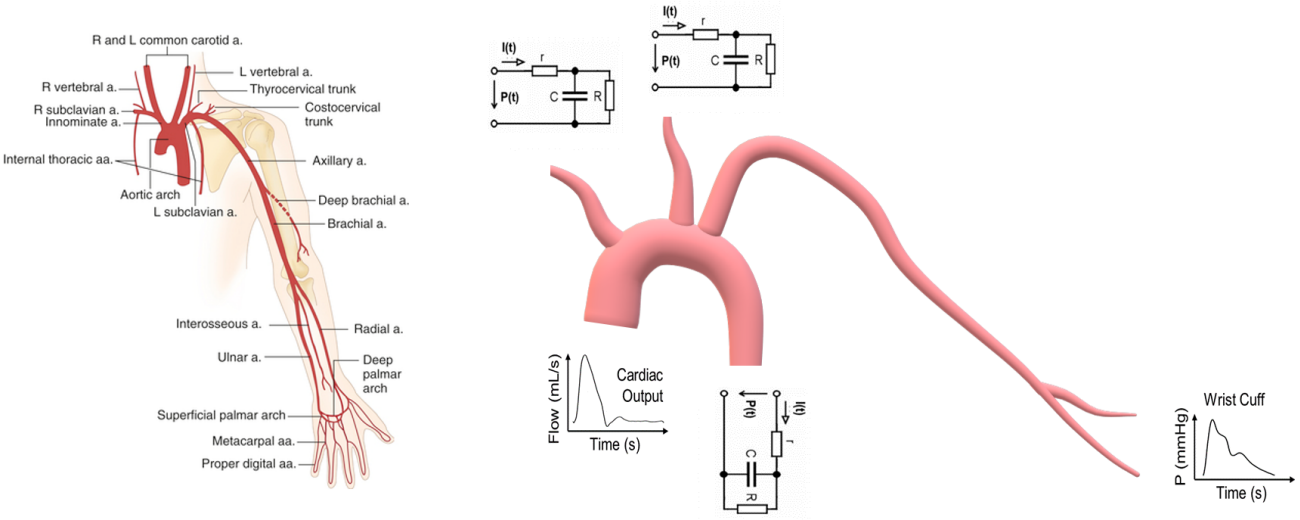


**Fig. 8.2.** – Schematics of the Left arm's main arteries used for indirect measurements of cardiovascular parameters. The detailed left arm arteries picture on the left is reproduced from [258].

Assuming successful personalization of properties for the human subject, an inlet BC, which is usually a flow waveform in one heartbeat is restored. The direct problem evaluating distributions of pressure, flow and lumen cross-sectional area waveforms can then be solved in a few seconds using our reduced quasi-1D fluid-structure interaction (FSI) model, CardioFAN (Cardiovascular Flow ANalysis).

The objective here is to solve the inverse problem, where the SV, aortic BP, flow, should be identified. For this goal, the first step is to calibrate the arterial properties and outlet BCs. After the calibration is completed the measured peripheral BP and PTT from heart to wrist will act as control input values, to detect proximal signals. Eventually, the measured and calculated PTT and BPs are equated

$$\begin{aligned} PTT_{calc}(CO, properties) &= PTT_{measured} \\ BP_{periphery,calc} &= BP_{periphery,meas} \end{aligned} \tag{8.1}$$

and governing PDEs are solved with respect to a variable SV. By plotting the numerical PTT and wrist BP against the SV and equating with the measured PTT and wrist BP, patient-specific proximal BP and SV can be deduced (as shown hypothetically in figure 8.3).

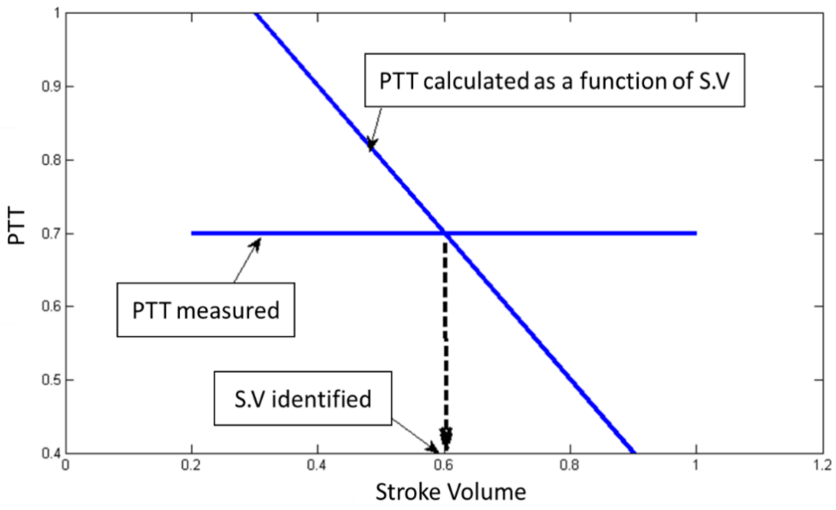


**Fig. 8.3.** – Measured and calculated PTT as a function of SV.

Now the problem comes down to, acquiring PTT and peripheral BP, and how to calibrate the vessel wall properties, arterial geometry and outlet BCs.

## 8.3 Patient-Specific Vessel Wall Properties and Windkessel Coefficients

Patient-specific models require a robust method to fit an algorithm to a specific person. Here, a strategy for calibrating the reduced-order model, CardioFAN is explained. Figure 8.4 displays the process for the proposed cardiovascular parameter evaluation framework based on peripheral measurements and a reduced modeling. The personalized anatomical and mechanical properties of the arterial system are identified, and a calibration procedure is employed iteratively to identify the winkessel BC parameters. Eventually, the calibrated model is used to predict SV, BP, flow and distensibility of all vessels along the path.

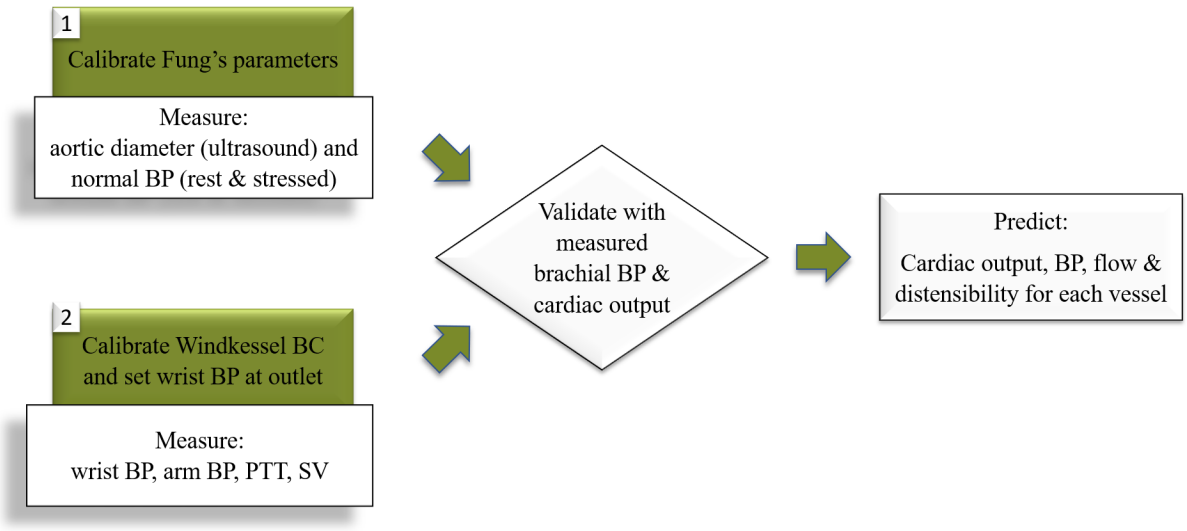


**Fig. 8.4.** – General calibration and validation procedure flowchart for the computational model

: The detailed description of these steps are presented in the following sections.

### 8.3.1 Geometry and Mechanical Properties Calibration

Calibration starts at the aorta. Systolic and diastolic diameters of aorta are measured as a function of time using doppler ultrasound imaging, while the blood pressure is recorded simultaneously at the upper arm. Hyperelastic properties of the vessel wall, represented by two constants derived from Y.C. Fung's exponential constitutive model [25] (as described in section 5.2.2.3 and repeated here 8.2), $a$ - hyperelasticity coefficient, $E$ - tangential modulus at zero stress level used in $C_{MK}$ and $\eta$ - circumferential strain, need to be identified. Fung's hyperelastic model 8.2, with the extracted systolic and diastolic aortic diameters from ultrasound images and BPs from upper arm cuff measurements, relates arterial distensibility to BP. Systolic and diastolic BPs are measured using BIOPAC sphygmomanometer on upper arm in both sitting and supine condition. To add more variation, they have also been measured in normal and stressed heart rates. This information is then used to calibrate the hyperelastic constitutive equation parameter, $a$. Systolic, diastolic and zero stress aortic diameters are found, and the tangential elasticity modulus $E$ is calibrated for the test subject.

In order to have multiple data points, the patient is required to repeat a second session of ultrasound measurement in physical stress condition, or 75% of their maximum heart Rate (HR). Maximum heart rate (MHR) is calculated as shown in 8.2:

$$P = 2\rho c_{mk}^2 \eta \, e^{a\eta^2}; \qquad c_{mk}^2 = \frac{Eh}{2\rho r}; \qquad 220 - age = MHR \tag{8.2}$$

#### 8.3.1.1 Ultrasound Imaging and Analysis

Ultrasound measurements are conducted on the author. Chest ultrasound at the ascending aorta and arm BP are recorded by medical doctors at the echocardiology lab in the Strong Memorial Hospital, University of Rochester. M-mode echo [259], which provides a 1D window, is used to obtain the changes in diameter of the ascending aorta as a function of time for several heart beats. M-mode echocardiography is derived from an M line superimposed on a cross sectional image, in this case the ascending aorta. The M-mode trace shows time as 2nd dimension. This technique enables accurate measurements of the intervals in cardiac cycle, and has excellent temporal resolution of moving structures combined with precise measurement of thickness and cavity size.

As mentioned earlier, measurements are conducted in normal and physical stress conditions. An example of the ultrasound image of the aorta is shown in figure 8.5. This was recorded when subject was sitting and had normal HR.

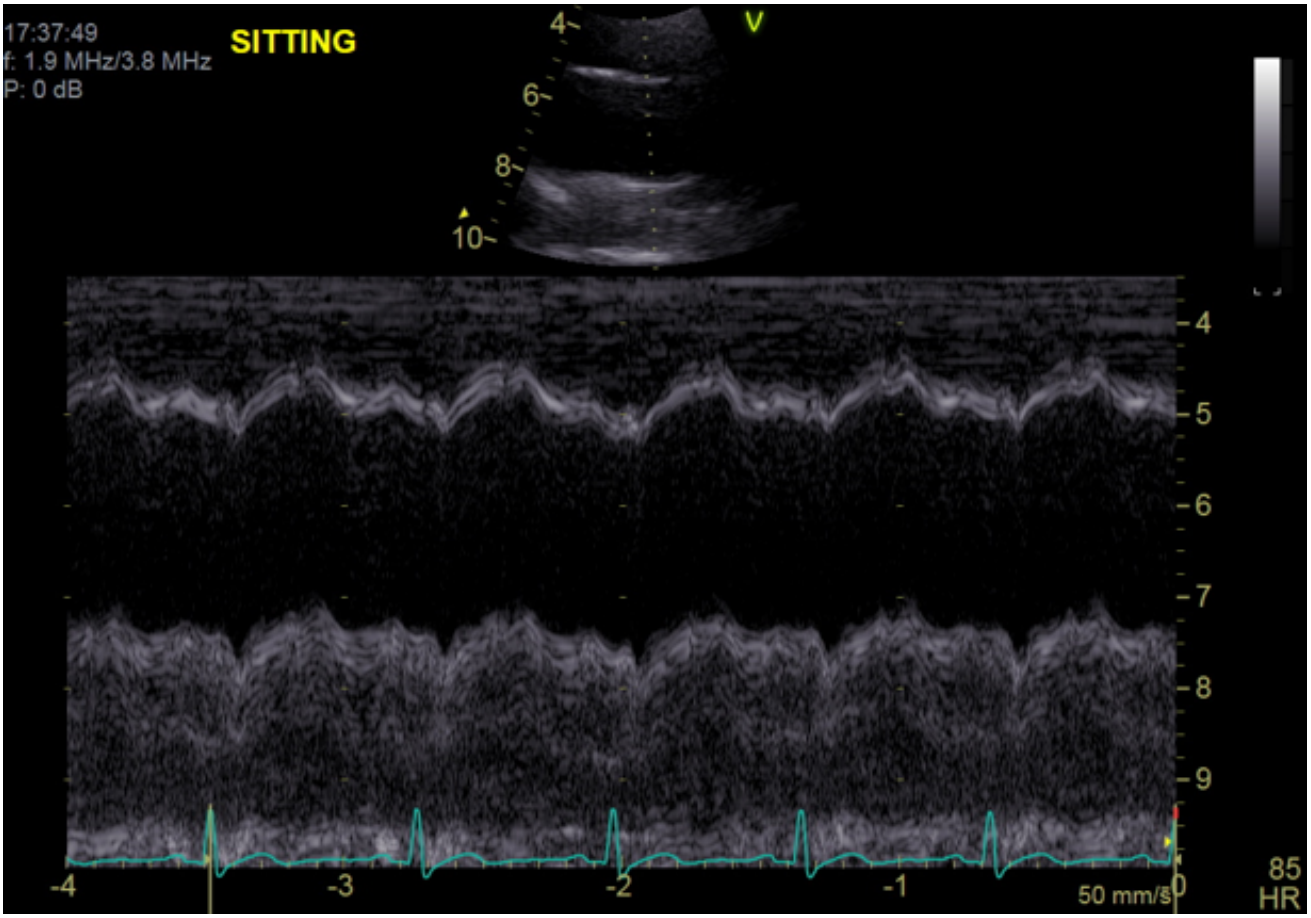


**Fig. 8.5.** – Doppler ultrasound of the ascending aorta in normal heart rate and sitting upright condition. Courtesy of Karl Q. Schwarz, MD.

The cavity observed in the m-mode is a time envelope of the movements in a single cross-section on the ascending aorta. It also synchronizes the deformations with the ECG signal, thereby a clear beat to beat response can be measured. It can be seen that there are 6 beats and thereby each pixel represents $0.14084507\ mm$ distance in this image. Traditionally, the maximum and minimum diameters in a single heart beat were measured based on the experience of medical doctors in pinpointing the correct points from the m-mode image. Here, however, an image analysis algorithm, is developed to detect the continuous diameter deformation as a function of time by counting only the image pixels inside the lumen area.

The developed algorithm takes the m-mode picture and executes the following procedure:

1. Crops it to only include the deforming aorta.

2. Puts artificial noise to the image (salt and pepper noise).

3. Blurs the image.

4. Intensifies the contrast and make it a binary black and white picture by putting a certain contrast threshold, above which the pixel is counted as white.

5. Counts columns of pixel between the two white stripes, representing the arterial lumen.

6. Smoothens the graphs, using a "sgolayfilt" filter in MATLAB.

7. Plots the diameter as a function of time in multiple cardiac cycles for each image.

The detected diameters are shown as colored stripes, as can be seen in figure 8.6.

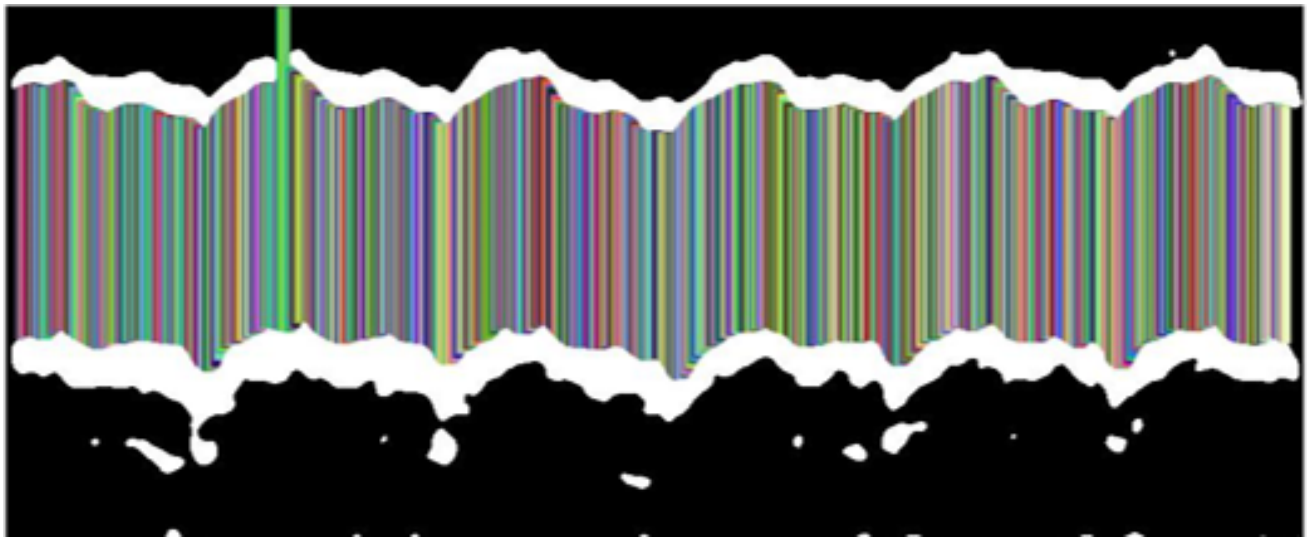

**Fig. 8.6.** – Diameter detection from processed ultrasound image.

Finally the diameter as a function of time is plotted in figure 8.7 for normal HR and sitting condition.

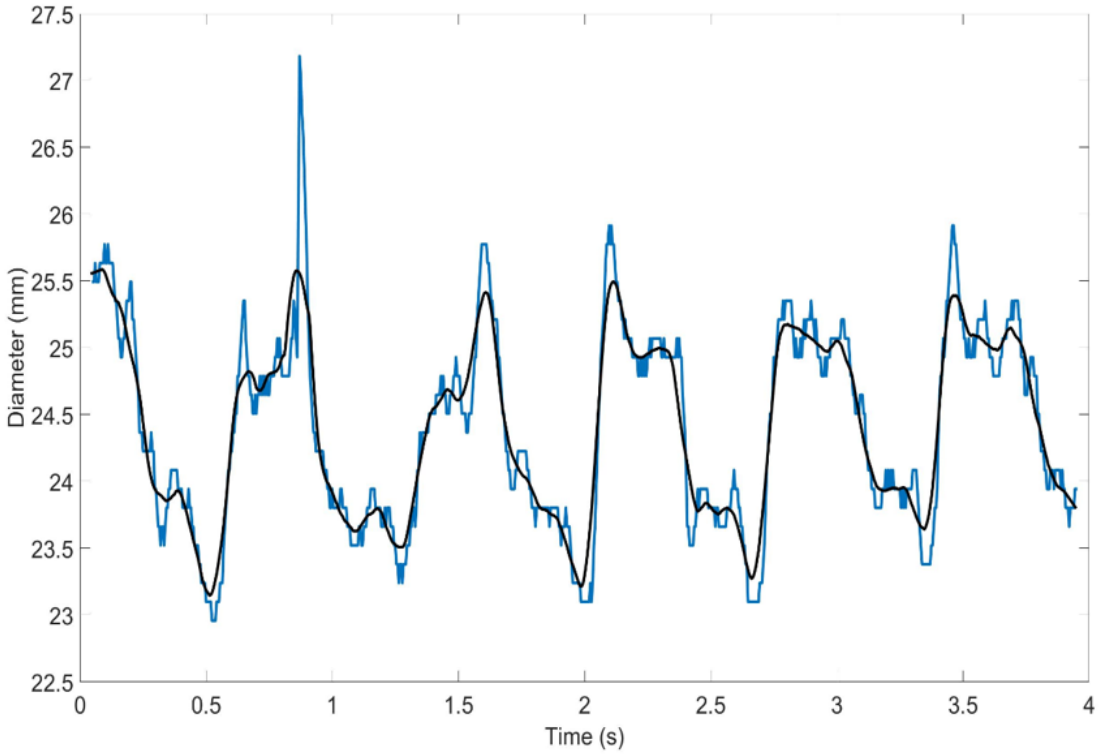


**Fig. 8.7.** – Lumen diameter as a function of time.

Lumen thickness can also be measured using this technique. In post stress condition, however, the diameters extracted using this technique become very noisy. This is due to the variable HR and the tendency of heart to bring the HR back to normal while the ultrasound measurements is still in process.

To resolve this, ensemble averaging technique is utilized on the ultrasound image over several heartbeats. This is done by, superimposing the pixel information related to variations at each heartbeat on top of each other to generate an ensemble image of a single heartbeat (see figure 8.8)

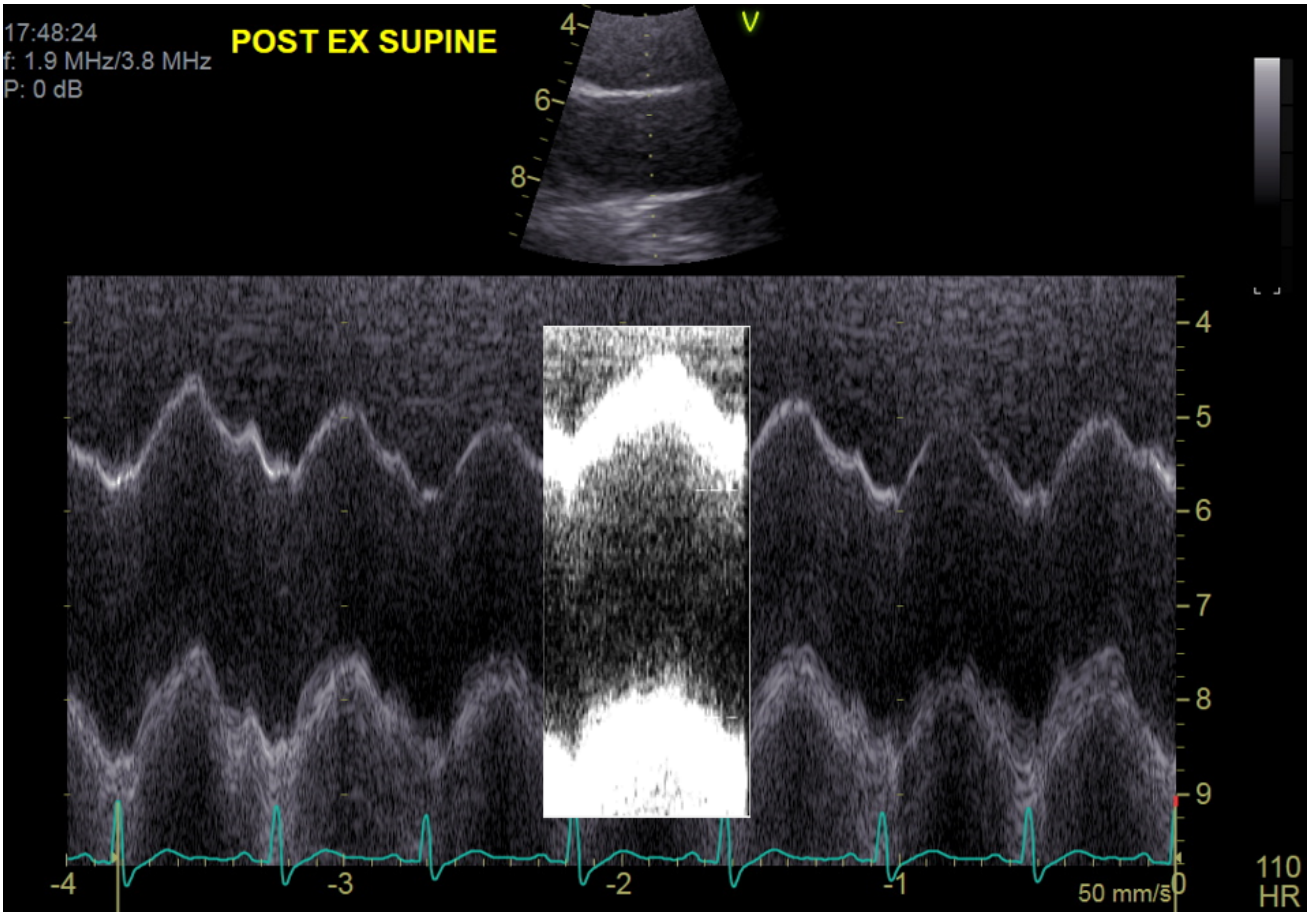


**Fig. 8.8.** – Ensemble averaged image after physical stress and in supine condition. Courtesy of Karl Q. Schwarz, MD.

Finally, the pixels will be counted and diameter change in a single heartbeat is recorded.

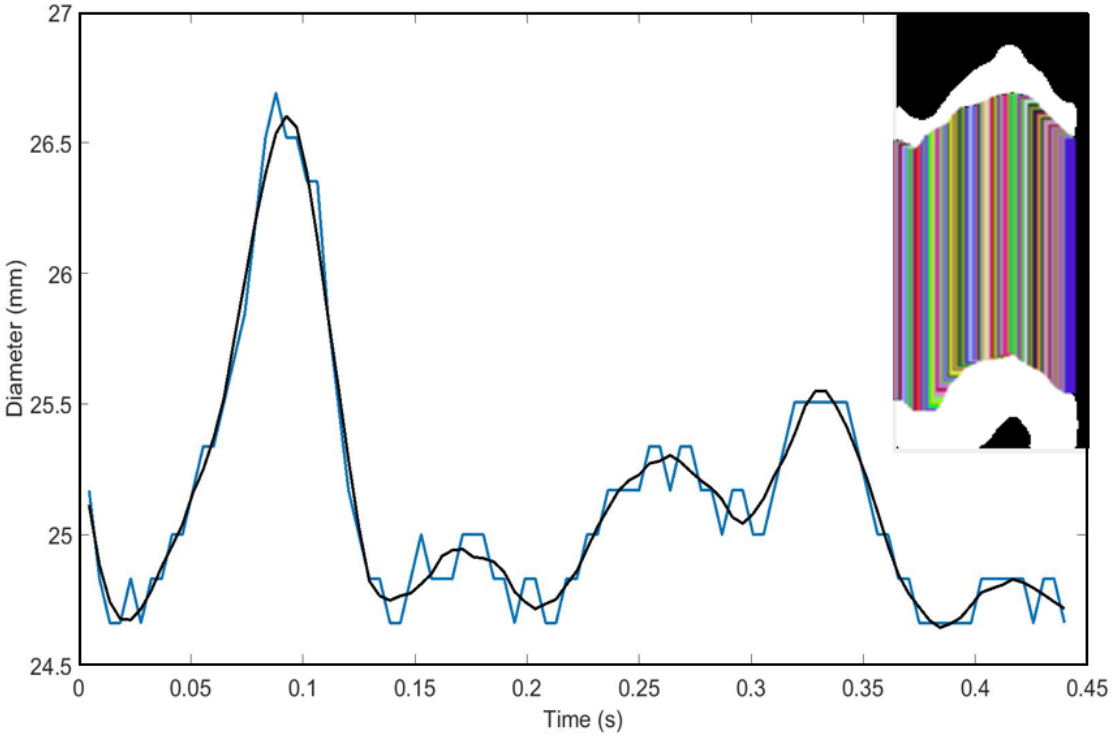


**Fig. 8.9.** – Diameter extraction from ensemble averaged picture of lumen.

In supine condition, 2 normal and two stressed (75% of max HR) ultrasound images are taken. same process is repeated in sitting condition. Meanwhile, cuff BP is also recorded. The raw data collected is stored in a github repository. For inquiries about this please contact the author [1].

In table 8.1 a summary of the data analysis results are presented.

The diameters reported in table 8.1 are the averaged values over the number of heartbeats at each image and for each recording session. For instance, the systolic diameter in normal supine condition, is a result of two doppler ultrasound images, where each contain data for 6 heartbeats. BP values are also averaged between the recordings, while there were 3 BP measurements for each recording. For instance, normal supine condition consists of two repetitions, where each repetition has three BP recordings, resulting to the BP data reported in row 1, columns 4 and 5.

[1] Contact Yashar Seyed Vahedein with your full name, affiliated institution and email address to receive a link to the raw data in Github Repository: yashar.seyed.vahedein@rit.edu

**Tab. 8.1.** – Systolic and diastolic diameter and pressure recordings for normal and physical stressed conditions. The data is reported for both supine and sitting positions.

| **HR condition & Position** | $Sys/Dia\ Diameter(mm)$ | | $Sys/Dia\ Pressure(mmHg)$ | |
|---|---|---|---|---|
| Normal Supine | 26.65 | 24.63 | 127.0 | 66.0 |
| Stressed Supine | 27.86 | 23.24 | 154.0 | 71.5 |
| Normal Sitting | 26.45 | 23.77 | 126.5 | 72.5 |
| Stressed Sitting | 27.42 | 24.75 | 144.5 | 74.5 |

This data is plotted in figure 8.10. An exponential function similar to the Fung's hyperelastic tissue model is fitted to the data from both the supine and sitting positions. Using the fit and equation 8.2, the parameters, $a,\ D_0,\ \eta$ and $E$ are calibrated for the authors body.

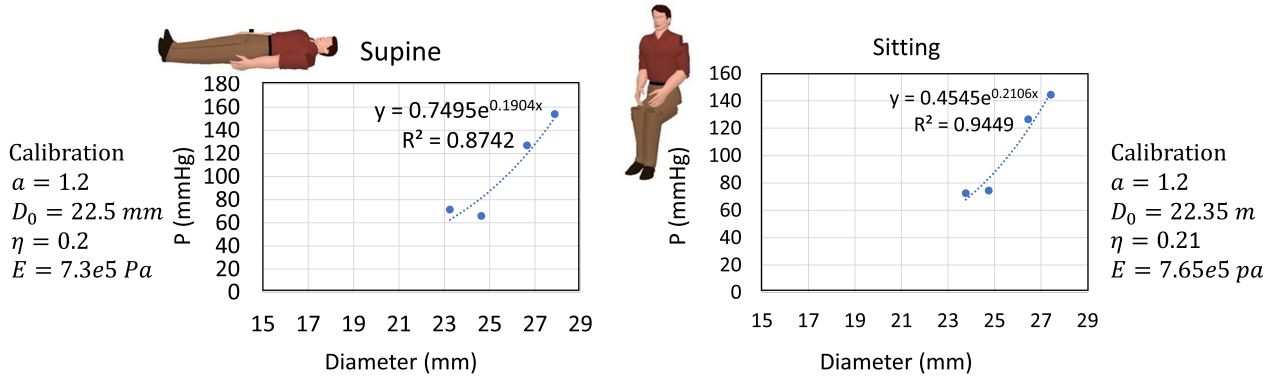


**Fig. 8.10.** – Shows pressure over diameter plots in sitting and supine condition, their exponential fits and calibrated parameters, where $a$ - is the hyperelastic coefficient, $D_0$ - pre-stress lumen diameter, $\eta = \sqrt{\frac{A}{A_0}} - 1$ - circumferential strain, and $E$ - is the tangential elasticity modulus.

This concludes the calibration of the ascending aorta diameter and properties.

#### 8.3.1.2 Extending the Geometry to Desired Arterial Path

Murray's physiological principle of minimum work [92], presents relationship between the radii of arteries immediately upstream from a branch point (parent artery), and immediately downstream (daughter arteries). In its simplest form the relationship termed Murray's law states that the radius of the parent artery cubed is equal to the sum of radii of daughter arteries cubed. Murray's original analysis was intended to determine the vessel radius

that required minimum expenditure of energy by the organism to function properly. Larger vessels need lower energy in pumping blood because the pressure drop in the vessels reduces with increasing diameter according to the Hagen-Poiseuille equation. However, larger vessels increase the overall volume of blood in the system. Minimizing the total energy, the following relationship between parent vessel diameter $D_P$ and the $i^{th}$ daughter's diameter $D_{d,i}$ was obtained in a form $D_P^3 = \sum D_{d,i}^3$. If cross sectional area is divided into *n* branches of equal size, the following relationship for the daughter vessels can be used $D_d = D_P / \sqrt[3]{n}$. The power "3" in Murray's law is very general. It has been debated by others [93], that for arterial bifurcation this number can be found based on parent diameter and is between 1 to 3.

After finding the aortic diameter from Doppler ultrasound, a branching law similar to Zamir's arterial network generation coefficients [93] is used to calculate diameters of the arteries branching out from the aorta up to the wrist. Further refinement was done using the information provided in a detailed model of the human arterial system, titled "ADAN", which is developed by Blanco *et al.* [82]. This model is used to deduce the proportions for diameters and lengths in the geometry of right and left arm arteries in a $168\ cm$ tall human male (subject_Y) and a $164\ cm$ tall female (subject_K), respectively. For subject_K, since the ultrasound imaging was not available, an additional scaling correction, with a 30% reduction of diameters based on [260], was also applied after the height adjustments to the diameters.

### 8.3.2 Windkessel Parameter Calibration and Properties Tuning

Identifying three element windkessel parameters is essential for designing a patient-specific model (Figure 8.1). These conditions are responsible for the redistribution of the flow and pressure between bifurcated branches when they will eventually be connected to the terminal Windkessel BCs (Equation 5.39, re-written here).

$$(\dot{VA})_T = \left[ \frac{\dot{P}_e}{R_c} + \frac{P_e - P_{out}}{R_c R_p C_T} - \left(1 + \frac{R_c}{R_p}\right) \frac{VA}{R_c C_T} \right]_T \tag{8.3}$$

During calibration stage upper arm BP (using commercial sphygmograph), wrist BP (using wrist sphygmograph), fingertip PPG, PTT from heart to wrist, and stroke volume (using BCG/ECG and PPG signals) are recorded. While the SV and wrist BP serve as inlet and terminal boundary conditions, respectively, the PTT and upper arm BP are used in the following minimization function to estimate the optimal values of resistance and compliances along with a correction to average $C_m k$ and hyperelastic constant $a$ in a given range.

$$\sum_{i=1}^{m} \left[ \left(1 - \frac{P_{sys,\ comp}}{P_{sys,\ meas}}\right)_i^2 + \left(1 - \frac{P_{dias,\ comp}}{P_{dias,\ meas}}\right)_i^2 + \left(1 - \frac{PTT_{comp}}{PTT_{meas}}\right)_i^2 \right] \rightarrow get\ R_{Total}, Compliance, a, C_{MK} \tag{8.4}$$

Where $m$ is the total number of measurements. The normalized errors give unified weights to each of the terms in 8.4. The combination of $C_{MK}$, $a$, $R$, and $C$ giving the lowest error is selected.

#### 8.3.2.1 Measuring ECG, BCG, and PPG with an Accessible Device

The FIT seat [261], is used to measure the ECG, BCG, PPG signals. This smart toilet seat, located in Borkholder's Lab at Rochester Institute of Technology, can capture the cardiac signals ECG/BCG/PPG as well as measure SV and PTT values while sitting in normal upright position.

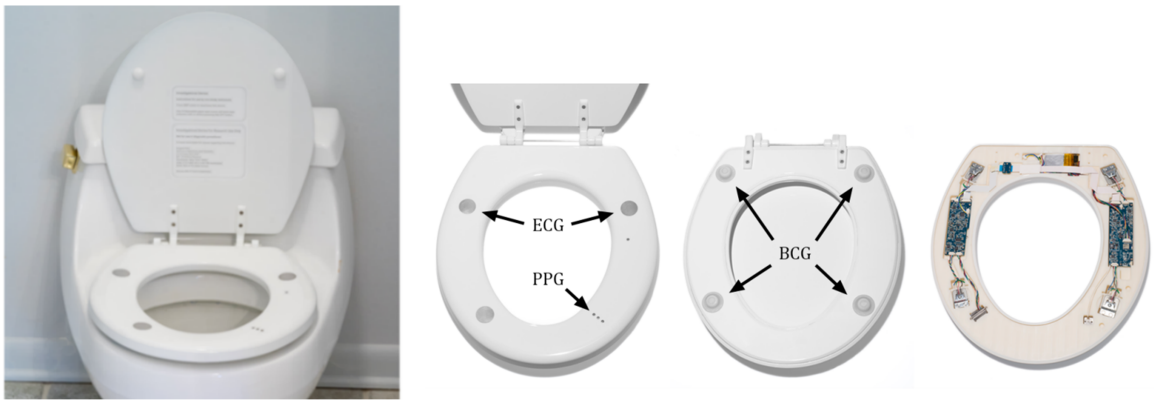


**Fig. 8.11.** – The toilet seat–based cardiovascular monitoring system can measure the electrocardiogram (ECG), photoplethysmogram (PPG), and the ballistocardiogram (BCG). Images reproduced from [22].

as described in chapter 4, electrocardiography (ECG) is a measure of the electrical activity of the heart at each cardiac cycle [166]. Ballistocardiography (BCG) is a measure of the recoil forces of the body in response to the blood ejection from the heart and blood movement through the vasculature at each cardiac cycle [167], [168]. Photoplethysmogram (PPG) is an optical measure of local blood volume variations [169]. A PPG is often obtained by using a pulse oximeter which illuminates the skin and measures changes in light absorption.

The seat is capable of measuring the SV with an accuracy comparable to the echocardiogram (echo) [22]. It is using BCG and foot of the PPG signals to measure PTT. The measurement technique is described in the patents of the FIT seat [261].

Since the PTT from heart to hand was the desired measurement path, the sensors on FIT seat were used in a specific manner. This is discussed in the next sections.

#### 8.3.2.2 Measuring Stroke Volume, PTT and Peripheral BP

The experiment was conducted in multiple recording sessions during one month. The intention was to capture day to day cardiovascular variability. Each recording session was comprised of 4-6 recordings on the FIT seat, where each recording takes 60 to 120 seconds.

Since the interest was in capturing the heart to wrist PTT, SV, wrist BP and upper arm BP, the recordings were carried out in a few iterations per session:

1. **Record ECG and BCG:** Subject is asked to sit upright to capture BCG and ECG. This allows the toilet seat to report the stroke volume.

2. **Capturing PTT:** Sitting upright, but with a 45 degree angle rotation toward left, to make PPG sensor available. The patient is asked to put their finger on PPG sensor on the seat. In the meantime, the seat is recording patient's BCG and ECG.

3. **Record arm BP while sitting:** in upright sitting pose, arm cuff BP monitoring device (BIOPAC systems inc.) is connected to the upper arm of the subject, they are then asked to put their finger on PPG sensor, while their arm BP is recorded 2 times. BCG and ECG are also recorded.

4. **Record wrist BP while sitting:** same as previous item, however, this time with wrist BP monitor (The Omron 7 Series Wrist Blood Pressure Monitor (BP652N)). BP is measured once at the heart level and 2 more times when the patient's finger is on PPG. The goal is to measure and correct the difference in BP and PTT due to the effect of gravity and the patient potentially leaning forward from upright sitting position. The BP and PTT correction procedure will be explained in the next chapter, section 9.2.

5. Repeat steps 1-4 for in post-exercise condition ($HR = 75\% max(HR)$).

Schematics of these steps are shown in figure 8.12.

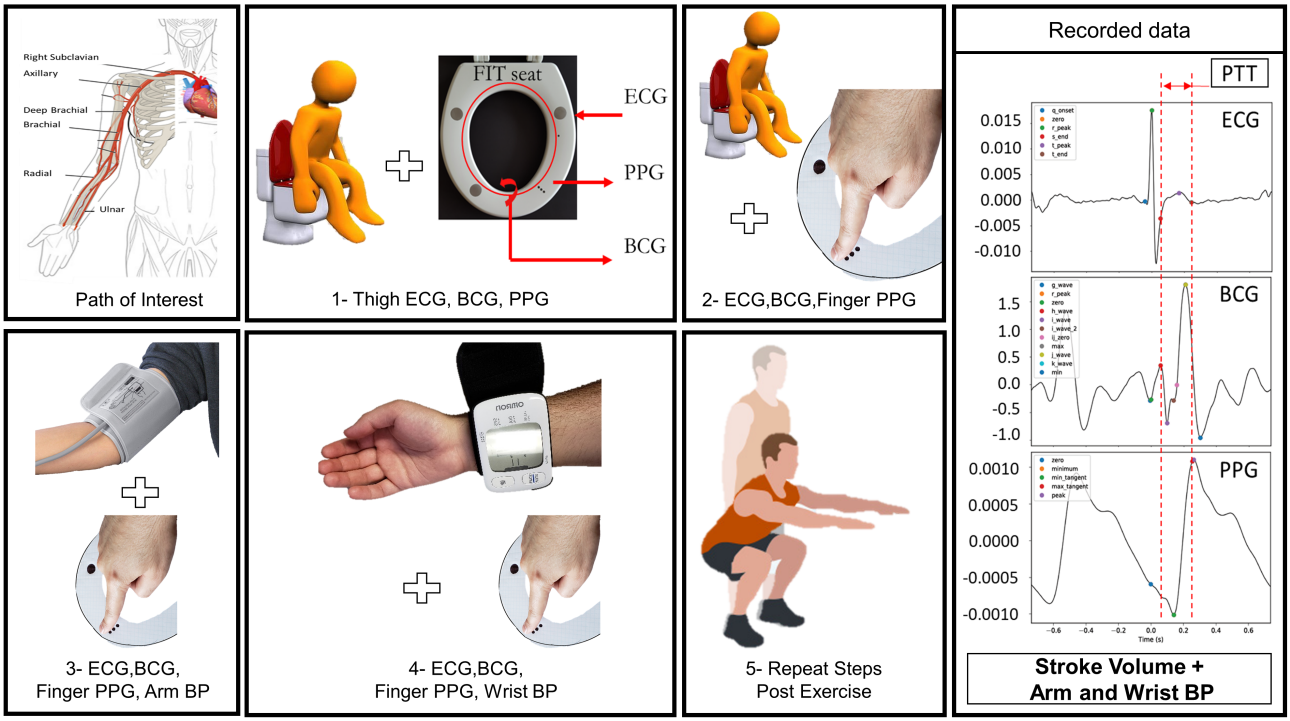


**Fig. 8.12.** – Arterial pathway of interest and the measurement steps and conditions to obtain ECG, BCG, PPG, PTT and SV.

For subject_Y (Male, 30 years old, right hand), 7 sessions of normal and stressed condition values of SV, PTT, wrist BP and Arm BP are collected, from which 4 sets are used for calibrating $R_{Total}, Compliance, a, C_{MK}$. For subject_K (Female, 24 years old, left hand), data for a total of 5 sessions were successfully recorded, from which 3 are used for calibration. It should be noted that the recorded data for subject_K demonstrated larger variations compared to subject_Y.

#### 8.3.2.3 Calibration of 1D Code with the Measured Data

The recorded and analyzed data, in section 8.3.1, is used to define patient-specific geometry and segment properties for the numerical model in CardioFAN. Arterial segment lengths, vessel wall properties, such as tangential elasticity modulus and Fung's hyperelastic tissue coefficient in the numerical model can now be defined.

After prescribing the geometric and arterial properties into the numerical model, the next step is to use SV and wrist BP obtained from the seat to close the terminal BCs of the 1D model. Table 8.2 shows 4 sets of SV, HR, BP and PTT data for subject_Y (Male 30) and 3 sets for subject_K (Female 24), used for calibration.

**Tab. 8.2.** – For subject_Y, four of the recorded data sets are selected for calibration. These are the data sets with minimum, maximum and mid-points of PTT. For subject_K three sets of data sets are selected. This table reports the SV: stroke volume, HR: heart rate, BP: blood pressure at the wrist and arm for each of these PTTs. Data for Subjects Y and K corresponds to right and left arm recordings, respectively.

| **DATA SET** | $PTT(ms)$ | $SV(mL)$ | $HR(beats/min)$ | $WristBP(mmHg)$ | | $ArmBP(mmHg)$ | |
|---|---|---|---|---|---|---|---|
| | | | | SYS | DIA | SYS | DIA |
| SubY_MIN | 0.1385 | 61.86 | 81 | 139 | 82 | 135 | 80 |
| SubY_MID1 | 0.1511 | 60.35 | 87 | 139 | 88 | 133 | 80 |
| SubY_MID2 | 0.1523 | 69.07 | 91 | 141 | 84 | 136 | 77 |
| SubY_MAX | 0.1790 | 56.03 | 77 | 138 | 84 | 133 | 82 |
| SubK_MIN | 0.1743 | 40.32 | 87 | 89 | 49 | 101.0 | 64 |
| SubK_MID | 0.1776 | 37.75 | 73 | 107 | 49 | 103.5 | 64 |
| SubK_MAX | 0.1957 | 38.54 | 90 | 94 | 52 | 99.0 | 65 |

The PTT is corrected to account for effect of gravity. The correction procedure is explained in chapter 9. To make the calibration faster a first guess for resistance and compliance at the outlet is provided using the approximation technique used by Xiao *et al.* [67]. The resulting resistance and compliance values are used as a first guess and calibration is carried out by tuning multipliers to these initial values; These initial values are found using the following equations:

$$
\begin{aligned}
P_m &= P_{dia} + \frac{1}{3}\left(P_{sys} + P_{dia}\right) = 97 \;\; [mmHg] \\
R_T &= \frac{(P_{mean} - P_{out})}{(\overline{Q_{in}})} = 0.015934 \;\; [(mmHG.Min)/mL] \\
R_{conduit} &= \frac{(\rho C_{mk})}{A_{diastolic}} = 0.00174 \;\; [(mmHG.Min)/mL] \\
R_{periphery} &= R_T - R_c = 0.01419 \;\; [(mmHG.Min)/mL] \\
C_T &= \frac{(timeofdiastolicdecay(\tau))}{R_T} = 18.828 \;\; [mL/mmHg]
\end{aligned}
\tag{8.5}
$$

The geometry of the calibrated networks are shown in figure 8.13 for both test subjects. Table 8.3 shows the properties for each of the heart to right arm arteries for subject_Y. Doppler ultrasound data for subject_K was not available, therefore, thus the geometrical properties were estimated based on the correlation between arterial diameter and sex/age as published in [262].

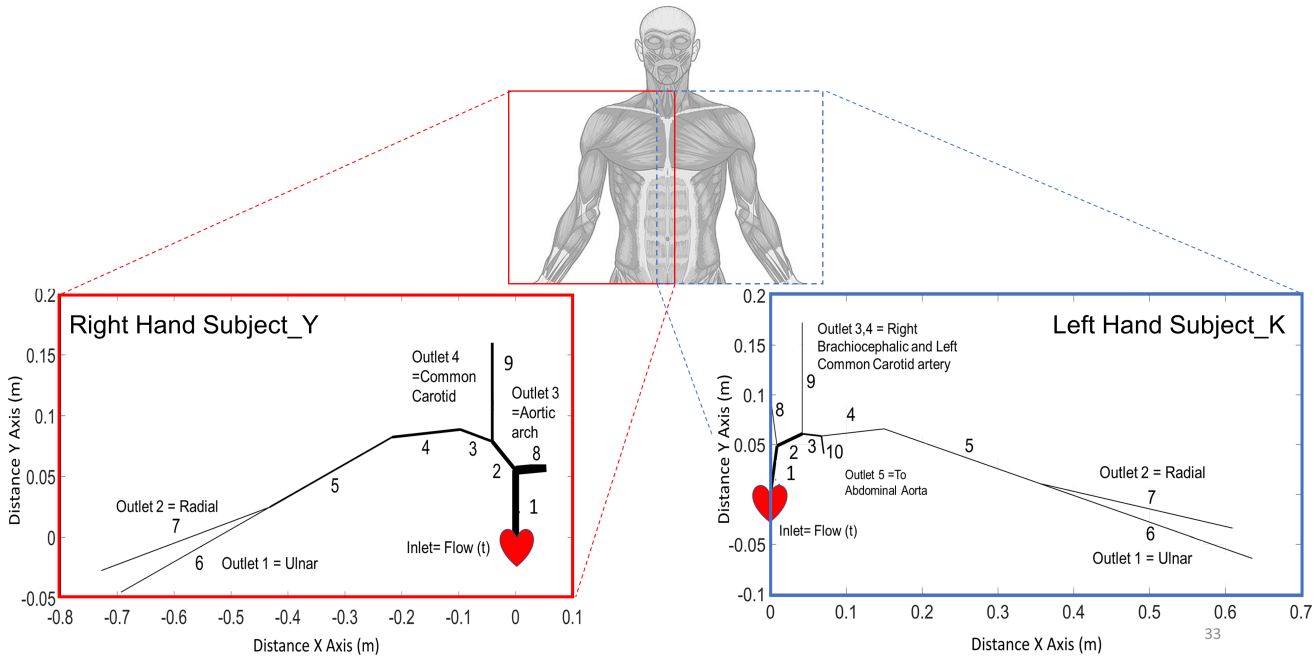


**Fig. 8.13.** – Arterial pathway of interest drawn automatically in CardioFAN. Inlets and outlets are highlighted. Upper image corresponds to the right and lower image to the left arm arteries.

**Tab. 8.3.** – Arterial segment names and properties.

| **Artery ID-name** | Length (mm) | Radius (mm) | | $C_{MK}(m/s)$ | Inlet | Outlet |
|---|---|---|---|---|---|---|
| | | $Seg_IN$ | $Seg_OUT$ | | | |
| 1-Ascending Aorta | 55.00 | 11.25 | 11.00 | 4.69 | $Flow(t)$ | 135 |
| 2-Brachiocephalic | 47.40 | 6.16 | 6.73 | 4.69 | - | - |
| 3-Subclavian | 56.90 | 4.89 | 2.30 | 4.69 | - | - |
| 4-Axillary | 120.00 | 2.30 | 2.08 | 4.69 | - | - |
| 5-Brachial | 223.00 | 2.08 | 1.83 | 4.69 | - | - |
| 6-Ulnar | 270.00 | 1.41 | 0.70 | 4.69 | - | $R_T/(1.4\%)$ |
| 7-Radial | 300.20 | 1.40 | 0.75 | 4.69 | - | $R_T/(1.0\%)$ |
| 8-Aortic Arch | 54.00 | 11.00 | 10.50 | 4.69 | - | $R_T/(84.7\%)$ |
| 9-Common Carotid | 81.25 | 3.32 | 4.47 | 4.69 | - | $R_T/(13\%)$ |

Based on the Murray's law of minimum work, the contribution of each outlet to the total resistance can be related to the amount of flow to each outlet branch. This will result to the following distribution of total resistance between outlets: $ulnar: R_T/(1.4\%)$, $radial: R_T/(1.0\%)$, $aorta: R_T/(84.7\%)$, $carotid: R_T/(13\%)$ for subject_Y

and $ulnar : R_T/(1.4\%),\ radial : R_T/(1.0\%),\ RBrachiocephalic : R_T/(1.0\%),\ aorta : R_T/(69.1\%), Lcarotid : R_T/(5.2\%)$. Since the upstream vessels are healthy the total resistance is mostly attributed to the terminal branches. Similar percentages are applied to the total compliance values. This assumption might not be valid when there are upstream occlusions. In that scenario a more time-consuming terminal resistance calibration with a wider range of initial guess tuning will be required.

**Calibration Algorithm:** The calibration of $R_{Total}, Compliance, a, C_{MK}$ is carried out by minimizing the equation 8.4 with recorded arm BP and PTT data. This algorithm solves the PDEs nearly 5000 times with different values of $R_{Total}, Compliance, a, C_{MK}$. The total time for a full calibration is nearly 1 day and a calibration with good initial guesses takes approximately 8 hours. The algorithm is designed such that it can bypass and report errors during calibration. This optimization algorithm is attached to CardioFAN and while it is not open source, it is stored in a private github repository. for inquiries about this please contact the author [2].

Final steps of the calibration are carried out as follows:

1. For each of the 4 data sets, the diastolic BP at the wrist is imposed at the outlet.

2. Flow waveform amplitude is tuned for each calibration data set in such a way that with the given the $HR$, it would generate a SV equal to the experimentally recorded SV.

3. The systolic and diastolic value at each data set is used for calibration.

4. The PTT at each data set is used for calibration.

5. Each parameters of interest are varied iteratively amounting to 3000-4000 calibration iterations, for each calibration data set.

6. calibrated values of desired parameters are the following for subject_Y: $averagedC_MK = 4.69m/s$, $a = 4.00$, $R_multiplier = 1.40, C_multiplier = 3.00$. For subject_K they are: $averagedC_MK = 2.82m/s$, $a = 0.33$, $R_multiplier = 1.00, C_multiplier = 0.67$.

[2] Contact Yashar Seyed Vahedein with your full name, affiliated institution and email address to request a link to the calibration algorithm and raw PPG/PTT/SV/ECG/BCG data stored in a Github Repository: yashar.seyed.vahedein@rit.edu

In the next chapter a more detailed analysis of the gravity related corrections to the calibration data is presented. In addition, success of the inverse reconstruction method is evaluated by presenting the results of its validation against the recordings from the FIT seat and upper arm cuff BP monitor.

# 9

# Noninvasive PTT-Based Central BP and Cardiac Output Measurement - Part 3: Validation with Human Subject Data

## 9.1 Introduction

Chapter 5 was dedicated to the development and validation of a robust reduced-order modeling framework for blood flow and pulse wave propagation in the human arteries. In chapter 6, some of the applications of this framework were discussed, which led to chapter 7 describing its application in numerically calculating the pulse transit time and proximal signals. It was shown that CardioFAN is capable of inversely reconstructing the flow and pressure waveforms in proximal locations in an environment were the blood vessel properties and boundary conditions are known, *i.e.* a well-controlled manufactured scenario. In chapter 8, an accessible calibration methodology (summarized in figure 9.1) is introduced to make CardioFAN a patient-specific platform measuring cardiac output along with central and peripheral blood flow/pressure signals.

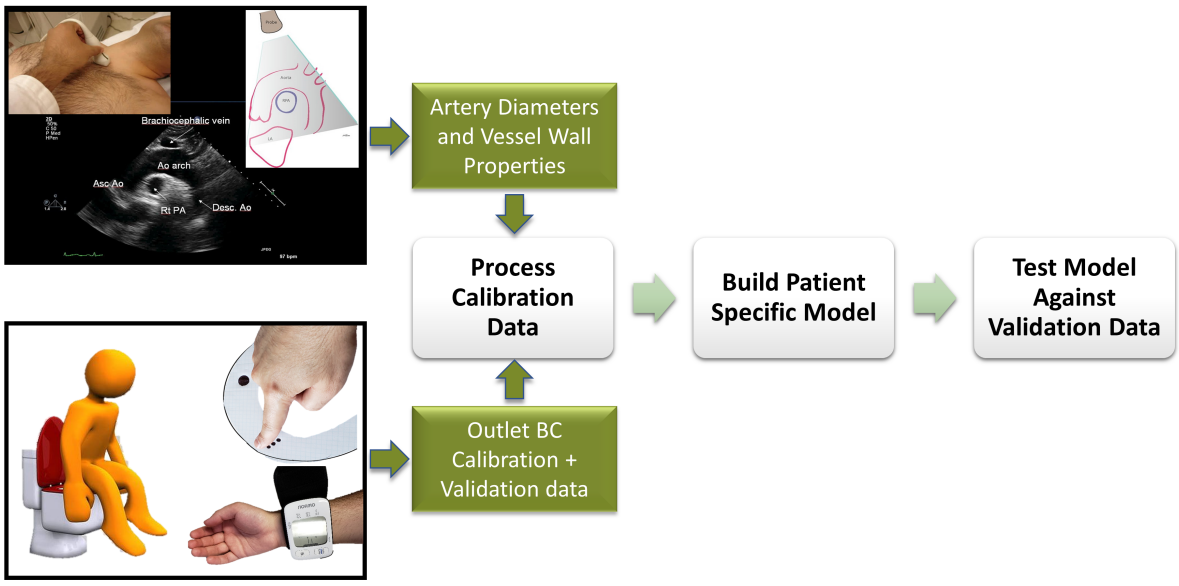


**Fig. 9.1.** – Summarizing the calibration sessions performed to make CardioFAN patient-specific.

In this chapter, first we look at the calibrated data from PTT and BP calibration session with FIT seat and describe the literature-based modifications needed in order to account for gravity and body posture. The extra recordings for validation purposes are demonstrated, and the proposed method of inversely reconstructing these recordings using the calibrated CardioFAN is explained. BP, PTT and cardiac output results from both the clinical experiment and numerical work are plotted against each other and the accuracy of proximal waveform prediction is investigated. Implementation of this algorithm into other wearable devices with ECG,BCG and PPG sensors, as well as its clinical implications and current limitations are explained.

## 9.2 Data Acquisition and Effect of Gravity on PTT and BP

BP and PTT changes as a function of height are reported by Thomas *et al.* [263] as well as Liu *et al.* [264]. Liu *et al.* investigated the effect of limb height on PTT and BP. with continuous measurements, they showed high correlation between PTT, BP and height. They measured PTT as the time interval from the peak of the ECG R-wave to upstroke of PPG signal in the same cardiac cycle. BP was measured on the patient's wrist and arm using Omron HEM-907 and National EW280, respectively. The patient was asked to change the location of their limb for each recording session. Increased(decreased) PTT and decreased (increased) radial BP with the

rising(falling) height were observed during the hand elevation process. This study provided insight on the PTT variation when limb position is at different elevations with respect to the heart. In a 2016 study by Thomas *et al.*, a watch-shaped device is used to measure ECG and PPG, and thus PTT. They also provide BP and PTT data on the wrist as a function of wrist elevation relative to the heart. A model is also proposed to predict this relationship. Both of these studies also refer to a pioneering work by Poon *et al.* [183], where they show the consistent effect of the hydrostatic component on PTT.

As described in chapter 8, the second calibration experiment is conducted in a sitting position, and therefore, knowing the implications of hydrostatic effect is important for the work presented here. The reported PTT is for a subject that was asked to sit upright while their finger was on the PPG sensor, located on the seat close to their thighs. In this scenario the blood pressure (BP) at the wrist will be elevated due to it's lower elevation compared to heart. This difference in BP from its original value without the effect of gravity can be approximated by $P_{elevation} = \rho g h$ [264]. The data reported by aforementioned literature were used to form a correlation between elevation and change in PTT. Mean arterial pressure (MAP) and PTT data is taken from [263] for different elevations of the wrist and translated into pressure and PTT variations. These variations are plotted against each other in figure 9.2 showing a nearly linear correlation.

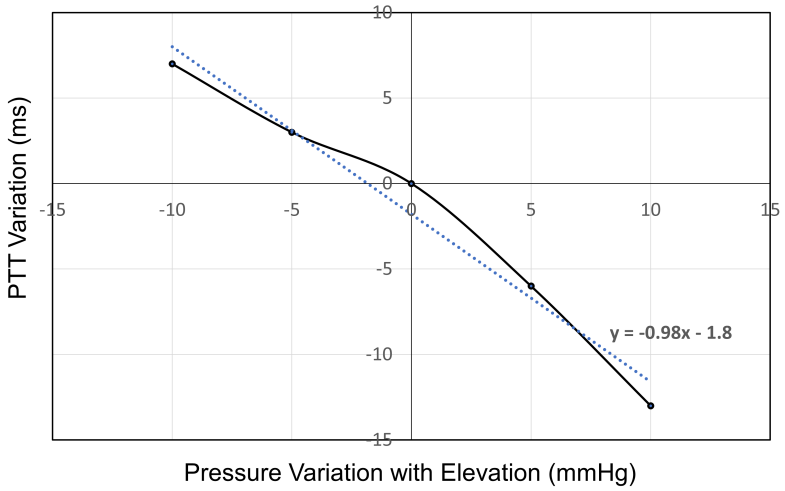


**Fig. 9.2.** – Change in PTT as a function of hydrostatic pressure variations $P_{elevation} = \rho g h$.

In the calibration procedure presented in this work, the wrist BP at the heart and seat levels are both recorded, thus heart and seat level MAP can also be calculated; when subtracted, they produced BP variation as a function

of height, $\Delta BP = MAP_{seatlevel} - MAP_{heartlevel}$. The PTT variation can be captured by using the linear fit equation shown in figure 9.2. This results in a correction to each of the original PTT values recorded by FIT seat, to negate the effect of height difference. Original PTT, wrist and arm BP, SV, HR and corrected values of PTT for FIT seat-based calibration and extra data acquisition are shown in table 9.1.

**Tab. 9.1.** – Recorded data during human subject tests with FIT seat. Here $PTT$ refers to pulse transit time, $HC$ - height correction, $SV$ - stroke volume, $HR$ - heart rate, $W$ - wrist, $A$ - arm, $MAP$ - mean arm pressure, $MWP$ - mean wrist pressure.

| **Test ID** | $PTT(ms)$ | $PTT_{HC}(ms)$ | $SV(mL)$ | $HR(\frac{b}{min})$ | $W\ BP(mmHg)$ | | | $A\ BP(mmHg)$ | | |
|---|---|---|---|---|---|---|---|---|---|---|
| | | | | | SYS | DIA | MWP | SYS | DIA | MAP |
| Y_EL_9 | 0.1262 | 0.1477 | 59.1615 | 103 | 145 | 85 | 105 | 137 | 77 | 97 |
| Y_RE_9 | 0.1340 | 0.1498 | 52.6121 | 99 | 141 | 91 | 108 | 134 | 79 | 97 |
| Y_EL_10 | 0.1245 | 0.1385 | 61.8648 | 81 | 139 | 82 | 101 | 135 | 80 | 98 |
| Y_Re_11 | 0.1419 | 0.1620 | 56.2727 | 73 | 135 | 81 | 99 | 133 | 78 | 96 |
| Y_EL_13 | 0.1402 | 0.1523 | 69.0719 | 91 | 141 | 84 | 103 | 136 | 77 | 97 |
| Y_Re_13 | 0.1433 | 0.1591 | 58.1251 | 86 | 136 | 79 | 98 | 133 | 79 | 97 |
| Y_Re_14 | 0.1415 | 0.1511 | 60.3555 | 87 | 139 | 88 | 105 | 133 | 80 | 98 |
| Y_EL_14 | 0.1440 | 0.1649 | 58.9557 | 80 | 138 | 83 | 101 | 131 | 82 | 98 |
| Y_Re_15 | 0.1630 | 0.1790 | 56.0348 | 77 | 138 | 84 | 102 | 133 | 82 | 99 |
| K_EL_1 | 0.1470 | 0.1743 | 40.3204 | 87 | 89 | 49 | 62 | 101 | 64 | 76 |
| K_RE_1 | 0.1520 | 0.1760 | 37.1607 | 77 | 102 | 60 | 74 | 105 | 73 | 84 |
| K_RE_2 | 0.1490 | 0.1776 | 37.7510 | 74 | 107 | 49 | 68 | 103 | 64 | 77 |
| K_EL_2 | 0.1610 | 0.1850 | 39.5915 | 92 | 96 | 58 | 71 | 106 | 69 | 81 |
| K_RE_3 | 0.1660 | 0.1957 | 38.5447 | 91 | 94 | 52 | 66 | 99 | 65 | 76 |

The data used for second calibration procedure was previously shown in table 8.2, and can be seen among the raw data obtained, table 9.1. Apart from the data points used for calibration, the rest will be used only to evaluate inverse reconstruction accuracy. Here, arm BP(proximal) and cardiac output ($SV \times HR$) are used for validating the results, while wrist BP (peripheral) and PTT are used as inputs to the calibrated model.

### 9.2.1 Experimental BP, PTT and CO Recordings

Relationship between the PTT and BP values are commonly demonstrated as a direct relationship described in linear, inversely linear or logarithmic forms, as demonstrated in section 4.3. In this experiment, however, it can be seen that at some data points equal BP values exist while PTT varies (Figure 9.3). This cannot be explained with the previous direct relationships between PTT and BP.

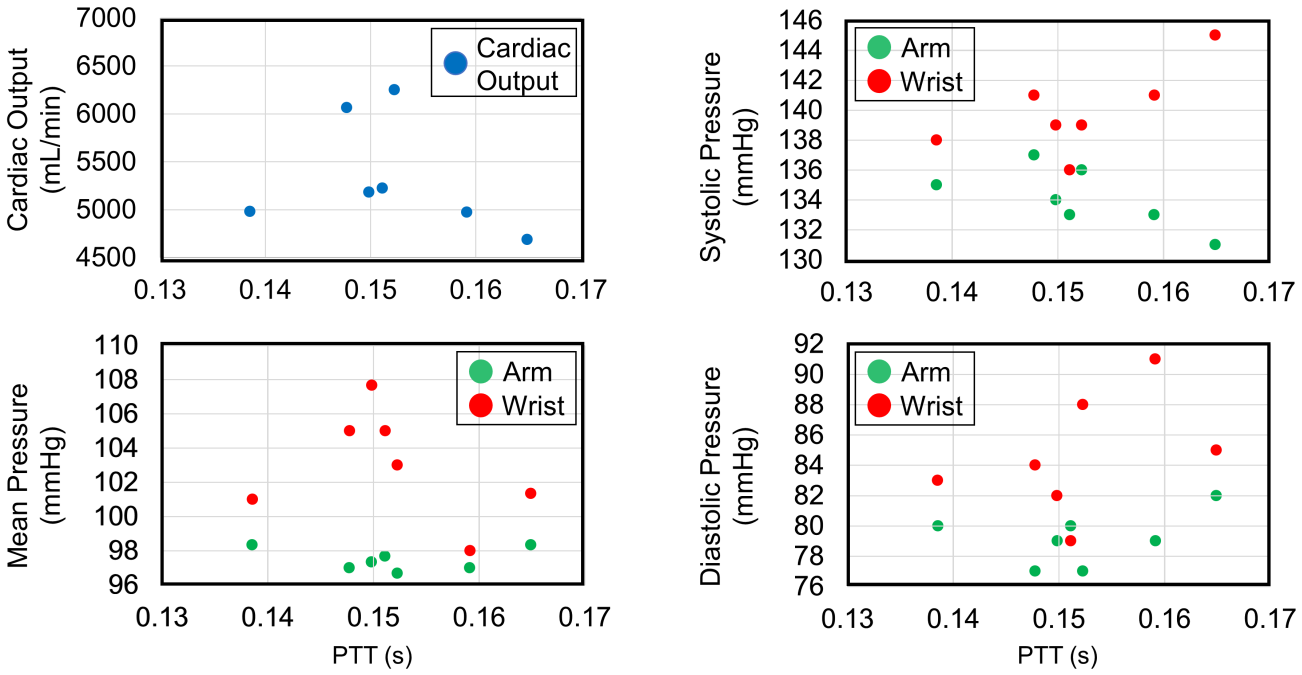


**Fig. 9.3.** – Measured cardiac output, systolic/diastolic/mean arm and wrist BP, each as a function of PTT measured.

As can be seen in figure 9.3, two very different PTTs can exist for the same value of arm BP (*i.e.* the validated pressure). For instance, Mean BP of approximately $97\ mmHg$ is measured for both $PTT = 0.15\ s$ and $PTT = 0.159\ s$. Looking at the cardiac output for the same PTTs, this difference can be attributed to the cardiac output differences ($5182\ mL/min$ for $PTT = 0.15\ s$ and $4969\ mL/min$ for $PTT = 0.159\ s$). These results suggest that PTT and BP relationship are more nonlinear than previously predicted. This agrees with previous findings of [184] and [192]. In addition to cardiac output the presented calibration and analysis technique accounts for total terminal resistance and compliance.

## 9.3 Inverse Reconstruction of Numerical BP, PTT, CO

The two-step calibration procedure (sections 8.3.1 and 8.3.2) provides a personalized CardioFAN algorithm. The calibrated vessel wall properties, average speed of pulse propagation $C_{MK}$, and the windkessel parameters, are all imposed inside the inverse reconstruction technique as known input parameters. Therefore, the only value that is not fully known is cardiac output to close the model. Eventually, cardiac output as well as proximal BP values, such as BP measured with the arm cuff BP monitor, are the parameters that we seek to compare against clinically measured values.

### 9.3.1 Considerations

**SV, HR and Cardiac Output:** The method used here is very similar to section 7.3. A generic flow profile is used at the inlet of the calibrated model, which corresponds to a specific SV and the cardiac cycle length (*i.e.* HR). Changing the magnitude and period of this generic profile, the numerical cardiac output can be controlled. During the calibration, the period and magnitude of the flow profile were kept fixed to specify a known cardiac output. However, for inverse problem, they are used as variable parameters to give us a range of solutions. In other words, using the flow waveform specified for the calibration as a reference, the flow waveform magnitude and cycle period are changed 20-30% above and below the reference point to encapsulate the range of available cardiac output recordings [265].

**Auto Regulation:** In human body, an acute increase in arterial BP causes immediate rise in blood flow, however, the blood flow returns almost to the normal level in less than a minute, even in instances that the BP remains elevated. This automatic control for flow forcing it towards the normal state is called auto-regulation [24]. This mechanism is triggered by various reasons, such as intrinsic myogenic tone, endothelial cell signaling and neuro-humoral control [266], which result to changing the microvascular resistance by vasodilation or vasoconstriction mechanisms, thus regulating the overall blood flow. The test protocol for this study, appendix C, requires the subject to stay seated more than a minute in order to have accurate reading of their SV and PTT, surely triggering the auto-regulation effects. Although windkessel parameters are previously calibrated for the test subjects of this work, auto-regulation can amount to changes post exercise or in normal day by day changes in aortic BP and stroke volume; all depending on the physical, emotional and mental state of the subjects [267]. The inverse solution procedures requires the change in terminal BP according to the obtained wrist cuff BP monitor recordings. Therefore, the calibrated model is also run with variations in minimum to maximum diastolic terminal BPs

$(79 - 91mmHg)$. A second variation may also be introduced on the calibrated value of total resistance at the outlet; changing it $\pm 20\%$ in order to capture auto-regulation effects.

**Exact Terminal Boundary at the Wrist:** Two methods of assigning boundary conditions at the wrist are used in this study. Method WK, uses Windkessel resistance and compliance parameters at the ulnar and radial artery at the wrist. Method $P_{out}$, fits a wrist BP waveform picked from [14] to the recorded systolic/diastolic values of BP with a similar HR. These can be viewed in figure 9.4.

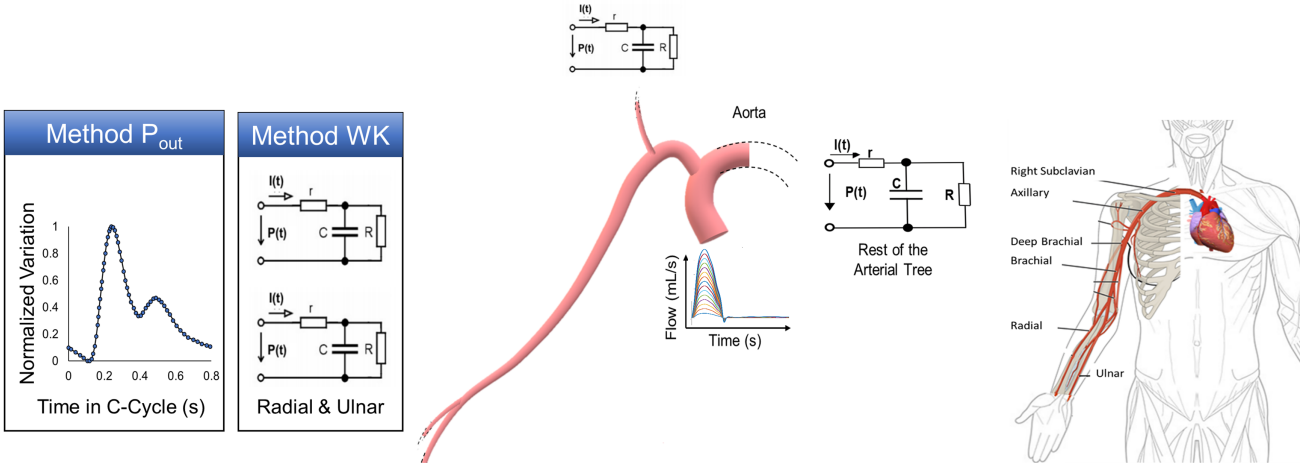


**Fig. 9.4.** – Terminal boundary conditions for heart to wrist geometry, showing WK and $P_out$ methods.

These two methods each come with benefits and limitations. Method WK is more universal and can be applied to inverse problem cases where other parameters rather than peripheral BP are known. It can also take into account the auto-regulation effects at the wrist. In contrast, while not being universal, exact systolic/diastolic BP waveform at the wrist closes terminal BCs at the wrist without the need for resistance and compliance calibration, and thus it is faster.

## 9.4 Results and Discussion

Result of solving PDEs with the varying inlet and outlet BCs is a pool of data points associated to the test subject. These data points represent subject's carotid, wrist, arm and aortic BP in addition to the cardiac output and PTT from heart to wrist. This data consist of stressed (elevated HR) and normal condition signals for the heart to wrist

network of arteries. This pool of data points are presented as 2D plots over the calculated PTT for subject_Y (figure 9.5).

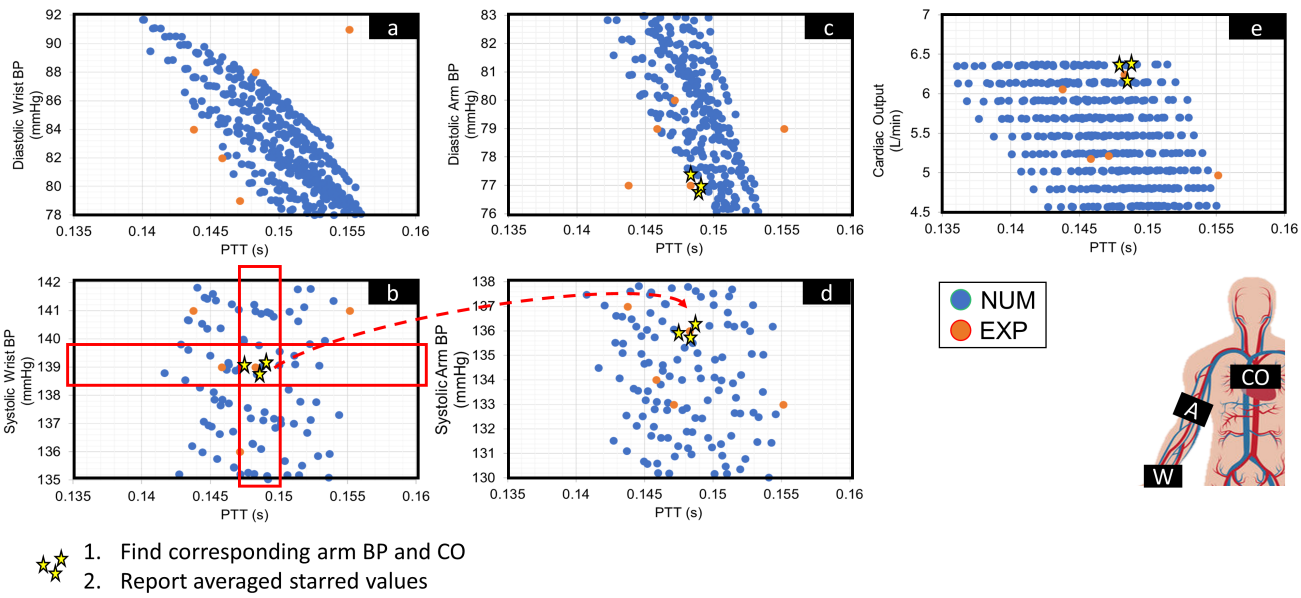


**Fig. 9.5.** – Numerically calculated Systolic/diastolic BP at the wrist (a,b), arm (c,d) and cardiac output (e) each as a function of PTT measured. Stars inside the red square refer to selected data points at the periphery (wrist) during the scanning method, and the stars in Systolic/Diastolic BP and cardiac output refer to the corresponding numerically predicted points based on peripheral (wrist) PTT and BP data.

As previously mentioned, the wrist BP and heart to wrist PTT will be treated as control parameters in order to find the correct proximal BP or cardiac outputs among the pool of numerical results. All the numerical data points are stored in a $.mat$ format. A scanning MATLAB algorithm is written that can go through all the numerical data points and identify/interpolate the numerical PTT and wrist BP values closest to the measured data,the starred points inside the red region in figure 9.5b. It can then report the corresponding arm BP and cardiac output along with an estimation error, starred points in figure 9.5c,d,e. The algorithm is part of the extended inverse reconstruction add-on for CardioFAN, which is not available in open-source format at the moment.

### 9.4.1 Compare Predicted SV, and Arm BP with Measured Values

Figures 9.6 and 9.7 shows the BP and cardiac output predictions as a function of different recording sessions, for Lax-Wendroff based and TVD-based CardioFAN. Each is associated with a unique PTT and HR. Using the

aforementioned scanning algorithm, predicted parameters are compared with the corresponding measured values and individual errors as well as the mean prediction errors are reported as a table underneath the figures.

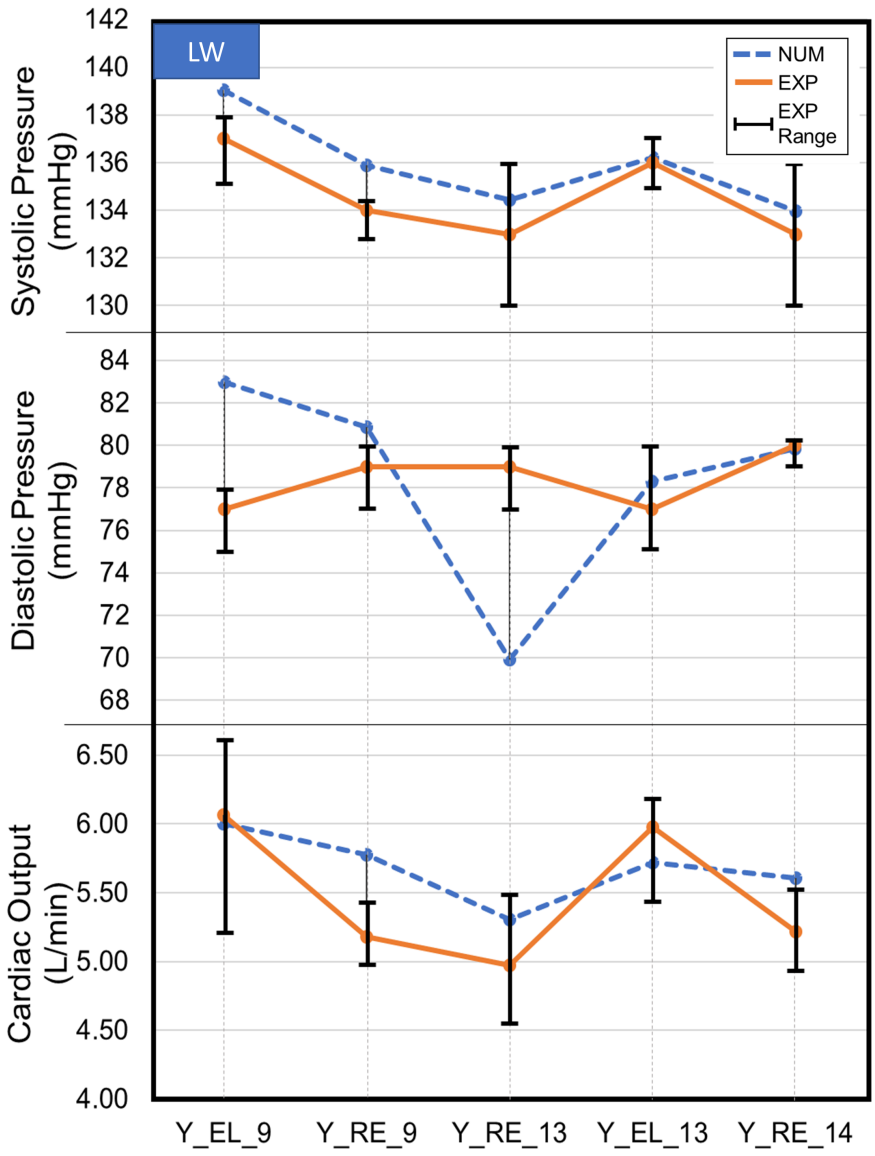


Measurement Session Data and Prediction Error

| Session | PTT (s) | HR | Err-SYS(%) | Err-Dia (%) | Err-CO (%) |
|---|---|---|---|---|---|
| Y_EL_9 | 0.1478 | 103 | 1.50 | 7.75 | 1.01 |
| Y_RE_9 | 0.1498 | 99 | 1.42 | 2.35 | 11.47 |
| Y_EL_13 | 0.1523 | 91 | 0.15 | 1.72 | 4.23 |
| Y_RE_13 | 0.1591 | 86 | 1.09 | 11.49 | 6.78 |
| Y_RE_14 | 0.1511 | 87 | 0.72 | 0.21 | 7.44 |
| | | **Mean Err** | 0.97 | 4.70 | 6.19 |

**Fig. 9.6.** – Cardiac output and upper arm (systolic/diastolic) blood pressure. Inversely reconstructed values (dotted blue line) against experimental measurements (solid orange line). Table demonstrates data associated with each session and the individual and average prediction errors.EL: elevated HR, RE: resting HR, CO: cardiac output.

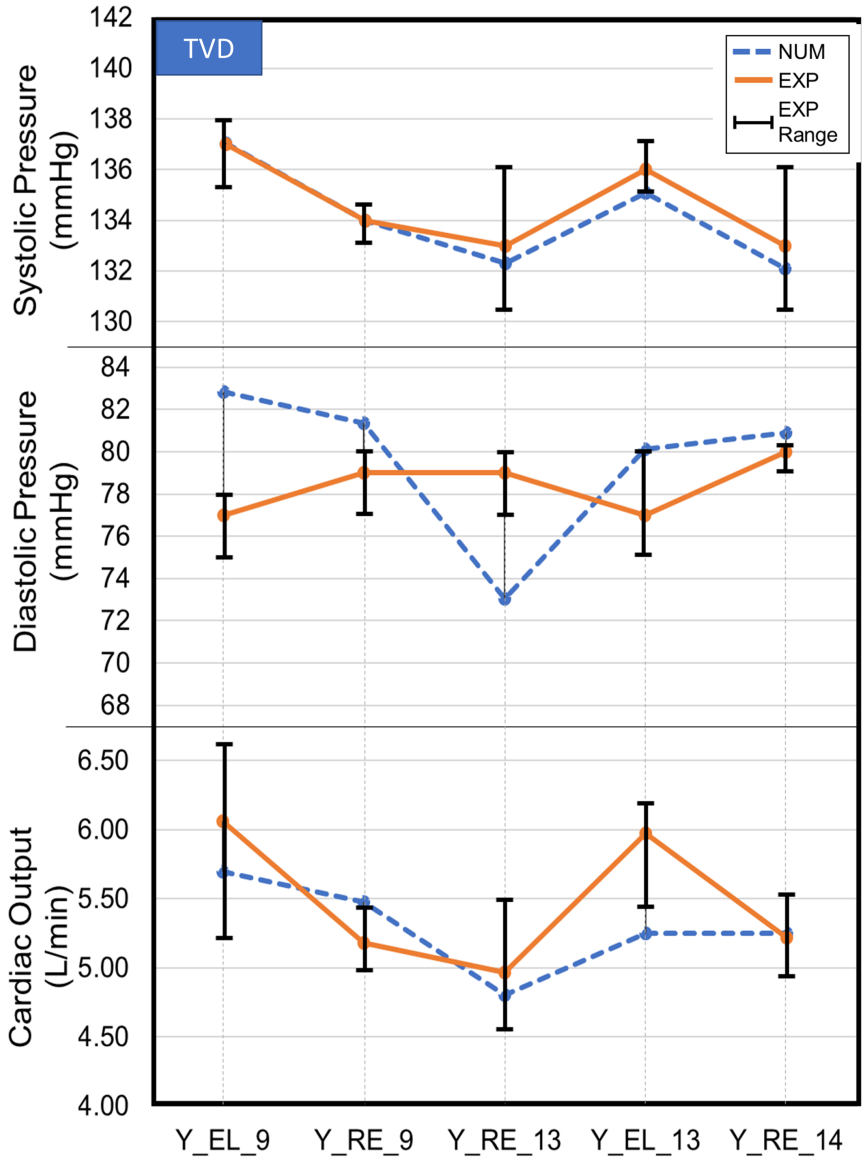


| Session | PTT (s) | HR | Err-SYS(%) | Err-Dia (%) | Err-CO (%) |
|---|---|---|---|---|---|
| Y_RE_9 | 0.1478 | 103 | 0.03 | 7.57 | 6.02 |
| Y_EL_9 | 0.1498 | 99 | 0.01 | 3.00 | 5.66 |
| Y_RE_13 | 0.1591 | 86 | 0.53 | 7.55 | 3.29 |
| Y_EL_13 | 0.1523 | 91 | 0.66 | 4.06 | 12.13 |
| Y_RE_14 | 0.1511 | 87 | 0.67 | 1.13 | 0.57 |
| | | **Mean Err** | 0.38 | 4.66 | 5.54 |

**Fig. 9.7.** – Cardiac output and upper arm (systolic/diastolic) blood pressure. Inversely reconstructed values (dotted blue line) obtained using TVD version of CardioFAN, against experimental measurements (solid orange line). Table demonstrates data associated with each session and improved prediction error using TVD CardioFAN. EL: elevated HR, RE: resting HR, CO: cardiac output.

The error bars indicate the range of experimental data obtained at each of the recording sessions and the cirled markers indicate the averaged values. Root mean squared deviations for the inversely reconstructed data, using both the Lax-Wendroff(LW) and TVD versions of CardioFAN, show very good agreement with the clinical measurements. This agreements exists in terms of both the individual recordings as well as capturing the trend of changes. As can be seen in figure 9.7, the prediction errors are lower in TVD version compared to LW. Average errors are as low as 0.33% and 3.56% for systolic and diastolic BP at the upper arm and 4.70% for the predicted cardiac output.

Systolic BPs are captured very accurately with errors of less than 1 mmHg. This is a very important outcome of this work as in many of the works aiming to predict central pressure from peripheral BP, transfer functions are usually used to match *systolic BP* [268]. This might be due to lower variation in diastolic blood pressure compared to systolic pressure as we move from heart toward the wrist. Therefore, this work is a very important step forward in the direction of having a noninvasive peripheral (close to the heart) BP measurement, showing the potential of deterministic reduced-order FSI models of cardiovascular system.

Although in acceptable prediction range of $< 5\ mmHg$ difference, as mentioned in AHA and UC Berkeley study of BP measurements at the arm and wrist [269], [270] and IEEE, ANSI, BHS and ESH-IP standards as shown by [153], [271], there is more room for improvement in prediction of diastolic BP. For instance the difference between the value recorded in session 9 of resting condition for subject Y is 3 mmHg higher than the maximum measured diastolic BP. In session 13 with resting HR, the blood pressure is under-predicted by 4 mmHg. These errors might be attributed to the wrist and arm cuff BP variations. The number of consecutive BP measurements can increase the confidence interval of the experimentally measured diastolic BPs. Discrepancies has the potential to be further alleviated by more rigorous calibration and testing sessions, to pinpoint the root cause.

Another important outcome is the cardiac output results. The predicted values show strong correlation with experimental measurements, with the worst error being 9.55% in recording session 13th-elevated HR. However, if the range of the measured data is considered the prediction is still in less than <5% error compared to the minimum value measured. Since the data recording session takes more than 60 seconds in the current calibration technique, the cardiac output and BP values during elevated HR are usually prone to larger errors; becauese this gives the subject's body enough time to bring down the elevated HR and BP while measurement is still in process. The stroke volume and HR values can also be extracted from the cardiac output, especially since each simulation takes into account these factors to calculate cardiac output.

For the second subject, the data was obtained for the pathway from heart to left hand, as shown in 9.8. Ultrasound measurement was not obtained for subject 2, therefore the blood vessel diameter and arterial properties were scaled using [260], [272] and the body height and weight of the second subject. Other properties such as Fung parameter and terminal resistance and compliances were all calibrated using 3 data sets from FIT seat recording sessions. It should be noted that the uncertainty in peripheral and proximal measurements were higher in this case compared to the first subject (see figure 9.9). Although the results were expected to have lower accuracy, specifically due to the lower reproduciblity of the PTT data for subject_K and lack of ultrasound imaging data, they are still in an acceptable range, especially the BP is predicted very accurately (average errors of 2.29% and 5.6% respectively). Except one point in systolic and one in diastolic BPs that undergo larger errors (>6%). Cardiac output predictions show an average error of 12.12%. Showing a large error again at point K_RE_2. These results can be improved by obtaining more data points for second subject. Especially, large error bars for experimental recordings reduce the confidence on the exact location of a physiologically valid averaged BP or cardiac output. The most important point intended with this experiment is to show that even with limited data for calibration this technique can provide users with acceptable accuracy with results mostly falling in the acceptable range of prediction. Results are assembled in a day by day plot similar to subject_Y. Figure 9.9 also includes a table representing the errors associated with the systolic and diastolic BP as well as cardiac output measurements.

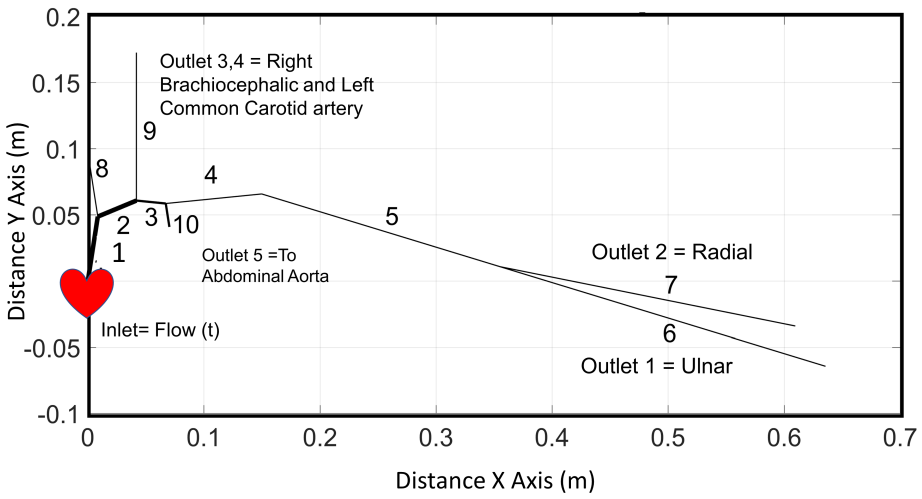


**Fig. 9.8.** – The pathway from heart to radial and ulnar artery at the wrist wrist, including supra aortic and terminal artery leading to abdominal aorta.

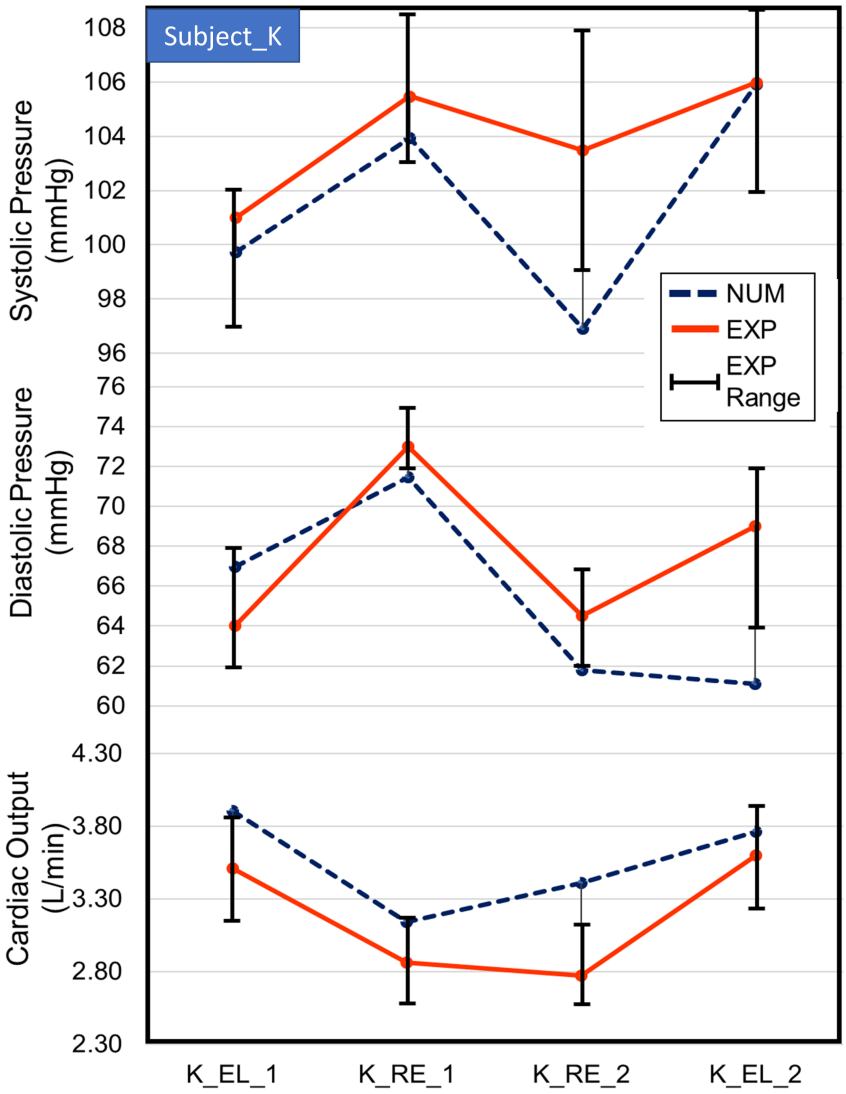


Measurement Session Data and Prediction Error

| Session | PTT (s) | HR | Err-SYS(%) | Err-Dia (%) | Err-CO (%) |
|---|---|---|---|---|---|
| K_EL_1 | 0.1743 | 87 | 1.26 | 4.66 | 11.32 |
| K_RE_1 | 0.1760 | 77 | 1.49 | 2.11 | 9.74 |
| K_RE_2 | 0.1776 | 74 | 6.37 | 4.20 | 22.84 |
| K_EL_2 | 0.1850 | 92 | 0.05 | 11.44 | 4.57 |
| | | **Mean Err2** | 2.29 | 5.60 | 12.12 |

**Fig. 9.9.** – Cardiac output and upper arm (systolic/diastolic) blood pressure. Inversely reconstructed values (dotted dark blue lines) obtained using TVD version of CardioFAN, against experimental measurements (solid dark red lines). Table demonstrates data associated with each session and prediction error for subject_K. EL: elevated HR, RE: resting HR, CO: cardiac output.

### 9.4.2 Prediction of Proximal/Central BP

A common noninvasive way of measuring central BP is by using peripheral BPs such as wrist or arm BP (with applanation tonometry or cuff BP monitors) and using statistically derived transfer functions to deduce central BP [273]. As the systolic BP has two components, the early and late systolic BP, central BP determination might not be accurate and transfer function for each individual might be different. Since catheter or applanation tonometry measurements were not available, here a transfer function cannot be used to estimate central BP from measured wrist or arm BP cuff monitor values. Numerical BP waveform at the ascending aorta can only be compared qualitatively by looking at the shape of the ascending aorta diameter variation as a function of time. Therefore, in figure 9.10 the central diameter variation reported by CardioFAN is compared against the shape of diameter changes in one cardiac cycle, measured by doppler ultrasound (analysis shown in chapter 8). Normalized and absolute values are compared at the ascending aorta, showing very promising results.

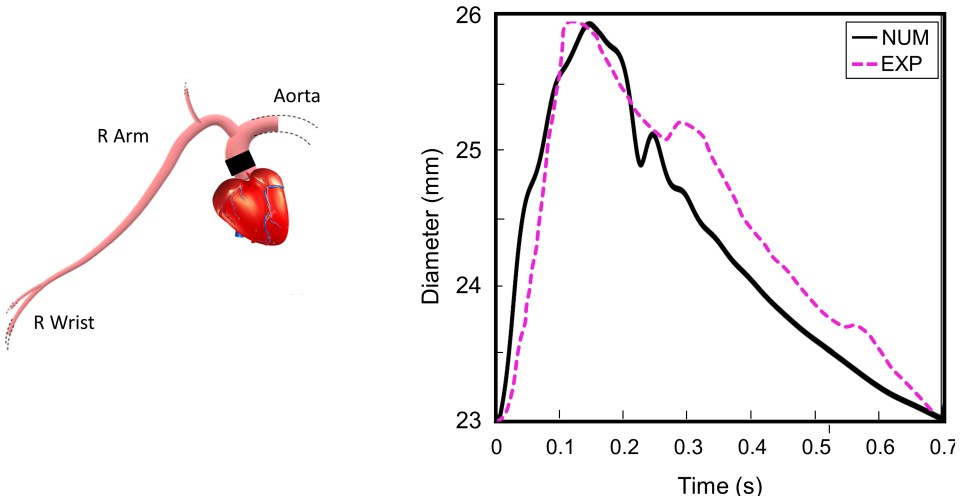


**Fig. 9.10.** – Comparison of the central aortic diameter variation from doppler ultrasound and numerically reconstructed signal.

Another comparison is made between the shape and phase difference between the waveforms captured at the ascending aorta (aortic root), upper arm (brachial) and wrist (radial). As can be seen in figure 9.11, CardioFAN can reconstruct the shape of the waveforms along the desired measurement path at different arterial sites. Here, since the experiental shape of the waveforms were not available, only the systolic and diastolic values are shown on the figure. However, the shape of the waveforms are in good qualitative agreement with the expected waveforms at the proximal and peripheral locations, as previously shown by McEniery *et al.* [36].

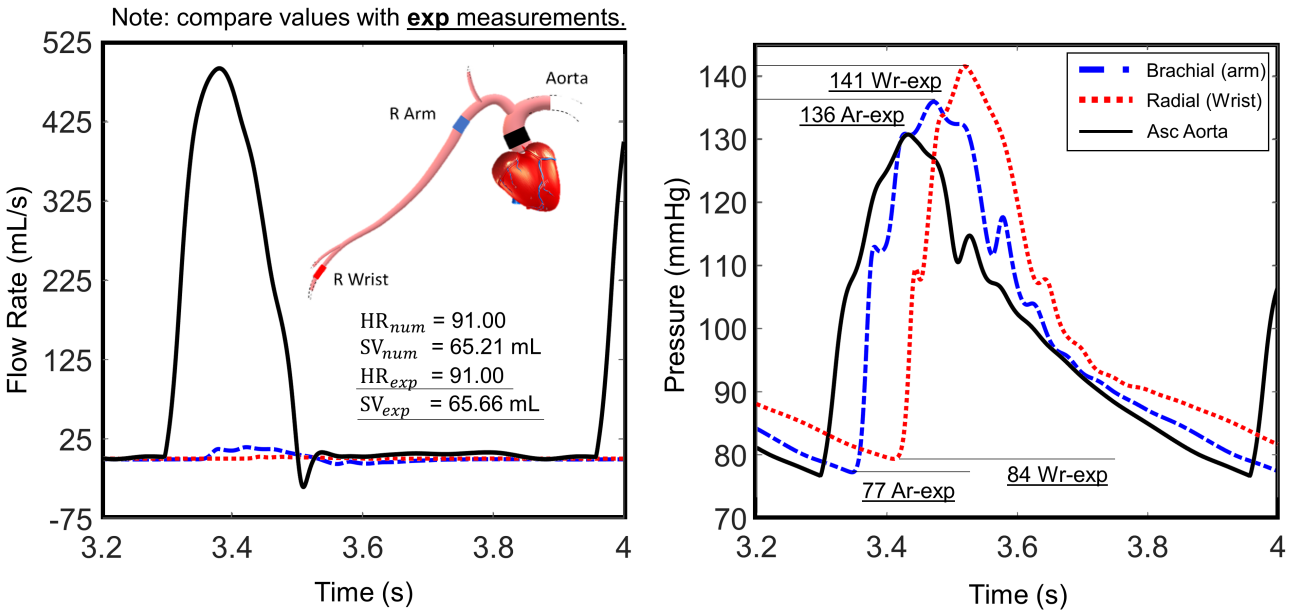


**Fig. 9.11.** – Blood flow (left) and pressure (right) at the ascending aorta, brachial artery and radial artery. The experimentally measured values are from measurement session $Y\_EL\_13$, showing well-matched stroke volume, systolic/diastolic BP for PTT= 152.3 ms. experimental measurements are specified with underlined terms.

While this needs further confirmation, these efforts act as a preliminary qualitative comparison based on the direct relationship between arterial blood pressure and diameter as described by tube law and other constitutive equations for blood vessel deformation. Having applanation tonometry data at the carotid artery or radial artery, it would be possible to use a transfer function between radial and central BP waveforms [268]. BP measured using a catheter still remains the gold standard in order to evaluate the accuracy of this work in predicting central BP.

### 9.4.3 Clinical Implications

The success of this initial test as well as previous case shown in chapter 7 has important clinical implications. This can allow doctors to have an accurate initial insight on the BP and cardiac output before sending the patient to surgical room to get a catheter-based measurement. This algorithm has the potential to be paired with smart devices measuring vital signals such as BCG/ECG/PPG peripherally to provide accurate readings for BP and cardiac output for the patients. In addition to systolic and diastolic values, this technique is capable of generating the shape of patient's blood pressure and flow waveforms. Therefore, it will be able to detect unusual changes in the patient's pressure pulse and cardiac output along the measurement path, signaling risk of atrial fibliration, hypertention, stenosis or arterial aneurysm.

On the other hand this study can introduce a new deterministic method for the efforts involving noninvasive prediction of central blood pressure using wrist or arm oscillometric cuff BP monitoring devices. Therefore, the previously faced issues with the treatment of uncertainties in pressure wave variations and wave reflections when using transfer function or moving average peripheral signal analysis techniques [268] might potentially be eliminated.

### 9.4.4 Implementation Suggestions

To the knowledge of author, this is the first time that a reduced-order model with hyperelastic vessel wall properties is directly coupled to clinical peripheral measurements to noninvasively obtain information on the proximal values of blood pressure and flow during the cardiac cycle. Clear implementation and data acquisition procedures are presented in this work. Ease of implementation makes this algorithm appealing for wearable devices or peripheral BP detectors, in order to improve proximal blood pressure and cardiac output measurement capabilities.

Suggested list of sensors required in devices that intend to use this algorithm are as follows:

1. Combination 1: BCG sensor, and PPG sensor, to provide cardiac output, HR, and PTT.

2. Combination 2: ECG sensor and PPG sensor to capture PTT and HR. In addition a cuff BP monitor at a peripheral site.

3. Combination 3: Two PPG sensors for PTT and a cuff BP monitor at a peripheral site.

4. Combination 4: ECG/PPG/BCG sensor combined with a peripheral BP monitor, allowing the algorithm to generate more accurate prediction of proximal BP, since cardiac output can be calculated from ECG and BCG data.

## 9.5 Limitations

The current study is looking at the arm cuff blood pressure as the proximal BP value predicted. It would be interesting, however to have gold standard measurements of central BP to evaluate the accuracy of this technique

in predicting central signals. In addition to systolic and diastolic values, the shape of the pressure waveforms consisting of systolic rise, dicrotic notch and diastolic decay can be evaluated when continuous BP measurement is available. For instance, BP at the common carotid artery can be measured continuously with applanation tonometry and evaluated against predicted carotid BP waveform. Currently the only indication of BP waveform is the variations in aortic diameter as a function of time in one cardiac cycle (figure 9.10).

For a more robust validation, the peripheral BP and PTT as well as the proximal BP should be captured synchronously. For the current phase of this work, this technology was not accessible.

Tests were performed on healthy patients only in normal and stressed conditions. Patient self-assesment claimed no indication of cardiovascular problems, and it was confirmed that patient Y has healthy blood flow with the ultrasound imaging of the aorta. However, it is interesting to observe how this algorithm performs when using data captured from both healthy and unhealthy subjects.

The variations are only studied here for 2 subjects. Uncertainties might increase when calibrating and analyzing the data from multiple subjects. It would be interesting to do an stochastic analysis and come up with sensitivity and specificity of the technique for a larger number of test subjects. On the other hand the sensitivity of the algorithm and limits of its application during the increase and decreasing of the heart rate is an interesting study for the future.

Due to the amount of blood flow and vessel structure related information carried by a propagating arterial pulse, PTT and PWV are now widely being treated as a surrogate for BP [274]. This work introduces a robust cardiovascular signal prediction and analysis tool that can utilize the existing PTT measurement technology in smart devices, to noninvasively provide a more comprehensive analysis of the arterial BP and cardiac output close to the heart in addition to capturing the BP and flow in peripheral sites.

# 10 Conclusions and Future Recommendations

## 10.1 Conclusions

This work was dedicated to developing a novel reduced-order fluid-structure interaction (FSI) numerical algorithm for modeling human arterial network to enable noninvasive diagnostics and monitoring of cardiovascular health. The model is designed such that it can be applied both for direct and inverse modeling of cardiovascular scenarios. When the root and terminal boundary conditions (BCs) are known and the prediction of a certain parameter, such as blood pressure (BP), pulse transit time (PTT) or flow waveform at an arterial site is sought, the simulation is solved directly. However, when the root conditions, such as BP or cardiac output are unknown, developed code is capable of reconstructing these variables based on the measured peripheral vitals and blood vessel properties. This is a hybrid approach, combining noninvasive measurements and numerical modeling to improve prediction accuracy.

### 10.1.1 Reduced-Order FSI Model Built for Patient-Specific Diagnosis

A rigorous literature review is conducted highlighting the prior art for *in silico* models of cardiovascular system, pinpointing the missing links that prevents them from becoming patient-specific and capable of inverse reconstruction of properties. Second part of the background work, focuses on pulse transit time and its connection to blood pressure measurement and cardiovascular diagnostics in general. It highlights the gap between reduced-order hemodynamics models and recent PTT-based noninvasive blood pressure measurement techniques, identifying the need for a hybrid approach for measuring proximal BP and cardiac output. Therefore the first step is considered to be developing a robust reduced order model with local nonlinear pulse wave velocity (PWV) calculation capabilities.

Governing equations are derived using Hamiltonian principle to obtain a unique solution and easy *multiscale coupling* capabilities for the developed quasi-1D code, CardioFAN (Cardiovascular Flow ANalysis), making it

readily available for coupling with local 3D and 0D (lumped parameter) models. Such versatility broadens the usage of this code to studying aneurysms, stenosis, aortic arch and other local phenomena experiencing 3D effects (such as wall shear stress or recirculation).
On the other hand, total variational diminishing (TVD) Lax-Wendroff scheme makes CardioFAN a monotonicity preserving numerical code, meaning it does not experience artificial oscillations in second-order PDE approximations. This holds true in case of arterial network simulations containing natural discontinuity in properties, such as stented artery or sudden change in geometrical shape. *Visco-hyperelasticity* of the systemic arteries is the last piece in the chain, allowing CardioFAN to capture physiologically nonlinear range of arterial wall distensibility (compliance). This feature builds the foundation for correct prediction of PWV or its surrogate PTT, which are considered important biomarkers for patient-specific diagnosis of cardiovascular abnormalities. calculated PTT and peripheral BP are later used for noninvasive measurement of proximal BP and cardiac output.

CardioFAN is verified with manufactured solutions and three validation tests are conducted against numerical, *in vitro* and *in vivo* experiments on three popular arterial network geometries in the literature. The vessel geometry and properties are prescribed in CardioFAN. Results are improved compared to previous cardiovascular hemodynamics simulators. A new method for calculating the numerical PTT is also introduced. When used in conjunction with experimental PTT to correct the speed of pulse propagation in arteries, validation results are improved an average of 1.5% in prediction of the clinically measured blood flow, lumen cross-sectional area and BP. The corresponding average errors of prediction are now smaller than 5.2%, 2.8% and 1.6%, respectively.

### 10.1.2 Novel Calibration and Inverse Reconstruction of Central Signals

Second part of this dissertation is dedicated to the development of a two-step calibration procedure for nonlinear properties of the blood vessel and terminal BCs, as well as evaluating the capability of CardioFAN for inverse reconstruction of proximal/central BP and cardiac output. Preliminary evaluation is conducted by inversely reconstructing stroke volume and carotid BP in a human aorta, where complete measurement of BP waveform, blood vessel properties, diameters and flow waveforms were available from literature. It is shown that by matching numerical and measured PTT, it is possible to predict stroke volume and carotid BP waveform with a 0.5% and 7.1% accuracy, respectively.

This technique was then tested against a human subject for an arterial pathway from heart to wrist. To calibrate aortic diameter and vessel wall properties, the Doppler ultrasound imaging and upper arm cuff BP are measured in normal and post-exercise conditions. Running an optimization code on this data combined with Murray's law to

find proportional diameters of the downstream bifurcated arterial network enabled the calculation of parameters for Fung's anisothropic blood vessel wall model. Second calibration was conducted on terminal BC parameters, resistance and compliance. They are extracted after subject's PTT, wrist and arm BPs, HR, and stroke volume (SV) are measured using the sensors on an in-home smart care device, called FIT seat, in normal and post-exercise conditions. This resulted in 15 recordings among two subjects, where 3-4 used for terminal boundary parameter optimization, and the rest are used for validation of proximal BP and cardiac output reconstruction.

By matching numerical wrist BP and heart to wrist PTT with experimentally measured values, the proximal BP and cardiac output are inversely restored. The results show a good agreement between the reconstructed and measured values of upper arm BP and cardiac output. For a human subject that went through both calibration procedures, the prediction accuracy for the upper arm BP is 0.33% for systolic and 3.56% for diastolic BP, while cardiac output shows a 4.7%. The accuracy is reduced for the second subject, where no ultrasound calibration was available, by nearly 2% for BP and 7% for cardiac output. This work lays the foundation for predicting central BP and cardiac output, by using peripheral BP and PTT readings captured from smart sensors, readily available in modern wearables and smart in-home healthcare devices. This can revolutionize the wearable and smart device based health monitoring by providing a continuous and accurate in-home proximal/distal arterial BP, flow and cardiac output measurements instead of current invasive and uncomfortable methods that are only available based on the physician's request. By alerting patient's physician of sudden changes, an in-home monitoring algorithm such as the presented work, can help with early detection of hypertension, and changes in cardiac output, caused by heart failure, stenosis or other cardiovascular disorders.

## 10.2 Future Recommendations

The future directions are divided to three separate efforts: alternative or more accessible calibration techniques; running tests on larger pool of subjects and validating against data obtained from gold standard measurement methods; integration into wearables/smart devices.

### 10.2.1 Overcoming Calibration Technique Limitations

With the advent of wearable technology, such as earbuds capable of measuring BCG/ECG/PPG/HR and thus PTT signals [20], CardioFAN can potentially get integrated into these wearables to provide continuous BP and cardiac output measurements. PTT measurement technique used here was based on BCG and PPG signals, while many

others are using ECG and PPG or two PPG signals for measuring PTT. Depending on the ease of access, cost and accuracy, alternative sensors can be utilized to obtain the experimental PTT. CardioFAN can be tested in conjunction with these PTT measurement techniques to evaluate its accuracy based on the available sensors.

One of the limitations of the current calibration setup is obtaining robust PTT and BP recordings in post-stress conditions. This was due to having post-exercise recording times of more than 60 seconds in the sitting position, giving subject's body enough time to trigger parasympathetic nervous system and regulate the high heart rate. With an alternative calibration setup, such as taking measurements while on a bicycle, or increasing HR by organic stimuli such as caffeine, this limitation can be alleviated. However, new noise cancellation strategy might be needed for excess recording noise as a result of high body movement and breathing during exercise.

Replacing wrist pressure cuffs with applanation tonometry device can give a continuous BP signal at the periphery. Currently, in the first inverse reconstruction method (assigning wrist BP directly), the systolic and end diastolic pressures are scaled and fitted by a generic wrist BP waveform. Since it is not the exact waveform it can result in non-physiological waves reflecting back from terminal boundary at the wrist. The second wrist BC method introduced here, used calibrated windkessel models at the periphery. Applanation tonometry gives a clear picture of diastolic decay in pressure at the wrist, therefore making it easier to find windkessel outlet pressure and resistances. Therefore, for either method, applanation tonometry can enhance the calibration and even the validation efforts.

It is shown here that posture significantly affects PTT and BP, due to the effect of gravity. Although this was treated by assuming PTT and BP correction as a function of height, measurements in supine position can give the most accurate depiction of CardioFAN's accuracy. For future calibration efforts using CardioFAN it is proposed to use ECG and PPG signals to obtain PTT from a subject in supine position, both before and after exercise. In addition, due to scarcity of research on the effect of posture on central BP and peripheral PTT, it is suggested that the same ECG-PPG technique be used while the bench underneath the laying patient is tilted up or downward, changing the direction of gravity effect.

Lastly, identifying subjects with cardiovascular disorders and calibrating CardioFAN for them is another interesting direction. This can potentially help the patients to track the progress of their cardiovascular disorder by monitoring vital signals.

### 10.2.2 Subject Testing

So far BP monitoring technique is tested on 2 subjects. The next step in testing this algorithm is to start a second pilot study by recruiting more than 21 patients, to obtain a robust statistical confidence interval for the results. Institute review board (IRB) approval will be required for human subject testing. PTT measurement technique on the other hand, might affect the accuracy of the final results. For the proof of concept study involving more patients, gold standard PTT calculation and BP measurement methods are suggested to ensure external errors are not affecting the BP and cardiac output predictions. Central BP measurements, however, might be difficult to obtain without the catheter insertion or during angiography. Magnetic Resonance Imaging (MRI) data can also give a better picture of the flow distributions across the arterial network of interest, both for calibration and validation purposes. Another interesting addition to make calibration of vessel diameters and wall properties more accessible is by using the new portable ultrasound technology, which can be attached to a handheld smartphone [275].

### 10.2.3 Integration into Smart/Wearable Devices

To implement the inverse reconstruction capabilities of CardioFAN into wearable devices, will require programming the sensors and interface between current algorithm and existing firmware of those devices. In addition, big data handling techniques for storing and tracking variation of parameters and finding trends are needed to help use it as a continuous monitoring algorithm. In addition, by changing PTT based calibration method this code can be adapted to work with various combinations of inputs coming from a wearable device (*e.g.* ECG, BCG, PPG, BP and SV *etc.*).

## 10.3 Final Remarks

This work is demonstrating the first steps toward development and introduction of a data assimilation approach to blood pressure, blood flow and cardiac output measurement. The novel open-source algorithm, CardioFAN, its patient-specific calibration and coupling capabilities, and high accuracy in capturing numerical PTT, BP and blood flow distributions in arbitrary arterial networks, makes it an easy to implement health-monitoring algorithm for in-home and wearable smart devices. While the current limitations and the suggested solutions are clearly stated, the preliminary results demonstrate strong potential for revolutionizing the proximal flow and pressure signal prediction using the presented approach.

# Bibliography


[1] *The Global Atlas on Cardiovascular Disease Prevention and Control | World Heart Federation* (Cited on pages 1, 10).

[2] G. Cancrini and A. Iori, "[Traditional and innovative diagnostic tools: When and why they should be applied]", ita, *Parassitologia*, vol. 46, no. 1-2, pp. 173–176, Jun. 2004 (Cited on page 1).

[3] J. Bronzino, "1 - BIOMEDICAL ENGINEERING: A HISTORICAL PERSPECTIVE", in *Introduction to Biomedical Engineering (Second Edition)*, J. D. Enderle, S. M. Blanchard, and J. D. Bronzino, Eds., Boston: Academic Press, Jan. 2005, pp. 1–29. DOI: 10.1016/B978-0-12-238662-6.50003-3 (Cited on pages 1, 43).

[4] R. A. Gray and P. Pathmanathan, "Patient-Specific Cardiovascular Computational Modeling: Diversity of Personalization and Challenges", en, *Journal of Cardiovascular Translational Research*, pp. 1–9, Mar. 2018. DOI: 10.1007/s12265-018-9792-2 (Cited on pages 2, 3, 43).

[5] T. M. J. v. Bakel, K. D. Lau, J. Hirsch-Romano, S. Trimarchi, A. L. Dorfman, *et al.*, "Patient-Specific Modeling of Hemodynamics: Supporting Surgical Planning in a Fontan Circulation Correction", en, *Journal of Cardiovascular Translational Research*, pp. 1–11, Jan. 2018. DOI: 10.1007/s12265-017-9781-x (Cited on page 2).

[6] C. f. D. a. R. Health, *Medical Devices - Non-Clinical Engineering Tests and Recommended Labeling for Intravascular Stents and Associated Delivery Systems - Guidance for Industry and FDA Staff*, en, WebContent (Cited on pages 2, 33).

[7] A. Veneziani and C. Vergara, "Inverse problems in Cardiovascular Mathematics: Toward patient-specific data assimilation and optimization", en, *International Journal for Numerical Methods in Biomedical Engineering*, vol. 29, no. 7, pp. 723–725, Jul. 2013. DOI: 10.1002/cnm.2566 (Cited on pages 3, 5, 29, 43–45, 71).

[8] W. W. Nichols and D. G. Edwards, "Arterial elastance and wave reflection augmentation of systolic blood pressure: Deleterious effects and implications for therapy", eng, *Journal of Cardiovascular Pharmacology and Therapeutics*, vol. 6, no. 1, pp. 5–21, Jan. 2001. DOI: 10.1177/107424840100600102 (Cited on pages 4, 10, 43).

[9] W. J. Rogers, Y.-L. Hu, D. Coast, D. A. Vido, C. M. Kramer, *et al.*, "Age-associated changes in regional aortic pulse wave velocity", en, *Journal of the American College of Cardiology*, vol. 38, no. 4, pp. 1123–1129, Oct. 2001. DOI: 10.1016/S0735-1097(01)01504-2 (Cited on page 4).

[10] J. P. Merillon, G. Motte, C. Masquet, I. Azancot, A. Guiomard, *et al.*, “Relationship between physical properties of the arterial system and left ventricular performance in the course of aging and arterial hypertension”, en, *European Heart Journal*, vol. 3, no. suppl_A, pp. 95–102, Jan. 1982. DOI: 10.1093/eurheartj/3.suppl_A.95 (Cited on page 4).

[11] T. Pereira, C. Correia, and J. Cardoso, “Novel Methods for Pulse Wave Velocity Measurement”, *Journal of Medical and Biological Engineering*, vol. 35, no. 5, pp. 555–565, 2015. DOI: 10.1007/s40846-015-0086-8 (Cited on pages 4, 44).

[12] X. Ding, B. P. Yan, Y.-T. Zhang, J. Liu, N. Zhao, *et al.*, “Pulse Transit Time Based Continuous Cuffless Blood Pressure Estimation: A New Extension and A Comprehensive Evaluation”, en, *Scientific Reports*, vol. 7, no. 1, p. 11 554, Sep. 2017. DOI: 10.1038/s41598-017-11507-3 (Cited on page 4).

[13] M. Willemet, P. Chowienczyk, and J. Alastruey, “A database of virtual healthy subjects to assess the accuracy of foot-to-foot pulse wave velocities for estimation of aortic stiffness”, *American Journal of Physiology-Heart and Circulatory Physiology*, vol. 309, no. 4, H663–H675, Jun. 2015. DOI: 10.1152/ajpheart.00175.2015 (Cited on page 4).

[14] J. Smith, L. Camporota, and R. Beale, “Monitoring Arterial Blood Pressure and Cardiac Output using Central or Peripheral Arterial Pressure Waveforms”, en, in *Yearbook of Intensive Care and Emergency Medicine*, ser. Yearbook of Intensive Care and Emergency Medicine, J.-L. Vincent, Ed., Berlin, Heidelberg: Springer Berlin Heidelberg, 2009, pp. 285–296. DOI: 10.1007/978-3-540-92276-6_27 (Cited on pages 4, 131).

[15] C. DeMarco, *Should you get a central line for chemotherapy?*, en (Cited on page 4).

[16] A. Esmaili, M. Kachuee, and M. Shabany, “Nonlinear Cuffless Blood Pressure Estimation of Healthy Subjects Using Pulse Transit Time and Arrival Time”, *IEEE Transactions on Instrumentation and Measurement*, vol. 66, no. 12, pp. 3299–3308, Dec. 2017. DOI: 10.1109/TIM.2017.2745081 (Cited on pages 4, 35, 39).

[17] L. Tarassenko, M. Villarroel, A. Guazzi, J. Jorge, D. A. Clifton, *et al.*, “Non-contact video-based vital sign monitoring using ambient light and auto-regressive models”, eng, *Physiological Measurement*, vol. 35, no. 5, pp. 807–831, May 2014. DOI: 10.1088/0967-3334/35/5/807 (Cited on page 4).

[18] N. H. Pijls, B. de Bruyne, K. Peels, P. H. van der Voort, H. J. Bonnier, *et al.*, “Measurement of Fractional Flow Reserve to Assess the Functional Severity of Coronary-Artery Stenoses”, *New England Journal of Medicine*, vol. 334, no. 26, pp. 1703–1708, Jun. 1996. DOI: 10.1056/NEJM199606273342604 (Cited on pages 4, 16).

[19] F. N. v. d. Vosse and N. Stergiopulos, “Pulse Wave Propagation in the Arterial Tree”, *Annual Review of Fluid Mechanics*, vol. 43, no. 1, pp. 467–499, 2011. DOI: 10.1146/annurev-fluid-122109-160730 (Cited on pages 4, 5, 12, 16, 18, 20, 21, 23, 25, 44).

[20] E. S. Winokur, D. Da He, and C. G. Sodini, “A Wearable Vital Signs Monitor at the Ear for Continuous Heart Rate and Pulse Transit Time Measurements”, *Conference proceedings : ... Annual International Conference of the IEEE Engineering in Medicine and Biology Society. IEEE Engineering in Medicine and Biology Society. Annual Conference*, vol. 2012, pp. 2724–2727, 2012. DOI: 10.1109/EMBC.2012.6346527 (Cited on pages 4, 145).

[21] Y.-L. Zheng, B. P. Yan, Y.-T. Zhang, and C. C. Y. Poon, “An Armband Wearable Device for Overnight and Cuff-Less Blood Pressure Measurement”, *IEEE Transactions on Biomedical Engineering*, vol. 61, no. 7, pp. 2179–2186, Jul. 2014. DOI: 10.1109/TBME.2014.2318779 (Cited on page 4).

[22] N. J. Conn, K. Q. Schwarz, and D. A. Borkholder, “In-Home Cardiovascular Monitoring System for Heart Failure: Comparative Study”, en, *JMIR mHealth and uHealth*, vol. 7, no. 1, e12419, Jan. 2019. DOI: 10.2196/12419 (Cited on pages 4, 118).

[23] J. D. Humphrey, “Mechanics of the arterial wall: Review and directions”, eng, *Critical Reviews in Biomedical Engineering*, vol. 23, no. 1-2, pp. 1–162, 1995 (Cited on pages 5, 44).

[24] Y. Shi, P. Lawford, and R. Hose, “Review of Zero-D and 1-D Models of Blood Flow in the Cardiovascular System”, *BioMedical Engineering OnLine*, vol. 10, p. 33, Apr. 2011. DOI: 10.1186/1475-925X-10-33 (Cited on pages 5, 18, 130).

[25] Y. C. Fung, K. Fronek, and P. Patitucci, “Pseudoelasticity of arteries and the choice of its mathematical expression”, eng, *The American Journal of Physiology*, vol. 237, no. 5, H620–631, Nov. 1979 (Cited on pages 6, 13, 20, 24, 44, 48, 109).

[26] G. Hou, J. Wang, and A. Layton, “Numerical Methods for Fluid-Structure Interaction — A Review”, *Communications in Computational Physics*, vol. 12, no. 2, pp. 337–377, Aug. 2012. DOI: 10.4208/cicp.291210.290411s (Cited on pages 6, 30).

[27] H. Obeid, G. Soulat, E. Mousseaux, S. Laurent, N. Stergiopulos, *et al.*, “Numerical assessment and comparison of pulse wave velocity methods aiming at measuring aortic stiffness”, en, *Physiological Measurement*, 2017. DOI: 10.1088/1361-6579/aa905a (Cited on page 6).

[28] F. D. Kolodgie, G. Nakazawa, G. Sangiorgi, E. Ladich, A. P. Burke, *et al.*, “Pathology of Atherosclerosis and Stenting”, *Neuroimaging clinics of North America*, vol. 17, no. 3, pp. 285–vii, Aug. 2007. DOI: 10.1016/j.nic.2007.03.006 (Cited on pages 6, 44).

[29] L. Formaggia, D. Lamponi, and A. Quarteroni, “One-dimensional models for blood flow in arteries”, en, *Journal of Engineering Mathematics*, vol. 47, no. 3-4, pp. 251–276, Dec. 2003. DOI: 10.1023/B:ENGI.0000007980.01347.29 (Cited on pages 6, 19, 24, 25, 33, 73).

[30] J. Humphrey and C. Taylor, “Intracranial and Abdominal Aortic Aneurysms: Similarities, Differences, and Need for a New Class of Computational Models”, *Annual review of biomedical engineering*, vol. 10, pp. 221–246, 2008. DOI: 10.1146/annurev.bioeng.10.061807.160439 (Cited on page 6).

[31] L.-D. Jou, D. H. Lee, H. Morsi, and M. E. Mawad, “Wall Shear Stress on Ruptured and Unruptured Intracranial Aneurysms at the Internal Carotid Artery”, en, *American Journal of Neuroradiology*, vol. 29, no. 9, pp. 1761–1767, Oct. 2008. DOI: 10.3174/ajnr.A1180 (Cited on pages 6, 91).

[32] I. G. H. Jansen, J. J. Schneiders, W. V. Potters, P. van Ooij, R. van den Berg, *et al.*, “Generalized versus patient-specific inflow boundary conditions in computational fluid dynamics simulations of cerebral aneurysmal hemodynamics”, eng, *AJNR. American journal of neuroradiology*, vol. 35, no. 8, pp. 1543–1548, Aug. 2014. DOI: 10.3174/ajnr.A3901 (Cited on page 6).

[33] K. Funamoto and T. Hayase, “Reproduction of pressure field in ultrasonic-measurement-integrated simulation of blood flow”, en, *International Journal for Numerical Methods in Biomedical Engineering*, vol. 29, no. 7, pp. 726–740, Nov. 2012. DOI: 10.1002/cnm.2522 (Cited on pages 7, 29, 60).

[34] C. M. McEniery, n. Yasmin, B. McDonnell, M. Munnery, S. M. Wallace, *et al.*, “Central pressure: Variability and impact of cardiovascular risk factors: The Anglo-Cardiff Collaborative Trial II”, eng, *Hypertension (Dallas, Tex.: 1979)*, vol. 51, no. 6, pp. 1476–1482, Jun. 2008. DOI: 10.1161/HYPERTENSIONAHA.107.105445 (Cited on pages 7, 60).

[35] S. Reule and P. E. Drawz, “Heart Rate and Blood Pressure: Any Possible Implications for Management of Hypertension?”, *Current hypertension reports*, vol. 14, no. 6, pp. 478–484, Dec. 2012. DOI: 10.1007/s11906-012-0306-3 (Cited on pages 7, 60).

[36] C. M. McEniery, J. R. Cockcroft, M. J. Roman, S. S. Franklin, and I. B. Wilkinson, “Central blood pressure: Current evidence and clinical importance”, en, *European Heart Journal*, vol. 35, no. 26, pp. 1719–1725, Jul. 2014. DOI: 10.1093/eurheartj/eht565 (Cited on pages 7, 60, 139).

[37] D. Mozaffarian, E. J. Benjamin, A. S. Go, D. K. Arnett, M. J. Blaha, *et al.*, “Heart Disease and Stroke Statistics—2016 Update”, en, *Circulation*, CIR.0000000000000350, Jan. 2015. DOI: 10.1161/CIR.0000000000000350 (Cited on page 10).

[38] P. A. Heidenreich, J. G. Trogdon, O. A. Khavjou, J. Butler, K. Dracup, *et al.*, “Forecasting the future of cardiovascular disease in the United States: A policy statement from the American Heart Association”, ENG, *Circulation*, vol. 123, no. 8, pp. 933–944, Mar. 2011. DOI: 10.1161/CIR.0b013e31820a55f5 (Cited on page 10).

[39] C. J. Malanga, “Structure and Function of the Heart”, in *xPharm: The Comprehensive Pharmacology Reference*, New York: Elsevier, 2007, pp. 1–5. DOI: 10.1016/B978-008055232-3.60302-2 (Cited on page 11).

[40] D. Sidebotham and I. J. Le Grice, “Chapter 1 - Physiology and Pathophysiology”, in *Cardiothoracic Critical Care*, Philadelphia: Butterworth-Heinemann, 2007, pp. 3–27. DOI: 10.1016/B978-075067572-7.50004-7 (Cited on page 11).

[41] M. Thiriet and K. H. Parker, “Physiology and pathology of the cardiovascular system: A physical perspective”, en, in *Cardiovascular Mathematics*, ser. MS&A 1, L. Formaggia, A. Quarteroni, and A. Veneziani, Eds., Springer Milan, 2009, pp. 1–45. DOI: 10.1007/978-88-470-1152-6_1 (Cited on pages 11, 13).

[42] E. O. Ofili, M. J. Kern, J. A. St Vrain, T. J. Donohue, R. Bach, *et al.*, “Differential characterization of blood flow, velocity, and vascular resistance between proximal and distal normal epicardial human coronary arteries: Analysis by intracoronary Doppler spectral flow velocity”, eng, *American Heart Journal*, vol. 130, no. 1, pp. 37–46, Jul. 1995 (Cited on page 12).

[43] N. L. Mills, J. J. Miller, A. Anand, S. D. Robinson, G. A. Frazer, *et al.*, *Increased arterial stiffness in patients with chronic obstructive pulmonary disease: A mechanism for increased cardiovascular risk – – Thorax*, en (Cited on page 13).

[44] C. G. Caro, T. J. Pedley, R. C. Schroter, W. A. Seed, and K. H. Parker, *The Mechanics of the Circulation*, en, Dec. 2011. DOI: 10.1017/CBO9781139013406 (Cited on page 13).

[45] C. G. Caro, T. J. Pedley, R. C. Schroter, and W. A. Seed, *The Mechanics of the Circulation:* 2nd ed. Cambridge: Cambridge University Press, Dec. 2011 (Cited on pages 14, 45, 46).

[46] R. Fåhræus and T. Lindqvist, “The viscosity of the blood in narrow capillary tubes”, *American Journal of Physiology-Legacy Content*, vol. 96, no. 3, pp. 562–568, Mar. 1931. DOI: 10.1152/ajplegacy.1931.96.3.562 (Cited on page 14).

[47] A. R. Pries, D. Neuhaus, and P. Gaehtgens, “Blood viscosity in tube flow: Dependence on diameter and hematocrit”, en, *American Journal of Physiology - Heart and Circulatory Physiology*, vol. 263, no. 6, H1770–H1778, Dec. 1992 (Cited on pages 14, 23, 45).

[48] D. S. Sankar and K. Hemalatha, “A non-Newtonian fluid flow model for blood flow through a catheterized artery—Steady flow”, *Applied Mathematical Modelling*, vol. 31, no. 9, pp. 1847–1864, Sep. 2007. DOI: 10.1016/j.apm.2006.06.009 (Cited on pages 14, 45).

[49] K. L. Parkhurst, H.-F. Lin, A. E. DeVan, J. N. Barnes, T. Tarumi, *et al.*, “Contribution of blood viscosity in the assessment of flow-mediated dilation and arterial stiffness”, en, *Vascular Medicine*, vol. 17, no. 4, pp. 231–234, Aug. 2012. DOI: 10.1177/1358863X12450095 (Cited on pages 14, 45).

[50] J. A. Alastruey, “Numerical modelling of pulse wave propagation in the cardiovascular system : Development, validation and clinical applications.”, eng, PhD thesis, University of London, 2006 (Cited on pages 14, 28, 43, 45, 50).

[51] M. Zamir, *The Physics of Pulsatile Flow*, en, ser. Biological and Medical Physics, Biomedical Engineering. New York: Springer-Verlag, 2000 (Cited on page 14).

[52] O. Frank, *Die Grundform des arteriellen pulses: Mathematische Analyse. Erste Abhandlung*, ser. Zeitschrift für Biologie. Offprint. 1899 (Cited on page 15).

[53] *A Tale of Coronary Artery Disease and Myocardial Infarction | NEJM* (Cited on page 16).

[54] S. Oparil, M. C. Acelajado, G. L. Bakris, D. R. Berlowitz, R. Cífková, *et al.*, “Hypertension”, en, *Nature Reviews Disease Primers*, vol. 4, p. 18 014, Mar. 2018. DOI: 10.1038/nrdp.2018.14 (Cited on pages 16, 17, 34).

[55] R. N. Isnard, B. M. Pannier, S. Laurent, G. M. London, B. Diebold, *et al.*, “Pulsatile diameter and elastic modulus of the aortic arch in essential hypertension: A noninvasive study”, *Journal of the American College of Cardiology*, ACC Anniversary Seminar, vol. 13, no. 2, pp. 399–405, Feb. 1989. DOI: 10.1016/0735-1097(89)90518-4 (Cited on page 16).

[56] P. Segers, E. R. Rietzschel, M. L. D. Buyzere, S. J. Vermeersch, D. D. Bacquer, *et al.*, “Noninvasive (Input) Impedance, Pulse Wave Velocity, and Wave Reflection in Healthy Middle-Aged Men and Women”, en, *Hypertension*, vol. 49, no. 6, pp. 1248–1255, Jun. 2007. DOI: 10.1161/HYPERTENSIONAHA.106.085480 (Cited on pages 16, 44).

[57] S. Laurent and P. Boutouyrie, “The Structural Factor of Hypertension”, en, *Circulation Research*, vol. 116, no. 6, pp. 1007–1021, Mar. 2015. DOI: 10.1161/CIRCRESAHA.116.303596 (Cited on page 16).

[58] J. G. Y. Luc, C. A. Pierre, K. Phan, Y. S. Vahedein, A. S. Liberson, *et al.*, “Fluid structure interaction model analysis of cerebrospinal fluid circulation in patients with continuous-flow left ventricular assist devices”, eng, *The International Journal of Artificial Organs*, p. 0, Nov. 2017. DOI: 10.5301/ijao.5000657 (Cited on page 16).

[59] A. M. Malek, S. L. Alper, and S. Izumo, “Hemodynamic shear stress and its role in atherosclerosis”, eng, *JAMA*, vol. 282, no. 21, pp. 2035–2042, Dec. 1999 (Cited on page 16).

[60] *Brain aneurysm - Symptoms and causes*, en (Cited on page 16).

[61] S. Dong, J. Insley, N. T. Karonis, M. E. Papka, J. Binns, *et al.*, “Simulating and Visualizing the Human Arterial System on the TeraGrid”, *Future Gener. Comput. Syst.*, vol. 22, no. 8, pp. 1011–1017, Oct. 2006. DOI: 10.1016/j.future.2006.03.019 (Cited on page 18).

[62] L Grinberg, T Anor, J. Madsen, A Yakhot, and G. Karniadakis, “Large-Scale Simulation of the Human Arterial Tree”, en, *Clinical and Experimental Pharmacology and Physiology*, vol. 36, no. 2, pp. 194–205, Feb. 2009. DOI: 10.1111/j.1440-1681.2008.05010.x (Cited on pages 18, 20).

[63] P. D. Morris, A. Narracott, H. v. Tengg-Kobligk, D. A. S. Soto, S. Hsiao, *et al.*, "Computational fluid dynamics modelling in cardiovascular medicine", en, *Heart*, heartjnl–2015–308044, Oct. 2015. DOI: 10.1136/heartjnl-2015-308044 (Cited on page 18).

[64] C. G. Rizo, "The Digital and In Silico Therapeutics Revolution", en, in *Digital Health: Scaling Healthcare to the World*, ser. Health Informatics, H. Rivas and K. Wac, Eds., Cham: Springer International Publishing, 2018, pp. 197–214. DOI: 10.1007/978-3-319-61446-5_15 (Cited on page 18).

[65] P. S. Douglas, B. De Bruyne, G. Pontone, M. R. Patel, B. L. Norgaard, *et al.*, "1-Year Outcomes of FFRCT-Guided Care in Patients With Suspected Coronary Disease: The PLATFORM Study", eng, *Journal of the American College of Cardiology*, vol. 68, no. 5, pp. 435–445, 2016. DOI: 10.1016/j.jacc.2016.05.057 (Cited on pages 18, 95).

[66] B. Baillargeon, N. Rebelo, D. D. Fox, R. L. Taylor, and E. Kuhl, "The Living Heart Project: A robust and integrative simulator for human heart function", eng, *European Journal of Mechanics. A, Solids*, vol. 48, pp. 38–47, Nov. 2014. DOI: 10.1016/j.euromechsol.2014.04.001 (Cited on pages 18, 95).

[67] N. Xiao, J. Alastruey, and C. A. Figueroa, "A Systematic Comparison between 1-D and 3-D Hemodynamics in Compliant Arterial Models", *International journal for numerical methods in biomedical engineering*, vol. 30, no. 2, pp. 204–231, Feb. 2014. DOI: 10.1002/cnm.2598 (Cited on pages 18, 30, 57, 64, 65, 68, 70, 95, 121).

[68] C. M. Colciago, S. Deparis, and A. Quarteroni, "Comparisons between reduced order models and full 3d models for fluid–structure interaction problems in haemodynamics", *Journal of Computational and Applied Mathematics*, Current Trends and Progresses in Scientific Computation, vol. 265, pp. 120–138, Aug. 2014. DOI: 10.1016/j.cam.2013.09.049 (Cited on page 18).

[69] A. Quarteroni, A. Manzoni, and C. Vergara, "The cardiovascular system: Mathematical modelling, numerical algorithms and clinical applications", *Acta Numerica*, vol. 26, pp. 365–590, 2017. DOI: 10.1017/S0962492917000046 (Cited on page 18).

[70] L. Taelman, J. Degroote, P. Verdonck, J. Vierendeels, and P. Segers, "Modeling Hemodynamics in Vascular Networks Using a Geometrical Multiscale Approach: Numerical Aspects", en, *Annals of Biomedical Engineering*, vol. 41, no. 7, pp. 1445–1458, Dec. 2012. DOI: 10.1007/s10439-012-0717-y (Cited on pages 18, 31).

[71] A. Quarteroni, A. Veneziani, and C. Vergara, "Geometric multiscale modeling of the cardiovascular system, between theory and practice", *Computer Methods in Applied Mechanics and Engineering*, vol. 302, pp. 193–252, Apr. 2016. DOI: 10.1016/j.cma.2016.01.007 (Cited on pages 18, 19, 31, 86).

[72] M. Anliker, R. L. Rockwell, and E. Ogden, "Nonlinear analysis of flow pulses and shock waves in arteries", en, *Zeitschrift für angewandte Mathematik und Physik ZAMP*, vol. 22, no. 2, pp. 217–246, 1970. DOI: 10.1007/BF01591407 (Cited on pages 19, 44).

[73] N. Westerhof, G. Elzinga, and P. Sipkema, "An artificial arterial system for pumping hearts", ENG, *Journal of Applied Physiology*, vol. 31, no. 5, pp. 776–781, Nov. 1971 (Cited on pages 19, 21, 44).

[74] L. Formaggia, D. Lamponi, M. Tuveri, and A. Veneziani, "Numerical modeling of 1d arterial networks coupled with a lumped parameters description of the heart", *Computer Methods in Biomechanics and Biomedical Engineering*, vol. 9, no. 5, pp. 273–288, Oct. 2006. DOI: 10.1080/10255840600857767 (Cited on pages 19, 21).

[75] T. J. R. Hughes and J. Lubliner, “On the one-dimensional theory of blood flow in the larger vessels”, *Mathematical Biosciences*, vol. 18, no. 1, pp. 161–170, Oct. 1973. DOI: 10.1016/0025-5564(73)90027-8 (Cited on page 19).

[76] N. Stergiopulos, D. F. Young, and T. R. Rogge, “Computer simulation of arterial flow with applications to arterial and aortic stenoses”, *Journal of Biomechanics*, vol. 25, no. 12, pp. 1477–1488, Dec. 1992. DOI: 10.1016/0021-9290(92)90060-E (Cited on page 19).

[77] S. J. Sherwin, V. Franke, J. Peiró, and K. Parker, “One-dimensional modelling of a vascular network in space-time variables”, en, *Journal of Engineering Mathematics*, vol. 47, no. 3-4, pp. 217–250, Sep. 2003. DOI: 10.1023/B:ENGI.0000007979.32871.e2 (Cited on pages 19, 21, 23, 25, 43, 60, 61).

[78] K. S. Matthys, J. Alastruey, J. Peiró, A. W. Khir, P. Segers, *et al.*, “Pulse wave propagation in a model human arterial network: Assessment of 1-D numerical simulations against in vitro measurements”, *Journal of Biomechanics*, vol. 40, no. 15, pp. 3476–3486, Jan. 2007. DOI: 10.1016/j.jbiomech.2007.05.027 (Cited on pages 19, 45, 46, 58, 60, 62–64).

[79] J. Alastruey, A. W. Khir, K. S. Matthys, P. Segers, S. J. Sherwin, *et al.*, “Pulse wave propagation in a model human arterial network: Assessment of 1-D visco-elastic simulations against in vitro measurements”, *Journal of Biomechanics*, vol. 44, no. 12, pp. 2250–2258, Aug. 2011. DOI: 10.1016/j.jbiomech.2011.05.041 (Cited on pages 19, 24, 178, 179).

[80] M. S. Olufsen, C. S. Peskin, W. Y. Kim, E. M. Pedersen, A. Nadim, *et al.*, “Numerical Simulation and Experimental Validation of Blood Flow in Arteries with Structured-Tree Outflow Conditions”, en, *Annals of Biomedical Engineering*, vol. 28, no. 11, pp. 1281–1299, Nov. 2000. DOI: 10.1114/1.1326031 (Cited on pages 19, 21, 24, 47).

[81] A. Quarteroni, M. Tuveri, and A. Veneziani, “Computational vascular fluid dynamics: Problems, models and methods”, *Computing and Visualization in Science*, vol. 2, no. 4, pp. 163–97, 2000. DOI: 10.1007/s007910050039 (Cited on pages 19, 21, 30).

[82] P. J. Blanco, S. M. Watanabe, M. A. R. F. Passos, P. A. Lemos, and R. A. Feijóo, “An Anatomically Detailed Arterial Network Model for One-Dimensional Computational Hemodynamics”, *IEEE Transactions on Biomedical Engineering*, vol. 62, no. 2, pp. 736–753, Feb. 2015. DOI: 10.1109/TBME.2014.2364522 (Cited on pages 19, 117).

[83] T. Du, D. Hu, and D. Cai, “Outflow Boundary Conditions for Blood Flow in Arterial Trees”, *PLoS ONE*, vol. 10, no. 5, May 2015. DOI: 10.1371/journal.pone.0128597 (Cited on page 20).

[84] J. Y. Moon, D. C. Suh, Y. S. Lee, Y. W. Kim, and J. S. Lee, “Considerations of Blood Properties, Outlet Boundary Conditions and Energy Loss Approaches in Computational Fluid Dynamics Modeling”, *Neurointervention*, vol. 9, no. 1, pp. 1–8, Feb. 2014. DOI: 10.5469/neuroint.2014.9.1.1 (Cited on page 20).

[85] J. Alastruey, K. H. Parker, J. Peiró, S. M. Byrd, and S. J. Sherwin, “Modelling the circle of Willis to assess the effects of anatomical variations and occlusions on cerebral flows”, eng, *Journal of Biomechanics*, vol. 40, no. 8, pp. 1794–1805, 2007. DOI: 10.1016/j.jbiomech.2006.07.008 (Cited on page 21).

[86] S. J. Sherwin, V. Franke, J. Peiró, and K. Parker, “One-dimensional modelling of a vascular network in space-time variables”, en, *Journal of Engineering Mathematics*, vol. 47, no. 3-4, pp. 217–250, DOI: 10.1023/B:ENGI.0000007979.32871.e2 (Cited on page 21).

[87] J. Alastruey, K. H. Parker, and S. J. Sherwin, “Lumped parameter outflow models for 1-D blood flow simulations: Effect on pulse waves and parameter estimation”, *Commun. Comput. Phys*, 2008 (Cited on pages 21, 56).

[88] S. Epstein, M. Willemet, P. J. Chowienczyk, and J. Alastruey, “Reducing the number of parameters in 1d arterial blood flow modeling: Less is more for patient-specific simulations”, *American Journal of Physiology - Heart and Circulatory Physiology*, vol. 309, no. 1, H222–H234, Jul. 2015. DOI: 10.1152/ajpheart.00857.2014 (Cited on page 21).

[89] K. DeVault, P. A. Gremaud, V. Novak, M. S. Olufsen, G. Vernières, *et al.*, “Blood Flow in the Circle of Willis: Modeling and Calibration”, en, *Multiscale Modeling & Simulation*, vol. 7, no. 2, pp. 888–909, Jan. 2008. DOI: 10.1137/07070231X (Cited on page 21).

[90] P. J. Blanco, S. M. Watanabe, and R. A. Feijóo, “Identification of vascular territory resistances in one-dimensional hemodynamics simulations”, *Journal of Biomechanics*, vol. 45, no. 12, pp. 2066–2073, Aug. 2012. DOI: 10.1016/j.jbiomech.2012.06.002 (Cited on page 21).

[91] M. S. Olufsen, “Structured tree outflow condition for blood flow in larger systemic arteries”, en, *American Journal of Physiology - Heart and Circulatory Physiology*, vol. 276, no. 1, H257–H268, Jan. 1999 (Cited on page 21).

[92] C. D. Murray, “The Physiological Principle of Minimum Work”, *Proceedings of the National Academy of Sciences of the United States of America*, vol. 12, no. 3, pp. 207–214, Mar. 1926 (Cited on pages 21, 116).

[93] M. Zamir, “On Fractal Properties of Arterial Trees”, *Journal of Theoretical Biology*, vol. 197, no. 4, pp. 517–526, Apr. 1999. DOI: 10.1006/jtbi.1998.0892 (Cited on pages 21, 117).

[94] W. Cousins and P. A. Gremaud, “Boundary conditions for hemodynamics: The structured tree revisited”, *Journal of Computational Physics*, vol. 231, no. 18, pp. 6086–6096, Jul. 2012. DOI: 10.1016/j.jcp.2012.04.038 (Cited on page 21).

[95] D. Guan, F. Liang, and P. A. Gremaud, “Comparison of the Windkessel model and structured-tree model applied to prescribe outflow boundary conditions for a one-dimensional arterial tree model”, *Journal of Biomechanics*, vol. 49, no. 9, pp. 1583–1592, Jun. 2016. DOI: 10.1016/j.jbiomech.2016.03.037 (Cited on pages 21, 22).

[96] I. Vignon-Clementel, C. A. Figueroa, K. E. Jansen, and C. A. Taylor, “Outflow boundary conditions for 3d simulations of non-periodic blood flow and pressure fields in deformable arteries”, *Computer Methods in Biomechanics and Biomedical Engineering*, vol. 13, no. 5, pp. 625–640, Oct. 2010, arXiv: 1012.0736. DOI: 10.1080/10255840903413565 (Cited on page 21).

[97] M. U. Qureshi, G. D. Vaughan, C. Sainsbury, M. Johnson, C. S. Peskin, *et al.*, “Numerical simulation of blood flow and pressure drop in the pulmonary arterial and venous circulation”, *Biomechanics and modeling in mechanobiology*, vol. 13, no. 5, pp. 1137–1154, Oct. 2014. DOI: 10.1007/s10237-014-0563-y (Cited on pages 21, 25).

[98] P. Perdikaris, L. Grinberg, and G. E. Karniadakis, “An Effective Fractal-Tree Closure Model for Simulating Blood Flow in Large Arterial Networks”, en, *Annals of Biomedical Engineering*, vol. 43, no. 6, pp. 1432–1442, Jun. 2015. DOI: 10.1007/s10439-014-1221-3 (Cited on page 21).

[99] D. Valdez-Jasso, D. Bia, Y. Zócalo, R. L. Armentano, M. A. Haider, *et al.*, "Linear and Nonlinear Viscoelastic Modeling of Aorta and Carotid Pressure–Area Dynamics Under In Vivo and Ex Vivo Conditions", en, *Annals of Biomedical Engineering*, vol. 39, no. 5, pp. 1438–1456, May 2011. DOI: 10.1007/s10439-010-0236-7 (Cited on pages 21, 24).

[100] L. Formaggia, D. Lamponi, and A. Quarteroni, "One-dimensional models for blood flow in arteries", en, *Journal of Engineering Mathematics*, vol. 47, no. 3-4, pp. 251–276, Aug. 2003. DOI: 10.1023/B:ENGI.0000007980.01347.29 (Cited on pages 23, 43, 44, 74).

[101] J. Alastruey, K. H. Parker, and S. J. Sherwin, "Arterial pulse wave haemodynamics", in *11th International Conference on Pressure Surges*, S Anderson, Ed., Virtual PiE Led t/a BHR Group, 2012, pp. 401–443 (Cited on pages 24, 45, 60–62).

[102] P. B. Canham, H. M. Finlay, J. G. Dixon, D. R. Boughner, and A. Chen, "Measurements from light and polarised light microscopy of human coronary arteries fixed at distending pressure", eng, *Cardiovascular Research*, vol. 23, no. 11, pp. 973–982, Nov. 1989 (Cited on page 24).

[103] J. Zhou and Y. C. Fung, "The degree of nonlinearity and anisotropy of blood vessel elasticity", en, *Proceedings of the National Academy of Sciences*, vol. 94, no. 26, pp. 14 255–14 260, Dec. 1997 (Cited on page 24).

[104] P. Reymond, F. Merenda, F. Perren, D. Rüfenacht, and N. Stergiopulos, "Validation of a one-dimensional model of the systemic arterial tree", en, *American Journal of Physiology - Heart and Circulatory Physiology*, vol. 297, no. 1, H208–H222, Jul. 2009. DOI: 10.1152/ajpheart.00037.2009 (Cited on pages 24, 100, 102).

[105] A. S. Liberson, J. S. Lillie, S. W. Day, and D. A. Borkholder, "A physics based approach to the pulse wave velocity prediction in compliant arterial segments", *Journal of Biomechanics*, vol. 49, no. 14, pp. 3460–3466, Oct. 2016. DOI: 10.1016/j.jbiomech.2016.09.013 (Cited on pages 24, 40, 96, 101).

[106] J. Humphrey and M Epstein, "Cardiovascular Solid Mechanics: Cells, Tissues, and Organs", en, *Applied Mechanics Reviews*, vol. 55, no. 5, B103, 2002. DOI: 10.1115/1.1497492 (Cited on page 24).

[107] L. O. Muller, "Mathematical modelling and simulation of the human circulation with emphasis on the venous system: Application to the CCSVI condition", phd, University of Trento, Apr. 2014 (Cited on page 25).

[108] B. A. Martin, P. Reymond, J. Novy, O. Balédent, and N. Stergiopulos, "A coupled hydrodynamic model of the cardiovascular and cerebrospinal fluid system", eng, *American Journal of Physiology. Heart and Circulatory Physiology*, vol. 302, no. 7, H1492–1509, Apr. 2012. DOI: 10.1152/ajpheart.00658.2011 (Cited on page 25).

[109] K. H. Parker, "A brief history of arterial wave mechanics", *Medical & Biological Engineering & Computing*, vol. 47, no. 2, pp. 111–118, Feb. 2009. DOI: 10.1007/s11517-009-0440-5 (Cited on page 25).

[110] J. Peiró and A. Veneziani, "Reduced models of the cardiovascular system", en, in *Cardiovascular Mathematics*, ser. MS&A 1, L. Formaggia, A. Quarteroni, and A. Veneziani, Eds., Springer Milan, 2009, pp. 347–394. DOI: 10.1007/978-88-470-1152-6_10 (Cited on page 25).

[111] V. L. Berdichevsky, "Principle of Least Dissipation", en, in *Variational Principles of Continuum Mechanics*, ser. Interaction of Mechanics and Mathematics, Springer Berlin Heidelberg, 2009, pp. 495–508. DOI: 10.1007/978-3-540-88467-5_12 (Cited on page 26).

[112] E. Kock and L. Olson, “Fluid-structure interaction analysis by the finite element method–a variational approach”, en, *International Journal for Numerical Methods in Engineering*, vol. 31, no. 3, pp. 463–491, Mar. 1991. DOI: 10.1002/nme.1620310305 (Cited on page 26).

[113] W. H. Reed and T. R. Hill, “Triangular mesh methods for the neutron transport equation”, English, Los Alamos Scientific Lab., N.Mex. (USA), Tech. Rep. LA-UR-73-479; CONF-730414-2, Oct. 1973 (Cited on page 26).

[114] A. Harten, “High resolution schemes for hyperbolic conservation laws”, *Journal of Computational Physics*, vol. 49, no. 3, pp. 357–393, Mar. 1983. DOI: 10.1016/0021-9991(83)90136-5 (Cited on pages 27, 44, 53).

[115] S. K. Godunov, “A difference method for numerical calculation of discontinuous solutions of the equations of hydrodynamics”, *Mat. Sb. (N.S.)*, vol. 47 (89), no. 3, pp. 271–306, 1959 (Cited on page 27).

[116] R. J. LeVeque, *Finite Volume Methods for Hyperbolic Problems*, ser. Cambridge Texts in Applied Mathematics. Cambridge: Cambridge University Press, 2002. DOI: 10.1017/CBO9780511791253 (Cited on pages 27, 54, 55, 58, 77).

[117] *Cardiovascular Mathematics - Modeling and simulation of the | Luca Formaggia | Springer* (Cited on pages 27, 33, 73, 83).

[118] G. Schmitz, “Lighthill, J., Waves in Fluids. Cambridge-London-New York-Melbourne, Cambridge University Press 1978. XV, 504 S., £ 17.50 A”, en, *ZAMM - Journal of Applied Mathematics and Mechanics / Zeitschrift für Angewandte Mathematik und Mechanik*, vol. 59, no. 11, pp. 671–671, DOI: 10.1002/zamm.19790591148 (Cited on page 27).

[119] P. Moireau, C. Bertoglio, N. Xiao, C. A. Figueroa, C. A. Taylor, *et al.*, “Sequential identification of boundary support parameters in a fluid-structure vascular model using patient image data”, en, *Biomechanics and Modeling in Mechanobiology*, vol. 12, no. 3, pp. 475–496, Jun. 2013. DOI: 10.1007/s10237-012-0418-3 (Cited on page 29).

[120] M. Cluitmans, R. Peeters, R. Westra, and P. Volders, “Noninvasive reconstruction of cardiac electrical activity: Update on current methods, applications and challenges”, *Netherlands Heart Journal*, vol. 23, no. 6, pp. 301–311, Jun. 2015. DOI: 10.1007/s12471-015-0690-9 (Cited on page 29).

[121] M. Perego, A. Veneziani, and C. Vergara, “A Variational Approach for Estimating the Compliance of the Cardiovascular Tissue: An Inverse Fluid-Structure Interaction Problem”, *SIAM Journal on Scientific Computing*, vol. 33, no. 3, pp. 1181–1211, Jan. 2011. DOI: 10.1137/100808277 (Cited on page 29).

[122] P. E. Barbone and A. A. Oberai, “Elastic modulus imaging: Some exact solutions of the compressible elastography inverse problem”, eng, *Physics in Medicine and Biology*, vol. 52, no. 6, pp. 1577–1593, Mar. 2007. DOI: 10.1088/0031-9155/52/6/003 (Cited on page 29).

[123] L. S. Graham and D. Kilpatrick, “Estimation of the bidomain conductivity parameters of cardiac tissue from extracellular potential distributions initiated by point stimulation”, eng, *Annals of Biomedical Engineering*, vol. 38, no. 12, pp. 3630–3648, Dec. 2010. DOI: 10.1007/s10439-010-0119-y (Cited on page 29).

[124] S. Pant, B. Fabrèges, J.-F. Gerbeau, and I. E. Vignon-Clementel, “A methodological paradigm for patient-specific multi-scale CFD simulations: From clinical measurements to parameter estimates for individual analysis”, en, *International Journal for Numerical Methods in Biomedical Engineering*, vol. 30, no. 12, pp. 1614–1648, Dec. 2014. DOI: 10.1002/cnm.2692 (Cited on pages 29, 95).

[125] I. Sazonov, A. W. Khir, W. S. Hacham, E. Boileau, J. M. Carson, *et al.*, "A novel method for non-invasively detecting the severity and location of aortic aneurysms", en, *Biomechanics and Modeling in Mechanobiology*, pp. 1–18, Feb. 2017. DOI: 10.1007/s10237-017-0884-8 (Cited on page 29).

[126] M. McGarry, P. Nauleau, I. Apostolakis, and E. Konofagou, "In vivo repeatability of the pulse wave inverse problem in human carotid arteries", *Journal of Biomechanics*, vol. 64, pp. 136–144, Nov. 2017. DOI: 10.1016/j.jbiomech.2017.09.017 (Cited on page 29).

[127] K. Perktold, M. Prosi, and P. Zunino, "Mathematical models of mass transfer in the vascular walls", en, in *Cardiovascular Mathematics*, ser. MS&A 1, L. Formaggia, A. Quarteroni, and A. Veneziani, Eds., Springer Milan, 2009, pp. 243–278. DOI: 10.1007/978-88-470-1152-6_7 (Cited on page 30).

[128] C. A. Taylor, T. J. R. Hughes, and C. K. Zarins, "Finite element modeling of blood flow in arteries", *Computer Methods in Applied Mechanics and Engineering*, vol. 158, no. 1, pp. 155–196, May 1998. DOI: 10.1016/S0045-7825(98)80008-X (Cited on page 30).

[129] C. A. Figueroa, I. E. Vignon-Clementel, K. E. Jansen, T. J. R. Hughes, and C. A. Taylor, "A coupled momentum method for modeling blood flow in three-dimensional deformable arteries", *Computer Methods in Applied Mechanics and Engineering*, John H. Argyris Memorial Issue. Part II, vol. 195, no. 41–43, pp. 5685–5706, Aug. 2006. DOI: 10.1016/j.cma.2005.11.011 (Cited on page 30).

[130] C. Farhat, K. G. van der Zee, and P. Geuzaine, "Provably second-order time-accurate loosely-coupled solution algorithms for transient nonlinear computational aeroelasticity", *Computer Methods in Applied Mechanics and Engineering*, Fluid-Structure Interaction, vol. 195, no. 17–18, pp. 1973–2001, Mar. 2006. DOI: 10.1016/j.cma.2004.11.031 (Cited on page 30).

[131] L. Formaggia, F. Nobile, A. Quarteroni, and A. Veneziani, "Multiscale modelling of the circulatory system: A preliminary analysis", en, *Computing and Visualization in Science*, vol. 2, no. 2-3, pp. 75–83, Jun. 1999. DOI: 10.1007/s007910050030 (Cited on pages 30, 86).

[132] L. Formaggia, J. Gerbeau, F. Nobile, and A. Quarteroni, "Numerical Treatment of Defective Boundary Conditions for the Navier–Stokes Equations", *SIAM Journal on Numerical Analysis*, vol. 40, no. 1, pp. 376–401, Jan. 2002. DOI: 10.1137/S003614290038296X (Cited on pages 30, 31).

[133] S. A. Urquiza, P. J. Blanco, M. J. Vénere, and R. A. Feijóo, "Multidimensional modelling for the carotid artery blood flow", *Computer Methods in Applied Mechanics and Engineering*, vol. 195, no. 33–36, pp. 4002–4017, Jul. 2006. DOI: 10.1016/j.cma.2005.07.014 (Cited on pages 30, 31).

[134] F. Nobile, "Coupling strategies for the numerical simulation of blood flow in deformable arteries by 3d and 1d models", *Mathematical and Computer Modelling*, Trends in Application of Mathematics to MedicineTrends in Application of Mathematics to Medicine, vol. 49, no. 11–12, pp. 2152–2160, Jun. 2009. DOI: 10.1016/j.mcm.2008.07.019 (Cited on page 30).

[135] P. J. Blanco and R. A. Feijóo, "A dimensionally-heterogeneous closed-loop model for the cardiovascular system and its applications", *Medical Engineering & Physics*, vol. 35, no. 5, pp. 652–667, May 2013. DOI: 10.1016/j.medengphy.2012.07.011 (Cited on page 30).

[136] L. Formaggia, J. F. Gerbeau, F. Nobile, and A. Quarteroni, "On the coupling of 3d and 1d Navier–Stokes equations for flow problems in compliant vessels", *Computer Methods in Applied Mechanics and Engineering*, Minisymposium on Methods for Flow Simulation and Modeling, vol. 191, no. 6–7, pp. 561–582, Dec. 2001. DOI: 10.1016/S0045-7825(01)00302-4 (Cited on pages 30, 32).

[137] J. G. Heywood, R. Rannacher, and S. Turek, “Artificial Boundaries and Flux and Pressure Conditions for the Incompressible Navier–Stokes Equations”, en, *International Journal for Numerical Methods in Fluids*, vol. 22, no. 5, pp. 325–352, Mar. 1996. DOI: 10.1002/(SICI)1097-0363(19960315)22:5<325::AID-FLD307>3.0.CO;2-Y (Cited on page 31).

[138] P. J. Blanco, R. A. Feijóo, and S. A. Urquiza, “A unified variational approach for coupling 3d–1d models and its blood flow applications”, *Computer Methods in Applied Mechanics and Engineering*, vol. 196, no. 41–44, pp. 4391–4410, Sep. 2007. DOI: 10.1016/j.cma.2007.05.008 (Cited on page 31).

[139] J. Galindo, A. Tiseira, P. Fajardo, and R. Navarro, “Coupling methodology of 1d finite difference and 3d finite volume CFD codes based on the Method of Characteristics”, *Mathematical and Computer Modelling*, Mathematical models of addictive behaviour, medicine & engineering, vol. 54, no. 7–8, pp. 1738–1746, Oct. 2011. DOI: 10.1016/j.mcm.2010.11.078 (Cited on page 32).

[140] Y. Bazilevs, M.-C. Hsu, Y. Zhang, W. Wang, X. Liang, *et al.*, “A fully-coupled fluid-structure interaction simulation of cerebral aneurysms”, en, *Computational Mechanics*, vol. 46, no. 1, pp. 3–16, Oct. 2009. DOI: 10.1007/s00466-009-0421-4 (Cited on page 32).

[141] H. Ho, G. Sands, H. Schmid, K. Mithraratne, G. Mallinson, *et al.*, “A Hybrid 1d and 3d Approach to Hemodynamics Modelling for a Patient-Specific Cerebral Vasculature and Aneurysm”, en, in *Medical Image Computing and Computer-Assisted Intervention – MICCAI 2009*, ser. Lecture Notes in Computer Science 5762, G.-Z. Yang, D. Hawkes, D. Rueckert, A. Noble, and C. Taylor, Eds., Springer Berlin Heidelberg, Sep. 2009, pp. 323–330. DOI: 10.1007/978-3-642-04271-3_40 (Cited on page 32).

[142] E. A. Finol and C. H. Amon, “Blood flow in abdominal aortic aneurysms: Pulsatile flow hemodynamics”, ENG, *Journal of Biomechanical Engineering*, vol. 123, no. 5, pp. 474–484, Oct. 2001 (Cited on page 32).

[143] S. Chandra, S. S. Raut, A. Jana, R. W. Biederman, M. Doyle, *et al.*, “Fluid-Structure Interaction Modeling of Abdominal Aortic Aneurysms: The Impact of Patient-Specific Inflow Conditions and Fluid/Solid Coupling”, *Journal of Biomechanical Engineering*, vol. 135, no. 8, pp. 0 810 011–08 100 114, Aug. 2013. DOI: 10.1115/1.4024275 (Cited on page 32).

[144] J. Gunn, N. Arnold, K. H. Chan, L. Shepherd, D. C. Cumberland, *et al.*, “Coronary artery stretch versus deep injury in the development of in-stent neointima”, eng, *Heart (British Cardiac Society)*, vol. 88, no. 4, pp. 401–405, Oct. 2002 (Cited on page 33).

[145] D. Dvir, H. Marom, A. Assali, and R. Kornowski, “Bifurcation lesions in the coronary arteries: Early experience with a novel 3-dimensional imaging and quantitative analysis before and after stenting”, eng, *EuroIntervention: Journal of EuroPCR in Collaboration with the Working Group on Interventional Cardiology of the European Society of Cardiology*, vol. 3, no. 1, pp. 95–99, May 2007 (Cited on page 33).

[146] E. Cecchi, C. Giglioli, S. Valente, C. Lazzeri, G. F. Gensini, *et al.*, “Role of hemodynamic shear stress in cardiovascular disease”, eng, *Atherosclerosis*, vol. 214, no. 2, pp. 249–256, Feb. 2011. DOI: 10.1016/j.atherosclerosis.2010.09.008 (Cited on page 33).

[147] H. J. Kim, I. E. Vignon-Clementel, J. S. Coogan, C. A. Figueroa, K. E. Jansen, *et al.*, “Patient-Specific Modeling of Blood Flow and Pressure in Human Coronary Arteries”, en, *Annals of Biomedical Engineering*, vol. 38, no. 10, pp. 3195–3209, Jun. 2010. DOI: 10.1007/s10439-010-0083-6 (Cited on page 33).

[148] S. Morlacchi and F. Migliavacca, “Modeling Stented Coronary Arteries: Where We are, Where to Go”, en, *Annals of Biomedical Engineering*, vol. 41, no. 7, pp. 1428–1444, Jul. 2013. DOI: 10.1007/s10439-012-0681-6 (Cited on page 33).

[149] C. Capelli, G. Biglino, L. Petrini, F. Migliavacca, D. Cosentino, *et al.*, “Finite Element Strategies to Satisfy Clinical and Engineering Requirements in the Field of Percutaneous Valves”, en, *Annals of Biomedical Engineering*, vol. 40, no. 12, pp. 2663–2673, Dec. 2012. DOI: 10.1007/s10439-012-0617-1 (Cited on page 33).

[150] E. Köklü,
bibinitperiodI. Ö. Yüksel, Ş. Arslan, N. Bayar, F. Köklü, *et al.*, “Short and Long-Term Effect of Carotid Artery Stenting on Arterial Blood Pressure Measured through Ambulatory Blood Pressure Monitoring”, *Acta Cardiologica Sinica*, vol. 32, no. 3, pp. 343–350, May 2016. DOI: 10.6515/ACS20150604A (Cited on page 33).

[151] G. J. Hall and E. P. Kasper, “Comparison of Element Technologies for Modeling Stent Expansion”, *Journal of Biomechanical Engineering*, vol. 128, no. 5, pp. 751–756, Mar. 2006. DOI: 10.1115/1.2264382 (Cited on page 33).

[152] P. A. James, S. Oparil, B. L. Carter, W. C. Cushman, C. Dennison-Himmelfarb, *et al.*, “2014 Evidence-Based Guideline for the Management of High Blood Pressure in Adults: Report From the Panel Members Appointed to the Eighth Joint National Committee (JNC 8)”, en, *JAMA*, vol. 311, no. 5, pp. 507–520, Feb. 2014. DOI: 10.1001/jama.2013.284427 (Cited on page 34).

[153] X. Ding and Y.-T. Zhang, “Pulse transit time technique for cuffless unobtrusive blood pressure measurement: From theory to algorithm”, en, *Biomedical Engineering Letters*, vol. 9, no. 1, pp. 37–52, Feb. 2019. DOI: 10.1007/s13534-019-00096-x (Cited on pages 34, 36–38, 136).

[154] Pickering Thomas G., Hall John E., Appel Lawrence J., Falkner Bonita E., Graves John, *et al.*, “Recommendations for Blood Pressure Measurement in Humans and Experimental Animals”, *Circulation*, vol. 111, no. 5, pp. 697–716, Feb. 2005. DOI: 10.1161/01.CIR.0000154900.76284.F6 (Cited on page 35).

[155] Dolan Eamon, Stanton Alice, Thijs Lut, Hinedi Kareem, Atkins Neil, *et al.*, “Superiority of Ambulatory Over Clinic Blood Pressure Measurement in Predicting Mortality”, *Hypertension*, vol. 46, no. 1, pp. 156–161, Jul. 2005. DOI: 10.1161/01.HYP.0000170138.56903.7a (Cited on page 35).

[156] “A Randomized Trial of Intensive versus Standard Blood-Pressure Control”, *New England Journal of Medicine*, vol. 373, no. 22, pp. 2103–2116, Nov. 2015. DOI: 10.1056/NEJMoa1511939 (Cited on page 35).

[157] Y. Zheng, X. Ding, C. C. Y. Poon, B. P. L. Lo, H. Zhang, *et al.*, “Unobtrusive Sensing and Wearable Devices for Health Informatics”, *IEEE Transactions on Biomedical Engineering*, vol. 61, no. 5, pp. 1538–1554, May 2014. DOI: 10.1109/TBME.2014.2309951 (Cited on page 35).

[158] L. Peter, N. Noury, and M. Cerny, “A review of methods for non-invasive and continuous blood pressure monitoring: Pulse transit time method is promising?”, *IRBM*, vol. 35, no. 5, pp. 271–282, Oct. 2014. DOI: 10.1016/j.irbm.2014.07.002 (Cited on page 35).

[159] D. Buxi, J.-M. Redouté, and M. R. Yuce, “A survey on signals and systems in ambulatory blood pressure monitoring using pulse transit time”, eng, *Physiological Measurement*, vol. 36, no. 3, R1–26, Mar. 2015. DOI: 10.1088/0967-3334/36/3/R1 (Cited on page 35).

[160] J. M. J. Huttunen, L. Karkkainen, and H. Lindholm, “Improving pulse transit time estimation of aortic pulse wave velocity and blood pressure using machine learning and simulated training data”, en, p. 38, (Cited on pages 35, 41).

[161] P. Tavallali, M. Razavi, and N. M. Pahlevan, "Artificial Intelligence Estimation of Carotid-Femoral Pulse Wave Velocity using Carotid Waveform", *Scientific Reports*, vol. 8, Jan. 2018. DOI: 10.1038/s41598-018-19457-0 (Cited on pages 35, 42, 44).

[162] G. Weltman, G. Sullivan, and D. Bredon, "The continuous measurement of arterial pulse wave velocity", en, *Medical electronics and biological engineering*, vol. 2, no. 2, pp. 145–154, Apr. 1964. DOI: 10.1007/BF02484213 (Cited on page 36).

[163] A. Steptoe, H. Smulyan, and B. Gribbin, "Pulse Wave Velocity and Blood Pressure Change: Calibration and Applications", en, *Psychophysiology*, vol. 13, no. 5, pp. 488–493, 1976. DOI: 10.1111/j.1469-8986.1976.tb00866.x (Cited on page 36).

[164] P. A. Obrist, K. C. Light, J. A. McCubbin, J. S. Hutcheson, and J. L. Hoffer, "Pulse transit time: Relationship to blood pressure", en, *Behavior Research Methods & Instrumentation*, vol. 10, no. 5, pp. 623–626, Sep. 1978. DOI: 10.3758/BF03205360 (Cited on page 36).

[165] G. V. Marie, C. R. Lo, J. V. Jones, and D. W. Johnston, "The Relationship between Arterial Blood Pressure and Pulse Transit Time During Dynamic and Static Exercise", en, *Psychophysiology*, vol. 21, no. 5, pp. 521–527, 1984. DOI: 10.1111/j.1469-8986.1984.tb00235.x (Cited on page 36).

[166] W. B. Fye, "A History of the origin, evolution, and impact of electrocardiography", *The American Journal of Cardiology*, vol. 73, no. 13, pp. 937–949, May 1994. DOI: 10.1016/0002-9149(94)90135-X (Cited on pages 36, 118).

[167] I. Starr, A. J. Rawson, H. A. Schroeder, and N. R. Joseph, "Studies on the estimation of cardiac ouptut in man, and of abnormalities in cardiac function, from the heart's recoil and the blood's impacts; the ballistocardiogram", *American Journal of Physiology-Legacy Content*, vol. 127, no. 1, pp. 1–28, Jul. 1939. DOI: 10.1152/ajplegacy.1939.127.1.1 (Cited on pages 36, 118).

[168] O. T. Inan, P. Migeotte, K. Park, M. Etemadi, K. Tavakolian, *et al.*, "Ballistocardiography and Seismocardiography: A Review of Recent Advances", *IEEE Journal of Biomedical and Health Informatics*, vol. 19, no. 4, pp. 1414–1427, Jul. 2015. DOI: 10.1109/JBHI.2014.2361732 (Cited on pages 36, 118).

[169] A. B. Hertzman, "The blood supply of various skin areas as estimated by the photoelectric plethysmograph", *American Journal of Physiology-Legacy Content*, vol. 124, no. 2, pp. 328–340, Oct. 1938. DOI: 10.1152/ajplegacy.1938.124.2.328 (Cited on pages 36, 118).

[170] L. A. Geddes, M. H. Voelz, C. F. Babbs, J. D. Bourland, and W. A. Tacker, "Pulse Transit Time as an Indicator of Arterial Blood Pressure", en, *Psychophysiology*, vol. 18, no. 1, pp. 71–74, 1981. DOI: 10.1111/j.1469-8986.1981.tb01545.x (Cited on page 36).

[171] M. H. Pollak and P. A. Obrist, "Aortic-Radial Pulse Transit Time and ECG Q-Wave to Radial Pulse Wave Interval as Indices of Beat-By-Beat Blood Pressure Change", en, *Psychophysiology*, vol. 20, no. 1, pp. 21–28, 1983. DOI: 10.1111/j.1469-8986.1983.tb00895.x (Cited on page 36).

[172] N. Westerhof, N. Stergiopulos, and M. I. M. Noble, "Wave Travel and Velocity", en, in *Snapshots of Hemodynamics: An Aid for Clinical Research and Graduate Education*, N. Westerhof, N. Stergiopulos, and M. I. Noble, Eds., Boston, MA: Springer US, 2010, pp. 139–146. DOI: 10.1007/978-1-4419-6363-5_20 (Cited on page 38).

[173] J. Alastruey, N. Xiao, H. Fok, T. Schaeffter, and C. A. Figueroa, "On the impact of modelling assumptions in multi-scale, subject-specific models of aortic haemodynamics", en, *Journal of The Royal Society Interface*, vol. 13, no. 119, p. 20 160 073, Jun. 2016. DOI: 10.1098/rsif.2016.0073 (Cited on pages 38, 96, 102–104).

[174] N. J. Conn, "(71) Applicants:David A . Borkholder, Canandaigua, NY (US); Nicholas J. Conn, Winston Salem , NC (US);Masoumeh Haghpanahi, Rochester, NY (US) (72) Inventors: David A . Borkholder, Canandaigua," en, p. 18, (Cited on page 38).

[175] Bank Alan J., Wang Hongyu, Holte James E., Mullen Kathleen, Shammas Roger, *et al.*, "Contribution of Collagen, Elastin, and Smooth Muscle to In Vivo Human Brachial Artery Wall Stress and Elastic Modulus", *Circulation*, vol. 94, no. 12, pp. 3263–3270, Dec. 1996. DOI: 10.1161/01.CIR.94.12.3263 (Cited on page 38).

[176] C. C. Y. Poon and Y. T. Zhang, "Cuff-less and Noninvasive Measurements of Arterial Blood Pressure by Pulse Transit Time", in *2005 IEEE Engineering in Medicine and Biology 27th Annual Conference*, Jan. 2005, pp. 5877–5880. DOI: 10.1109/IEMBS.2005.1615827 (Cited on page 39).

[177] W. Chen, T. Kobayashi, S. Ichikawa, Y. Takeuchi, and T. Togawa, "Continuous estimation of systolic blood pressure using the pulse arrival time and intermittent calibration", en, *Medical and Biological Engineering and Computing*, vol. 38, no. 5, pp. 569–574, Sep. 2000. DOI: 10.1007/BF02345755 (Cited on page 39).

[178] Y. Chen, C. Wen, G. Tao, M. Bi, and G. Li, "Continuous and Noninvasive Blood Pressure Measurement: A Novel Modeling Methodology of the Relationship Between Blood Pressure and Pulse Wave Velocity", en, *Annals of Biomedical Engineering*, vol. 37, no. 11, pp. 2222–2233, Nov. 2009. DOI: 10.1007/s10439-009-9759-1 (Cited on page 39).

[179] G. Lopez, M. Shuzo, H. Ushida, K. Hidaka, S. Yanagimoto, *et al.*, "BIO-05 CONTINUOUS BLOOD PRESSURE MONITORING IN DAILY LIFE(Bio-medical Equipments II,Technical Program of Oral Presentations)", *Proceedings of JSME-IIP/ASME-ISPS Joint Conference on Micromechatronics for Information and Precision Equipment : IIP/ISPS joint MIPE*, vol. 2009, pp. 223–224, 2009. DOI: 10.1299/jsmemipe.2009.223 (Cited on page 39).

[180] D. B. McCombie, A. T. Reisner, and H. H. Asada, "Motion based adaptive calibration of pulse transit time measurements to arterial blood pressure for an autonomous, wearable blood pressure monitor", in *2008 30th Annual International Conference of the IEEE Engineering in Medicine and Biology Society*, Aug. 2008, pp. 989–992. DOI: 10.1109/IEMBS.2008.4649321 (Cited on page 39).

[181] B. M. McCarthy, B. O\textquotesingleFlynn, and A. Mathewson, "An Investigation of Pulse Transit Time as a Non-Invasive Blood Pressure Measurement Method", en, *Journal of Physics: Conference Series*, vol. 307, p. 012 060, Aug. 2011. DOI: 10.1088/1742-6596/307/1/012060 (Cited on page 39).

[182] T Wibmer, K Doering, C Kropf-Sanchen, S Rüdiger, I Blanta, *et al.*, "Pulse Transit Time and Blood Pressure During Cardiopulmonary Exercise Tests", en, vol. 63, p. 10, 2014 (Cited on page 39).

[183] C. C. Y. Poon, Y. Zhang, and Y. Liu, "Modeling of Pulse Transit Time under the Effects of Hydrostatic Pressure for Cuffless Blood Pressure Measurements", in *2006 3rd IEEE/EMBS International Summer School on Medical Devices and Biosensors*, Sep. 2006, pp. 65–68. DOI: 10.1109/ISSMDBS.2006.360098 (Cited on pages 39, 127).

[184] J. Muehlsteff, X. L. Aubert, and M. Schuett, “Cuffless Estimation of Systolic Blood Pressure for Short Effort Bicycle Tests: The Prominent Role of the Pre-Ejection Period”, in *2006 International Conference of the IEEE Engineering in Medicine and Biology Society*, Aug. 2006, pp. 5088–5092. DOI: 10.1109/IEMBS.2006.260275 (Cited on pages 39, 40, 129).

[185] R. Mukkamala, J.-O. Hahn, O. T. Inan, L. K. Mestha, C.-S. Kim, *et al.*, “Toward Ubiquitous Blood Pressure Monitoring via Pulse Transit Time: Theory and Practice”, eng, *IEEE transactions on bio-medical engineering*, vol. 62, no. 8, pp. 1879–1901, Aug. 2015. DOI: 10.1109/TBME.2015.2441951 (Cited on pages 39, 42, 45).

[186] C. C. Young, J. B. Mark, W. White, A. DeBree, J. S. Vender, *et al.*, “Clinical evaluation of continuous noninvasive blood pressure monitoring: Accuracy and tracking capabilities”, en, *Journal of Clinical Monitoring*, vol. 11, no. 4, pp. 245–252, Jul. 1995. DOI: 10.1007/BF01617519 (Cited on page 39).

[187] P. Fung, G. Dumont, C. Ries, C. Mott, and M. Ansermino, “Continuous noninvasive blood pressure measurement by pulse transit time”, in *The 26th Annual International Conference of the IEEE Engineering in Medicine and Biology Society*, ISSN: null, vol. 1, Sep. 2004, pp. 738–741. DOI: 10.1109/IEMBS.2004.1403264 (Cited on page 39).

[188] M. Kachuee, M. M. Kiani, H. Mohammadzade, and M. Shabany, “Cuffless Blood Pressure Estimation Algorithms for Continuous Health-Care Monitoring”, *IEEE Transactions on Biomedical Engineering*, vol. 64, no. 4, pp. 859–869, Apr. 2017. DOI: 10.1109/TBME.2016.2580904 (Cited on page 39).

[189] Z. Ghasemi, C.-S. Kim, E. Ginsberg, J. Duell, A. Gupta, *et al.*, “Estimation of Central Aortic Blood Pressure From Non-Invasive Cuff Pressure Oscillation Signals via System Identification”, en, American Society of Mechanical Engineers Digital Collection, Feb. 2017. DOI: 10.1115/DSCC2016-9785 (Cited on page 40).

[190] J. Mariscal Harana, A. van Engelen, T. Schneider, M. Florkow, P. Charlton, *et al.*, “Non-invasive, MRI-based estimation of patient-specific aortic blood pressure using one-dimensional blood flow modelling”, *Artery Research*, vol. 20, pp. 54–55, Dec. 2017. DOI: 10.1016/j.artres.2017.10.036 (Cited on page 40).

[191] D. Lombardi, “Inverse problems in 1d hemodynamics on systemic networks: A sequential approach”, en, *International Journal for Numerical Methods in Biomedical Engineering*, vol. 30, no. 2, pp. 160–179, Feb. 2014. DOI: 10.1002/cnm.2596 (Cited on page 40).

[192] J. S. Lillie, A. S. Liberson, and D. A. Borkholder, “Improved Blood Pressure Prediction Using Systolic Flow Correction of Pulse Wave Velocity”, eng, *Cardiovascular Engineering and Technology*, vol. 7, no. 4, pp. 439–447, 2016. DOI: 10.1007/s13239-016-0281-y (Cited on pages 41, 66, 129).

[193] A. Chandrasekhar, C.-S. Kim, M. Naji, K. Natarajan, J.-O. Hahn, *et al.*, “Smartphone-based blood pressure monitoring via the oscillometric finger-pressing method”, *Science translational medicine*, vol. 10, no. 431, Mar. 2018. DOI: 10.1126/scitranslmed.aap8674 (Cited on page 41).

[194] N. Pahlevan, D. Rinderknecht, P. Tavallali, M. Razavi, T. Tran, *et al.*, “Noninvasive iPhone Measurement of Left Ventricular Ejection Fraction Using Intrinsic Frequency Methodology*”, ENGLISH, *Critical Care Medicine*, vol. 45, no. 7, pp. 1115–1120, Jul. 2017. DOI: 10.1097/CCM.0000000000002459 (Cited on page 41).

[195] K. Perktold, M. Resch, and R. O. Peter, “Three-dimensional numerical analysis of pulsatile flow and wall shear stress in the carotid artery bifurcation”, *Journal of Biomechanics*, vol. 24, no. 6, pp. 409–420, Jan. 1991. DOI: 10.1016/0021-9290(91)90029-M (Cited on page 43).

[196] S. Dong, J. Insley, N. T. Karonis, M. E. Papka, J. Binns, *et al.*, "Simulating and Visualizing the Human Arterial System on the TeraGrid", *Future Gener. Comput. Syst.*, vol. 22, no. 8, pp. 1011–1017, Oct. 2006. DOI: 10.1016/j.future.2006.03.019 (Cited on page 43).

[197] C. A. Figueroa, S. Baek, C. A. Taylor, and J. D. Humphrey, "A Computational Framework for Fluid-Solid-Growth Modeling in Cardiovascular Simulations", *Computer methods in applied mechanics and engineering*, vol. 198, no. 45-46, pp. 3583–3602, Sep. 2009. DOI: 10.1016/j.cma.2008.09.013 (Cited on page 43).

[198] T. M. J. v. Bakel, K. D. Lau, J. Hirsch-Romano, S. Trimarchi, A. L. Dorfman, *et al.*, "Patient-Specific Modeling of Hemodynamics: Supporting Surgical Planning in a Fontan Circulation Correction", en, *Journal of Cardiovascular Translational Research*, pp. 1–11, Jan. 2018. DOI: 10.1007/s12265-017-9781-x (Cited on page 43).

[199] L. M. Itu, P. Sharma, and C. Suciu, Eds., *Patient-specific Hemodynamic Computations: Application to Personalized Diagnosis of Cardiovascular Pathologies*, en. Springer International Publishing, 2017 (Cited on page 43).

[200] G. F. Mitchell, "Arterial Stiffness and Wave Reflection: Biomarkers of Cardiovascular Risk", *Artery research*, vol. 3, no. 2, pp. 56–64, Jun. 2009. DOI: 10.1016/j.artres.2009.02.002 (Cited on page 44).

[201] M. Djelić, S. Mazić, and D. Žikić, "A novel laboratory approach for the demonstration of hemodynamic principles: The arterial blood flow reflection", en, *Advances in Physiology Education*, vol. 37, no. 4, pp. 321–326, Dec. 2013. DOI: 10.1152/advan.00176.2012 (Cited on page 44).

[202] G. García, M. Teresa, T. Acevedo, M. Fernanda, M. Rodriguez Guzmán, *et al.*, "Can Pulse Transit Time Be Useful for Detecting Hypertension in Patients in a Sleep Unit?", es, *Archivos de Bronconeumología (English Edition)*, vol. 50, no. 7, pp. 278–284, Jul. 2014. DOI: 10.1016/j.arbr.2014.05.001 (Cited on page 44).

[203] F. Liang, D. Guan, and J. Alastruey, "Determinant Factors for Arterial Hemodynamics in Hypertension: Theoretical Insights From a Computational Model-Based Study", *Journal of Biomechanical Engineering*, vol. 140, no. 3, pp. 031 006–031006–14, Jan. 2018. DOI: 10.1115/1.4038430 (Cited on page 44).

[204] J. Y. A. Foo and C. S. Lim, "Pulse transit time as an indirect marker for variations in cardiovascular related reactivity", eng, *Technology and Health Care: Official Journal of the European Society for Engineering and Medicine*, vol. 14, no. 2, pp. 97–108, 2006 (Cited on page 44).

[205] G. Sharwood-Smith, J. Bruce, and G. Drummond, "Assessment of pulse transit time to indicate cardiovascular changes during obstetric spinal anaesthesia", en, *BJA: British Journal of Anaesthesia*, vol. 96, no. 1, pp. 100–105, Jan. 2006. DOI: 10.1093/bja/aei266 (Cited on page 44).

[206] J. Poleszczuk, M. Debowska, W. Dabrowski, A. Wojcik-Zaluska, W. Zaluska, *et al.*, "Subject-specific pulse wave propagation modeling: Towards enhancement of cardiovascular assessment methods", en, *PLOS ONE*, vol. 13, no. 1, e0190972, Jan. 2018. DOI: 10.1371/journal.pone.0190972 (Cited on page 44).

[207] Y. Shi, P. Lawford, and R. Hose, "Review of Zero-D and 1-D Models of Blood Flow in the Cardiovascular System", *BioMedical Engineering OnLine*, vol. 10, p. 33, Apr. 2011. DOI: 10.1186/1475-925X-10-33 (Cited on page 44).

[208] J. Humphrey and C. Taylor, "Intracranial and Abdominal Aortic Aneurysms: Similarities, Differences, and Need for a New Class of Computational Models", *Annual review of biomedical engineering*, vol. 10, pp. 221–246, 2008. DOI: 10.1146/annurev.bioeng.10.061807.160439 (Cited on page 44).

[209] A. S. Liberson, J. S. Lillie, S. W. Day, and D. A. Borkholder, “A physics based approach to the pulse wave velocity prediction in compliant arterial segments”, *Journal of Biomechanics*, vol. 49, no. 14, pp. 3460–3466, Oct. 2016. DOI: 10.1016/j.jbiomech.2016.09.013 (Cited on page 44).

[210] Y. S. Vahedein and A. S. Liberson, “Reduced Modeling Framework of Circulatory System Revisited”, en, Aug. 2017. DOI: 10.11159/ffhmt17.174 (Cited on pages 45, 177).

[211] Seyed Vahedein, Yashar, Y. Karnam, and A. S. Liberson, “Predictive Multiscale Approach (3d-1d) for Blood Flow Simulations in Cardiovascular Networks”, *IEEE Engineering in Medicine and Biology (EMBC) 2018*, p. 1, Nov. 2018 (Cited on page 45).

[212] J. Alastruey, A. W. Khir, K. S. Matthys, P. Segers, S. J. Sherwin, *et al.*, “Pulse wave propagation in a model human arterial network: Assessment of 1-D visco-elastic simulations against in vitro measurements”, *Journal of Biomechanics*, vol. 44, no. 12, pp. 2250–2258, Aug. 2011. DOI: 10.1016/j.jbiomech.2011.05.041 (Cited on pages 45, 50, 63, 64).

[213] J. Alastruey, N. Xiao, H. Fok, T. Schaeffter, and C. A. Figueroa, “On the impact of modelling assumptions in multi-scale, subject-specific models of aortic haemodynamics”, en, *Journal of The Royal Society Interface*, vol. 13, no. 119, p. 20 160 073, Jun. 2016. DOI: 10.1098/rsif.2016.0073 (Cited on pages 45, 46, 60, 65–71).

[214] A. M. Carek, J. Conant, A. Joshi, H. Kang, and O. T. Inan, “SeismoWatch: Wearable Cuffless Blood Pressure Monitoring Using Pulse Transit Time”, *Proc. ACM Interact. Mob. Wearable Ubiquitous Technol.*, vol. 1, no. 3, 40:1–40:16, Sep. 2017. DOI: 10.1145/3130905 (Cited on page 45).

[215] A. S. Liberson, Y. S. Vahedein, and D. A. Borkholder, “Application of Variational Principle to Form Reduced Fluid-Structure Interaction Models in Bifurcated”, en, *Journal of Fluid Flow, Heat and Mass Transfer (JFFHMT)*, vol. 4, no. 1, pp. 1–9, Aug. 2017 (Cited on pages 46, 47, 54, 66).

[216] V. L. Berdichevsky, “Variational Principles”, en, in *Variational Principles of Continuum Mechanics*, ser. Interaction of Mechanics and Mathematics, Springer Berlin Heidelberg, 2009, pp. 3–44. DOI: 10.1007/978-3-540-88467-5_1 (Cited on page 46).

[217] D. L. Schultz, D. S. Tunstall-Pedoe, G. d. J. Lee, A. J. Gunning, and B. J. Bellhouse, “Velocity Distribution and Transition in the Arterial System”, en, in *Ciba Foundation Symposium - Circulatory and Respiratory Mass Transport*, Wiley-Blackwell, 2008, pp. 172–202. DOI: 10.1002/9780470719671.ch11 (Cited on page 47).

[218] J. Peiró and A. Veneziani, “Reduced models of the cardiovascular system”, en, in *Cardiovascular Mathematics: Modeling and simulation of the circulatory system*, ser. MS&A, L. Formaggia, A. Quarteroni, and A. Veneziani, Eds., Milano: Springer Milan, 2009, pp. 347–394. DOI: 10.1007/978-88-470-1152-6_10 (Cited on pages 47, 53).

[219] S. J. Sherwin, L. Formaggia, J. Peiró, and V. Franke, “Computational modelling of 1d blood flow with variable mechanical properties and its application to the simulation of wave propagation in the human arterial system”, en, *International Journal for Numerical Methods in Fluids*, vol. 43, no. 6-7, pp. 673–700, Oct. 2003. DOI: 10.1002/fld.543 (Cited on page 47).

[220] N. Smith, A. Pullan, and P. Hunter, “An Anatomically Based Model of Transient Coronary Blood Flow in the Heart”, *SIAM Journal on Applied Mathematics*, vol. 62, no. 3, pp. 990–1018, Jan. 2002. DOI: 10.1137/S0036139999355199 (Cited on page 50).

[221] P. L. Roe, “Generalized formulation of TVD Lax-Wendroff schemes”, Tech. Rep., Oct. 1984 (Cited on page 53).

[222] M. Back, G. Kopchok, M. Mueller, D. Cavaye, C. Donayre, *et al.*, “Changes in arterial wall compliance after endovascular stenting”, English, *Journal of Vascular Surgery*, vol. 19, no. 5, pp. 905–911, May 1994. DOI: 10.1016/S0741-5214(94)70017-6 (Cited on page 53).

[223] S. Mungkasi and G. I. J. Ningrum, “Numerical solution to the linear acoustics equations”, *AIP Conference Proceedings*, vol. 1746, no. 1, p. 020 056, Jun. 2016. DOI: 10.1063/1.4953981 (Cited on page 53).

[224] Y. S. Vahedein and A. S. Liberson, “Validation of a Multi-branched Patient Specific Computational Model for Human Arterial Systems”, en, Jun. 2018. DOI: 10.11159/ffhmt18.156 (Cited on page 54).

[225] M. Willemet, V. Lacroix, and E. Marchandise, “Inlet boundary conditions for blood flow simulations in truncated arterial networks”, *Journal of Biomechanics*, vol. 44, no. 5, pp. 897–903, Mar. 2011. DOI: 10.1016/j.jbiomech.2010.11.036 (Cited on page 56).

[226] L. Grinberg and G. E. Karniadakis, “Outflow Boundary Conditions for Arterial Networks with Multiple Outlets”, en, *Annals of Biomedical Engineering*, vol. 36, no. 9, pp. 1496–1514, Sep. 2008. DOI: 10.1007/s10439-008-9527-7 (Cited on page 56).

[227] S. Vennin, A. Mayer, Y. Li, H. Fok, B. Clapp, *et al.*, “Noninvasive calculation of the aortic blood pressure waveform from the flow velocity waveform: A proof of concept”, *American Journal of Physiology - Heart and Circulatory Physiology*, vol. 309, no. 5, H969–H976, Sep. 2015. DOI: 10.1152/ajpheart.00152.2015 (Cited on page 60).

[228] J. E. Sharman, M. Stowasser, R. G. Fassett, T. H. Marwick, and S. S. Franklin, “Central blood pressure measurement may improve risk stratification”, en, *Journal of Human Hypertension*, vol. 22, no. 12, pp. 838–844, Dec. 2008. DOI: 10.1038/jhh.2008.71 (Cited on page 60).

[229] M. R. Nelson, J. Stepanek, M. Cevette, M. Covalciuc, R. T. Hurst, *et al.*, “Noninvasive Measurement of Central Vascular Pressures With Arterial Tonometry: Clinical Revival of the Pulse Pressure Waveform?”, *Mayo Clinic Proceedings*, vol. 85, no. 5, pp. 460–472, May 2010. DOI: 10.4065/mcp.2009.0336 (Cited on page 60).

[230] P. Reymond, F. Merenda, F. Perren, D. Rüfenacht, and N. Stergiopulos, “Validation of a one-dimensional model of the systemic arterial tree”, en, *American Journal of Physiology - Heart and Circulatory Physiology*, vol. 297, no. 1, H208–H222, Jul. 2009. DOI: 10.1152/ajpheart.00037.2009 (Cited on page 61).

[231] Y. S. Vahedein and A. S. Liberson, “Validation and Application of a Physically Nonlinear ID Computational Model for Bifurcated Arterial Networks*”, in *2018 40th Annual International Conference of the IEEE Engineering in Medicine and Biology Society (EMBC)*, Jul. 2018, pp. 5253–5256. DOI: 10.1109/EMBC.2018.8513448 (Cited on page 62).

[232] M. Dúóng, N Nguyen, and M. Staat, *Physical response of hyperelastic models for composite materials and soft tissues.* 3. Jan. 2015, vol. 2, pp. 1–18. DOI: 10.1186/s40540-015-0015-x (Cited on page 62).

[233] D. H. Bergel, “The dynamic elastic properties of the arterial wall”, *The Journal of Physiology*, vol. 156, no. 3, pp. 458–469, May 1961 (Cited on page 62).

[234] A. Ghigo, X.-F. Wang, R. Armentano, P.-Y. Lagrée, and J.-M. Fullana, “Linear and nonlinear viscoelastic arterial wall models: Application on animals”, *arXiv:1607.07973 [physics]*, Jul. 2016, arXiv: 1607.07973 (Cited on page 62).

[235] N. R. Gaddum, J. Alastruey, P. Beerbaum, P. Chowienczyk, and T. Schaeffter, "A Technical Assessment of Pulse Wave Velocity Algorithms Applied to Non-invasive Arterial Waveforms", en, *Annals of Biomedical Engineering*, vol. 41, no. 12, pp. 2617–2629, Dec. 2013. DOI: 10.1007/s10439-013-0854-y (Cited on pages 65, 67, 98, 99).

[236] S. E. Parazynski, B. J. Tucker, M. Aratow, A. Crenshaw, and A. R. Hargens, "Direct measurement of capillary blood pressure in the human lip", eng, *Journal of Applied Physiology (Bethesda, Md.: 1985)*, vol. 74, no. 2, pp. 946–950, Feb. 1993. DOI: 10.1152/jappl.1993.74.2.946 (Cited on page 65).

[237] B. Trachet, P. Reymond, J. Kips, A. Swillens, M. De Buyzere, *et al.*, "Numerical validation of a new method to assess aortic pulse wave velocity from a single recording of a brachial artery waveform with an occluding cuff", eng, *Annals of Biomedical Engineering*, vol. 38, no. 3, pp. 876–888, Mar. 2010. DOI: 10.1007/s10439-010-9945-1 (Cited on page 66).

[238] H. Obeid, G. Soulat, E. Mousseaux, S. Laurent, N. Stergiopulos, *et al.*, "Numerical assessment and comparison of pulse wave velocity methods aiming at measuring aortic stiffness", en, *Physiological Measurement*, vol. 38, no. 11, p. 1953, 2017. DOI: 10.1088/1361-6579/aa905a (Cited on page 66).

[239] S. C. Chapra and R. P. Canale, *Numerical Methods for Engineers: With Programming and Software Applications*, 3rd. New York, NY, USA: McGraw-Hill, Inc., 1997 (Cited on page 66).

[240] S. I. Rabben, N. Stergiopulos, L. R. Hellevik, O. A. Smiseth, S. Slørdahl, *et al.*, "An ultrasound-based method for determining pulse wave velocity in superficial arteries", *Journal of Biomechanics*, vol. 37, no. 10, pp. 1615–1622, Oct. 2004. DOI: 10.1016/j.jbiomech.2003.12.031 (Cited on page 68).

[241] G. K. Nazarian, W. R. Austin, S. A. Wegryn, H. Bjarnason, D. J. Stackhouse, *et al.*, "Venous recanalization by metallic stents after failure of balloon angioplasty or surgery: Four-year experience", eng, *Cardiovascular and Interventional Radiology*, vol. 19, no. 4, pp. 227–233, Aug. 1996 (Cited on page 73).

[242] G. R. Kol and P. Woafo, "The design of a reflectionless arterial prosthesis", *Journal of Biological Physics*, vol. 37, no. 1, pp. 51–60, Jan. 2011. DOI: 10.1007/s10867-010-9196-2 (Cited on page 73).

[243] M. Back, G. Kopchok, M. Mueller, D. Cavaye, C. Donayre, *et al.*, "Changes in arterial wall compliance after endovascular stenting", eng, *Journal of Vascular Surgery*, vol. 19, no. 5, pp. 905–911, May 1994 (Cited on page 73).

[244] A. Tortoriello and G. Pedrizzetti, "Flow-tissue interaction with compliance mismatch in a model stented artery", eng, *Journal of Biomechanics*, vol. 37, no. 1, pp. 1–11, Jan. 2004 (Cited on page 74).

[245] A. J. Chorin, "A Numerical Method for Solving Incompressible Viscous Flow Problems", *Journal of Computational Physics*, vol. 135, no. 2, pp. 118–125, Aug. 1997. DOI: 10.1006/jcph.1997.5716 (Cited on page 79).

[246] F. Migliavacca, R. Balossino, G. Pennati, G. Dubini, T.-Y. Hsia, *et al.*, "Multiscale modelling in biofluidynamics: Application to reconstructive paediatric cardiac surgery", *Journal of Biomechanics*, vol. 39, no. 6, pp. 1010–1020, 2006. DOI: 10.1016/j.jbiomech.2005.02.021 (Cited on page 86).

[247] H. J. Kim, I. E. Vignon-Clementel, C. A. Figueroa, J. F. LaDisa, K. E. Jansen, *et al.*, "On Coupling a Lumped Parameter Heart Model and a Three-Dimensional Finite Element Aorta Model", en, *Annals of Biomedical Engineering*, vol. 37, no. 11, pp. 2153–2169, Nov. 2009. DOI: 10.1007/s10439-009-9760-8 (Cited on page 86).

[248] A. Quarteroni, A. Veneziani, and C. Vergara, "Geometric multiscale modeling of the cardiovascular system, between theory and practice", *Computer Methods in Applied Mechanics and Engineering*, vol. 302, pp. 193–252, Apr. 2016. DOI: 10.1016/j.cma.2016.01.007 (Cited on page 86).

[249] A. S. Liberson, Y. S. Vahedein, and D. A. Borkholder, "Variational Approach of Constructing Reduced Fluid-Structure Interaction Models in Bifurcated Networks", in *Proceedings of the 2nd World Congress on Momentum, Heat and Mass Transfer, Barselona*, 2017, pp. 6–8 (Cited on page 86).

[250] Y. Karnam, "Multiscale Fluid-Structure Interaction Models Development and Applications to the 3d Elements of a Human Cardiovascular System", *Theses*, Apr. 2019 (Cited on page 87).

[251] D. S. Mix, L. Yang, C. C. Johnson, N. Couper, B. Zarras, *et al.*, "Detecting Regional Stiffness Changes in Aortic Aneurysmal Geometries Using Pressure-Normalized Strain", *Ultrasound in Medicine & Biology*, vol. 43, no. 10, pp. 2372–2394, Oct. 2017. DOI: 10.1016/j.ultrasmedbio.2017.06.002 (Cited on page 89).

[252] Y. Seyed Vahedein and A. S. Liberson, "CardioFAN: Open source platform for noninvasive assessment of pulse transit time and pulsatile flow in hyperelastic vascular networks", en, *Biomechanics and Modeling in Mechanobiology*, May 2019. DOI: 10.1007/s10237-019-01163-z (Cited on pages 89, 96).

[253] P. Moireau, N. Xiao, M. Astorino, C. A. Figueroa, D. Chapelle, *et al.*, "External tissue support and fluid-structure simulation in blood flows", eng, *Biomechanics and Modeling in Mechanobiology*, vol. 11, no. 1-2, pp. 1–18, Jan. 2012. DOI: 10.1007/s10237-011-0289-z (Cited on page 93).

[254] P. J. Blanco, S. A. Urquiza, and R. A. Feijóo, "Assessing the influence of heart rate in local hemodynamics through coupled 3d-1d-0d models", en, *International Journal for Numerical Methods in Biomedical Engineering*, vol. 26, no. 7, pp. 890–903, Jul. 2010. DOI: 10.1002/cnm.1389 (Cited on page 95).

[255] P. J. Blanco, M. Discacciati, and A. Quarteroni, "Modeling dimensionally-heterogeneous problems: Analysis, approximation and applications", en, *Numerische Mathematik*, vol. 119, no. 2, p. 299, Jun. 2011. DOI: 10.1007/s00211-011-0387-y (Cited on page 95).

[256] Y. S. Vahedein, *YasharVahedein/CardioFAN: CardioFAN: Open Source Platform for Noninvasive Assessment of PTT and Pulsatile Flow in Hyperelastic Compliant Vascular Networks*, Dec. 2018. DOI: 10.5281/zenodo.1807137 (Cited on page 96).

[257] Yashar Seyed Vahedein and A. S. Liberson, "CardioFAN: Open Source Platform for Noninvasive Assessment of Pulse Transit Time and Pulsatile Flow in Hyperelastic Vascular Networks", (Cited on page 101).

[258] U. F. O. Themes, *Arterial Anatomy of the Extremities*, en-US, Mar. 2016 (Cited on page 107).

[259] L. L. Mertens, M. L. Rigby, E. S. Horowitz, and R. H. Anderson, "CHAPTER 18a - Cross Sectional Echocardiographic and Doppler Imaging", in *Paediatric Cardiology (Third Edition)*, R. H. Anderson, E. J. Baker, D. J. Penny, A. N. Redington, M. L. Rigby, *et al.*, Eds., Philadelphia: Churchill Livingstone, Jan. 2010, pp. 313–339. DOI: 10.1016/B978-0-7020-3064-2.00018-7 (Cited on page 110).

[260] J. T. Dodge, B. G. Brown, E. L. Bolson, and H. T. Dodge, "Lumen diameter of normal human coronary arteries. Influence of age, sex, anatomic variation, and left ventricular hypertrophy or dilation.", en, *Circulation*, vol. 86, no. 1, pp. 232–246, Jul. 1992. DOI: 10.1161/01.CIR.86.1.232 (Cited on pages 117, 137).

[261] D. A. Borkholder, N. J. Conn, and M. Haghpanahi, "Apparatus, System and Method for Medical Analyses of Seated Individual", en, pat. US20160374619A1, Dec. 2016 (Cited on page 118).

[262] M. C. Corretti, G. D. Plotnick, and R. A. Vogel, “The effects of age and gender on brachial artery endothelium-dependent vasoactivity are stimulus-dependent”, en, *Clinical Cardiology*, vol. 18, no. 8, pp. 471–476, 1995. DOI: 10.1002/clc.4960180810 (Cited on page 121).

[263] S. S. Thomas, V. Nathan, C. Zong, K. Soundarapandian, X. Shi, *et al.*, “BioWatch: A Noninvasive Wrist-Based Blood Pressure Monitor That Incorporates Training Techniques for Posture and Subject Variability”, *IEEE Journal of Biomedical and Health Informatics*, vol. 20, no. 5, pp. 1291–1300, Sep. 2016. DOI: 10.1109/JBHI.2015.2458779 (Cited on pages 126, 127).

[264] Y. Liu and Y. T. Zhang, “Pulse Transit Time and Arterial Blood Pressure at Different Vertical Wrist Positions”, en, p. 3, (Cited on pages 126, 127).

[265] H. Xiao, M. Butlin, I. Tan, and A. Avolio, “Effects of cardiac timing and peripheral resistance on measurement of pulse wave velocity for assessment of arterial stiffness”, En, *Scientific Reports*, vol. 7, no. 1, p. 5990, Jul. 2017. DOI: 10.1038/s41598-017-05807-x (Cited on page 130).

[266] S. S. Nijjer, G. A. de Waard, S. Sen, T. P. van de Hoef, R. Petraco, *et al.*, “Coronary pressure and flow relationships in humans: Phasic analysis of normal and pathological vessels and the implications for stenosis assessment: A report from the Iberian–Dutch–English (IDEAL) collaborators”, *European Heart Journal*, vol. 37, no. 26, pp. 2069–2080, Jul. 2016. DOI: 10.1093/eurheartj/ehv626 (Cited on page 130).

[267] J. R. Edwards and C. L. Cooper, “The impacts of positive psychological states on physical health: A review and theoretical framework”, *Social Science & Medicine*, vol. 27, no. 12, pp. 1447–1459, Jan. 1988. DOI: 10.1016/0277-9536(88)90212-2 (Cited on page 130).

[268] H. Xiao, M. Butlin, A. Qasem, I. Tan, D. Li, *et al.*, “N-Point Moving Average: A Special Generalized Transfer Function Method for Estimation of Central Aortic Blood Pressure”, *IEEE Transactions on Biomedical Engineering*, vol. 65, no. 6, pp. 1226–1234, Jun. 2018. DOI: 10.1109/TBME.2017.2710622 (Cited on pages 136, 140, 141).

[269] L. Smith, “New AHA Recommendations for Blood Pressure Measurement”, en, *American Family Physician*, vol. 72, no. 7, p. 1391, Oct. 2005 (Cited on page 136).

[270] E. Staff, *Blood Pressure Monitors: Wrist vs. Arm*, en-US, Feb. 2018 (Cited on page 136).

[271] “IEEE Standard for Wearable Cuffless Blood Pressure Measuring Devices”, *IEEE Std 1708-2014*, pp. 1–38, Aug. 2014. DOI: 10.1109/IEEESTD.2014.6882122 (Cited on page 136).

[272] S. Laurent, X. Girerd, J. J. Mourad, P. Lacolley, L. D. Beck, *et al.*, “Elastic modulus of the radial artery wall material is not increased in patients with essential hypertension.”, *Arteriosclerosis and thrombosis : a journal of vascular biology*, vol. 14, no. 7, pp. 1223–1231, 1994. DOI: 10.1161/01.ATV.14.7.1223 (Cited on page 137).

[273] M. Ryuzaki, S. Morimoto, M. Niiyama, Y. Seki, N. Yoshida, *et al.*, “The Relationships between the Differences in the Central Blood Pressure and Brachial Blood Pressure and Other Factors in Patients with Essential Hypertension”, *Internal Medicine*, vol. 56, no. 6, pp. 587–596, Mar. 2017 (Cited on page 139).

[274] M Radha, G Zhang, J Gelissen, K. d. Groot, R Haakma, *et al.*, “Arterial path selection to measure pulse wave velocity as a surrogate marker of blood pressure”, en, *Biomedical Physics & Engineering Express*, vol. 3, no. 1, p. 015 022, Feb. 2017. DOI: 10.1088/2057-1976/aa5b40 (Cited on page 142).

[275] *Handheld, portable ultrasound machine | Philips Lumify*, en-us (Cited on page 147).

# A

# Appendix A: Verification of TVD Algorithm and Comparison with Lax-Wendroff

## A.1 Test 1: *Sin* Shape Waveform with Undershoot

Schematic of a large and symmetric bifurcated structure with a single parent vessel and two daughter vessels are presented in Figure A.1. A single pulse with an undershoot is introduced at $X = 0.21\ m$ along the axis of the parent vessel (vessel 1). Using the TVD scheme, the propagation of the forward moving wave subject is simulated throughout vessels 1, 2 and 3. Outlets 2 and 3 are assigned with a no-reflection boundary conditions to prevent wave reflections. The complete physical time simulated was $t = 0.0312\ s$. Results presented in Fig. 1-3 correspond to the following input data: density $\rho$=0.25 $\frac{kg}{m^3}$ , Moens-Korteweg speed of propagation $C_{MK} = 2\frac{m}{s}$, initial velocity profile ($\frac{m}{sec}$)

$$V = 30\times\left(sin\left(\frac{\pi}{0.01}\times(X-0.21)\right)+cos\left(0.25\times\frac{\pi}{0.01}\times(X-0.21)\right)\right); \tag{A.1}$$

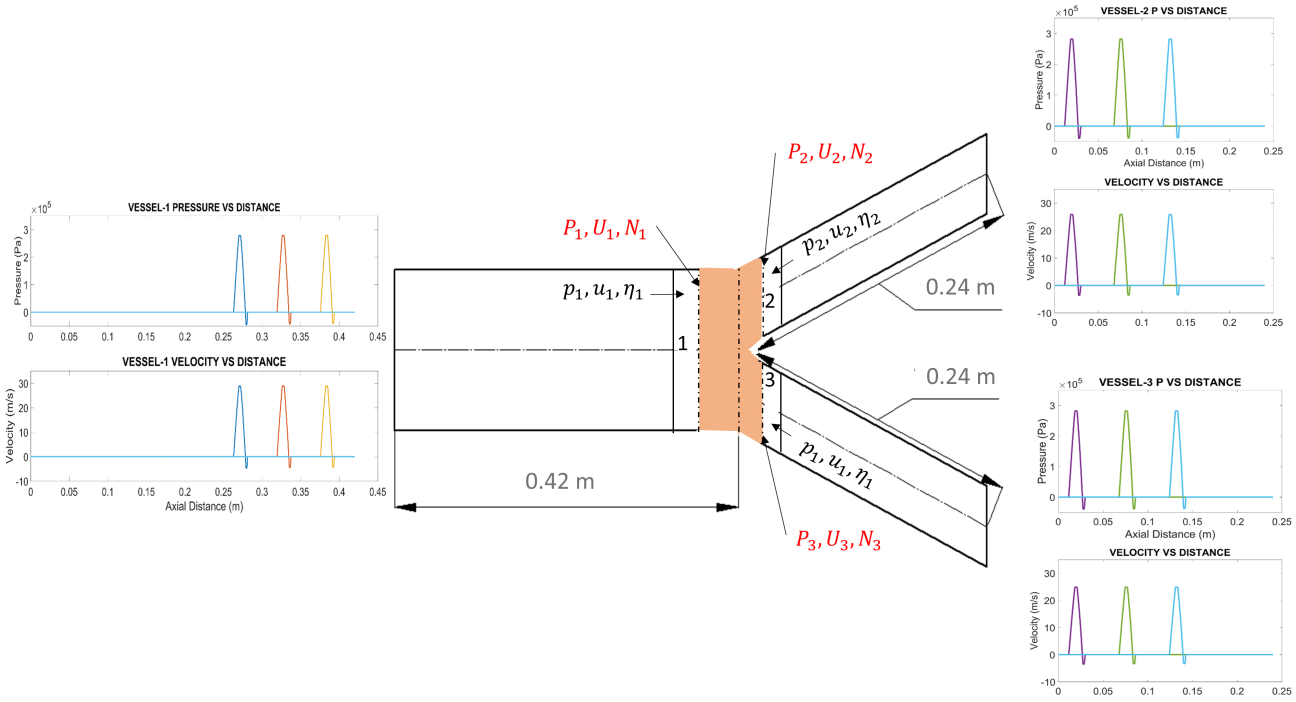


**Fig. A.1.** – Schematics of the bifurcated vessels and the pulse wave propagation at each vessel captured by TVD scheme.

As shown in this figure, the pressure and velocity waveform keep their shape and magnitude propagating down from vessel 1 and passing daughter vessels 2 and 3. Figure A.2 illustrates comparison of results obtained by TVD scheme with ones predicted by the Lax-Wendroff (LW) and Beam-Warming (BW) methods. Both LW and BW schemes are the finite volume methods with second-order of accuracy in time and space. As shown in figure A.2, LW and BW both efficiently approximate the wave in the continuous regions; however they show spurious numerical oscillations at the onset and after the wave undershoot, respectively. The latter indicates that LW and BW schemes are essentially dispersive schemes. In contrast, TVD method preserves the shape of the waveform in both continuous and discontinuous regions of the pulse wave.

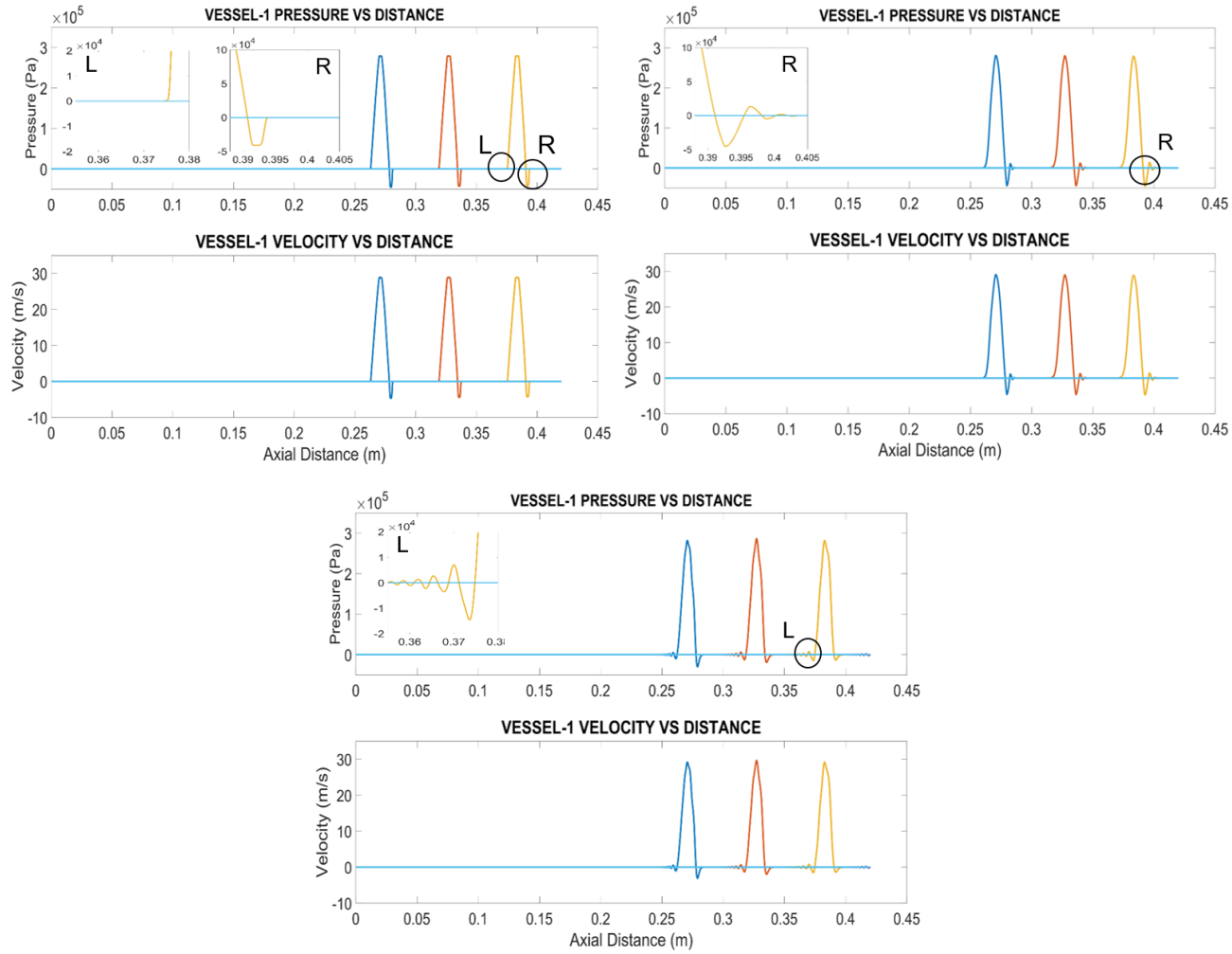


**Fig. A.2.** – From left to right and top to bottom: comparison of TVD; Beam-Warming; and Lax-Wendroff numerical methods in capturing the pressure and velocity sin wave (with undershoot) propagation in Vessel 1 ($t = 0.0312\ s$).

In addition the same behavior is observed in the daughter vessels, where TVD showing better performance in maintaining the shape of the waveform (Figure A.3).

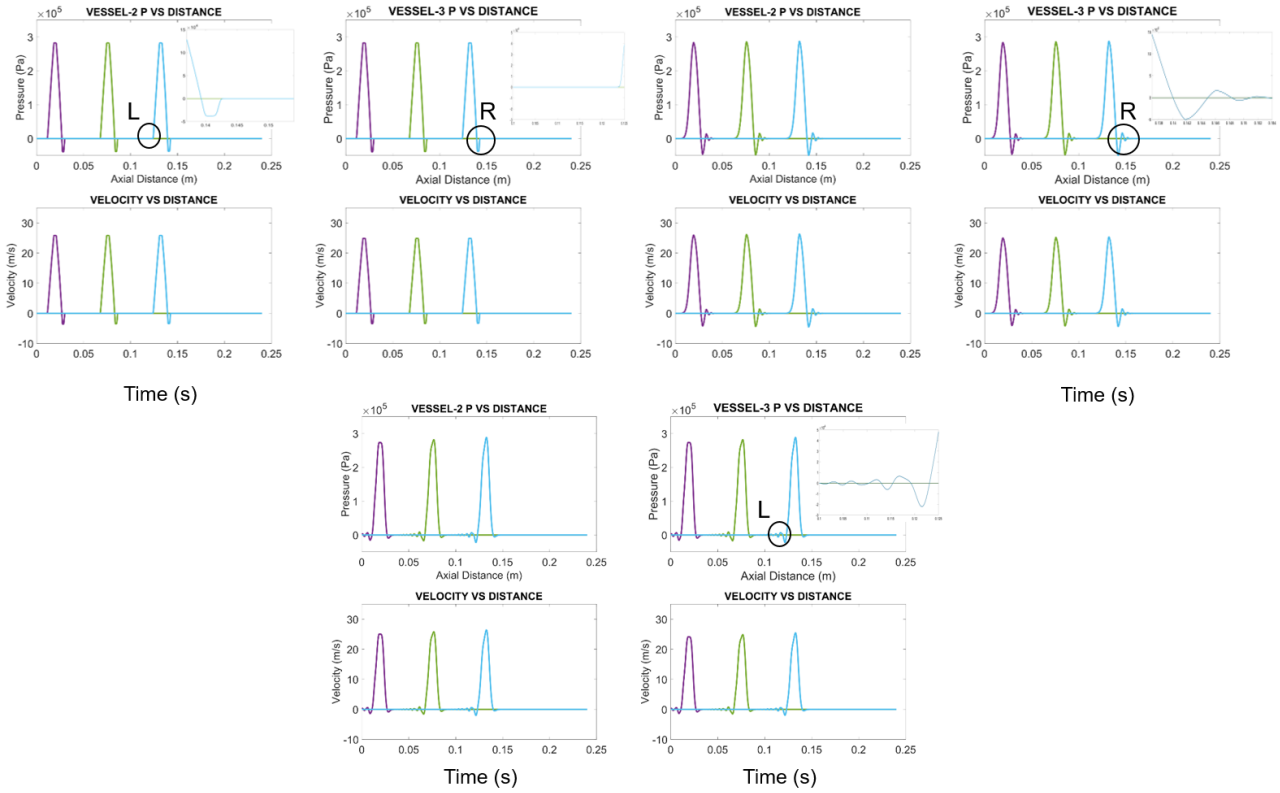


**Fig. A.3.** – From left to right and top to bottom: Comparison of TVD; Beam-Warming; and Lax-Wendroff numerical methods in capturing the pressure and velocity sin wave (with undershoot) propagation in Vessels 2 and 3 ($t = 0.0312\ s$).

In the zoomed-in pictures at each figure, the oscillations (dispersion) in BW and LW compared to TVD method can be seen more clearly.

### A.1.1 Test 2: Rectangular Pulse Waveform at Parent Vessel

A rectangular pulse in the middle of the parent vessel is introduced (figure A.4). The following properties are held the same as in previous section: $\rho$=0.25 $\frac{kg}{m^3}$ and $C_{MK} = 2\frac{m}{s}$. The step size is $0.02\ m$ and it starts at $X = 0.21\ m$. We compare the results of TVD scheme with Lax-Wendroff (L-W) and Beam-Warming (B-W) methods. Since the difference between the right and left side of the discontinuity is more severe, the dispersion effect manifests itself more clearly for B-W and L-W methods. As expected TVD scheme does not show any sign of dispersive effect and remains monotone. Any topological and material related alterations can cause dispersion in the circulatory system. Therefore, it is important to capture the shape of a moving pressure/velocity waveform without the loss in magnitude or monotonicity.

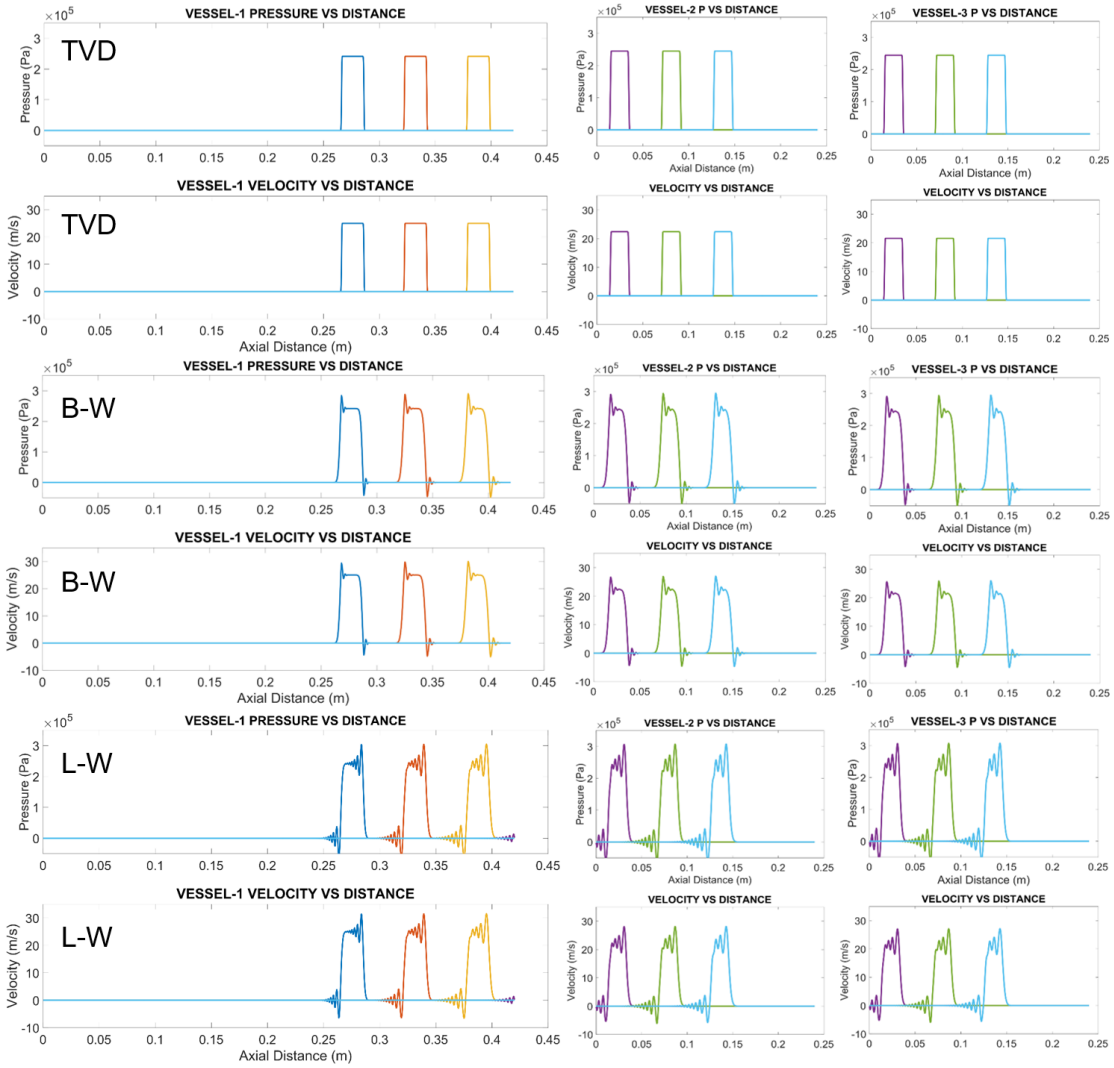


**Fig. A.4.** – From left to right and top to bottom: Comparison of TVD; Beam-Warming; and Lax-Wendroff numerical methods in capturing the pressure and velocity rectangular wave propagation in Vessels 1, 2 and 3 ($t = 0.0312\ s$).

The oscillatory behavior (in L-W and B-W) is amplifying as the pulse moves forward. In a circulatory system with variable vessel wall and compliance, these oscillations can lead to major errors in local predictions of pressure and velocity of the blood.

## A.2 Test 2: Break-Down Problem

Numerical solution of the break-down problem (or as it is commonly called Riemann problem) for the acoustics model, equation A.2, is simulated with the TVD and the Lax-Wendroff (figure A.5) methods.

$$\frac{\partial p}{\partial t}+\rho C^2\frac{\partial V}{\partial x}=0\frac{\partial V}{\partial t}+\frac{1}{\rho}\frac{\partial p}{\partial x}=0 \tag{A.2}$$

The solution was initialized with piece-wise constant initial pressure and velocity data (shown by the black line in Figures 14a and b). P and V values at the boundary were set to their constant initial values. The model runtime was set to stop before the wave front reach the boundaries. The same values of $\rho = 0.25\ \frac{kg}{m^3}$, $c = 2\frac{m}{s}$, Courant number $CFL = 0.5$ and cell count of N$= 100$ was used for both schemes. Discontinuity resolved by the TVD method, practically reproduces the exact solution (Figure 14a), whereas discontinuity simulated by the Lax-Wendroff method gives rise to artificial oscillations (Figure 14b). The Lax-Wendroff method is clearly dispersive, and does not perform well around discontinuities.

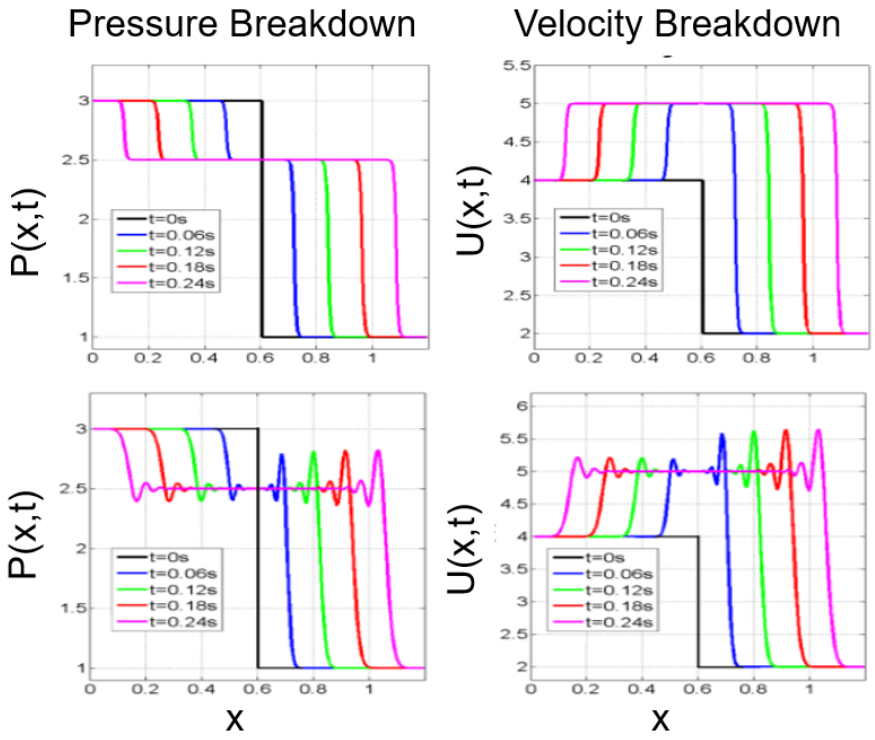


**Fig. A.5.** – TVD (top)versus LW method (bottom) in capturing introduced discontinuity, showing evolution of discontinuity.

## A.3 Test 3: *sin* Wave Introduced in the Middle of the Parent Vessel at a Bifurcation

Lastly, the effectiveness of TVD scheme in preserving the shape of a propagating wave is evaluated by introducing a single *sin* shape wave in the middle of the parent vessel. Figure 15 shows the propagation of this wave in a TVD based scheme compared to the Lax-Wendroff method. The flow properties similar are, $\rho$=0.25 $\frac{kg}{m^3}$ , $C_{mk} = 2$ $\frac{m}{s}$, $CFL = 0.25$ are used for both cases.

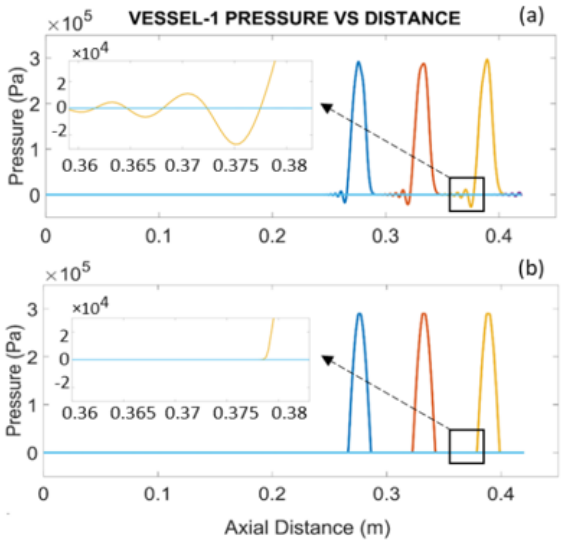


**Fig. A.6.** – Propagation of a *sin* pressure wave, starting from $x = 0.21\ m$ in the parent vessel. Lax-Wendroff based approximation (a), TVD based approximation (b)

It can be seen that small oscillations exist in the left side of the *sin* wave in case of the Lax-Wendroff approximation. These oscillations (dispersion) increases as the *sin* wave propagates forward. More testing cases demonstrating the advantage of TVD method are presented in [210].

# B

# Appendix B: Effect of Viscoelasticity on the Model of 37 Main Arteries

**Changes to the Lax-Wendroff Algorithm for Viscoelastic Properties:**

Viscoelastic properties are imposed to CardioFAN Viscoelastic solver using the measurements presented in Alastruey *et al.* [79], in which they experimentally measure the wall viscoelastic parameter $\Gamma$. Note that the definition for $\Gamma$ used here is based on viscoelastic equations presented in chapter 5 and is slightly different than [79]. In figure B.1, two sets of pressure waveform results along the aorta are compared; dotted lines are from in-house quasi 1D nonlinear model for a viscoelastic case, and thicker and thinner solid lines relate to values from measurements and elastic simulation, respectively. As hypothesized by Matthys *et al.*, we can see that the viscoelastic case has smoother results and thus closer to the experimentally measured pressures. CardioFan is capable of accounting for viscoelasticity as source terms of or inside the flux terms of the conservation equations. However, the results shown here are related to viscoelasticity applied as a source term. This technique changes the Lax-Wendroff formulation as follows:

For the $n^{th}$ node of a stencil

$$\dot{Q}_n = \mathrm{f}_n - [F(Q)]^{'}\ddot{Q}_n = \mathrm{f}_{n,n-1}\dot{Q}_{n-1} + \mathrm{f}_{n,n}\dot{Q}_n + \mathrm{f}_{n,n+1}\dot{Q}_{n+1} + \left[F_Q\dot{Q}\right]_n^{'} \tag{B.1}$$

where we have denoted $F_Q = \frac{\partial F}{\partial Q}; \quad \mathrm{f}_{n,k} = \frac{\partial f_n}{\partial Q_k}, \ k = n-1, n, n+1$. We now consider the Taylor series expansion truncated at the second order to yield solution at the following time level

$$Q^n = Q_n + \tau\dot{Q}_n(1 + \frac{\tau}{2}\mathrm{f}_{n,n}) + \frac{\tau^2}{2}(\mathrm{f}_{n,n-1}\dot{Q}_{n-1} + \mathrm{f}_{n,n+1}\dot{Q}_{n+1} + \left[F_Q\dot{Q}\right]_n^{'}) \tag{B.2}$$

where the superscript and subscript show the following and the current time levels, relating to the specified node number. The first order time derivatives in B.2 are replaced with the space coordinate differentiation according to the first equation B.1.

All simulation runs are assuming tapered cross sections for the arteries, and a 2666 kPa external pressure. The

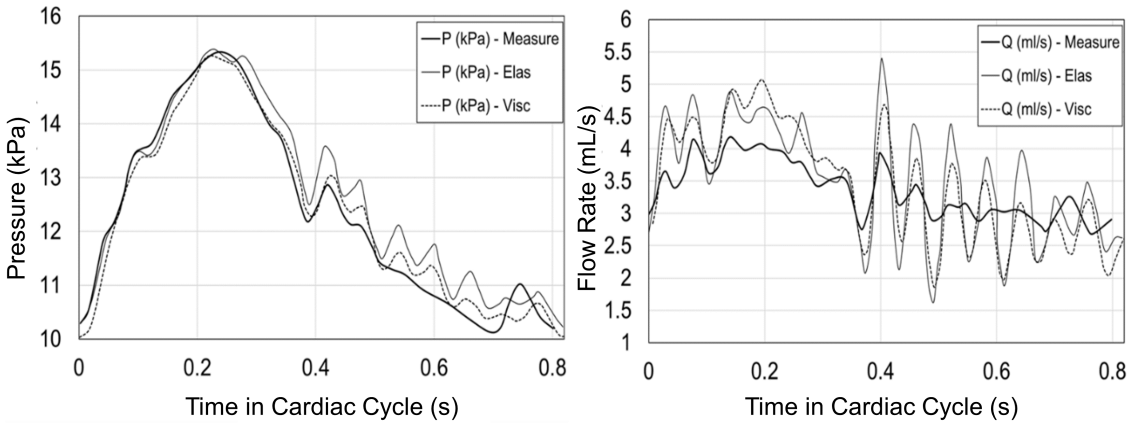


**Fig. B.1.** – Pressure and Flow waveforms at the ”Left Renal" artery (#24), for viscoelastic, elastic and experimental models. Elastic solution results and experimental measurements are reproduced from [79]

solution is for 10 cycles, and until a periodic solution is achieved. The difference between elastic and source-term based viscoelastic prediction is less than 0.5%.

# C

# Appendix C: Experimental Measurement Protocol

## C.1 Purpose of the Numerical Study

Demonstrate the accuracy of the procedure deriving the following cardiovascular markers: stroke volume (SV), cardiac output (CO), aortic blood pressure (BP), distensibility and compliance of aorta, - from peripheral pulse waveforms.

### C.1.1 Clinical Measurements Needed for the Numerical Code Calibration

*Measurements*

A two-step calibration procedure required, which includes personalization of the regional mechanical properties (session 1), and personalization of the Windkessel parameters in the outlet boundary conditions (sessions 2-5) at the truncated aorta and supra aortic branches. We have both activity and resting condition measurements in session 1, which is not required to be replicated at session 2. Therefore, sessions 2-5 can be conducted with the seating normal BP of the person coming in to the lab for the measurements at different days for 1 week.

## C.2 Clinical Validation of the Numerical Code

The same set of measurements relating to the FIT seat and cuff BP monitors, as shown in sessions 2-6, are required for validation. Therefore, at each of the sessions 2-6, an extra replicate set of measurements will be recorded to be used after completion of the tests for the validation of the predicted BP and SV as a function of

PTT. Data recorded in sessions 5 and 6 will be only used for validation, calibration in sessions 5 and 6 will be retained for reference only not to be used to calibrate the model.

### C.2.1 Session 1:

Geometric measurements. Collecting data to calibrate the mechanical properties.

Two sets of required recordings are specified below relating to the basic level of BP at rest condition (Condition 1) and an alternate BP condition as a result of a physical exercise: push-ups, sit-ups, cycling, etc., or drugs intake (Condition 2).

The systolic expansion and diastolic contraction diameters needs to be recorded using the doppler ultrasound at the same time as the upper arm BP recordings (leading to 2 systolic and 2 diastolic diameters). These measurements allow us to calibrate the nonlinear elastic constants for Fung's constitutive model by assuming a simple cylinder for the aorta and matching the measured and predicted diameters.

For condition 1 the following steps to record data are required:

1. Place the cuff on subject's bare left upper arm 1 inch above the bend of their elbow.

2. Instruct the subject to lay down in supine position as required for the doppler ultrasound.

3. Systolic and diastolic BPs will be recorded using the upper arm cuff BP monitor.

4. Aortic diameters during systolic expansion and diastolic contraction, at the same time as the BP measurements of previous bullet point, will be recorded using doppler ultrasound.

The subject should be asked to do one of the following activities, until they reach to 75% of their maximum Heart Rate (HR), to elevate the blood pressure: push-ups, sit-ups, cycling, etc., or drugs intake. For condition 2 the following steps to record data are required, immediately after reaching the desired HR:

1. Place the cuff on subject's bare left upper arm 1 inch above the bend of their elbow.

2. Instruct the subject to lay down in supine position as required for the doppler ultrasound.

3. Systolic and diastolic BPs will be recorded using the upper arm cuff BP monitor.

4. Aortic diameters during systolic expansion and diastolic contraction, at the same time as the BP measurements of previous bullet point, will be recorded using doppler ultrasound.

### C.2.2 Session 2:

Initial anatomical measurements,calibrating the windkessel constants and gathering validation data. Following Question will be asked from the subject prior to the start of the measurements.

1. Do you have a known medical condition or cardiovascular disease?

Following measurements are needed to be done just for the session 2:

1. Measure the distance (length) from upper arm, 1 inch above the inside bend of the elbow, to the wrist, 1/2 inch above the bottom of the palm, using a tape measure.

2. Measure the distance (length) from wrist, 1/2 inch above the bottom of the palm, to the tip of the index finger, using tape measure.

3. Measure the distance (length) from Upper arm, 1 inch above the bend of the elbow, to the approximate location of the heart, middle of the chest bone, using tape measure.

Calibrating the Windkessel constants. At the truncated aorta and supra aortic branches the windkessel boundary conditions are defined to control distribution of flow and total pressure between the analyzed and truncated branches; This requires a new set of calibration measurements. These measurements will be conducted with the FIT seat and using upper arm and wrist BP cuff monitors. All the following measurements are needed for both calibration and validation. PTT will be calculated based on BCG and PPG. To record wrist BP, subject's left arm and wrist need to be at the same level as their heart to get the most accurate measurement. The systolic

and diastolic BP recorded will be used to define a simplified time-dependent terminal boundary condition for the numerical model.

Using the left upper arm blood pressure and BCG the Windkessel boundary condition for truncated arteries and stroke volume will be calibrated. 3 replicates of each measurements are required to assure the accuracy of the calibration and accounting for the measurements variability. After this point 1 more replicate measurements will be recorded for model validation. Validation will be done after the completion of the tests.

At each session do the following measurements:

1. Normal sitting position, SV,ECG,BCG and with thigh PPG (90 seconds recoding)

2. Fingertip PPG with cloth covering ambient light (Left hand's thumb - 90 seconds recoding)

3. BCG

4. SV

5. ECG (or EKG)

6. PTT (From ejection to the tip of the left hand's thumb)

Instruct the subject to attach the wrist BP monitor while sitting on the FIT seat, then record:

1. Wrist BP, attached 1/2 inch above the bottom of the left palm

Instruct the subject to attach the Upper arm BP to their left arm, while sitting on the FIT seat, then record:

1. Upper arm BP (attached 1 inch above the bend of the left arm's elbow)

### C.2.3 Sessions 3, 4, 5 and 6:

Calibrating the Windkessel constants. At the truncated aorta and supra aortic branches the windkessel boundary conditions are defined to control distribution of flow and total pressure between the analyzed and truncated branches; This requires a new set of calibration measurements. These measurements will be conducted with the FIT seat and using upper arm and wrist BP cuff monitors. All the following measurements are needed for both calibration and validation. PTT will be calculated based on BCG and PPG. To record wrist BP, subject's left arm and wrist need to be at the same level as their heart to get the most accurate measurement. The systolic and diastolic BP recorded will be used to define a simplified time-dependent terminal boundary condition for the numerical model.

Using the left upper arm blood pressure and BCG the Windkessel boundary condition for truncated arteries and stroke volume will be calibrated. 3 replicates of each measurements are required to assure the accuracy of the calibration and accounting for the measurements variability. After this point 1 more replicate measurements will be recorded for model validation. Validation will be done after the completion of the tests.

At each session do the following measurements:

1. Normal sitting position, SV,ECG,BCG and with thigh PPG (90 seconds recoding)
2. Fingertip PPG with cloth covering ambient light (Left hand's thumb - 90 seconds recoding )
3. BCG
4. SV
5. ECG (or EKG)
6. PTT (From ejection to the tip of the left hand's thumb)

Instruct the subject to attach the wrist BP monitor while sitting on the FIT seat, then record:

1. Wrist BP, attached 1/2 inch above the bottom of the left palm

Instruct the subject to attach the Upper arm BP to their left arm, while sitting on the FIT seat, then record:

1. Upper arm BP (attached 1 inch above the bend of the left arm's elbow)

For each session repeat this process 4 times (4 replicates per session)

The forth replicate at each day is only required for validation, collecting wrist and arm BP, PTT and BCG. Wrist BP and PTT measurements are the inputs to predict SV and upper arm BP, which will be compared with SV and arm BP from measurements.

Retain the calibration data, obtained during the first three replicate measurements in sessions 5 and 6 for reference. This data will not be used in numerical model. The wrist BP and PTT from the last replicate measurement, related to the validation will be the only data that will be used in predictive model. The upper arm BP and SV calculated will be compared with the measured value.